

# 稀薄气体动力学

吴雷 李琪 编著

## 目 录

第 1 章 绪论 .....	1
1.1 气体的性质 .....	1
1.1.1 气体分子间的相互作用 .....	1
1.1.2 理想气体 .....	1
1.1.3 压强、温度、内能 .....	1
1.1.4 平均自由程 .....	1
1.1.5 简单输运现象 .....	1
1.2 Navier-Stokes-Fourier equations .....	2
1.3 Continuum breakdown .....	3
1.3.1 Reentry of space vehicle .....	3
1.3.2 Microelectromechanical systems .....	4
1.3.3 Shale gas extraction .....	5
1.3.4 Global wind profiling .....	6
1.4 Simple gas kinetic theory .....	7
1.5 Knudsen number .....	9
1.5.1 Spatial Knudsen number .....	9
1.5.2 Temporal Knudsen number .....	12
1.6 Molecular dynamics simulations .....	13
第 2 章 气体动理论 .....	15
2.1 理想气体 .....	15
2.2 速度分布函数与宏观量 .....	15
2.3 Boltzmann 方程 .....	15
2.3.1 偏转角和微分散射截面 .....	17
2.3.2 熵增原理 .....	19
2.3.3 线性化玻尔兹曼方程 .....	20
2.3.4 输运系数和弛豫率：表象与本质 .....	22
第 3 章 Fluid-dynamic Equations .....	26
3.1 Hilbert expansion .....	26
3.2 Chapman-Enskog expansion .....	27

---

3.3	Moment methods .....	32
3.4	Accuracy of macroscopic equations .....	34
3.5	Convergence speed of moment equations.....	40
第 4 章	快速谱方法.....	44
4.1	Inverse design of collision kernel .....	44
4.1.1	Power-law potential.....	44
4.1.2	Lennard-Jones potential.....	46
4.2	Normalization.....	47
4.3	Fast spectral method .....	48
4.3.1	Carleman representation .....	49
4.3.2	Fourier-Galerkin spectral method.....	50
4.3.3	Detailed implementation .....	54
4.3.4	Non-uniform discretization of velocity space .....	56
4.4	Accuracy in homogeneous relaxation .....	57
4.4.1	Bobylev-Krook-Wu solution .....	57
4.4.2	Discontinuous velocity distribution function.....	60
4.5	Accuracy in inhomogeneous problems.....	62
4.5.1	Normal shock waves.....	62
4.5.2	Force-driven Poiseuille flows .....	64
4.5.3	Thermal transpiration.....	65
4.6	Linearization .....	68
4.6.1	Lennard-Jones potential .....	70
4.6.2	Accurate transport coefficients.....	71
4.6.3	Poiseuille flow.....	72
4.7	Concluding remarks.....	73
第 5 章	单原子气体的简化动理论模型.....	74
5.1	模型方程 .....	74
5.1.1	BGK 模型.....	74
5.1.2	ES-BGK 模型 .....	75
5.1.3	Shakhov 模型.....	76
5.1.4	Gross-Jackson 模型及其非线性化.....	76

第 6 章 合成迭代加速算法.....	79
6.1 Problems of CIS .....	79
6.1.1 Slow convergence.....	79
6.1.2 False convergence.....	81
6.2 General synthetic iterative scheme.....	82
6.2.1 Scheme-I GSIS .....	83
6.2.2 Scheme-II GSIS .....	85
6.3 Properties of GSIS .....	85
6.3.1 Super convergence .....	85
6.3.2 Asymptotic preserving .....	87
6.4 Numerical tests .....	88
6.4.1 Coherent Rayleigh-Brillouin scattering.....	89
6.4.2 Planar Fourier flow .....	91
6.4.3 Couette flow between eccentric cylinders .....	94
6.5 Concluding remarks and Outlooks.....	95
第 7 章 Couette 流动.....	97
7.1 Planar Couette flow .....	97
7.2 Viscous slip .....	97
7.2.1 Viscous slip coefficient.....	98
7.2.2 Knudsen layer function .....	99
7.2.3 Comparison with experiments.....	103
7.3 Planar Fourier flows .....	106
7.4 Thermal transpiration.....	106
7.5 Poiseuille flow .....	108
7.5.1 Onsager-Casimir relation .....	112
7.6 Influence of intermolecular potential .....	113
7.7 Cercignani-Lampis boundary condition.....	113
7.7.1 Poiseuille flow through parallel plates .....	113
7.7.2 Poiseuille flow through long tube.....	115
第 8 章 分子气体的简化动理论模型.....	119
8.1 分子气体的特性 .....	119
8.1.1 体积粘性.....	121
8.1.2 热导率.....	122

8.1.3 DSMC 中的热弛豫速率 .....	124
8.2 分子气体的动理论模型及精度 .....	126
8.2.1 Hanson-Morse 线性化模型 .....	127
8.2.2 Hanson-Morse 模型的约化及非线性化 .....	129
8.2.3 非线性模型 .....	131
8.2.4 模型方程精度比较 .....	134
8.3 热弛豫速率不确定度量化 .....	138
8.3.1 正激波 .....	138
8.3.2 麦克斯韦妖驱动的微流动 .....	139
8.4 确定热流弛豫速率的方法 .....	140
8.4.1 分子动力学模拟 .....	140
8.4.2 瑞利-布里渊散射 .....	141
8.4.3 氮气分子的体积粘性与 Eucken 因子 .....	142
8.4.4 Bulk viscosity and Eucken factor of N <sub>2</sub> .....	142
8.5 总结与展望 .....	144
<b>第 9 章 Slip and Jump Coefficients .....</b>	<b>152</b>
9.1 State of the problem .....	152
9.2 Thermal slip .....	153
9.2.1 Thermal slip coefficient .....	153
9.2.2 Knudsen layer function .....	156
9.2.3 Molecular gases .....	157
9.2.4 Comparison with experiments .....	159
9.3 Temperature jump .....	162
参考文献 .....	167



## 第1章 绪论

Several engineering applications where the Navier-Stokes-Fourier equations fail to predict the behavior of rarefied gas flows are introduced, as well as the simple gas kinetic theory and molecular dynamics simulation.

### 1.1 气体的性质

一定宏观体积的气体由大量分子组成，这些分子以相当不规则的方式不断地运动。其运动状态的改变由分子间的相互作用力决定。一般用 Lennard-Jones 势描述分子间相互作用

$$\phi(r) = 4\epsilon \left[ \left( \frac{d_{LJ}}{r} \right)^{12} - \left( \frac{d_{LJ}}{r} \right)^6 \right], \quad (1-1)$$

where  $\epsilon$  is the potential depth and  $d_{LJ}$  is the distance at which the potential between two molecules is zero.

这种巨大的自由度使得每个分子的轨迹变得不可能。

#### 1.1.1 气体分子间的相互作用

#### 1.1.2 理想气体

#### 1.1.3 压强、温度、内能

#### 1.1.4 平均自由程

#### 1.1.5 简单输运现象

## 1.2 Navier-Stokes-Fourier equations

The fundamental and practical task in the study of gas dynamics is to obtain the macroscopic quantities, such as the mass density  $\rho$ , bulk velocity  $\mathbf{u}$ , temperature  $T$ , pressure tensor  $\mathbf{p}$ , and heat flux  $\mathbf{q}$ . Traditionally, the gas is treated as a continuum and the following equations are built based on the mass, momentum, and energy conservation:

$$\begin{aligned} \frac{\partial \rho}{\partial t} + \frac{\partial(\rho u_j)}{\partial x_j} &= 0, \\ \frac{\partial(\rho u_i)}{\partial t} + \frac{\partial(\rho u_i u_j + p_{ij})}{\partial x_j} &= \rho a_i, \\ \frac{\partial(\rho E)}{\partial t} + \frac{\partial(\rho E u_j + u_i p_{ij} + q_j)}{\partial x_j} &= \rho a_j u_j, \end{aligned} \quad (1-2)$$

where  $t$  is the time,  $\mathbf{x} \equiv (x_1, x_2, x_3)$  is the spatial Cartesian coordinates,  $\mathbf{a} \equiv (a_1, a_2, a_3)$  is the external acceleration, and  $E \equiv e + u_i u_i / 2$  is the specific energy with  $e$  being the specific internal energy that is a function of temperature  $T$ . The subscripts  $i, j, k = 1, 2, 3$  represent the three orthogonal spatial directions, and the Einstein summation convention is used.

Equation (2-29) is not closed because expressions for the pressure tensor  $\mathbf{p}$  and heat flux  $\mathbf{q}$  can not be determined from conservation laws. Usually, the phenomenological and empirical constitutive relations are adopted, e.g., Newton's law of viscosity

$$p_{ij} = \frac{\rho k_B T}{m} \delta_{ij} - \mu \left( \frac{\partial u_i}{\partial x_j} + \frac{\partial u_j}{\partial x_i} - \frac{2}{3} \frac{\partial u_k}{\partial x_k} \delta_{ij} \right) - \mu_b \frac{\partial u_k}{\partial x_k} \delta_{ij}, \quad (1-3)$$

and Fourier's law of heat conduction

$$q_i = -\kappa \frac{\partial T}{\partial x_i}, \quad (1-4)$$

where  $k_B$  is the Boltzmann constant,  $m$  is the molecular mass,  $\delta$  is the Kronecker delta,  $\mu$  is the shear viscosity,  $\mu_b$  is the bulk viscosity, and  $\kappa$  is the thermal conductivity.

Together with the non-velocity-slip and non-temperature-jump conditions at the solid surface, the Navier-Stokes-Fourier (NSF) equations have found a wide range of engineering applications.

## 1.3 Continuum breakdown

However, in some extreme conditions, the gas dynamics predicted by NSF equations can differ from experimental results significantly. The gas flow where the traditional NSF equations fail is called rarefied gas flow, and its dynamics is rarefied gas dynamics (RGD).

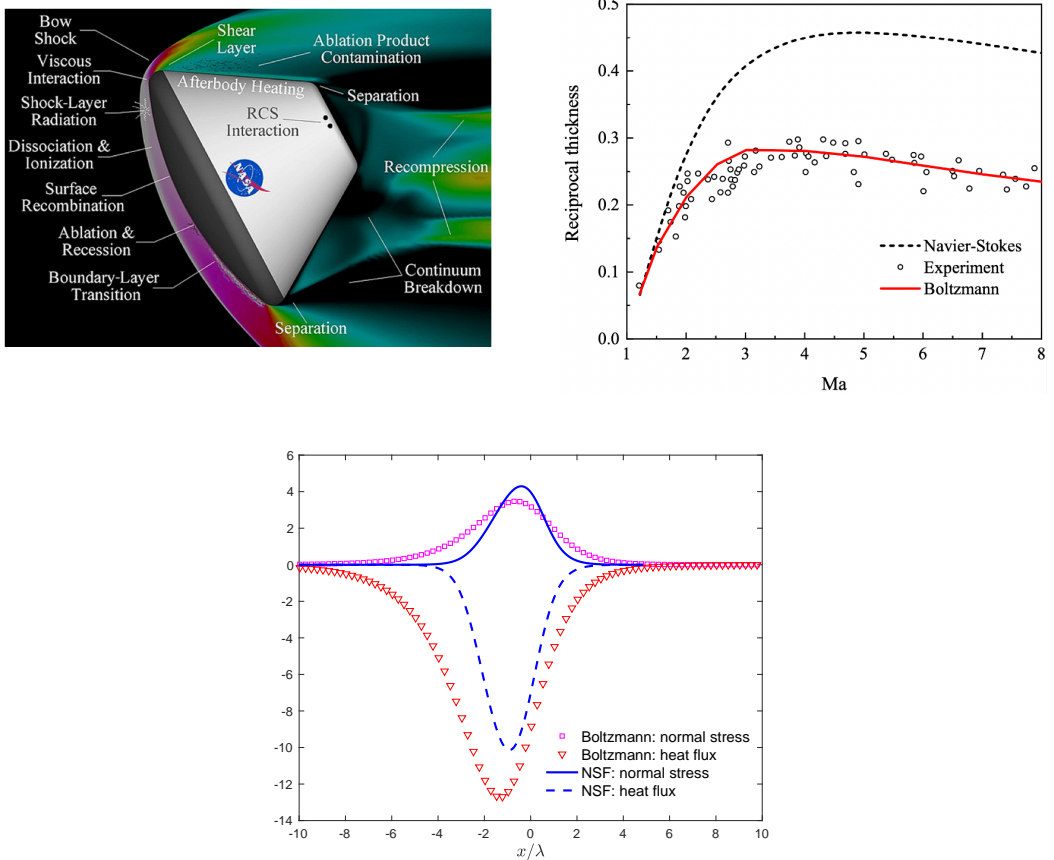


图 1-1 (Left) Complicated gas dynamics around the reentry capsule (image credit: NASA). (Right) Inverse thickness of the normal shock wave of argon as a function of the Mach number [2]. (Bottom) Dimensionless normal stress and heat flux of argon shock wave with a Mach number of 4; the distance is normalized by the mean free path ( $\lambda$ ) of the gas in upstream.

It is also called non-equilibrium gas dynamics because, as we shall see in later chapters, the velocity distribution function of gas molecules departs from the Maxwell equilibrium distribution significantly. Sometimes it is also called non-continuum gas dynamics. This is because the basic assumption in continuum mechanics that “the stress at a point is related to the strain and the rate of change of strain with respect to time at the same point” is violated.

Typical examples of rarefaction effects that lead to non-intuitive phenomena beyond the description of NSF equations, with applications from the sky, earth surface, and underground, are briefly illustrated below.

### 1.3.1 Reentry of space vehicle

Figure 1-1 sketches the complex flow physics around a reentry vehicle, where the reentry speed is about 8 km/s. Due to the violent interaction with atmosphere, a strong bow shock wave is generated in front of the vehicle. Intermolecular collisions also pro-

mote energy exchanges among the translational and internal (rotational, vibrational and electronic) modes, and eventually leads to non-equilibrium chemical reactions. Behind the shock wave, a massive amount of the kinetic energy of free stream is converted into the internal energy of surrounding gas, resulting in intense convective and radiative heating to the space vehicle. Meanwhile, supersonic expansion, flow separation, re-circulation, and re-compression take place as the flow passes through the vehicle.

Even for the simple normal shock wave, the NSF equations fail to predict its thickness when the Mach number is larger than 2. Although the thickness of shock wave is only a few mean free path (MFP, the average distance traveled by a moving molecule) of gas molecules, in high altitude flight it is comparable to the dimension of space vehicle and hence the rarefaction effects are significant. On the contrary, the Boltzmann equation well predicts the thickness of normal shock wave over a wide range of Mach number. When the Mach number is 4, the normal stress and heat flux predicted from NSF equations are quite different from those of the Boltzmann equation, which further confirms the failure of NSF equations. In-depth knowledge of RGD is key to predicting/controlling the entry of space objects.

### 1.3.2 Microelectromechanical systems

The rarefied gas flow at the micro-scale has a broad range of industrial applications, and has attracted particular attention due to the rapid development of microelectromechanical systems [50]. At small length scale, and sometimes the high oscillation frequency, the NSF equations loss validity.

Figure 1-2 shows the sound resonance between the transducer and receiver, where the sound pressure at the receiver is a function of the oscillation frequency  $\varpi$  and propagation distance  $L$ . When  $\varpi$  is 0.3 times of the mean collision frequency of gas molecules  $\bar{\nu}$ ,

$$\bar{\nu} = \frac{1}{\tau_c} = \frac{p}{\mu}, \quad (1-5)$$

the NSF equations fail to predict the sound pressure at the receiver; other high-order macroscopic equations, like the regularized 13 and 26 moment equations derived from the Boltzmann equation [112, 38], however, can well predict the sound pressure. When  $\varpi$  is increased to  $1.09\bar{\nu}$ , the difference between NSF predictions and experimental data further enlarges, and regularized 13 and 26 moment equations fail too. However, the Boltzmann equation predicts the sound pressure well [140].

## 声波中的自由度冻结

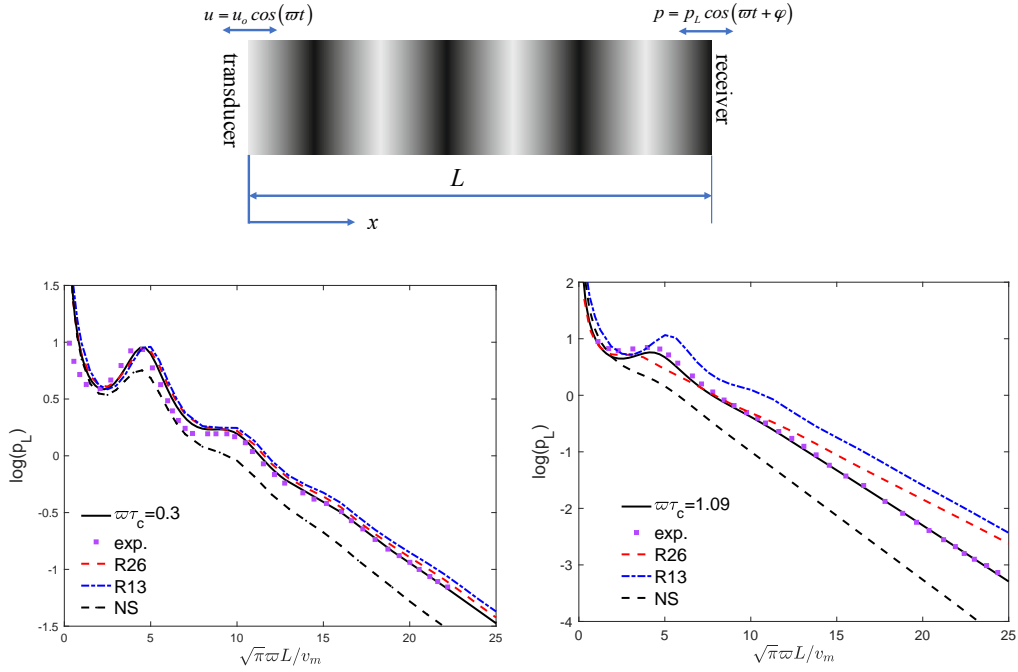


图 1-2 (Top) Sound propagation between transducer and receiver. (Bottom) Dimensionless sound amplitude  $p_L$  at the receiver as a function of the dimensionless length  $\sqrt{\pi\omega}L/v_m$ , where  $\varphi$  is the sound frequency and  $v_m$  is the most probable speed of gas molecules. Experimental data are collected from Ref. [99] when the gas medium is helium. Solid lines represent the numerical solutions of the Boltzmann equation with the diffuse boundary condition [140]. R13 and R26: the regularized 13 and 26 moment equations derived from the Boltzmann equation, which are more accurate than the NSF equations.

### 1.3.3 Shale gas extraction

Unconventional gas reservoirs have attracted significant attention due to the shale gas revolution, but the accurate prediction of gas production is a grand research challenge. In shale gas exploitation, the gas pressure could reach hundreds times of atmospheric pressure, but the flow passage is at the nanometer scale. Although the gas is dense [148, 142], its flow dynamics can still be rarefied<sup>①</sup>. Experimental data on gas flow through porous media is hard to measure and interpret, so we introduce the experiment of micro gas flow to demonstrate the influence of rarefaction effects [23].

The duct shown in the inset of Fig. 1-4 has a cross-section dimension of  $9.38 \mu\text{m} \times 492 \mu\text{m}$ , which is connected to two large reservoirs at the ends. Given the inlet and outlet pressures ( $p_{in}$  and  $p_{out}$ , respectively), the mass flow rate (MFR,  $\dot{M}$ ) is measured when the steady-state of the flow is reached. Then the normalized MFR

$$G = \frac{L\sqrt{2k_B T_0/m}}{H^2 w (p_{in} - p_{out})} \dot{M}, \quad (1-6)$$

<sup>①</sup> The antonym of “dense gas” is “dilute gas”, while the “rarefied gas” is referred to the gas in which the flow cannot be adequately described by NSF equations.

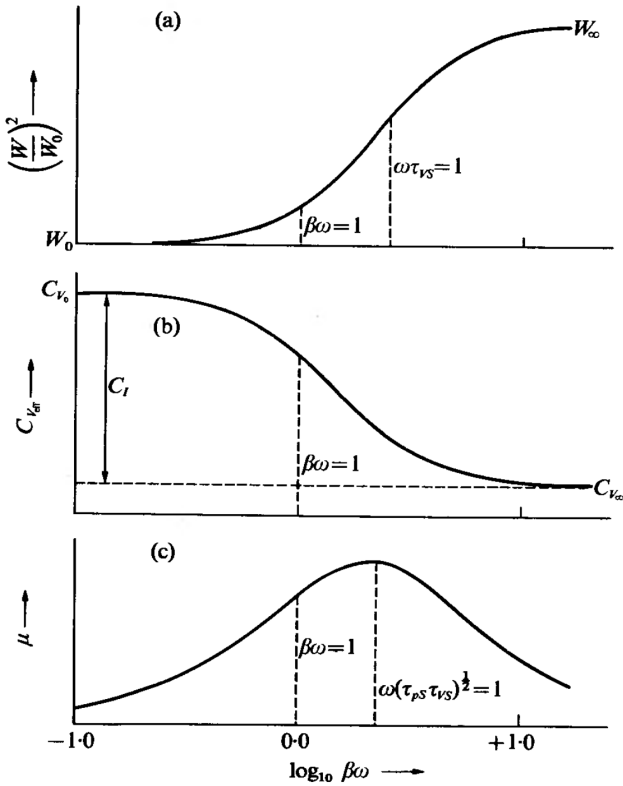


图 1-3 声波中的等效声速、等容热容和衰减率随声波频率的变化关系 [56]。

is plotted against the mean gas pressure  $p$ . At large gas pressures the NSF equations predict the MFR well. However, when the gas pressure is reduced, the normalized MFR predicted by NSF equations always decreases, while that from the experiment first decreases and then increases, resulting in the famous phenomenon of “Knudsen minimum”. At low pressures, the NSF equations could underpredict the MFR by several orders of magnitude; even with the correction of wall slip velocity, they underpredict the MFR by several times.

### 1.3.4 Global wind profiling

In 2018, the European Space Agency launched the satellite ADM-Aeolus to measure the global wind profile for an improved understanding of atmospheric dynamics. The ADM-Aeolus mission makes use of the Doppler Wind Lidar measurement technique, and the spectrum of scattered light is important for the accurate retrieval of wind profile. Due to the high scattering frequency and short laser wavelength, as compared respectively to the mean collision frequency and mean free path of gas molecules, the gas dynamics is not in equilibrium, and the NSF equations have large error, see Fig. 1-5.

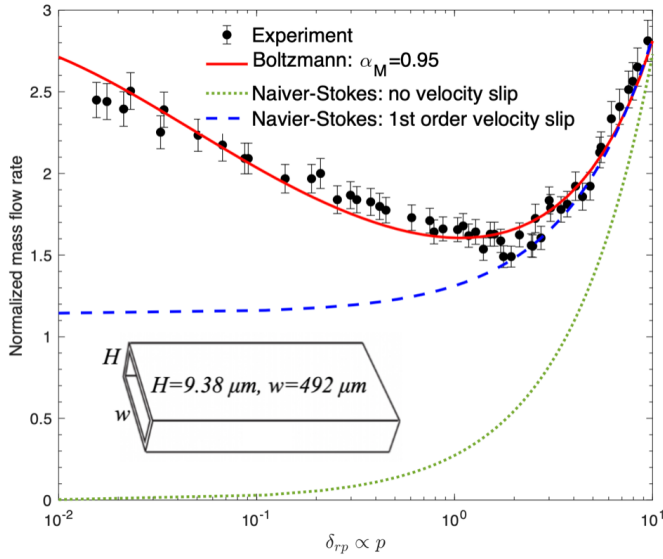


图 1-4 The normalized mass flow rate as a function of the rarefaction parameter (1-12), for the gas flow through a long and narrow duct [23, 145].

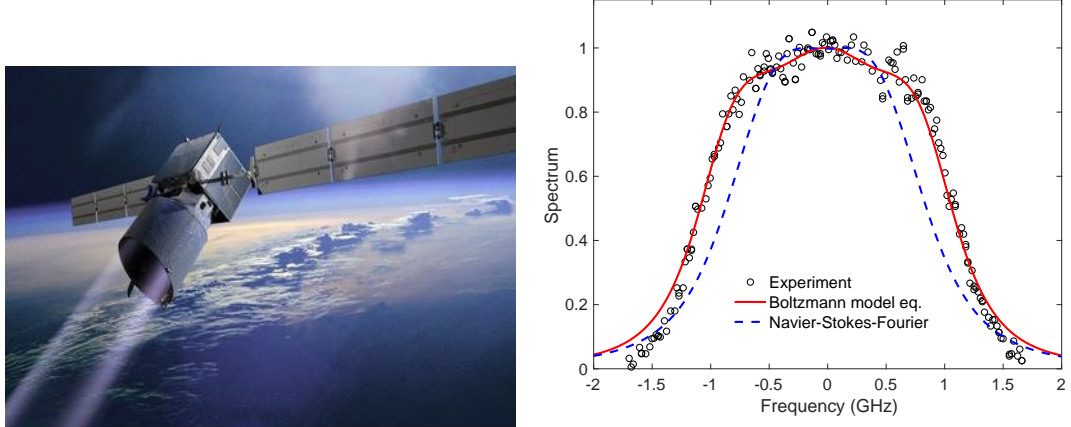


图 1-5 Comparisons in the spectra of spontaneous Rayleigh-Brillouin scattering between the experimental data [36], the linearized Boltzmann equation [140] (see Chapter ??), and the NSF equations. The light is scattered from CO<sub>2</sub> with zero flow velocity, at a pressure of 770 mm of Hg. The Knudsen number (1-10) is Kn = 0.14.

## 1.4 Simple gas kinetic theory

The breakdown of NSF constitutive relations may be understood qualitatively from the simple kinetic theory, which not only allows the estimation of transport coefficients such as the shear viscosity, thermal conductivity and self-diffusion coefficient, but also indicates the origin of rarefaction effects.

Consider a gas of hard-spheres (HS) of diameter  $\sigma$  and number density  $n$ , traveling with the average speed  $\bar{c}$ . Imagine a gas molecule moves through the gas with the average relative speed  $\sqrt{2}\bar{c}$ , while other molecules are fixed. During the time interval  $\Delta t$  the moving molecule sweeps a volume of  $\Delta V = \sqrt{2}\pi\sigma^2\bar{c}\Delta t$ , which encounters collisions

with  $n\Delta V$  molecules. Hence the average time for one collision is  $\tau_c = 1/\sqrt{2}n\pi\sigma^2\bar{c}$ , and the MFP is

$$\lambda = \bar{c}\tau_c = \frac{1}{\sqrt{2}n\pi\sigma^2}. \quad (1-7)$$

In simple kinetic theory it is assumed that one sixth of the molecules moves into each of the 6 directions of space, and within one mean free path there are no collisions among gas molecules (hence it can be derived from the ideal gas law  $p = nk_B T$  that the average speed is  $\bar{c} = \sqrt{3k_B T/m}$ ). Therefore, the number flux (the number of gas molecules per unit area per unit time) through a plane perpendicular to the  $x_1$ -axis is

$$J_1 = \frac{n(x_1 - \lambda)}{6}\bar{c} - \frac{n(x_1 + \lambda)}{6} \approx -\frac{\bar{c}}{3}\lambda \frac{dn}{dx_1}. \quad (1-8)$$

Similarly, the shear stress (momentum flux) and heat flux (due to the translational motion only) are

$$\begin{aligned} \sigma_{12} &= \frac{mn\bar{c}}{6} [u_2(x_1 - \lambda) - u_2(x_1 + \lambda)] \approx -\frac{mn\bar{c}}{3}\lambda \frac{\partial u_2}{\partial x_1}, \\ q_1 &= \frac{mn\bar{c}}{6} \left[ \frac{3}{2} \frac{k_B}{m} T(x_1 - \lambda) - \frac{3}{2} \frac{k_B}{m} T(x_1 + \lambda) \right] \approx -\frac{nk_B\bar{c}}{2}\lambda \frac{\partial T}{\partial x_1}, \end{aligned} \quad (1-9)$$

therefore the diffusion coefficient, shear viscosity, and thermal conductivity are respectively

$$D = \frac{\bar{c}}{3}\lambda, \quad \mu = \frac{mn\bar{c}}{3}\lambda, \quad \kappa = \frac{nk_B\bar{c}}{2}\lambda. \quad (1-10)$$

It is clear from Eqs. (1-7) and (1-8) that these transport coefficients are derived only when the first-order Taylor expansion is used; this requires the fluid system varies slowly on a spatial scale of the size of MFP, otherwise higher-order expansions are needed, and the constitutive relations will go beyond Newton's law of stress and Fourier's law of heat conduction. Therefore, the degree of rarefaction effects can be characterized by the ratio of mean free path to the characteristic flow length in which the macroscopic quantities vary.

## 1.5 Knudsen number

The RGD emerges in extreme conditions where the gas density is low, the characteristic flow length is small, and/or when the oscillation frequency is high. This brings us to the introduction of dimensionless parameter, the Knudsen number, to approximately measure the degree of non-equilibrium.

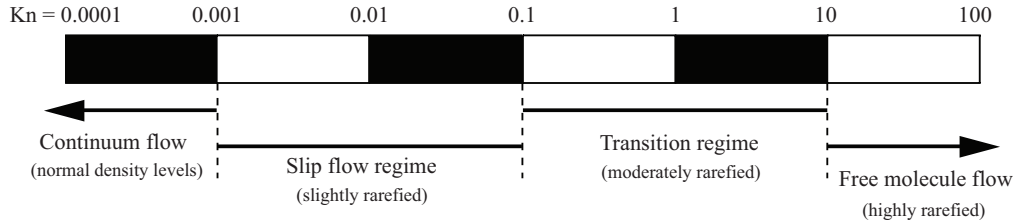


图 1-6 Flow regime classification based on the spatial Knudsen number [129, 27].

### 1.5.1 Spatial Knudsen number

The Knudsen number, defined as the ratio of the molecular MFP  $\lambda$  to the characteristic flow length  $L$ , is widely used:

$$\text{Kn} = \frac{\lambda}{L}, \quad (1-11)$$

where the MFP can be defined in terms of the shear viscosity as

$$\lambda = \frac{\mu}{p} \sqrt{\frac{\pi k_B T_0}{2m}}, \quad (1-12)$$

rather than Eq. (1-6) that is derived from the simple kinetic theory based on HS molecular model. This is obvious because for other types of intermolecular potential it is difficult to determine the molecular diameter.

This Knudsen number is known as the spatial Knudsen number as spatial length scales are involved. Note that sometimes the rarefaction parameter, which is inversely proportional to the spatial Knudsen number, is used instead:

$$\delta_{rp} = \frac{pL}{\mu v_m} = \frac{\sqrt{\pi}}{2\text{Kn}}. \quad (1-13)$$

This parameter appears in the kinetic model equations when the Boltzmann collision operator is simplified.

As shown in Fig. 1-6, the spatial Knudsen number is used to classify the gas flow into four regimes [129, 27]:

- Continuum flow regime. When  $\text{Kn} \lesssim 0.001$ , the NSF equations with the non-velocity-slip and non-temperature-jump boundary conditions are adopted to describe the gas dynamics<sup>①</sup>.
- Slip flow regime. When  $0.001 \lesssim \text{Kn} \lesssim 0.1$ , weak rarefaction effects such as the velocity slip and temperature jump emerge in the Knudsen layer, i.e., a small region within a few MFP away from the solid wall. With appropriate velocity-slip and temperature-jump

<sup>①</sup> There are some exceptions, where the NSF equations do not describe the gas dynamic accurately even when  $\text{Kn}$  approaches zero. For example, the ghost effect induced by the periodical variation of wall temperature [111].

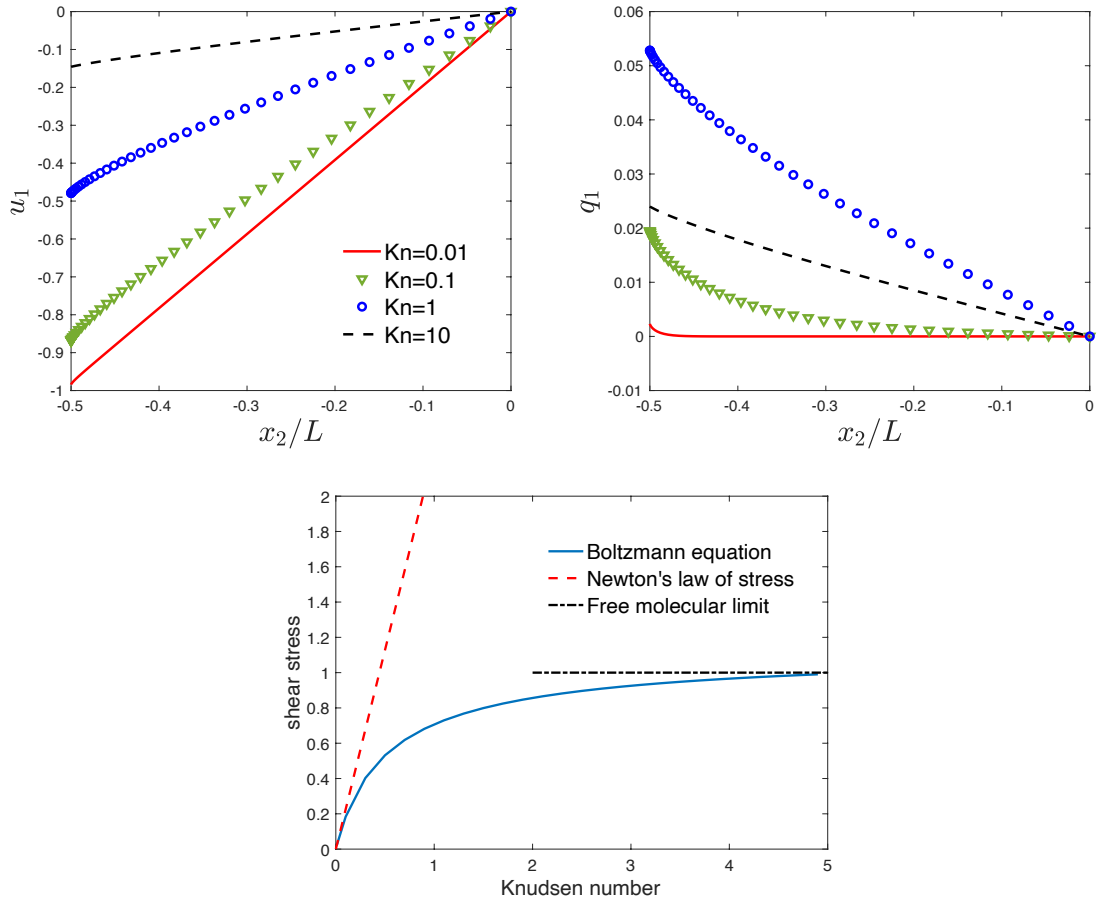


图 1-7 The flow velocity (normalized by wall velocity), heat flux (normalized by the product of gas pressure and wall velocity), and shear stress (normalized by the product of gas pressure and dimensionless velocity  $u_w / \sqrt{2k_B T_w / m}$ ) of the planar Couette flow at different values of spatial Knudsen number, obtained from the linearized Boltzmann equation for HS gas with the diffuse boundary condition.

boundary conditions, the NSF equations may still produce reasonable results.

- Transition flow regime. When  $0.1 \lesssim \text{Kn} \lesssim 10$ , strong rarefaction effects modify the constitutive relations as assumed in continuum mechanics so that the NSF equations break down completely, and gas-kinetic equations such as the Boltzmann equation is used to describe rarefied gas flows [20].

- Free-molecular flow regime. When  $\text{Kn} \gtrsim 10$ , the collision between gas molecules do not play an important role, while the collision between the gas and wall molecules (gas-surface interaction) is dominant.

**Route to nonequilibrium**—We take the planar Couette flow as an example to demonstrate how the rarefaction effects set in. Consider two parallel plates located at  $x_2 = -L/2$  and  $L/2$ , moving in the  $x_1$  direction with velocities  $-u_w$  and  $u_w$ , respectively. The wall velocity is small, then the gas temperature equals the wall temperature

$T_w$  when the steady state is reached, hence the shear viscosity and heat conductivity are constant in the whole domain. This problem is effectively one-dimensional. According to the NSF equations, the velocity  $u_1$  is linear and the heat flux  $q_1$  is zero. Also, if the gas pressure remains unchanged, but the wall distance is decreased, the NSF equation predicts a shear stress:

$$p_{12} = -\mu \frac{2u_w}{L} = -\frac{4}{\sqrt{\pi}} Kn, \quad (1-14)$$

which eventually goes to infinity when  $L \rightarrow 0$ .

Figure 1-7 shows the numerical solution from the Boltzmann equation with the diffuse boundary condition. When  $Kn = 0.01$ , the velocity profile is linear and the flow velocity at the two plates are very close to the wall velocity. Also the heat flux is zero in the bulk region, as predicted by the NSF equations; only in the vicinity of plates can we see a very small heat flux, which is due to the rarefaction effect inside the Knudsen layer: in fact, if we zoom in the velocity profile, we shall find a tiny velocity defect there; this can be described by the Knudsen layer function in Chapter 9. When  $Kn = 0.1$ , the Knudsen layer stretches to the whole domain, and the heat flux is not zero, which shows that the Fourier law of heat conduction cannot describe this rarefaction effect. The flow velocity is, however, nearly linear, but there is a considerable slip at the wall. If a proper velocity-slip boundary condition is given, the velocity can be predicted by the NSF equations. When  $Kn = 1$ , the velocity profile is nonlinear, with increased velocity slip at the wall; also, the magnitude of heat flux increases significantly. In the free molecular regime, the velocity and heat flux approach zero.

The shear stress at the wall is also shown. When  $Kn$  is small, Newton's law is accurate. When  $Kn > 0.2$ , large discrepancy between the Newton's law and prediction from the Boltzmann equation is clearly seen. Moreover, the shear stress does not approach infinity but saturates to a fixed value when  $Kn \rightarrow \infty$ , or when  $L \rightarrow 0$ .

In this simple problem, if an effective shear viscosity is introduced, one may get the shear stress correct in the whole range of Knudsen number, but not the velocity profile. Moreover, one can never get the streamwise heat flux correct from the NSF equations, because there is no temperature gradient at all. To take into accounts these rarefaction effects, high-order constitutive relations are needed since, as we can see from Eq. (1-8), the linear constitutive relations are only valid when the fluid system varies slowly on a spatial scale of the size of MFP, or equivalently, when the spatial Knudsen number is small.

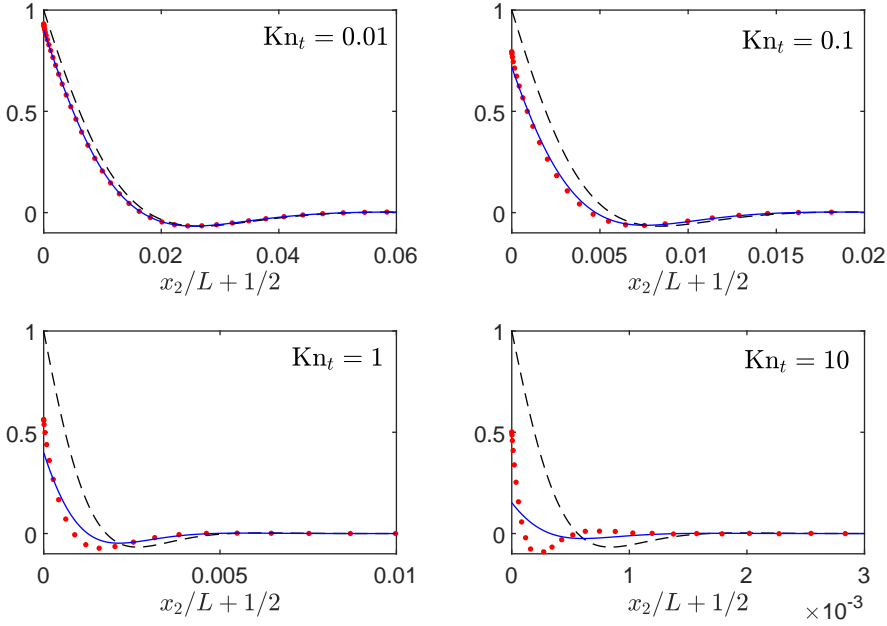


图 1-8 The real part of the flow velocity (normalized by the oscillation amplitude  $u_w$ ) at  $t = 2m\pi/\varpi$  with  $m = 0, 1, \dots$ , at different values of the temporal Knudsen number. The spatial Knudsen number is fixed at  $\text{Kn} = 0.001$ . Dashed and solid lines are the solution of the NSF equation without and with the first-order velocity-slip boundary conditions [106], respectively, while circles are solutions from the linearized Boltzmann equation for HS gas, with the diffuse boundary condition.

### 1.5.2 Temporal Knudsen number

When the ratio of the characteristic flow frequency  $\varpi$  to the mean collision frequency of gas molecules  $\bar{\nu} = 1/\tau_c$  becomes appreciable, the gas flow can also be in non-equilibrium, no matter what the spatial Knudsen number is. Thus, in addition to the spatial Knudsen number (1-10), it is necessary to define the temporal Knudsen number to measure the degree of non-equilibrium:

$$\text{Kn}_t = \varpi\tau_c = \varpi \frac{\mu}{p}. \quad (1-15)$$

Let us take the one-dimensional oscillatory Couette flow to demonstrate the rarefaction effects. The same setting as the planar Couette flow in the previous section is used, but now the plate at  $x_2 = -L/2$  oscillates in the  $x_1$  direction with frequency  $\varpi$  and amplitude  $u_m$ . Adopting the Navier-Stokes equations with the first-order velocity-slip

boundary condition, the analytical solution for the gas velocity is obtained [106]:

$$u_1 = u_w \exp(i\omega t) \frac{\sin \left[ (1+i)\delta_{rp} \sqrt{Kn_t} \left( \frac{1}{2} - \frac{x_2}{L} \right) \right]}{\sin \left[ (1+i)\delta_{rp} \sqrt{Kn_t} \right]} \times \frac{1 + (1+i)\sigma_P \sqrt{Kn_t} \cot \left[ (1+i)\delta_{rp} \sqrt{Kn_t} \left( \frac{1}{2} - \frac{x_2}{L} \right) \right]}{1 - 2i\sigma_P^2 Kn_t + 2(1+i)\sigma_P \sqrt{Kn_t} \cot \left[ (1+i)\delta_{rp} \sqrt{Kn_t} \right]}, \quad (1-16)$$

where  $i$  is the imaginary unit and  $\sigma_P$  is the viscous slip coefficient. Here we take  $\sigma_P = 1$ ; more sophisticated calculations will be given in Chapter 9.

By comparing the numerical solution of the Boltzmann equation with the analytical solution, we are able to classify the flow regime based on the temporal Knudsen number. To isolate the rarefaction effects associated with the spatial Knudsen number, we set  $Kn = 0.001$ . It is seen from Fig. 1-8 that, the slip solution (1-15) is valid up to  $Kn_t \approx 0.1$ , while when  $Kn_t = 10$  the velocity profile from the Boltzmann equation is very close to the collisionless limit [106], indicating that the flow has entered the free-molecular regime. Therefore, we conclude that Fig. 1-6 ( $Kn$  is replaced by  $Kn_t$ ) can also be used to classify the four flow regimes in terms of the temporal Knudsen number, when the spatial Knudsen number is in the continuum flow regime. When both spatial and temporal Knudsen numbers are not small, stronger rarefaction effects are expected.

## 1.6 Molecular dynamics simulations

Alternative methods should be adopted to study the RGD due to the breakdown of NSF equations in extreme conditions. Physically, when the intermolecular potential  $\phi$  is known, the molecular dynamics (MD) simulations, which is based on Newton's second law of motion, can be adopted to trace the movement of individual molecules:

$$m \frac{d^2 \mathbf{x}_i}{dt^2} = \sum_j \mathbf{F}_{ij}, \quad \text{with } \mathbf{F}_{ij} = -\nabla \phi(r_{ij}), \quad (1-17)$$

where  $\mathbf{x}_i$  is the position of the  $i$ -th molecule,  $\nabla$  is the gradient operator, and  $r_{ij}$  is the distance between the  $i$ -th and  $j$ -th molecules.

When the position and velocity of individual molecule are known, macroscopic quantities can be obtained through ensemble average. Suppose there are  $N$  molecules inside a volume  $V$ , the flow velocity  $\mathbf{u}$  and temperature  $T$  are given by:

$$\mathbf{u} = \frac{1}{N} \sum_{i=1}^N \mathbf{v}_i, \quad (1-18)$$

$$T = \frac{m}{3Nk_B} \sum_{i=1}^N c^2. \quad (1-19)$$

where

$$\mathbf{c} = \mathbf{v} - \mathbf{u} \quad (1-20)$$

is the peculiar velocity and its magnitude is denoted by  $c$ . Independent runs for transient flows or time averaging for steady flows are needed to reduce the intrinsic noise in particle-based simulations.

Transport coefficients such as the viscosity and heat conductivity that appear in the NSF equations can also be calculated in MD simulations, via the Green-Kubo formulas [34, 55]:

$$\mu = \frac{1}{V} \frac{1}{k_B T} \int_0^\infty \langle J_{xy}^p(0) J_{xy}^p(\tau) \rangle d\tau, \quad (1-21)$$

$$\frac{4}{3}\mu + \mu_b = \frac{1}{V} \frac{1}{k_B T} \int_0^\infty \langle J_{xx}^p(0) J_{xx}^p(\tau) \rangle d\tau, \quad (1-22)$$

$$\kappa = \frac{1}{V} \frac{1}{k_B T^2} \int_0^\infty \langle J_x^q(0) J_x^q(\tau) \rangle d\tau, \quad (1-23)$$

where the brackets  $\langle \dots \rangle$  denote the canonical ensemble average,  $\mathbf{J}^p = m\mathbf{c}_i\mathbf{c}_i - pV\mathbf{I}$  and  $\mathbf{J}^q = E_i\mathbf{c}_i$ , with  $\mathbf{I}$  being the identity matrix. For monatomic gas,  $E_i = mc_i^2/2$  and  $\kappa$  is the translational thermal conductivity  $\kappa_{tr}$ . For molecular gas, suppose  $E_i = \epsilon_i$  is the internal energy of the  $i$ -th molecule, then Eq. (8-50) calculates the internal thermal conductivity  $\kappa_i$ ; together with the translational thermal conductivity they form the total thermal conductivity  $\kappa$ .

The MD simulation is also an indispensable tool to investigate the gas-surface interaction, which, together with the gas-gas interaction, determines the gas dynamics in wall-bounded problems. However, since it is limited to small spatial and temporal scales, the MD simulation cannot be used efficiently in rarefied gas flow simulations. Therefore, the gas kinetic theory, a mesoscopic theory that bridges the physics at the microscopic level and flow dynamics (phenomenon) at the macroscopic level, is needed.

## 第2章 气体动理论

### 2.1 理想气体

### 2.2 速度分布函数与宏观量

在气体动理论中, 单原子气体在相空间中的概率密度由速度分布函数  $f(t, \mathbf{x}, \mathbf{v})$  表示, 是时间  $t$ , 空间坐标  $\mathbf{x} = (x_1, x_2, x_3)$  和分子速度  $\mathbf{v} = (v_1, v_2, v_3)$  的函数. 定义  $f(t, \mathbf{x}, \mathbf{v})d\mathbf{x}d\mathbf{v}$  是体积为  $d\mathbf{x}d\mathbf{v}$  的相空间上的分子数, 则气体的数密度  $n$ 、宏观速度  $\mathbf{u}$ 、温度  $T$ 、压力张量  $p_{ij}$  和热流  $\mathbf{q}$  可以分别通过对速度分布函数求矩得到:

$$\begin{aligned} n(t, \mathbf{x}) &= \int f(t, \mathbf{x}, \mathbf{v})d\mathbf{v}, \\ \mathbf{u}(t, \mathbf{x}) &= \frac{1}{n(t, \mathbf{x})} \int \mathbf{v}f(t, \mathbf{x}, \mathbf{v})d\mathbf{v}, \\ T(t, \mathbf{x}) &= \frac{m}{3k_B n(t, \mathbf{x})} \int c^2 f(t, \mathbf{x}, \mathbf{v})d\mathbf{v}, \\ p_{ij}(t, \mathbf{x}) &= m \int c_i c_j f(t, \mathbf{x}, \mathbf{v})d\mathbf{v}, \\ \mathbf{q}(t, \mathbf{x}) &= \frac{m}{2} \int c^2 \mathbf{c} f(t, \mathbf{x}, \mathbf{v})d\mathbf{v}, \end{aligned} \quad (2-1)$$

其中,  $\mathbf{c} = \mathbf{v} - \mathbf{u}$  是气体分子热运动速度, 即气体分子速度与当地宏观速度的矢量差, 而  $c$  是热运动速率. 定义应力偏量为

$$\sigma_{ij} = p_{ij} - p\delta_{ij}, \quad (2-2)$$

其中  $p = nk_B T$ ,  $\delta_{ij}$  为克罗内克函数.

### 2.3 Boltzmann 方程

The governing equation for the evolution of VDF of a dilute gas system is derived by Ludwig Boltzmann. In his description, molecules move in straight lines with fixed velocities until they encounter elastic collisions with other molecules. This is justified by the fact that, at standard temperature and pressure, the MFP of gas molecules is hundreds times of the nominal atomic diameter and about 30 times the average molecular separation.

Both molecular streaming and collision change the VDF in the phase space as per

the Boltzmann equation [20, 18, 112, 53]:

$$\frac{\partial f}{\partial t} + \boldsymbol{v} \cdot \frac{\partial f}{\partial \boldsymbol{x}} + \boldsymbol{a} \cdot \frac{\partial f}{\partial \boldsymbol{v}} = Q(f, f_*), \quad (2-3)$$

where the first term on the left hand side describes the change of VDF with respect to time, the second term is the convective change, and the third term represents the change of VDF induced by external acceleration (suppose it is independent of the molecular velocity). They together describe the streaming of gas molecules.

The quadratic collision operator  $Q(f, f_*)$  describes the change of molecular numbers per unit phase-space volume  $d\boldsymbol{x}d\boldsymbol{v}$  and per unit time. This change consists of two effects. First, when the molecule with velocity  $\boldsymbol{v}$  collides with another molecule with velocity  $\boldsymbol{v}_*$ , its velocity becomes  $\boldsymbol{v}'$ , which contributes to the loss of molecules with the very velocity  $\boldsymbol{v}$ . During time interval  $\Delta t$ , there are

$$f(t, \boldsymbol{x}, \boldsymbol{v}_*) v_r \Delta t b d\Omega d\boldsymbol{v}' \quad (2-4)$$

such collisions. Therefore, the number of molecule lost in the binary collision per unit phase-space volume and per time is

$$\begin{aligned} Q_{\text{loss}} &= \frac{\int f(t, \boldsymbol{x}, \boldsymbol{v}) d\boldsymbol{x}d\boldsymbol{v} \times f(t, \boldsymbol{x}, \boldsymbol{v}_*) v_r \Delta t b d\Omega d\boldsymbol{v}'}{d\boldsymbol{x}d\boldsymbol{v}\Delta t} \\ &= \frac{\int f(t, \boldsymbol{x}, \boldsymbol{v}) d\boldsymbol{x}d\boldsymbol{v} \times f(t, \boldsymbol{x}, \boldsymbol{v}_*) v_r \Delta t \sigma_D \sin \theta d\theta d\phi d\boldsymbol{v}_*}{d\boldsymbol{x}d\boldsymbol{v}\Delta t} \\ &= \int_{\mathbb{R}^3} \int_{\mathbb{S}^2} B(\cos \theta, v_r) f(t, \boldsymbol{x}, \boldsymbol{v}_*) f(t, \boldsymbol{x}, \boldsymbol{v}) d\Omega d\boldsymbol{v}_*. \end{aligned} \quad (2-5)$$

Second, when the molecule with velocity  $\boldsymbol{v}'$  collides with another molecule with the velocity  $\boldsymbol{v}'_*$ , its velocity becomes  $\boldsymbol{v}$ , which contributes to the gain of molecules with the very velocity  $\boldsymbol{v}$ . Therefore, with the facts that  $d\boldsymbol{v}d\boldsymbol{v}_* = d\boldsymbol{v}'d\boldsymbol{v}'_*$ ,  $v_r = v'_r$ , and the collision kernel is only determined by the relative collision speed and impact parameter, the gain part of the Boltzmann collision operator is

$$\begin{aligned} Q_{\text{gain}} &= \frac{\int f(t, \boldsymbol{x}, \boldsymbol{v}') d\boldsymbol{x}d\boldsymbol{v}' \times f(t, \boldsymbol{x}, \boldsymbol{v}'_*) v'_r \Delta t b d\Omega d\boldsymbol{v}'_*}{d\boldsymbol{x}d\boldsymbol{v}\Delta t} \\ &= \int_{\mathbb{R}^3} \int_{\mathbb{S}^2} B(\cos \theta, v_r) f(t, \boldsymbol{x}, \boldsymbol{v}'_*) f(t, \boldsymbol{x}, \boldsymbol{v}') d\Omega d\boldsymbol{v}_*. \end{aligned} \quad (2-6)$$

Finally, the Boltzmann collision operator is written in the following form (since it is local in time and space, for simplicity  $t$  and  $\boldsymbol{x}$  will be omitted in writing the collision operator):

$$Q(f, f_*) = \int_{\mathbb{R}^3} \int_{\mathbb{S}^2} B(\cos \theta, v_r) [f(\boldsymbol{v}') f(\boldsymbol{v}') - f(\boldsymbol{v}_*) f(\boldsymbol{v})] d\Omega d\boldsymbol{v}_*. \quad (2-7)$$

Note that the “Stosszahlansatz” or assumption of molecular chaos was used implicitly, that is, the value of VDF for different velocities are independent.

对于稀疏气体 (dilute gas, 分子间距远远大于分子直径), 在外部施加的加速度  $\mathbf{a} = (a_1, a_2, a_3)$  的作用下, 速度分布函数的演化由玻尔兹曼方程描述:

$$\frac{\partial f}{\partial t} + \mathbf{v} \cdot \frac{\partial f}{\partial \mathbf{x}} + \mathbf{a} \cdot \frac{\partial f}{\partial \mathbf{v}} = Q(f). \quad (2-8)$$

方程左边的三项分别表示速度分布函数在时间上的变化, 在速度作用下在物理空间的变化, 以及在外力作用下在速度空间的变化; 右边表示使得分布函数趋于平衡态的气体分子的碰撞过程. 在玻尔兹曼方程中, 二体碰撞的形式为:

$$Q(f) = \iint B(\theta, v_r) [f(\mathbf{v}'_*) f(\mathbf{v}') - f(\mathbf{v}_*) f(\mathbf{v})] d\Omega d\mathbf{v}_*. \quad (2-9)$$

其中,  $\mathbf{v}$  和  $\mathbf{v}_*$  分别是碰撞前两个分子的速度, 而  $\mathbf{v}'$  和  $\mathbf{v}'_*$  是它们碰撞后的速度. 由于碰撞前后两分子的距离足够远以至于它们的相互作用可以忽略不计, 根据动量和能量守恒定律, 碰撞前后速度关系如下:

$$\begin{aligned} \mathbf{v}' &= \frac{\mathbf{v} + \mathbf{v}_*}{2} + \frac{|\mathbf{v} - \mathbf{v}_*|}{2} \Omega, \\ \mathbf{v}'_* &= \frac{\mathbf{v} + \mathbf{v}_*}{2} - \frac{|\mathbf{v} - \mathbf{v}_*|}{2} \Omega. \end{aligned} \quad (2-10)$$

碰撞的示意图见图 2-1. 其中, 碰撞前两分子的相对速度为  $\mathbf{v}_r = \mathbf{v} - \mathbf{v}_*$ , 碰撞后的相对速度为  $\mathbf{v}' - \mathbf{v}'_*$ .  $\Omega$  为定义在单位球空间的矢量, 它与碰撞后的相对速度同方向. 于是相对速度的偏转角  $\theta$  与碰撞前相对速度满足如下关系:

$$\cos \theta = \Omega \cdot \frac{\mathbf{v}_r}{v_r}. \quad (2-11)$$

最后, 碰撞核  $B(\theta, v_r)$  是相对速度和碰撞偏转角度的函数, 具体形式取决于分子间的作用力.

### 2.3.1 偏转角和微分散射截面

假设分子间通过中心力场作用, 作用势  $\phi(r)$  已知, 其中  $r$  为分子间距, 则偏转角可以通过经典力学和量子力学两种方式求解. 若气体温度不低 (如氦气的温度高于 100 K), 两种方式得到的输运系数 (如粘性和热导率) 相同 [105]. 这里仅介绍经典力学的计算结果, 如图 2-1所示, 偏转角可以表示为:

$$\theta(b, v_r) = \pi - 2 \int_0^{W_1} \left[ 1 - W^2 - \frac{4\phi(r)}{mv_r^2} \right]^{-1/2} dW, \quad (2-12)$$

其中,  $W = b/r$  为瞄准距离  $b$  与分子间距  $r$  的比值, 积分上限  $W_1$  对应于最短分子间距, 即上式中括号内表达式等于零的方程的正根.

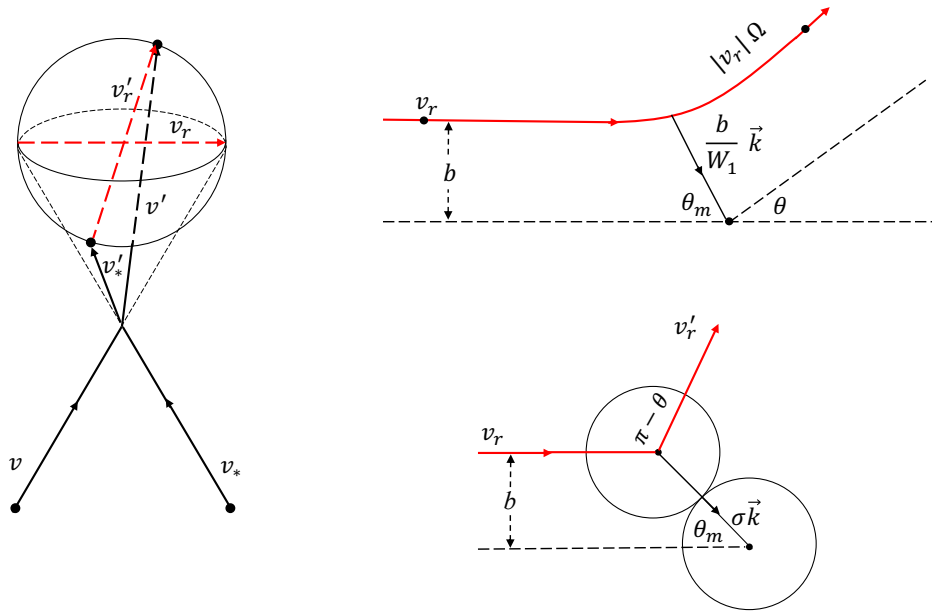


图 2-1 (左) 二体碰撞前后的速度分布. 由于动量和能量守恒, 碰撞前后的相对速度分布在球体上并且通过球心. (右上) 中心力场作用下的经典二体碰撞示意图, 其中  $b$  为瞄准距离,  $\mathbf{k}$  为沿两分子间最短距离方向的单位矢量. (右下) 直径为  $\sigma$  的硬球分子的两体碰撞.

在气体动理论中, 经常考虑如下形式的逆幂律分子作用势:

$$\phi(r) = \frac{K}{\eta - 1} r^{1-\eta}, \quad (2-13)$$

其中,  $K$  表征分子间相互作用的强度. 从公式(2-12)可知, 偏转角只与变量  $s$  有关, 即  $\theta = \theta(s)$ :

$$s = \left[ \frac{m(\eta - 1)}{4K} \right]^{\frac{1}{\eta-1}} b v_r^{\frac{2}{\eta-1}}. \quad (2-14)$$

微分散射截面定义为

$$\begin{aligned} \sigma_D &= \frac{b|db|}{\sin \theta |d\theta|} \\ &= \left( \frac{m(\eta - 1)}{4K} \right)^{\frac{2}{1-\eta}} v_r^{\frac{4}{1-\eta}} \frac{sds}{\sin \theta d\theta}, \end{aligned} \quad (2-15)$$

而碰撞核为

$$B(\theta, v_r) = v_r \sigma_D. \quad (2-16)$$

当公式(2-13)中  $\eta = 5$  时, 即为麦克斯韦分子, 此时碰撞核与相对碰撞速度无关, 记为  $B(\theta, v_r) = \sqrt{2K/m}B(\theta)$ . 对于硬球分子模型, 可看作式(2-13)中  $\eta = \infty$ , 从图 2-1可以看出, 偏转角可通过如下公式确定:  $b = \sigma \cos(\theta/2)$ , 其中  $\sigma$  为硬球直径. 因此微分散射截面为  $\sigma_D = \sigma^2/4$ , 而碰撞核为  $B(\theta, v_r) = \sigma^2 v_r / 4$ . 对于一般

的气体，它们的行为介于麦克斯韦分子和硬球分子之间.

### 2.3.2 熵增原理

对于任意关于分子速度的函数  $\Psi(\mathbf{v})$ , 对玻尔兹曼碰撞项 (2-9) 在速度空间积分, 具有如下对称性:

$$\begin{aligned} \int \Psi(\mathbf{v}) Q(\mathbf{v}) d\mathbf{v} &= \frac{1}{4} \iiint d\Omega d\mathbf{v}_* d\mathbf{v} \Delta[\Psi] B(\theta, v_r) \\ &\quad \times [f(\mathbf{v}'_*) f(\mathbf{v}') - f(\mathbf{v}_*) f(\mathbf{v})], \end{aligned} \quad (2-17)$$

其中  $\Delta[\Psi] = \Psi(\mathbf{v}_*) + \Psi(\mathbf{v}) - \Psi(\mathbf{v}'_*) - \Psi(\mathbf{v}')$ . 若  $\Psi$  满足  $\int \Psi(\mathbf{v}) Q d\mathbf{v} = 0$ , 则称其为碰撞不变量. 根据质量、动量和能量守恒, 可知  $\Psi = 1, \mathbf{v}, v^2$  为碰撞不变量, 而碰撞不变量的线性组合也是碰撞不变量.

定义  $H$  函数为:

$$H = - \iint f \ln f d\mathbf{v} d\mathbf{x}, \quad (2-18)$$

是与气体系统的熵相关的标量. 在无外力的情况下,  $H$  的时间导数可写为:

$$\begin{aligned} \frac{\partial H}{\partial t} &= - \iint (1 + \ln f) \frac{\partial f}{\partial t} d\mathbf{v} d\mathbf{x} \\ &= \iint \mathbf{v} \cdot \frac{\partial f \ln f}{\partial \mathbf{x}} d\mathbf{v} d\mathbf{x} - \iint (1 + \ln f) Q d\mathbf{v} d\mathbf{x} \\ &= \oint \int \mathbf{v} \cdot \mathbf{n} f \ln f d\mathbf{v} dS - \iint (1 + \ln f) Q d\mathbf{v} d\mathbf{x}. \end{aligned}$$

式中,  $\mathbf{n}$  为系统表面微元  $dS$  的外法线. 对于孤立系统, 上式右端第一项为零; 利用方程 (2-17), 右端项第二项可写为:

$$\begin{aligned} &\frac{1}{4} \iiint d\Omega d\mathbf{v}_* d\mathbf{v} B [f(\mathbf{v}'_*) f(\mathbf{v}') - f(\mathbf{v}_*) f(\mathbf{v})] \\ &\quad \times \{\ln[f(\mathbf{v}'_*) f(\mathbf{v}')] - \ln[f(\mathbf{v}_*) f(\mathbf{v})]\}. \end{aligned}$$

因为碰撞核  $B$  非负, 且对于任意的两个正整数  $a$  和  $b$ , 不等式  $(a-b)(\ln a - \ln b) \geq 0$  恒成立, 所以有

$$\frac{\partial H}{\partial t} \geq 0. \quad (2-19)$$

上式表明孤立系统的  $H$  函数不会减小, 这就是著名的玻尔兹曼的熵增原理.  $H$  随时间单调增加, 但存在有限的上界, 上界对应为式 (2-19) 中等号成立时的平衡态, 即  $\ln f(\mathbf{v}_*) + \ln f(\mathbf{v}) = \ln f(\mathbf{v}'_*) + \ln f(\mathbf{v}')$ . 因此,  $\ln f$  也是碰撞不变量, 可以表示为五个基本碰撞不变量的线性组合:  $\ln f = \alpha_1 + \alpha_2 \cdot \mathbf{v} + \alpha_3 v^2$ ; 给定系统的密度、速度和温度, 参数  $\alpha_1, \alpha_3$  和  $\alpha_2$  可以唯一确定. 此时, 麦克斯韦平衡态速度分布函

数为

$$F_{eq}(T) = n \left( \frac{m}{2\pi k_B T} \right)^{3/2} \exp \left( -\frac{mc^2}{2k_B T} \right). \quad (2-20)$$

### 2.3.3 线性化玻尔兹曼方程

线性化玻尔兹曼方程在气体动理论中具有重要地位。第一，线性化玻尔兹曼碰撞项的本征值与本征函数，不仅在渐近展开推导纳维-斯托克斯方程的过程中至关重要，而且是发展简化动力学模型方程的源头理论。第二，在许多微机电系统中，气体的压力梯度与温度梯度非常小，因此使用线性化方程可以高效准确地模拟微流动。第三，虽然玻尔兹曼方程是单粒子速度分布函数确定性演化的平均方程，但是在某些问题中（例如：第8.4.2节中的瑞利-布里渊散射）可以通过线化玻尔兹曼方程研究粒子涨落带来的影响。

通常将速度分布函数在全局平衡态

$$f_{eq} = n_0 \left( \frac{m}{2\pi k_B T_0} \right)^{3/2} \exp \left( -\frac{mv^2}{2k_B T_0} \right) \quad (2-21)$$

下展开为

$$f(t, \mathbf{x}, \mathbf{v}) = f_{eq}(\mathbf{v}) [1 + \phi(t, \mathbf{x}, \mathbf{v})], \quad (2-22)$$

其中扰动量  $\phi$  满足约束条件  $|\phi| \ll 1$ 。不考虑外力项，只保留  $\phi$  的一次项，玻尔兹曼方程 (2-8) 可线性化为如下形式：

$$\begin{aligned} \frac{\partial \phi}{\partial t} + \boldsymbol{\xi} \cdot \frac{\partial \phi}{\partial \mathbf{x}} &= \frac{\ell}{v_m} J(\phi) \\ &\equiv -\frac{\ell}{v_m} \iint B \Delta[\phi] f_{eq}(\mathbf{v}_*) d\Omega d\mathbf{v}_*. \end{aligned} \quad (2-23)$$

这里的速度和空间坐标分别通过最概然速率  $v_m$  和特征尺寸  $\ell$  进行无量纲化，时间用  $\ell/v_m$  归一化；无量纲分子速度为

$$\boldsymbol{\xi} = \frac{\mathbf{c}}{v_m(T_0)}, \quad (2-24)$$

其中

$$v_m(T) = \sqrt{\frac{2k_B T}{m}} \quad (2-25)$$

为气体分子的最概然速率，即与麦克斯韦速率分布的极大值对应的速率。

对于麦克斯韦分子，线性化玻尔兹曼碰撞项的本征值与本征函数为[137]：

$$\begin{aligned}
 J(\Phi_{rlm}) &= n\lambda_{rl}\Phi_{rlm}, \\
 \Phi_{rlm} &= g_{rl}(\xi)Y_l^m(\hat{\xi}) \\
 &= \sqrt{\frac{2\pi^{3/2}r!}{(r+l+\frac{1}{2})!}}S_{l+\frac{1}{2}}^{(r)}(\xi^2)\xi^l Y_l^m(\hat{\xi}), \\
 \lambda_{rl} &= 2\pi\sqrt{\frac{2K}{m}} \int_0^\pi d\theta \sin\theta B(\theta) \\
 &\quad \times \left[ -1 + \cos^{2r+l} \frac{\theta}{2} P_l\left(\cos \frac{\theta}{2}\right) \right. \\
 &\quad \left. - \delta_{r0}\delta_{l0} + \sin^{2r+l} \frac{\theta}{2} P_l\left(\sin \frac{\theta}{2}\right) \right]. \tag{2-26}
 \end{aligned}$$

式中， $P_l(x)$  是勒让德多项式， $S_{l+\frac{1}{2}}^{(r)}(\xi)$  是索南多项式， $Y_l^m(\hat{\xi})$  为  $\xi$  方向的球谐函数。

前三项本征值为  $\lambda_{00} = \lambda_{01} = \lambda_{10} = 0$ ，分别代表三大守恒律。另外两个非常重要的本征值为

$$\begin{aligned}
 \lambda_{02} &= \left(-\frac{3}{2}\right)\pi\sqrt{\frac{2K}{m}} \int_0^\pi d\theta \sin^3\theta B(\theta), \\
 \lambda_{11} &= \frac{2}{3}\lambda_{02}, \tag{2-27}
 \end{aligned}$$

它们决定剪切粘性系数和热导率的大小。若归一化的速度  $\xi$  在  $z$  轴的投影为  $\xi_z = \xi \cos\theta$ ，其中  $\theta$  为极距角，与上述本征值对应的本征函数为：

$$\begin{aligned}
 \Phi_{000} &= 1, \quad \Phi_{010} = \sqrt{2}\xi_z, \quad \Phi_{100} = \sqrt{\frac{2}{3}}\left(\frac{3}{2} - \xi^2\right), \\
 \Phi_{020} &= \frac{1}{3\sqrt{3}}\left(\xi_z^2 - \frac{\xi^2}{3}\right), \\
 \Phi_{110} &= \frac{2}{\sqrt{5}}\left(\frac{5}{2} - \xi^2\right)\xi_z.
 \end{aligned}$$

它们与气体的分子数密度、速度、温度、压力和热流的扰动密切相关：

$$\begin{aligned}
 [n, \mathbf{u}, T] &= \int \left[ 1, \xi, \frac{2}{3}\left(\xi^2 - \frac{3}{2}\right) \right] f_{eq}\phi d\xi, \\
 [\sigma_{ij}, \mathbf{q}] &= \int \left[ 2\xi_{\langle i}\xi_{j\rangle}, \left(\xi^2 - \frac{5}{2}\right)\xi \right] f_{eq}\phi d\xi. \tag{2-28}
 \end{aligned}$$

其中，下标中出现尖括号表示该张量是无迹张量，即  $\xi_{\langle i}\xi_{j\rangle} = \xi_i\xi_j - \xi^2\delta_{ij}/3$ 。为避免使用过多符号，在线性化问题中我们使用与原物理量相同的符号表示归一化的

扰动物理量，如这里的扰动数密度  $n$  应理解为偏离参考数密度  $n_0$  的那部分，再除以参考数密度；扰动温度  $T$  为偏离参考温度  $T_0$  的部分，再除以参考温度；在全局平衡态下，参考速度、应力偏量和热流全部为零，因此上式中它们分别以  $T_0$  下的最概然速率  $v_m$ 、 $n_0 k_B T_0$  和  $n_0 k_B T_0 v_m$  归一化。

### 2.3.4 输运系数和弛豫率：表象与本质

玻尔兹曼方程和纳维-斯托克斯方程分别在介观和宏观尺度上描述气体系统的演化，它们之间的关系一直是数学家和力学家研究的重要课题 [111]。对玻尔兹曼方程求守恒量  $m, mc, mc^2/2$  的矩，可以得到如下宏观方程组：

$$\begin{aligned} \frac{\partial \rho}{\partial t} + \frac{\partial(\rho u_j)}{\partial x_j} &= 0, \\ \frac{\partial(\rho u_i)}{\partial t} + \frac{\partial(\rho u_i u_j + p_{ij})}{\partial x_j} &= \rho a_i, \\ \frac{\partial(\rho E)}{\partial t} + \frac{\partial(\rho Eu_j + u_i p_{ij} + q_j)}{\partial x_j} &= \rho a_j u_j, \end{aligned} \quad (2-29)$$

其中  $E = 3k_B T/2m + u^2/2$ 。但是该方程组并不封闭，因为压力张量和热流的表达式不能用密度、速度和温度表示。有三种主要方法尝试封闭宏观方程组，它们分别是希尔伯特展开法 [46]，Chapman-Enskog 展开法 [19, 22, 20] 和矩方法 [33, 112]。这里我们介绍最常用的方法。

在 Chapman 和 Enskog [19, 22] 方法中，首先将玻尔兹曼方程改写为：

$$\frac{\partial f}{\partial t} + \boldsymbol{v} \cdot \frac{\partial f}{\partial \boldsymbol{x}} + \boldsymbol{a} \cdot \frac{\partial f}{\partial \boldsymbol{v}} = \frac{Q(f)}{\epsilon}. \quad (2-30)$$

然后将分布函数和玻尔兹曼碰撞项展开为  $\epsilon$  的幂级数：

$$\begin{aligned} f &= \sum_{k=0}^{\infty} \epsilon^k f^{(k)}, \\ Q &= \sum_{k=0}^{\infty} \epsilon^k Q^{(k)} = Q(f^{(0)}) + \epsilon J(f^{(1)}) + O(\epsilon^2). \end{aligned} \quad (2-31)$$

值得注意的是， $\epsilon$  是一个小的形式参数，主要用于监测展开的阶数。展开完成后，取  $\epsilon = 1$ 。

同时，压力和热流也相应展开如下：

$$\begin{aligned} p_{ij} &= \sum_{k=0}^{\infty} \epsilon^k p_{ij}^{(k)} \equiv \sum_{k=0}^{\infty} \epsilon^k \times m \int c_i c_j f^{(k)} d\mathbf{v}, \\ \mathbf{q} &= \sum_{k=0}^{\infty} \epsilon^k \mathbf{q}^{(k)} \equiv \sum_{k=0}^{\infty} \epsilon^k \times \frac{m}{2} \int \mathbf{c} c^2 f^{(k)} d\mathbf{v}. \end{aligned} \quad (2-32)$$

但是，碰撞不变量对应的宏观量  $C_M = \{\rho, \mathbf{u}, T\}$  仅由分布函数的零阶展开决定，即

$$[\rho, \rho \mathbf{u}, 3k_B \rho T] = m \int [1, \mathbf{v}, mc^2] f^{(0)} d\mathbf{v}, \quad (2-33)$$

而各个高阶展开对  $C_M$  的贡献均为零，这称为兼容性条件。

将公式 (3-4) 代入公式 (2-29)，可知时间导数亦可表示为  $\epsilon$  级数 [112]

$$\frac{\partial}{\partial t} = \sum_{k=0}^{\infty} \epsilon^k \frac{\partial}{\partial t_k}, \quad (2-34)$$

且对于零阶近似，可得到

$$\begin{aligned} \frac{\partial \rho}{\partial t_0} + \frac{\partial(\rho u_j)}{\partial x_j} &= 0, \\ \frac{\partial(\rho u_i)}{\partial t_0} + \frac{\partial(\rho u_i u_j + nk_B T \delta_{ij})}{\partial x_j} &= \rho a_i, \\ \frac{\partial(\rho E)}{\partial t_0} + \frac{\partial(\rho Eu_j + u_i n k_B T \delta_{ij})}{\partial x_j} &= \rho a_j u_j. \end{aligned} \quad (2-35)$$

从公式 (2-30) 和 (2-31) 易知  $Q(f^{(0)}) = 0$ 。因此，速度分布函数的零阶展开为

$$f^{(0)} = F_{eq}. \quad (2-36)$$

而速度分布函数的一阶近似  $f^{(1)} = F_{eq}\phi$  满足以下方程 [112]

$$\begin{aligned} J(\phi) &= \frac{1}{F_{eq}} \left[ \frac{\partial F_{eq}}{\partial t_0} + \mathbf{v} \cdot \frac{\partial F_{eq}}{\partial \mathbf{x}} + \mathbf{a} \cdot \frac{\partial F_{eq}}{\partial \mathbf{v}} \right] \\ &= 2\xi_{\langle i} \xi_{j\rangle} \frac{\partial u_{\langle i}}{\partial x_{j\rangle}} + \left( \xi^2 - \frac{5}{2} \right) \xi_i \sqrt{\frac{2k_B T}{m}} \frac{\partial \ln T}{\partial x_i}. \end{aligned} \quad (2-37)$$

其中，方程的推导过程中用到

$$\frac{\partial F_{eq}}{\partial t_0} = \frac{\partial F_{eq}}{\partial C_M} \frac{\partial C_M}{\partial t_0}, \quad \frac{\partial F_{eq}}{\partial \mathbf{x}} = \frac{\partial F_{eq}}{\partial C_M} \frac{\partial C_M}{\partial \mathbf{x}},$$

以及公式 (3-10)。注意公式 (2-23) 中的  $f_{eq}$  应改写为  $F_{eq}$ 。

积分方程 (3-12) 的解可分为齐次部分与非齐次部分，齐次部分满足  $J(\phi) = 0$ ，这说明  $\phi$  必然是碰撞不变量的线性组合，而兼容性条件要求所有线性组合的系数

都为零. 非齐次部分满足如下形式

$$\phi = -A(\xi)\xi_i \sqrt{\frac{2k_B T}{m}} \frac{\partial \ln T}{\partial x_i} - B(\xi)\xi_{\langle i}\xi_{j\rangle} \frac{\partial u_{\langle i}}{\partial x_{j\rangle}, \quad (2-38)$$

其中,  $A(\xi)$  和  $B(\xi)$  的解满足

$$\begin{aligned} J(A\xi_i) &= -\left(\xi^2 - \frac{5}{2}\right)\xi_i, \\ J(B\xi_{\langle i}\xi_{j\rangle}) &= -2\xi_{\langle i}\xi_{j\rangle}, \end{aligned} \quad (2-39)$$

且兼容性条件要求  $\int \xi^2 A(\xi) F_{eq} d\mathbf{v} = 0$ .

一旦得到  $A(\xi)$  和  $B(\xi)$ , 通过一阶展开就可以恢复牛顿粘性定理与傅里叶热传导定理:

$$\sigma_{ij}^{(1)} = -2\mu \frac{\partial u_{\langle i}}{\partial x_{j\rangle}, \quad q_i^{(1)} = -\kappa \frac{\partial T}{\partial x_i}, \quad (2-40)$$

且剪切粘性与热导率分别为

$$\begin{aligned} \mu &= \frac{2p}{15\pi^{3/2}} \int \exp(-\xi^2) B(\xi) \xi^4 d\xi, \\ \kappa &= \frac{2p}{3\pi^{3/2}} \frac{k_B}{m} \int \exp(-\xi^2) A(\xi) \xi^4 d\xi. \end{aligned} \quad (2-41)$$

一般将  $A(\xi)$  和  $B(\xi)$  展开为索南多项式级数

$$\begin{aligned} A(\xi) &= -\sum_{r=1}^{n_a} a_r S_{\frac{3}{2}}^{(r)}(\xi^2), \\ B(\xi) &= \sum_{r=0}^{n_b} b_r S_{\frac{5}{2}}^{(r)}(\xi^2), \end{aligned} \quad (2-42)$$

然后通过公式 (3-14) 和索南多项式的正交性求解输运系数. 对于麦克斯韦分子, 取第一项展开可得到准确的剪切粘性和热导率, 即取  $A(\xi) = a_1(\xi^2 - 5/2)$  和  $B(\xi) = b_0$ ; 而对于其它相互作用势, 仅考虑第一项展开得到的输运系数的相对误差也不超过 2%. 定义等效黏度截面为:

$$\sigma_\mu = \int \frac{B(\theta, v_r)}{v_r} \sin^2 \theta d\Omega, \quad (2-43)$$

则剪切粘性为

$$\mu = \frac{5\sqrt{\pi m k_B T}}{8 \left( \frac{m}{4k_B T} \right)^4 \int_0^\infty v_r^7 \sigma_\mu \exp\left(-\frac{mv_r^2}{4k_B T}\right) dv_r}, \quad (2-44)$$

而热导率为

$$\kappa = \frac{15}{4} \frac{k_B}{m} \mu, \quad (2-45)$$

从而单原子气体的普朗特数为

$$\begin{aligned} \text{Pr} &= c_p \frac{\mu}{\kappa} \\ &= \frac{5k_B}{2m} \frac{\mu}{\kappa} = \frac{2}{3}. \end{aligned} \quad (2-46)$$

对于逆幂律分子间相互作用势(2-13), 可以得出气体粘性和温度的关系

$$\mu(T) \propto T^\omega, \quad \omega = \frac{\eta + 3}{2(\eta - 1)}, \quad (2-47)$$

其中  $\omega$  是粘性温度幂指数. 对于麦克斯韦分子和硬球分子,  $\omega$  分别取 1 和 0.5; 对于其它气体,  $\omega$  一般介于 0.5 和 1 之间.

将公式 (2-40)代回公式 (2-29), 即可获得纳维-斯托克斯方程. 若继续计算 Chapman-Enskog 展开的高阶近似, 可以得到 Burnett、super-Burnett 等宏观方程组 [20]. 但是可能由于应力和热流与宏观量  $C_M$  展开的不匹配, 导致高阶方程组的线性不稳定. 同时, 由于边界条件数量随着方程组阶数升高而增加, 但对附加的边界条件提法缺少充分的研究, 因此高阶方程组很少被实际应用. 另一方面, 即使这些高阶方程组在某些情况下能得到精确解, 解的精度也不一定随着展开阶数的增加而增加 [? ].

值得一提的是, 对于麦克斯韦分子, 在空间均匀系统中, 本征值  $\lambda_{02}$  和  $\lambda_{11}$  与应力偏量和热流的弛豫速率相关, 而这些弛豫速率决定着剪切粘性系数和热传导的大小:

$$\begin{aligned} \frac{\partial \sigma_{ij}}{\partial t} &= -n\lambda_{02}\sigma_{ij} = -\frac{p}{\mu}\sigma_{ij}, \\ \frac{\partial q_i}{\partial t} &= -n\lambda_{11}q_i = -\frac{2p}{3\mu}q_i. \end{aligned} \quad (2-48)$$

可以认为这些弛豫过程是本质, 而粘性系数和热导率则为表象: 在稀薄气体流动中, 本构关系(2-40)和等效输运系数会随着克努森数的改变而改变, 但一旦分子作用势确定, 弛豫系数就会确定不变.

利用弛豫时间和输运系数的关系, 可以大大简化模型方程中输运系数的推导过程. 即, 如果应力偏量的弛豫时间为  $\tau$ , 则剪切粘性为  $p\tau$ . 如果热流的弛豫时间为  $\tau/A$ , 则普朗特数为  $A$ .

## 第3章 Fluid-dynamic Equations

The derivation of macroscopic equations in closed forms from the Boltzmann equation is of both fundamental and practical importance, since the structure of Boltzmann collision operator is complicated and difficult to handle both theoretically and numerically. And there are huge demanding of macroscopic equations that allow efficient and accurate calculation of rarefied gas dynamics with applications from aerodynamics to microfluidics. It has also been considered as an important part in the sixth Hilbert problem: “Thus Boltzmann’s work on the principles of mechanics suggests the problem of developing mathematically the limiting processes, which lead from the atomistic view to the laws of motion of continua” [45]. In this Chapter we first introduce how macroscopic equations are derived, and then assess the their accuracy.

### 3.1 Hilbert expansion

Macroscopic equations like Eq. (2-29) can be obtained by multiplying the Boltzmann equation (2-8) with the collision invariants and integrating with respect to the molecular velocity  $\boldsymbol{v}$ . However, the obtained moment system is not closed because expressions for the stress and heat flux are not known. Hilbert proposed to solve the Boltzmann equation via a formal asymptotic expansion of the VDF as [46]:

$$f(t, \boldsymbol{x}, \boldsymbol{v}) = \sum_{n=0}^{\infty} \epsilon^n f^{(n)}(t, \boldsymbol{x}, \boldsymbol{v}), \quad (3-1)$$

where  $\epsilon$  is a formal small parameter which plays the role of spatial Knudsen number for monitoring the order of terms and quantities appearing in the equations, which will be replaced by one when the solutions are obtained. Meanwhile, the Boltzmann collision operator is written as

$$\frac{Q}{\epsilon} = \sum_{n=0}^{\infty} \epsilon^{n-1} Q^{(n)}, \quad (3-2)$$

where  $Q^{(0)} = Q(f^{(0)}, f^{(0)})$  and  $Q^{(1)} = f^{(0)} \mathcal{J}(\phi)$  if we write  $f^{(1)} = f^{(0)} \phi$ .

The macroscopic variables are also expressed into the power series of  $\epsilon$  according to

Eq. (2-1):

$$\left[ \rho, \rho \mathbf{u}, \frac{3}{2} k_B \rho T \right] = \sum_{n=0}^{\infty} \epsilon^n \int \left[ 1, \mathbf{v}, \frac{1}{2} m c^2 \right] m f^{(n)} d\mathbf{v}, \quad (3-3)$$

and

$$\begin{aligned} p_{ij} &= \sum_{n=0}^{\infty} \epsilon^n p_{ij}^{(n)}, \quad p_{ij}^{(n)} = \int m c_i c_j f^{(n)} d\mathbf{v} \\ \mathbf{q} &= \sum_{n=0}^{\infty} \epsilon^n \mathbf{q}^{(n)}, \quad \mathbf{q}^{(n)} = \int \frac{1}{2} m c^2 \mathbf{c} f^{(n)} d\mathbf{v}. \end{aligned} \quad (3-4)$$

Substituting Eq. (3-1) into the Boltzmann equation and collecting powers of  $\epsilon$  yields an infinite system of integro-differential equations for  $f^{(n)}$ . At the order  $O(\epsilon^{-1})$  we have  $Q^{(0)} = 0$ . Therefore,  $f^{(0)}$  is the equilibrium distribution function (2-20):

$$f^{(0)} = \frac{\rho^{(0)}}{m} \left( \frac{m}{2\pi k_B T^{(0)}} \right)^{3/2} \exp \left( -\frac{m(\mathbf{v} - \mathbf{u}^{(0)})^2}{2k_B T^{(0)}} \right), \quad (3-5)$$

but the density, velocity and temperature are evaluated at the zeroth-order expansion, e.g.,  $\rho^{(0)} = \int m f^{(0)} d\mathbf{v}$ . If only this zeroth-order expansion is adopted, we have  $\rho^{(0)} = \rho$ ,  $\mathbf{u}^{(0)} = \mathbf{u}$ , and  $T^{(0)} = T$ . Therefore, the corresponding set of macroscopic equations are the Euler equations, i.e., Eq. (2-29) with  $p_{ij} = n k_B T \delta_{ij}$  and  $\mathbf{q} = 0$ . When the first-order expansion in VDF is considered:  $f = f^{(0)} + f^{(0)} \phi$ , we have

$$f^{(0)} \mathcal{J}(\phi) = \frac{\partial f^{(0)}}{\partial t} + \mathbf{v} \cdot \frac{\partial f^{(0)}}{\partial \mathbf{x}} + \mathbf{a} \cdot \frac{\partial f^{(0)}}{\partial \mathbf{v}}. \quad (3-6)$$

By solving Eq. (3-6), one can obtain  $\phi$  and hence  $f^{(1)}$ ; and the process can be carried on to obtain high-order approximations. We refer to the monograph of Sone [111] for more details. However, it should be noted that the NSF equations never emerge according to the Hilbert expansion.

## 3.2 Chapman-Enskog expansion

Chapman and Enskog independently proposed a new technique [19? ], which has become the standard procedure to derive macroscopic equations from the kinetic equation. The most successful part is that the transport coefficients in NSF equations can be derived as long as the intermolecular potential is known. In the Chapman-Enskog expansion, the VDF, stress and heat flux remain the same as the Hilbert expansion. However, the five conservative variables  $C_M = \{\rho, \mathbf{u}, T\}$  are calculated only according to the zeroth-order

expansion. That is,

$$\left[ \rho, \rho \mathbf{u}, \frac{3}{2} k_B \rho T \right] = m \int \left[ 1, \mathbf{v}, \frac{1}{2} mc^2 \right] f^{(0)} d\mathbf{v}, \quad (3-7)$$

with the compatibility condition

$$\int f^{(n)} d\mathbf{v} = \int \mathbf{v} f^{(n)} d\mathbf{v} = \int c^2 f^{(n)} d\mathbf{v} = 0, \quad \text{for } n \geq 1. \quad (3-8)$$

On substituting the above equations to Eq. (2-29), one finds that the time derivatives is formally written as a series in  $\epsilon$  [112]:

$$\frac{\partial}{\partial t} = \sum_{n=0}^{\infty} \epsilon^n \frac{\partial}{\partial t_n}. \quad (3-9)$$

Therefore, at the zeroth-order approximation, we have

$$\begin{aligned} \frac{\partial \rho}{\partial t_0} + \frac{\partial(\rho u_j)}{\partial x_j} &= 0, \\ \frac{\partial(\rho u_i)}{\partial t_0} + \frac{\partial(\rho u_i u_j + nk_B T \delta_{ij})}{\partial x_j} &= \rho a_i, \\ \frac{\partial(\rho E)}{\partial t_0} + \frac{\partial(\rho Eu_j + u_i n k_B T \delta_{ij})}{\partial x_j} &= \rho a_j u_j, \end{aligned} \quad (3-10)$$

while at other orders ( $n > 0$ ) we have

$$\frac{\partial \rho}{\partial t_n} = 0, \quad \frac{\partial(\rho u_i)}{\partial t_n} + \frac{\partial p_{ij}^{(n)}}{\partial x_j} = 0, \quad \frac{\partial(\rho E)}{\partial t_n} + \frac{\partial(u_i p_{ij}^{(n)} + q_j^{(n)})}{\partial x_j} = 0. \quad (3-11)$$

At the order  $O(\epsilon^{-1})$ , like the Hilbert expansion, we have  $Q(f^{(0)}, f^{(0)}) = 0$ . Hence  $f^{(0)}$  is just the equilibrium distribution function (2-20), because the conservative variables  $C_M$  are determined only according to the zeroth-order expansion.

At the order  $O(1)$ , the VDF  $f^{(1)} = F_{eq} \phi$  satisfies the following equation:

$$\begin{aligned} F_{eq} \mathcal{J}(\phi) &= \frac{\partial F_{eq}}{\partial t_0} + \mathbf{v} \cdot \frac{\partial F_{eq}}{\partial \mathbf{x}} + \mathbf{a} \cdot \frac{\partial F_{eq}}{\partial \mathbf{v}} \\ &= \left[ 2\xi_{\langle i} \xi_{j\rangle} \frac{\partial u_{\langle i}}{\partial x_{j\rangle}} + \left( \xi^2 - \frac{5}{2} \right) \xi_i \sqrt{\frac{2k_B T}{m}} \frac{\partial \ln T}{\partial x_i} \right] F_{eq}. \end{aligned} \quad (3-12)$$

Note that the final equation is obtained with the help of  $\frac{\partial F_{eq}}{\partial t_0} = \frac{\partial F_{eq}}{\partial C_M} \frac{\partial C_M}{\partial t_0}$ ,  $\frac{\partial F_{eq}}{\partial \mathbf{x}} = \frac{\partial F_{eq}}{\partial C_M} \frac{\partial C_M}{\partial \mathbf{x}}$ , and Eq. (3-10). Details can be found in Struchtrup's book [112].

The solution of the integral equation (3-12) can be decomposed into a homogeneous part and inhomogeneous part. The homogeneous part of solution satisfied  $\mathcal{J}(\phi) = 0$ , thus  $\phi$  must be linear combinations of collisional invariants. However, the compatibility condition (3-8) requires that all the combination coefficients are zero. The inhomogeneous

solution must be read

$$\phi = -A_\mu(\xi)\xi_{\langle i}\xi_{j\rangle} \frac{\partial u_{\langle i}}{\partial x_{j\rangle} - A_\kappa(\xi)\xi_i \sqrt{\frac{2k_B T}{m}} \frac{\partial \ln T}{\partial x_i}, \quad (3-13)$$

where  $\int \xi^2 A_\kappa(\xi) F_{eq} d\boldsymbol{v} = 0$  for the compatibility condition (3-8), and the solutions of  $A_\kappa(\xi)$  and  $A_\mu(\xi)$  satisfy

$$\mathcal{J}(A_\mu \xi_{\langle i}\xi_{j\rangle}) = -2\xi_{\langle i}\xi_{j\rangle}, \text{ and } \mathcal{J}(A_\kappa \xi_i) = -\left(\xi^2 - \frac{5}{2}\right)\xi_i. \quad (3-14)$$

Once  $A_\kappa(\xi)$  and  $A_\mu(\xi)$  are known, Newton's law for stress and Fourier's law for heat conduction can be obtained:

$$\sigma_{ij}^{(1)} = -2\mu \frac{\partial u_{\langle i}}{\partial x_{j\rangle}, \text{ and } q_i^{(1)} = -\kappa \frac{\partial T}{\partial x_i}, \quad (3-15)$$

where the shear viscosity and heat conductivity are

$$\begin{aligned} \mu &= \frac{2p}{15\pi^{3/2}} \int \exp(-\xi^2) A_\mu(\xi) \xi^4 d\xi, \\ \kappa &= \frac{2p}{3\pi^{3/2}} \frac{k_B}{m} \int \exp(-\xi^2) A_\kappa(\xi) \xi^4 d\xi. \end{aligned} \quad (3-16)$$

The NSF equations are obtained by combining Eqs. (3-9), (3-10) and (3-11) with  $n = 1$ , which is accurate to  $O(\text{Kn})$ .

### 3.2.0.1 Expansion in Sonine polynomials

Although Eq. (3-14) can be solved exactly by the fast spectral method so that the transport coefficients in Eq. (3-16) can be calculated exactly (see Section 4.6.2), an analytical derivation will be beneficial.

With the Sonine polynomials in Appendix ??, the integral equation (3-14) can be written as  $\mathcal{J}(A_\kappa \xi_i) = S_{\frac{3}{2}}^{(1)}(\xi^2)\xi_i$  and  $\mathcal{J}(A_\mu \xi_{\langle i}\xi_{j\rangle}) = -2S_{\frac{5}{2}}^{(0)}(\xi^2)\xi_{\langle i}\xi_{j\rangle}$ . For their solution,  $A_\kappa(\xi)$  and  $A_\mu(\xi)$  are expanded as

$$A_\kappa(\xi) = -\sum_{r=1}^{n_a} a_r S_{\frac{3}{2}}^{(r)}(\xi^2), \text{ and } A_\mu(\xi) = \sum_{r=0}^{n_b} b_r S_{\frac{5}{2}}^{(r)}(\xi^2). \quad (3-17)$$

Multiplying Eq. (3-14) with  $\exp(-\xi^2) S_{\frac{3}{2}}^{(s)}(\xi^2)\xi_i$  and  $\exp(-\xi^2) S_{\frac{5}{2}}^{(s)}(\xi^2)\xi_{\langle i}\xi_{j\rangle}$ , respectively, and taking advantage of the orthogonality of Sonine's polynomials, we have

$$\sum_{r=1}^{n_a} \alpha_{sr} a_r = \frac{15}{4} \pi^3 \frac{m}{\rho} \delta_{s1}, \quad \sum_{r=1}^{n_a} \beta_{sr} b_r = 5\pi^3 \frac{m}{\rho} \delta_{s0}, \quad (3-18)$$

where the matrices  $\alpha_{sr}$  and  $\beta_{sr}$  are

$$\alpha_{sr} = \left[ S_{\frac{3}{2}}^{(s)}(\xi^2)\xi_i, S_{\frac{3}{2}}^{(r)}(\xi^2)\xi_i \right], \quad \beta_{sr} = \left[ S_{\frac{5}{2}}^{(s)}(\xi^2)\xi_{\langle i}\xi_{j\rangle}, S_{\frac{5}{2}}^{(r)}(\xi^2)\xi_{\langle i}\xi_{j\rangle} \right], \quad (3-19)$$

with the bracket operator defined in Eq. (??).

Note that with the compatibility equation the last equation in Eq. (3-16) can be rewritten as  $\kappa = \frac{2p}{3\pi^{3/2}} \frac{k_B}{m} \int \exp(-\xi^2) A_\kappa(\xi) \xi_i \left( \xi^2 - \frac{5}{2} \right) \xi_i d\xi$ . Therefore, together with Eq. (3-17), we have

$$\mu = \frac{p}{2} b_0, \quad \kappa = \frac{p}{2} a_1. \quad (3-20)$$

In order to obtain the analytical expressions for shear viscosity and thermal conductivity, we need to compute  $\alpha_{sr}$  and  $\beta_{sr}$ , and their inverses. Their values depend on the numbers of  $n_a$  and  $n_b$  in Eq. (3-17). However, for Maxwell molecules, according to Eq. (2-26),  $\alpha_{sr}$  and  $\beta_{sr}$  are diagonal, so

$$\mu = \frac{p}{2} b_0 = \frac{5\pi^3}{2} k_B T \beta_{00}^{-1}, \quad \kappa = \frac{p}{2} a_1 = \frac{75\pi^3}{8} \frac{k_B}{m} k_B T \alpha_{11}^{-1}. \quad (3-21)$$

For other intermolecular potentials, this approximation already give a very accurate estimation of the transport coefficients, as we will see immediately below.

### 3.2.0.2 Expansion to the first-order

If only one element in each expansion in Eq. (3-17) is used, we get

$$\begin{aligned} \alpha_{11} &= \frac{1}{4} \int \exp(-\xi^2 - \xi_*^2) \mathcal{D}^2(\xi^2 \xi_i) B(\cos \theta, v_r) d\Omega d\xi_* d\xi, \\ \beta_{00} &= \frac{1}{4} \int \exp(-\xi^2 - \xi_*^2) \mathcal{D}^2(\xi_{\langle i} \xi_{j\rangle}) B(\cos \theta, v_r) d\Omega d\xi_* d\xi, \end{aligned} \quad (3-22)$$

where  $\mathcal{D}(\psi) = \psi + \psi_* - \psi' - \psi'_*$ .

If we define  $\eta_i = \xi_i - \xi_{*i}$ ,  $\zeta_i = \frac{1}{2}(\xi_i + \xi_{*i}) = \frac{1}{2}(\xi'_i + \xi'_{*i})$ ,  $\eta'_i = \xi'_i - \xi'_{*i}$ , and  $v_r = v_m \eta$ , we have  $\xi^2 + \xi_*^2 = 2\zeta^2 + \frac{1}{2}\eta^2$ ,  $d\xi_* d\xi = d\eta d\zeta$ ,  $D(\xi^2 \xi_i) = \zeta_i (\eta_i \eta_j - \eta'_i \eta'_j)$ ,  $D(\xi_{\langle i} \xi_{j\rangle}) = \frac{1}{2}(\eta_i \eta_j - \eta'_i \eta'_j)$ . Thus,

$$\begin{aligned} \mathcal{D}^2(\xi_{\langle i} \xi_{j\rangle}) &= \frac{1}{4}(\eta_i \eta_j - \eta'_i \eta'_j)(\eta_i \eta_j - \eta'_i \eta'_j) \\ &= \frac{1}{2}(\eta^4 - \eta_i \eta'_i \eta_j \eta'_j) = \frac{1}{2}\eta^4 \sin^2 \theta, \end{aligned}$$

where the last equation is obtained by the fact that the relative velocity is deflected by an angle of  $\theta$  after the binary collision, while its magnitude remains unchanged, see Fig. 2-1.

In the calculation of  $D^2(\xi^2 \xi_i)$ , if we ignore the terms which have zero contribution

to the integral in Eq. (3-22), we have

$$\begin{aligned}
 D^2(\zeta^2\zeta_i) &= \zeta_1^2(\eta_1\eta_j - \eta'_1\eta'_j)(\eta_1\eta_j - \eta'_1\eta'_j) + \zeta_2^2(\eta_2\eta_j - \eta'_2\eta'_j)(\eta_2\eta_j - \eta'_2\eta'_j) \\
 &\quad + \zeta_3^2(\eta_3\eta_j - \eta'_3\eta'_j)(\eta_3\eta_j - \eta'_3\eta'_j) \\
 &= \frac{\zeta^2}{3}(\eta_1\eta_j - \eta'_1\eta'_j)(\eta_1\eta_j - \eta'_1\eta'_j) + \frac{\zeta^2}{3}(\eta_2\eta_j - \eta'_2\eta'_j)(\eta_2\eta_j - \eta'_2\eta'_j) \\
 &\quad + \frac{\zeta^2}{3}(\eta_3\eta_j - \eta'_3\eta'_j)(\eta_3\eta_j - \eta'_3\eta'_j) \\
 &= \frac{2}{3}\zeta^2(\eta^4 - \eta_i\eta'_i\eta_j\eta'_j) = \frac{2}{3}\zeta^2\eta^4 \sin^2 \theta.
 \end{aligned}$$

After integration with respect to  $\zeta$  it can be shown that,

$$\alpha_{11} = \beta_{00} = \frac{1}{8}\sqrt{\frac{\pi}{2}}^3 4\pi v_m \int_0^\infty \exp\left(-\frac{\eta^2}{2}\right) \eta^7 \sigma_\mu d\eta, \quad (3-23)$$

where

$$\sigma_\mu = \int \frac{B(\cos \theta, v_r)}{v_r} \sin^2 \theta d\Omega = 2\pi \int_0^\pi \frac{B(\cos \theta, v_m \eta)}{v_m \eta} \sin^3 \theta d\theta, \quad (3-24)$$

is the viscosity cross-section. Therefore, the shear viscosity, which is obtained from Eq. (3-21) for the first approximation, is given by

$$\mu^{[1]} = \frac{5\sqrt{\pi m k_B T}}{8D}, \quad (3-25)$$

where

$$D = \left(\frac{m}{4k_B T}\right)^4 \int_0^\infty v_r^7 \sigma_\mu \exp\left(-\frac{mv_r^2}{4k_B T}\right) dv_r. \quad (3-26)$$

The corresponding thermal conductivity is given by

$$\kappa^{[1]} = \frac{15}{4} \frac{k_B}{m} \mu^{[1]}, \quad (3-27)$$

which results in a Prandtl number

$$\text{Pr} = \frac{\mu c_p}{\kappa} = \frac{5k_B}{2m} \frac{\mu}{\kappa} = \frac{2}{3}, \quad (3-28)$$

where  $c_p$  is the specific heat at constant pressure.

Finally, it is noted that the VDF from the first-order Chapman-Enskog expansion is

$$f = F_{eq} \left[ 1 - \frac{2m\kappa}{5nk_B^2 T} \left( \frac{mc^2}{2k_B T} - \frac{5}{2} \right) c_i \frac{\partial \ln T}{\partial x_i} - \frac{m\mu}{nk_B^2 T^2} \frac{\partial u_i}{\partial x_j} c_{\langle i} c_{j \rangle} \right].$$

### 3.2.0.3 Expansion to higher-orders

It turns out that the expansion to first-order is accurate enough for the shear viscosity and thermal conductivity: the results do not change much if we consider larger values of  $n_a$  and  $n_b$  in Eq. (3-17). For example, for inverse power-law potentials (2-13), expansion to the second-order leads to

$$\begin{aligned}\mu^{[2]} &= \left[ 1 + \frac{3(\eta - 5)^2}{2(\eta - 1)(101\eta - 113)} \right] \mu^{[1]}, \\ \kappa^{[2]} &= \left[ 1 + \frac{(\eta - 5)^2}{4(\eta - 1)(11\eta - 13)} \right] \kappa^{[1]}.\end{aligned}$$

For Maxwell molecules, Eqs. (3-26) and (3-27) are exact, while for HS molecules, if we consider  $n_a = n_b = 4$ , we have

$$\mu^{[4]} = 1.016\mu^{[1]}, \text{ and } \kappa^{[4]} = 1.025\kappa^{[1]}. \quad (3-29)$$

For inverse power-law potentials (2-13) with exponents  $5 \leq \eta < \infty$ , the correction factors fall between these for Maxwell and HS molecules.

### 3.2.0.4 Problems of Chapman-Enskog expansion

The Chapman-Enskog expansion [20] leads to respectively the Euler, NS, Burnett, and super-Burnett equations at the zeroth-, first-, second-, and third-order approximations. However, it received criticisms because

- the Burnett and super-Burnett equations are unstable to perturbation with small wavelength [10, 29];
- one does not know what step of the approximation is required or sufficient to obtain a solution that is correct up to  $\text{Kn}^n$  [17, 111], e.g., the super-Burnett equations are not necessarily more accurate than the Burnett equations.

Although the augmented Burnett equations [151] solves the instability problem, the second criticism remains.

## 3.3 Moment methods

Another way to obtain the closed macroscopic equations is proposed by Grad [33]. In his method, the state of a gas is described by a set of moments (e.g.,  $\rho$ ,  $\mathbf{u}$ ,  $T$ ,  $p_{ij}$ , and  $\mathbf{q}$  are used in Grad 13 method). In addition to Eq. (2-29), he obtained macroscopic equations for the evolution of shear stress and heat flux by respectively multiplying Eq. (4-10) with

$c_i c_j$  and  $c_i c^2$  and integrating over molecular velocity space:

$$\begin{aligned} \frac{D\sigma_{ij}}{Dt} + \frac{\partial u_{ijk}^0}{\partial x_k} + \frac{4}{5} \frac{\partial q_{\langle i}}{\partial x_{j\rangle}} + 2\sigma_{k\langle i} \frac{\partial u_{j\rangle}}{\partial x_k} + \sigma_{ij} \frac{\partial u_k}{\partial x_k} + 2p \frac{\partial u_{\langle i}}{\partial x_{j\rangle}} &= -\frac{p}{\mu} \sigma_{ij}, \\ \frac{Dq_i}{Dt} + \frac{5}{2} p \frac{\partial \theta}{\partial x_i} - \sigma_{ik} \frac{\partial \theta}{\partial x_k} - \sigma_{ik} \theta \frac{\partial \ln \rho}{\partial x_k} - \frac{\sigma_{ik}}{\rho} \frac{\partial \sigma_{kl}}{\partial x_l} - \frac{5}{2} \theta \frac{\partial \sigma_{ik}}{\partial x_k} + \frac{1}{2} \frac{\partial u_{ik}^1}{\partial x_k} \\ + \frac{1}{6} \frac{\partial w}{\partial x_i} + u_{ijk}^0 \frac{\partial u_k}{\partial x_l} + \frac{7}{5} q_i \frac{\partial u_k}{\partial x_k} + \frac{7}{5} q_k \frac{\partial u_i}{\partial x_k} + \frac{2}{5} q_k \frac{\partial u_k}{\partial x_i} &= -\frac{p}{\mu} q_i, \end{aligned} \quad (3-30)$$

where  $\theta = k_B T/m$ , the indices in angular brackets denote the symmetric and trace-free part of a tensor, the terms in the right-hand-side of equation are obtained from the Boltzmann equation for Maxwell molecules, and

$$\frac{D}{Dt} = \frac{\partial}{\partial t} + u_k \frac{\partial}{\partial x_k} \quad (3-31)$$

is the material derivative.

The system is not closed because of the following unknown quantities:

$$[u_{ijk}^0, u_{ij}^1] = m \int [c_{\langle i} c_j c_{k\rangle}, c^2 c_{\langle i} c_{j\rangle}] f d\mathbf{v}, \quad w = m \int c^4 (f - F_{eq}) d\mathbf{v}. \quad (3-32)$$

Grad closed the moment equations by expanding the VDF into the Hermite polynomials of the peculiar velocity, with the coefficients related to the considered low-order moments:

$$f = F_{eq} \left[ 1 + \frac{\sigma_{ij}}{2\rho(k_B T/m)^2} c_{\langle i} c_{j\rangle} + \frac{2}{5} \frac{q_i}{\rho(k_B T/m)^2} c_i \left( \frac{c^2}{2RT} - \frac{5}{2} \right) \right]. \quad (3-33)$$

As a result,  $u_{ijk}^0 = w = 0$  and  $u_{ij}^1 = 7\theta\sigma_{ij}$ .

Similarly, higher-order equations such as the Grad 26 moments equations are constructed by adding more moments to the VDF. Generally speaking, when the rarefaction effects become significant, the number of moments should be increased. For example, for normal shock waves with Mach number up to 1.65 and 1.887, at least 13 and 21 moments are needed to capture the shock profiles [138]. Contrary to the Burnett and super-Burnett equations, the Grad moment systems are linearly stable, and hence research into the Grad moment equations remains active and significant progress has been made. To remove the problem of hyperbolicity that results in discontinuities in the simulation of shock waves with large Mach numbers, Struchtrup & Torrihon derived the regularized 13 (R13) moment equations by combining Grad's moment method and Chapman-Enskog expansion [114]. Later, Gu & Emerson developed the R26 moment equations [38]. R13 and R26 are both linearly stable, and are accurate to the order of  $Kn^3$  and  $Kn^5$ , respectively. For instance, the regularized 13 moment equations have been successfully applied to the lid-driven flow up to  $Kn \sim 0.7$  [93] and the regularized 26 moment equations are

applied to micro-channel flows in the transition regime [38].

### 3.4 Accuracy of macroscopic equations

The accuracy of many macroscopic equations have been assessed in wall-bounded problems, where the rarefaction and boundary effects are tangled. Note that the boundary conditions are not easy to construct for macroscopic equations involving higher-order derivatives/moments. Therefore, they may be not imposed in a strict manner, and whether these macroscopic equations capture the rarefaction effects or not are unclear. Therefore, to fully assess the accuracy of macroscopic equations, we need to find a problem without the influence of gas-wall interaction. The structure of normal shock wave is one of the perfect examples where the gas-wall interaction is absent. However, due to the stability issue some macroscopic equations may not be able to produce converged solutions.

Hence we consider the spontaneous Rayleigh-Brillouin scattering (RBS), where the light is scattered by the density fluctuation of gas molecules; more details is presented in Section ???. It provides a perfect test bed to assess whether the macroscopic equations can capture the rarefaction effect or not, since i) it does not involve any gas-wall interactions; ii) it is effectively 1D and can be linearized, which makes the macroscopic equations simple and solvable.

We introduce the following dimensionless quantities:

$$\begin{aligned}\tilde{x} &= \frac{x_1}{L_0}, & \tilde{t} &= \frac{t}{L/v_0}, & \tilde{\rho} &= \frac{\rho}{\rho_0} - 1, & \tilde{u} &= \frac{u_1}{v_0}, \\ \tilde{T} &= \frac{T}{T_0} - 1, & \tilde{\sigma} &= \frac{\sigma_{11}}{p_0}, & \tilde{q} &= \frac{q_1}{p_0 v_0},\end{aligned}\quad (3-34)$$

where  $v_0 = \sqrt{k_B T_0 / m}$ , and linearize Eq. (2-29) into the following forms (tildes are omitted for clarity):

$$\begin{aligned}\frac{\partial \rho}{\partial t} + \frac{\partial u}{\partial x} &= 0, \\ \frac{\partial u}{\partial t} + \frac{\partial \rho}{\partial x} + \frac{\partial T}{\partial x} + \frac{\partial \sigma}{\partial x} &= 0, \\ \frac{3}{2} \frac{\partial T}{\partial t} + \frac{\partial u}{\partial x} + \frac{\partial q}{\partial x} &= 0,\end{aligned}\quad (3-35)$$

which, as stated before, are not closed since expressions for the stress  $\sigma$  and the heat flux  $q$  are not known.

### 3.4.0.1 Equations from Chapman-Enskog expansion

In Rayleigh-Brillouin scattering, the stress and heat flux in Eq. (3-35) are given by<sup>①</sup>

$$\sigma^{(NS)} = -\frac{4}{3}Kn \frac{\partial u}{\partial x}, \quad q^{(NS)} = -\frac{15}{4}Kn \frac{\partial T}{\partial x}. \quad (3-36)$$

Applying the Laplace transform for  $t$  and the Fourier transform for  $x$  in the spontaneous RBS, Eqs. (3-35) and (3-36) are turned into the following matrix form [71]:

$$\begin{bmatrix} -i\varpi & 2i\pi & 0 \\ 2i\pi & -i\varpi + \frac{16}{3}\pi^2Kn & 2i\pi \\ 0 & 2i\pi & -\frac{3}{2}i\varpi + 15\pi^2Kn \end{bmatrix} \begin{bmatrix} \hat{\rho} \\ \hat{u} \\ \hat{T} \end{bmatrix} = \begin{bmatrix} 1 \\ 0 \\ 0 \end{bmatrix}, \quad (3-37)$$

where  $\hat{\rho}$ ,  $\hat{u}$ , and  $\hat{T}$  are the spectra of the perturbation density, velocity, and temperature, respectively, and  $\varpi$  is the angular frequency normalized by  $v_0/L$  (and hence  $\varpi = 2\sqrt{2}\pi f_s$ ).

The spectrum of the spontaneous RBS is the real part density disturbance  $\hat{\rho}$ . By solving Eq. (3-37) we find that the spectrum can be described by:

$$S_s^{NS} = \text{Re} \left( \frac{160iKn^2\pi^4 + 46Kn\varpi\pi^2 - 3i\varpi^2 + 8i\pi^2}{160Kn^2\varpi\pi^4 - 46iKn\varpi^2\pi^2 + 120iKn\pi^4 - 3\varpi^3 + 20\varpi\pi^2} \right).$$

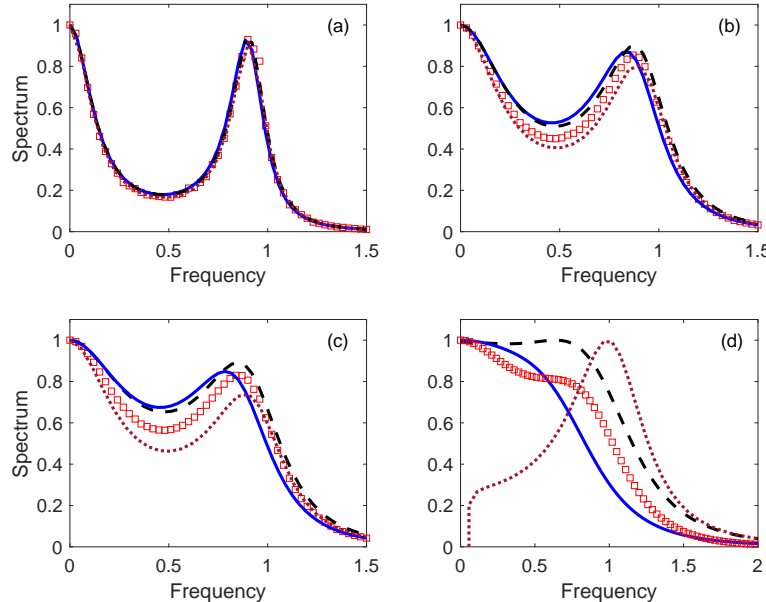


图 3-1 Spontaneous RBS spectra when (a)  $Kn = 0.02$ , (b)  $Kn = 0.04$ , (c)  $Kn = 0.05$ , and (d)  $Kn = 0.1$ . Solid, dashed and dotted lines are results from the NS, Burnett and super-Burnett equations, respectively.

If the Chapman-Enskog expansion is applied to the second-order of  $Kn$ , the Burnett equations can be derived. For Maxwellian molecules, the linearized constitutive relations

<sup>①</sup> Note that in this chapter  $Kn$  is  $\sqrt{2/\pi}$  times of the Knudsen number defined in Eq. (1-10).

for the stress and heat flux become

$$\begin{aligned}\sigma^{(B)} &= \sigma^{(NS)} - \text{Kn}^2 \left( \frac{4}{3} \frac{\partial^2 \rho}{\partial x^2} - \frac{2}{3} \frac{\partial^2 T}{\partial x^2} \right), \\ q^{(B)} &= q^{(NS)} - \frac{7}{4} \text{Kn}^2 \frac{\partial^2 u}{\partial x^2}.\end{aligned}\quad (3-38)$$

The super-Burnett equations can be derived if the Chapman-Enskog expansion is applied to the third-order of Kn, where the stress and heat flux in this particular problem are [108]:

$$\begin{aligned}\sigma^{(SB)} &= \sigma^{(B)} + \frac{2}{9} \text{Kn}^3 \frac{\partial^3 u}{\partial x^3}, \\ q^{(SB)} &= q^{(B)} + \text{Kn}^3 \left( \theta_7 \frac{\partial^3 T}{\partial x^3} - \frac{5}{8} \frac{\partial^3 \rho}{\partial x^3} \right),\end{aligned}\quad (3-39)$$

with  $\theta_7 = -157/16$  for Maxwellian molecules.

Figure 3-1 shows the spectra of spontaneous RBS. It is seen that the NSF equations perform well up to  $\text{Kn} \approx 0.02$ . The Burnett equations, although accurate to the second-order of Kn, seems do not improve the accuracy in predicting the spectra of spontaneous RBS. It is surprising that the super-Burnett equations derived to the third-order of Kn in the Chapman-Enskog expansion perform much worse than the Burnett equations that are obtained from the Chapman-Enskog expansion to the second-order of Kn, especially when  $\text{Kn} = 0.1$ . This conforms the criticism that one does not know what step of the approximation is required or sufficient to obtain a solution that is correct up to order  $\text{Kn}^n$  [17, 111].

### 3.4.0.2 Moment equations

In Rayleigh-Brillouin scattering the stress and heat flux in the G13 equations satisfy the following equations:

$$\begin{aligned}\frac{\partial \sigma}{\partial t} + \frac{4}{3} \frac{\partial u}{\partial x} + \frac{8}{15} \frac{\partial q}{\partial x} &= -\frac{\sigma}{\text{Kn}}, \\ \frac{\partial q}{\partial t} + \frac{\partial \sigma}{\partial x} + \frac{5}{2} \frac{\partial T}{\partial x} &= -\frac{2}{3} \frac{q}{\text{Kn}}.\end{aligned}\quad (3-40)$$

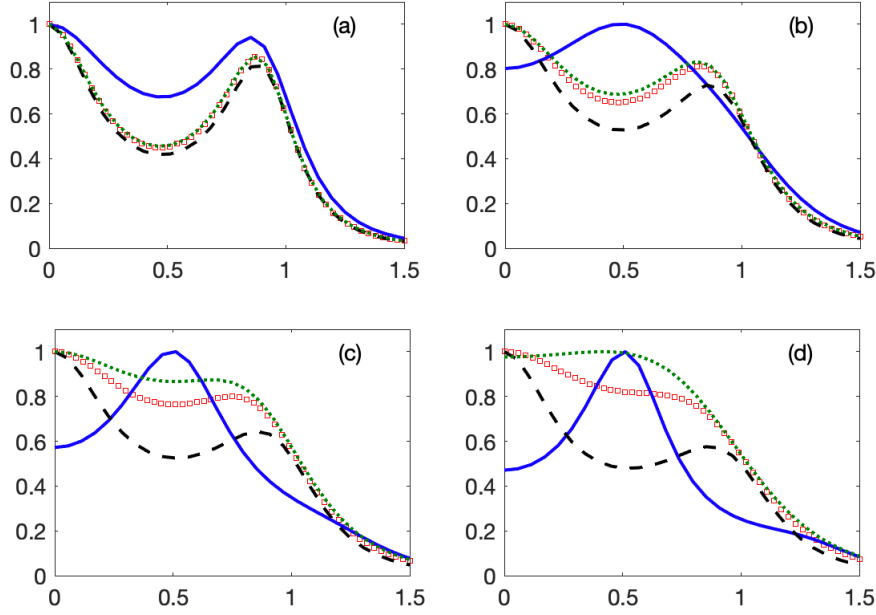


图 3-2 Spectra of the spontaneous RBS. The horizontal and vertical axis are the normalized frequency and spectrum, respectively. Form the left to right, the Knudsen numbers in each column are 0.04, 0.06, 0.08, and 0.1, respectively. Solid, dashed, and dotted lines are the results from the G13, R13, and R26 moment equations, respectively.

The spectrum of spontaneous RBS can be obtained by solving the following matrix:

$$\begin{bmatrix} -i\omega & 2i\pi & 0 & 0 & 0 \\ 2i\pi & -i\omega & 2i\pi & 2i\pi & 0 \\ 0 & 2i\pi & -\frac{3}{2}i\omega & 0 & 2i\pi \\ 0 & \frac{8}{3}i\pi & 0 & -i\omega + \frac{1}{Kn} & \frac{16}{15}i\pi \\ 0 & 0 & 5i\omega & 2i\omega & -i\omega + \frac{2}{3Kn} \end{bmatrix} \begin{bmatrix} \hat{\rho} \\ \hat{u} \\ \hat{T} \\ \hat{\sigma} \\ \hat{q} \end{bmatrix} = \begin{bmatrix} 1 \\ 0 \\ 0 \\ 0 \\ 0 \end{bmatrix}, \quad (3-41)$$

where  $\hat{\sigma}$  and  $\hat{q}$  are respectively the Laplace-Fourier transform of  $\sigma$  and  $q$  in the temporal-spatial domains.

Note that the G13 equations are accurate to the second-order of  $Kn$ , which have been extended to the R13 equations that are accurate to the third-order of  $Kn$  [112]. The governing equations for the stress and heat flux become

$$\begin{aligned} \frac{\partial \sigma}{\partial t} + \frac{4}{3} \frac{\partial u}{\partial x} + \frac{8}{15} \frac{\partial q}{\partial x} - \frac{6}{5} Kn \frac{\partial^2 \sigma}{\partial x^2} &= -\frac{\sigma}{Kn}, \\ \frac{\partial q}{\partial t} + \frac{\partial \sigma}{\partial x} + \frac{5}{2} \frac{\partial T}{\partial x} - \frac{18}{5} Kn \frac{\partial^2 q}{\partial x^2} &= -\frac{2}{3} \frac{q}{Kn}. \end{aligned} \quad (3-42)$$

Similarly, the evolution of the stress and heat flux in the linearized R26 equations,

which are accurate up to the fifth-order of Kn, are governed by [38]:

$$\begin{aligned}\frac{\partial \sigma}{\partial t} + \frac{4}{3} \frac{\partial u}{\partial x} + \frac{8}{15} \frac{\partial q}{\partial x} + \frac{\partial \bar{m}}{\partial x} &= -\frac{\sigma}{Kn}, \\ \frac{\partial q}{\partial t} + \frac{5}{2} \frac{\partial T}{\partial x} + \frac{\partial \sigma}{\partial x} + \frac{1}{6} \frac{\partial \bar{\Delta}}{\partial x} + \frac{1}{2} \frac{\partial \bar{R}}{\partial x} &= -\frac{2}{3} \frac{q}{Kn},\end{aligned}\quad (3-43)$$

where the higher-order moments  $\bar{m}$ ,  $\bar{\Delta}$ , and  $\bar{R}$  are governed by the following equations:

$$\begin{aligned}\frac{\partial \bar{m}}{\partial t} + \frac{9}{5} \frac{\partial \sigma}{\partial x} + \frac{9}{35} \frac{\partial \bar{R}}{\partial x} - \frac{16}{7} \frac{Kn}{A_{\phi 1}} \frac{\partial^2 \bar{m}}{\partial x^2} &= -\frac{3}{2} \frac{\bar{m}}{Kn}, \\ \frac{\partial \bar{\Delta}}{\partial t} + 8 \frac{\partial q}{\partial x} - \frac{7Kn}{3} \frac{\partial^2 \bar{\Delta}}{\partial x^2} - 4Kn \frac{\partial^2 \bar{R}}{\partial x^2} &= -\frac{2}{3} \frac{\bar{\Delta}}{Kn}, \\ \frac{\partial \bar{R}}{\partial t} + \frac{56}{15} \frac{\partial q}{\partial x} + 2 \frac{\partial \bar{m}}{\partial x} - \frac{Kn}{5} \left( \frac{54}{7A_{\psi 1}} + \frac{16}{3} \right) \frac{\partial^2 \bar{R}}{\partial x^2} - \frac{28Kn}{45} \frac{\partial^2 \bar{\Delta}}{\partial x^2} &= -\frac{7}{6} \frac{\bar{R}}{Kn},\end{aligned}\quad (3-44)$$

with  $A_{\phi 1} = 2.097$  and  $A_{\psi 1} = 1.698$ .

Figure 3-2 shows the RBS spectra obtained from the G13, R13, and R26 moment equations. When  $Kn = 0.02$ , all the moment equations predict the same spectrum as that from the LBE. However, even when  $Kn$  is increased to  $Kn = 0.04$ , spectra predicted by the G13 equations deviate significantly from those of the LBE. The R13 equations are accurate up to  $Kn \approx 0.04$ , while the R26 equations are accurate up to  $Kn \approx 0.06$ .

### 3.4.0.3 Discussions

Based on the benchmarking solutions from the Boltzmann equation for the spectra of Rayleigh-Brillouin scattering, we have assessed the accuracy of macroscopic equations. Interestingly, as the order of Chapman-Enskog expansion increases, the accuracy of the obtained macroscopic equations does not necessarily increase (say, when  $Kn \gtrsim 0.03$ , the super-Burnett equations are less accurate than the Burnett equations), which confirms the criticism that one does not know what step of the approximation is required or sufficient to obtain a solution that is correct up to order  $Kn^n$ . For the (regularized) moment equations, however, the accuracy in the prediction of RBS spectra is consistent with the accuracy in deriving these equations, that is, increases monotonically from the G13, R13, to the R26 moment equations.

From these comparisons, it may be concluded that the regularized moment method is a proper way to derive higher-order macroscopic equations to describe the rarefied gas dynamics, where the derivation is straightforward, and its accuracy is definitive and controllable, that is, the accuracy increases with the number of moments or order of Hermite polynomials used to approximate the VDF. This is quite important in numerical simula-

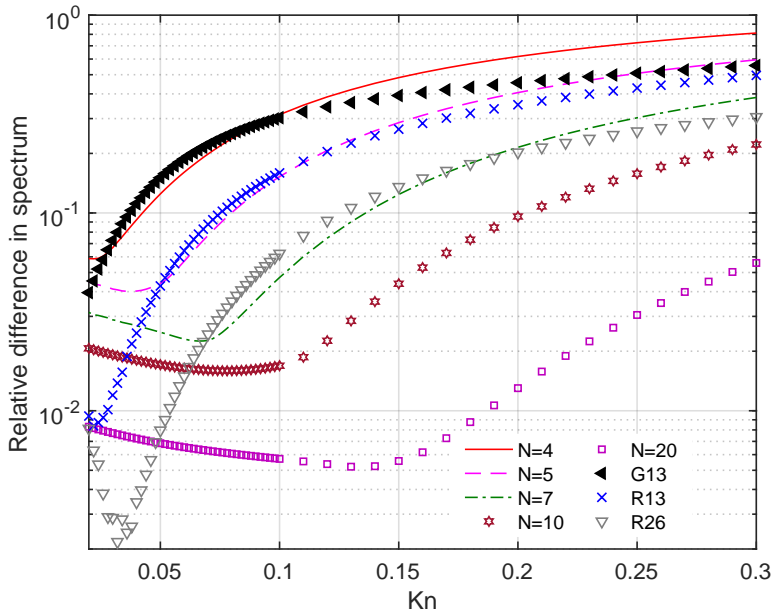


图 3-3 Difference  $\int_{\infty}^{\infty} |S_{\text{LBE}} - S_{\text{GH}}^N| df_s$  in the spectrum of spontaneous RBS, where  $S_{\text{GH}}^N$  is the spectrum obtained by solving the Shakhov kinetic model in section 5.1.3 with the Gauss-Hermite quadrature of order  $N$ . Note that before the comparison, areas of RBS spectra are normalized to unity. The solution may be viewed being accurate when the relative difference is less than 0.05. Also note that the relative difference when  $N = 5, 7, 10$  and 20 does not decrease with  $\text{Kn}$  when  $\text{Kn} \lesssim 0.1$  is probably because the spectrum between the Rayleigh and Brillouin peaks is nearly zero [see Fig. ??] so any tiny difference is magnified.

tions, where the error may be estimated in prior. To further illustrate this point, we study the performance of higher-order moment method, by solving the linearized Shakhov equation numerically using the discrete velocity method based on the Gauss-Hermite quadrature [100], which is equivalent to the Grad moment method at different order of approximations [101]. To be specific, if the  $N$ -th order Gauss-Hermite quadrature is considered in the discretization of molecular velocity space, the moment up to the order  $N - 1$  can be captured accurately [101]. Consider the fact that the G13 equations where the distribution function is expanded up to third-order Hermite polynomials are accurate to  $O(\text{Kn}^2)$ , the numerical solution of the Shakhov equation based on the Gauss-Hermite quadrature of order  $N$  has an accuracy of  $O(\text{Kn}^{N-2})$ .

Using solutions of the Shakhov model approximated by the 60th-order Gauss-Hermite quadrature as reference, we analyze the accuracy of various orders of moment equations in Fig. 3-3. We also show the relative error in the spectrum from comparisons between the G13/R13/R26 equations and the LBE. Obviously, as more moments (i.e., higher-order quadrature) are included, the accuracy increases monotonically. When  $N = 4$ , the Gauss-Hermite quadrature yields an equivalent moment system accurate to

$O(\text{Kn}^2)$ , therefore, the relative difference curve almost overlaps that from the G13 equations. Similarly,  $N = 5$  and 7 yield equivalent moment systems accurate to  $O(\text{Kn}^3)$  and  $O(\text{Kn}^5)$ , respectively. Therefore, relative difference curves nearly overlap with those from the R13 and R26 moment equations in a wide range of Knudsen numbers.

It can also be seen from Fig. 3-3 that at large values of Kn the convergence rate of moment equations is slow. For example, when  $\text{Kn} = 0.3$ , when  $N$  is increased from 5 to 20, that is, when the accuracy of the equivalent moment systems is increased from  $O(\text{Kn}^3)$  to  $O(\text{Kn}^{18})$ , the error is only reduced by about one order of magnitude. And the solution of  $N = 20$  can be marginally viewed as accurate. Accuracy of moment systems may become worse in wall-bounded problems such as the Poiseuille flow between two parallel plates [116], as Gauss-Hermite polynomials are not good at capturing the discontinuities in VDF.

To conclude, higher-order Chapman-Enskog expansion does not necessarily lead to more accurate prediction of rarefied gas dynamics, while the moment method produces more accurate results when more moments are included, but the convergence to true solutions may be slow when the Knudsen number is large.

### 3.5 Convergence speed of moment equations

We now assess the accuracy of macroscopic equations in the problem of sound propagation in gas confined between the transducer and receiver [140], see Fig. 1-2. We use the linearized Shakhov kinetic model equation, as the Gauss-Hermite quadrature can be applied [101] to mimic the behavior of moment equations at any order, replacing the complicated derivation and solving of high-order moment equations beyond R26; the numerical method is given in Section ??, where the numerical solution agrees well with experimental data of Schotter [99], see Fig. 1-2.

Macroscopic equations are the same as in the Rayleigh-Brillouin scattering problem, except for the R26 equations we have  $A_M = 1 = A_{\alpha 1} = A_{\Omega 1} = A_{\phi 1} = A_{\psi 1} = A_{R1} = 1$  in Eq. (3-44), as derived from the Shakhov kinetic model. The boundary conditions for NS and R13 equations corresponding to the diffuse boundary condition for gas kinetic model equations can be found in Ref. [113], while that for R26 equations is given in Ref. [38].

The parameter  $\varpi \tau_c$  in Fig. 1-2 is proportional to the temporal Knudsen number  $\text{Kn}_t$  as  $\varpi \tau_c = 2\sqrt{2}\pi \text{Kn}_t$ . Therefore, as  $\varpi \tau_c$  increases, the rarefaction effects become stronger, so macroscopic equations gradually lose accuracy. The NSF equations are accurate when

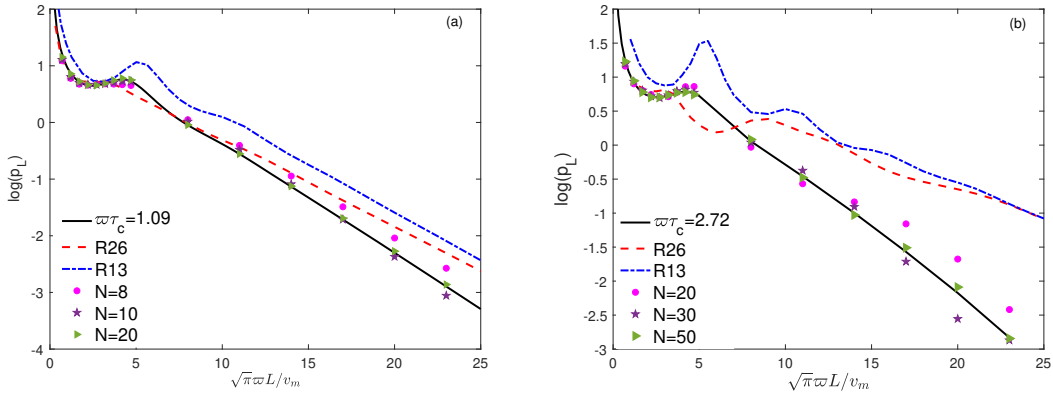


图 3-4 Convergence test of moment equations: sound amplitude at the receiver as function of the dimensionless length  $\sqrt{\pi\omega L}/v_m$ . Solid lines represent the accurate results from the Shakhov model solved by the discrete velocity method [119]. Symbols are approximate solutions of the Shakhov model when the molecular velocity space  $\boldsymbol{v}$  is discretized according to Gauss-Hermite quadrature of order  $N$ ; these solutions are equivalent to those of Grad moment equations (having  $(N+1)(N+2)(N+3)/6$  moments) that are accurate up to the order of  $\text{Kn}^{N-2}$ .

$\omega\tau_c = 0.1$  (not shown), but are already very inaccurate when  $\omega\tau_c = 0.3$ ; R13 equations, which are accurate to the order of  $\text{Kn}^3$ , give reasonable good results up to  $\omega\tau_c = 0.3$ , see Fig. 1-2. While R26 equations, which are accurate to the order of  $\text{Kn}^5$ , predict the normal pressure at the receiver fairly well up to  $\omega\tau_c = 0.67$ . This finding is in agreement with that in the spontaneous RBS, i.e., the accuracy of moment equations increases when more moments are included in macroscopic equations.

Now we consider the speed of convergence of moment systems for moderate and highly rarefied gas flows, that is, we are interested in how many moments should be included to give reasonable prediction of sound pressure.

Typical results are depicted in Fig. 3-4. When  $\omega\tau_c = 1.09$ , the result of using Gauss-Hermite quadrature of order 8 is more accurate than that of R26 equations. This is because  $N = 8$  corresponding to Grad moment equations of accuracy  $O(\text{Kn}^6)$ , one order more accurate than R26 equations. In order to obtain accurate results, however, the VDF has to be expanded into Hermite polynomials to the 20-th order. We say the convergence is rather slow as increasing  $N$  from 10 to 20 only results in marginal improvement of accuracy. This situation becomes more severe when  $\omega\tau_c$  increases to 2.72. From Fig. 3-4(b) we see that R13 and R26 moments equations are quite inaccurate; in order to have accurate results, Gauss-Hermite quadrature of order higher than 50 is needed.

The slow convergence of moment systems in describing rarefied gas flows may be explained at the mesoscopic level. To this end we note that when the steady oscillation is reached, the derivation VDF  $f - F_{eq}$  is proportional to the real part of  $\exp(i\omega t)h(x_1, \boldsymbol{v})$ .

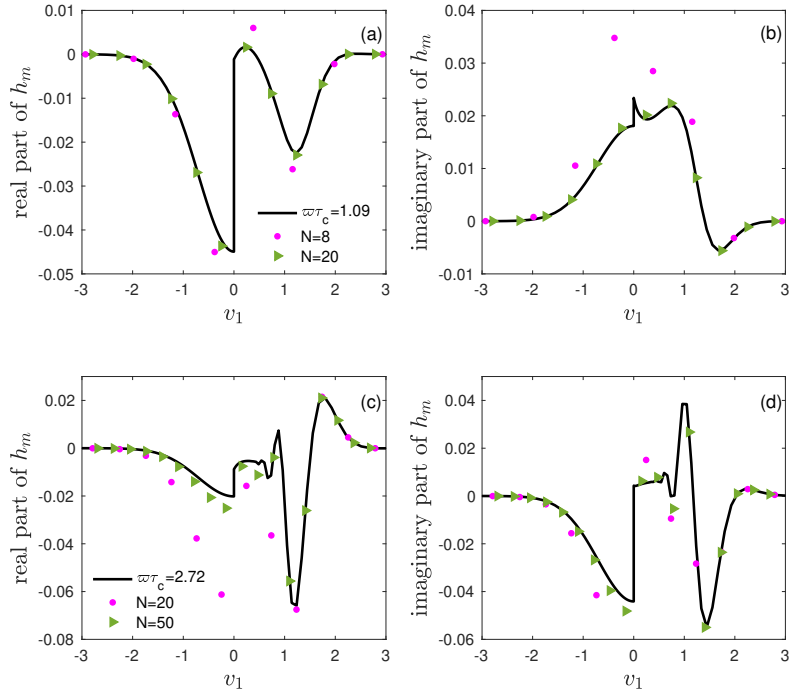


图 3-5 Marginal VDF at the receiver. (a, b)  $\varpi\tau_c = 1.09$  and (c,d)  $\varpi\tau_c = 2.72$ . In both cases,  $\sqrt{\pi}\varpi L/v_m = 20$ . Solid lines represent the accurate results from the Shakhov model solved by the discrete velocity method [119], while symbols are approximate solutions of the Shakhov model when the molecular velocity space  $\nu$  is discretized by the Gauss-Hermite quadrature of order  $N$ .

The marginal VDF  $h_m = \iint h dv_2 v_3$  at the resting receiver is plotted in Fig. 3-5. When  $\varpi\tau_c = 1.09$ , the spatial and temporal Knudsen numbers are respectively  $\text{Kn} = 0.069$  and  $\text{Kn}_t = 0.123$ , the VDF is smooth, except it has a huge jump at  $v_1 = 0$ . This kind of jump (discontinuities) is typical in wall-bounded rarefied gas flows. The VDF when  $v_1 < 0$  is described by the Gaussian function as per Maxwell's diffuse boundary condition, while that at  $v_1 > 0$  deviates from the equilibrium distribution because of the relative large value of  $\text{Kn}_t$  so that the system does not have enough time to reach equilibrium. The Gauss-Hermite quadrature of order  $N = 8$  cannot predict the gas pressure in Fig. 3-4(a) because the VDF in Fig. 3-5(a,b), when  $v_1 > 0$ , cannot be well fitted by the Hermite polynomials up to the 8th order. Only the Gauss-Hermite quadrature of order higher than  $N = 20$  can give reasonable good prediction of macroscopic gas pressure at the receiver. However, from the comparison in VDF we see that this is not enough in capturing accurately the physics at the mesoscopic level. When  $\varpi\tau_c = 2.72$ , the two Knudsen numbers are  $\text{Kn} = 0.171$  and  $\text{Kn}_t = 0.306$ , the rarefaction effects are even stronger, and the VDF becomes more and more irregular: it not only has jump at  $v_1 = 0$ , but has rapid variations. To capture this rapid variations, the order of Gauss-Hermite quadrature needs to be very

high. From the comparisons in Fig. 3-4(b) and Fig. 3-5(c,d) we see that although Gauss-Hermite quadrature of order  $N = 50$  can predict the gas pressure at the receiver, it still produces some discrepancy in the mesoscopic VDF.

Thus, the large discontinuities and rapid variations in the VDF is the underlying reason for the slow convergence of Grad moment systems, since the smooth Hermite polynomials are not good at resolving these irregular structures. In the framework of Gauss-Hermite quadrature, adding more discrete velocity grids is not economic. In highly rarefied gas flows, it is beneficial to directly solve the kinetic equation by the discrete velocity method using numerical quadratures that are more suitable for wall-bounded problems [116, 81, 3], instead of deriving and solving higher-order moment systems [15].

## 第4章 快速谱方法

The Boltzmann collision operator can be viewed as a generalized convolution, therefore, it is better solved by the Fourier spectral method powered by the convolution theorem. In this chapter the fast spectral method is introduced. First, we show how to inversely design the collision kernel to recover the shear viscosity. Second, we present detailed spectral approximation of the Boltzmann collision operator and assess its accuracy by comparing the numerical results with some exact solutions for Maxwell molecules. Third, the conventional iterative scheme is used to find steady-state solutions of space-inhomogeneous problems, and the fast spectral method is validated by experiment and molecular dynamics simulation. Finally, some challenging microflows inside two-dimensional cavity are solved to reveal the role of intermolecular potentials.

### 4.1 Inverse design of collision kernel

To fully harness the power of Fourier spectral method and convolution theorem, the collision kernel  $B(\theta, v_r)$  in the Boltzmann collision operator should be carefully designed, otherwise the numerical complexity will be increased by one order of magnitude; this aspect will be discussed in the next chapter. Here we show how to design the collision kernel to recover the temperature-dependence of shear viscosity. When the shear viscosity is fixed, according to the structure of Boltzmann collision operator, the thermal conductivity is automatically recovered.

#### 4.1.1 Power-law potential

From Eq. (2-15) it is seen that the collision kernel for the power-law potential (2-13) is a power-law function of the relative collision velocity:

$$B = \frac{b|db|}{\sin \theta |d\theta|} v_r \equiv c_\alpha(\theta) v_r^\alpha, \quad \alpha = \frac{\eta - 5}{\eta - 1}, \quad (4-1)$$

and it is shown in Eq. (??) that  $c_\alpha(\theta)$  approaches  $\theta^{(\alpha-5)/2}$  at the grazing collision limit  $\theta \rightarrow 0$ . This indicates that the total cross-section  $\int \sigma_D d\Omega$  is infinite. Although the global existence and rapid relax-to-equilibrium of the classical solutions has been proven [35], a finite cutoff is introduced in numerical simulations. One way to eliminate the infinity

is to cut off  $c_\alpha(\theta)$ , e.g., by setting  $c_\alpha(\theta) = 0$  when  $\theta$  is smaller than a fixed value, or equivalently, when the aiming distance  $b$  is larger than a fixed value. This is justified by the fact that the grazing collision only leads to small change of system state. Another prevalent way is to replace  $c_\alpha(\theta)$  with the constant  $C_\alpha$ , yielding the variable-hard-sphere (VHS) model in DSMC [9]:

$$B = C_\alpha v_r^\alpha, \quad (4-2)$$

where the constant  $C_\alpha$  is determined by equating the shear viscosity of the Boltzmann equation when the collision kernels are given by Eq. (4-1) and Eq. (4-2), respectively. The expression of shear viscosity from the Chapman-Enskog expansion is given by Eq. (3-26). Accordingly, we have

$$C_\alpha = \frac{3}{4} \left( \frac{2K}{m} \right)^{\frac{2}{\eta-1}} A_2(\eta), \quad (4-3)$$

with  $A_2(\eta) = \int_0^\infty \sin^2 \theta W_0 dW_0$  and  $W_0 = b(mv_r^2/2K)^{1/(\eta-1)}$  [9]. Note that the shear viscosity is a power-law function of temperature:

$$\mu \propto T^\omega, \quad \omega = \frac{\eta + 3}{2(\eta - 1)}, \quad (4-4)$$

where  $\omega$  is the viscosity index.

In the VHS model, the differential cross-section  $\sigma_D = C_\alpha v_r^{\alpha-1}$  is independent of the deflection angle  $\theta$ . This model is widely used in DSMC, and the isotropic cross-section makes DSMC easy to implement when  $\alpha \geq 0$ . To recover both the shear viscosity and self-diffusion coefficient, the variable-soft-sphere model is used, where the deflection angle satisfies  $b = \sigma \cos^{\alpha'} \left( \frac{\theta}{2} \right)$ , and hence the collision kernel is

$$B = \frac{\alpha b \sigma}{4} \cos^{\alpha'-2} \left( \frac{\theta}{2} \right) v_r^\alpha. \quad (4-5)$$

When  $\alpha' = 1$  the HS collision is recovered, see Fig. 2-1.

Likewise, to achieve maximum efficiency in the numerical approximation of Boltzmann collision operator, special forms of collision kernel are needed. For example, Mouhot and Pareschi [80] suggested to use the anisotropic collision kernel:

$$B = C'_\alpha \sin^{\alpha-1} \left( \frac{\theta}{2} \right) v_r^\alpha, \quad (4-6)$$

where  $C'_\alpha$  is a constant. This special  $\theta$ -dependent collision kernel not only enables the development of FSM for computing the collision operator deterministically, but also mimics the growth trend of the collision kernel when decreasing the deflection angle. Like the

VHS model in DSMC, the constant  $C'_\alpha$  should be determined by equating the shear viscosities of the Boltzmann equation when the collision kernels are given by Eq. (4-1) and Eq. (4-6), yielding  $C'_\alpha = (\alpha + 3)(\alpha + 5)C_\alpha/24$ . Note that for HS molecules ( $\alpha = 1$ ), the VHS collision kernel and the collision kernel (4-6) are exactly the same.

With the identity

$$\int_0^{\pi/2} \sin^p \theta \cos^q \theta d\theta = \frac{\Gamma[(p+1)/2]\Gamma[(q+1)/2]}{2\Gamma[(p+q+2)/2]},$$

we find that the collision kernel (4-6) can be generalized to

$$B = \frac{\Gamma[(7+\alpha)/2]C_\alpha}{6\Gamma[(3+\alpha+\gamma)/2]\Gamma(2-\gamma/2)} \sin^{\alpha+\gamma-1}\left(\frac{\theta}{2}\right) \cos^{-\gamma}\left(\frac{\theta}{2}\right) v_r^\alpha, \quad (4-7)$$

where the additional parameter  $\gamma$  introduces plenty of flexibility, not only to extend the applicability of FSM to all inverse power-law potentials except the Coulomb potential, but also to recover the ratio between shear viscosity and self-diffusion coefficient.

#### 4.1.2 Lennard-Jones potential

The power-law potential is a phenomenological model. In reality, the potential between monatomic gas is better described by the Lennard-Jones potential (??). Unlike the power-law potential, the shear viscosity is not a single power-law function of temperature over the whole temperature range [20]. Only when the temperature does not vary too much could the parameter  $D$  in Eq. (3-26) be approximated by a single power-law function of temperature. For instance, when  $k_B T/\epsilon$  is large (or small), the repulsive (or attractive) part of the force dominants, and  $D \propto T^{-1/6}$  (or  $D \propto T^{-1/3}$ ). Also, when  $2 < k_B T/\epsilon < 3$ , we have  $D \propto T^{-0.31}$  such that  $\mu \propto T^{0.81}$ , see Fig. 4-1. In these regions, the VHS model can be successfully implemented in DSMC. However, a single power-law fit is not adequate over a wider temperature range. To tackle this problem, the generalized VHS model [44], the variable-soft-sphere model [73], and the generalized soft sphere model [24], have been proposed in DSMC.

Here we employ the concept of the generalized VHS model to construct the collision kernel that is suitable for FSM to solve the Boltzmann collision operator. According to Eq. (3-26), we observe that the special form of  $D$  given by the fit function in Fig. 4-1 can be recovered if the collision kernel takes the form of

$$B = \frac{d_{LJ}^2}{8\pi} \sum_{j=1}^3 \frac{(m/4\epsilon)^{(\alpha_j-1)/2}}{\Gamma(\frac{3+\alpha_j}{2})} b_j \sin^{\alpha_j-1}\left(\frac{\theta}{2}\right) v_r^{\alpha_j}, \quad (4-8)$$

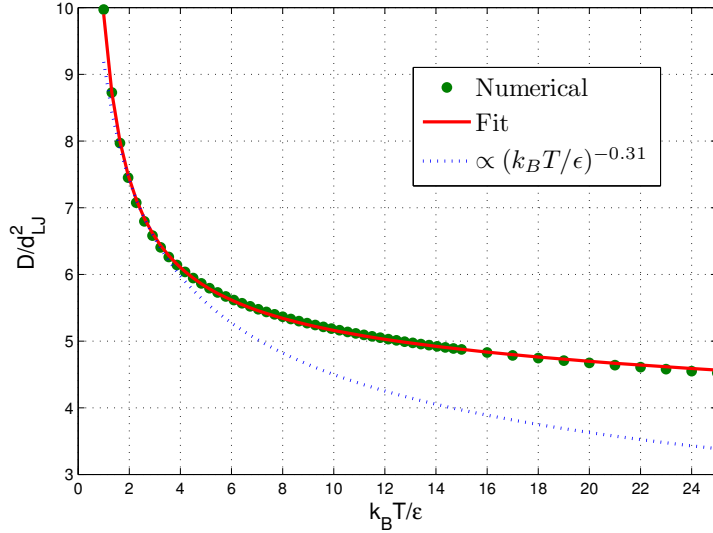


图 4-1 The parameter  $D$  (3-26) as a function of  $k_B T / \epsilon$  for the Lennard-Jones potential (??), which is fitted by  $D/d_L^2 = b_1(k_B T / \epsilon)^{-0.4} + b_2(k_B T / \epsilon)^{-0.45} + b_3(k_B T / \epsilon)^{-0.5}$ , where  $b_1 = 407.4$ ,  $b_2 = -811.9$ , and  $b_3 = 414.4$ .

where  $\alpha_1 = 0.2$ ,  $\alpha_2 = 0.1$ ,  $\alpha_3 = 0$ , and the values of  $b_j$  are shown in Fig. 4-1.

For argon with the potential depth  $\epsilon = 119.18 k_B$  in Eq. (??), the fit in Fig. 4-1 covers the temperature range from 120 K to 3000 K, while the VHS model with  $\mu \propto T^{0.81}$  (dotted line) works only when  $240 \text{ K} < T < 360 \text{ K}$ . For wider temperature range, more terms with different values of  $\alpha_j$  and  $b_j$  may be needed. We note that, however, no matter how many terms are added (as long as  $\alpha_j > -1$ ), the computational time of the corresponding collision operator will not increase.

## 4.2 Normalization

For practical calculations, it is convenient to introduce the following dimensionless variables:

$$\begin{aligned}\tilde{f} &= \frac{v_m^3}{n_0} f, & \tilde{\mathbf{x}} &= \frac{\mathbf{x}}{L}, & (\tilde{\mathbf{v}}, \tilde{\mathbf{u}}, \tilde{\mathbf{c}}) &= \frac{(\mathbf{v}, \mathbf{u}, \mathbf{c})}{v_m}, \\ \tilde{t} &= \frac{v_m}{L} t, & \tilde{\mathbf{a}} &= \frac{L}{v_m^2} \mathbf{a}, & \tilde{n} &= \frac{n}{n_0}, \\ \tilde{T} &= \frac{T}{T_0}, & \tilde{\mathbf{p}} &= \frac{\mathbf{p}}{n_0 k_B T_0}, & \tilde{\mathbf{q}} &= \frac{\mathbf{q}}{n_0 k_B T_0 v_m},\end{aligned}\tag{4-9}$$

where  $n_0$  is the average number density of gas molecules,  $L$  is the characteristic flow length,  $v_m$  is the most probable speed at the reference temperature  $T_0$ .

Under these normalization, the Boltzmann equation (2-8) with the collision ker-

nel (4-7) takes the following form

$$\frac{\partial \tilde{f}}{\partial t} + \tilde{\mathbf{v}} \cdot \frac{\partial \tilde{f}}{\partial \tilde{\mathbf{x}}} + \tilde{\mathbf{a}} \cdot \frac{\partial \tilde{f}}{\partial \tilde{\mathbf{v}}} = Q^+ - \nu \tilde{f}. \quad (4-10)$$

Here, the gain term of the collision operator is

$$Q^+ = \frac{1}{Kn'} \iint \sin^{\alpha+\gamma-1} \left( \frac{\theta}{2} \right) \cos^{-\gamma} \left( \frac{\theta}{2} \right) \tilde{v}_r^\alpha \tilde{f}(\tilde{\mathbf{v}}'_*) \tilde{f}(\tilde{\mathbf{v}}') d\Omega d\tilde{\mathbf{v}}_*, \quad (4-11)$$

while the loss term of the collision operator is  $\nu \tilde{f}$ , where the collision frequency is

$$\nu = \frac{1}{Kn'} \iint \sin^{\alpha+\gamma-1} \left( \frac{\theta}{2} \right) \cos^{-\gamma} \left( \frac{\theta}{2} \right) \tilde{v}_r^\alpha \tilde{f}(\tilde{\mathbf{v}}'_*) d\Omega d\tilde{\mathbf{v}}_*, \quad (4-12)$$

and

$$Kn' = \frac{64\sqrt{2}^\alpha}{5} \Gamma \left( \frac{\alpha + \gamma + 3}{2} \right) \Gamma \left( 2 - \frac{\gamma}{2} \right) Kn. \quad (4-13)$$

It should be noted that in DSMC, the MFP of VHS model (i.e.,  $\lambda_{vhs}$  in Eq. (4.52) in Ref. [9]) is frequently used. In order to compare the numerical results obtained from FSM and DSMC, the following relation should be taken into account:

$$Kn = \frac{15\pi}{2(7-2\omega)(5-2\omega)} Kn_{vhs}. \quad (4-14)$$

For the Lennard-Jones potential, when the collision kernel is approximated by Eq. (4-8), the term  $\sin^{\alpha+\gamma-1}(\theta/2) \cos^{-\gamma}(\theta/2) v_r^\alpha / Kn'$  in Eqs. (4-11) and (4-12) should be replaced by

$$\frac{5 \sum_{j=1}^3 b_j (k_B T_0 / 2\epsilon)^{(\alpha_j-1)/2} \sin^{\alpha_j-1}(\theta/2) \tilde{v}_r^{\alpha_j} / \Gamma(\frac{\alpha_j+3}{2})}{64\sqrt{2}Kn \sum_{j=1}^3 b_j (k_B T_0 / \epsilon)^{(\alpha_j-1)/2}}. \quad (4-15)$$

Considering the above normalization scheme, the normalized macroscopic quantities are related to the normalized VDF as follows:

$$[\tilde{n}, \tilde{\mathbf{u}}, \tilde{T}, \tilde{p}_{ij}, \tilde{q}_i] = \int \left[ 1, \tilde{\mathbf{v}}, \frac{2}{3\tilde{n}} \tilde{c}^2, 2\tilde{c}_i \tilde{c}_j, \tilde{c}^2 \tilde{c}_i \right] \tilde{f} d\tilde{\mathbf{v}}. \quad (4-16)$$

For simplicity, the tildes on normalized quantities will be omitted hereafter.

### 4.3 Fast spectral method

The numerical approximation of the Boltzmann collision operator by the FSM is introduced. For its main properties we refer to the original paper by Mouhot and Pareschi [80]. Detailed calculations are presented because literature gives different results for the kernel mode [80, 26, 47].

### 4.3.1 Carleman representation

We rewrite the Boltzmann collision operator using the Carleman representation. With the basic identity

$$\begin{aligned} 2 \int_{\mathbb{R}^3} \delta(2\mathbf{y} \cdot \mathbf{v}_r + y^2) f(\mathbf{y}) d\mathbf{y} &= 2 \int_{\mathbb{R}^3} \delta(|\mathbf{y} + \mathbf{v}_r|^2 - v_r^2) f(\mathbf{y}) d\mathbf{y} \\ &= 2 \int_{\mathbb{R}^3} \delta(y^2 - v_r^2) f(\mathbf{y} - \mathbf{v}_r) d\mathbf{y} \\ &= v_r \int_{\mathbb{S}^2} f(v_r \Omega - \mathbf{v}_r) d\Omega, \end{aligned}$$

and Eq. (2-10) for the post-collision velocities, the gain part of the collision operator (4-11) is rewritten as

$$\begin{aligned} Q^+ &= \frac{1}{Kn'} \iint \theta v_r f\left(\mathbf{v}_* - \frac{v_r \Omega - \mathbf{v}_r}{2}\right) f\left(\mathbf{v} + \frac{v_r \Omega - \mathbf{v}_r}{2}\right) d\Omega d\mathbf{v}_* \\ &= \frac{2}{Kn'} \iint \theta \delta(2\mathbf{y} \cdot \mathbf{v}_r + y^2) f\left(\mathbf{v}_* - \frac{\mathbf{y}}{2}\right) f\left(\mathbf{v} + \frac{\mathbf{y}}{2}\right) dy d\mathbf{v}_* \\ &= \frac{4}{Kn'} \iint \theta \delta(\mathbf{y} \cdot \mathbf{v}_r + y^2) f(\mathbf{v}_* - \mathbf{y}) f(\mathbf{v} + \mathbf{y}) dy d\mathbf{v}_* \\ &= \frac{4}{Kn'} \iint \theta \delta(\mathbf{y} \cdot \mathbf{z}) f(\mathbf{v} + \mathbf{z}) f(\mathbf{v} + \mathbf{y}) dy dz, \end{aligned} \quad (4-17)$$

where  $\theta = \sin^{\alpha+\gamma-1}(\theta/2) \cos^{-\gamma}(\theta/2) v_r^{\alpha-1}$  if we consider the simple case where the collision kernel is given by Eq. (4-7). Other collision kernels introduced in the above section can be handled in the same way.

Notice that in the step-by-step calculations of Eq. (4-17) we have used the transformations  $\mathbf{y} = (v_r \Omega - \mathbf{v}_r)/2$  and  $\mathbf{z} = \mathbf{v}_* - \mathbf{v} - \mathbf{y} = -\mathbf{v}_r - \mathbf{y}$ ; also the delta function requires that  $\mathbf{y}$  to be perpendicular to  $\mathbf{z}$ . Therefore, the deflection angle  $\theta$  satisfies

$$\cos \theta = \frac{\Omega \cdot \mathbf{v}_r}{v_r} = \frac{-(\mathbf{y} - \mathbf{z}) \cdot (\mathbf{y} + \mathbf{z})}{|\mathbf{y} + \mathbf{z}|^2} \stackrel{\mathbf{y} \perp \mathbf{z}}{=} \frac{z^2 - y^2}{y^2 + z^2}, \quad (4-18)$$

which results in

$$\sin\left(\frac{\theta}{2}\right) = \frac{|\mathbf{y}|}{\sqrt{y^2 + z^2}}, \quad \cos\left(\frac{\theta}{2}\right) = \frac{|\mathbf{z}|}{\sqrt{y^2 + z^2}}. \quad (4-19)$$

Hence  $\theta = |\mathbf{y}|^{\alpha+\gamma-1} |\mathbf{z}|^{-\gamma}$  and the collision operator is simplified to

$$\begin{aligned} Q &= \frac{4}{Kn'} \iint dy dz \delta(\mathbf{y} \cdot \mathbf{z}) |\mathbf{y}|^{\alpha+\gamma-1} |\mathbf{z}|^{-\gamma} \\ &\quad \times [f(\mathbf{v} + \mathbf{z}) f(\mathbf{v} + \mathbf{y}) - f(\mathbf{v} + \mathbf{y} + \mathbf{z}) f(\mathbf{v})]. \end{aligned} \quad (4-20)$$

### 4.3.2 Fourier-Galerkin spectral method

In FSM, the VDF is periodized on the domain  $\mathcal{D}_L = [-L_\nu, L_\nu]^3$ . We adopt uniform grid points in the velocity space:

$$v_k(j_k) = 2 \frac{L_\nu}{N_k} j_k, \quad (k = 1, 2, 3) \quad (4-21)$$

where  $j_k \in [-N_k/2, -N_k/2+1, \dots, N_k/2-1]$  and  $N_k$  is the number of velocity grid points in the  $k$ -th velocity direction. Suppose  $\mathcal{B}_S$ , a sphere of radius  $S$  centered at the origin, is the support of VDF. Usually the minimum value  $L_\nu = (3 + \sqrt{2})S/2$  is chosen to avoid the aliasing error caused by the periodicity of VDF [90]. The VDF is then approximated by a truncated Fourier series,

$$f(\boldsymbol{\nu}) = \sum_{j=-(N_1, N_2, N_3)/2}^{(N_1, N_2, N_3)/2-1} \hat{f}_j \exp(i\boldsymbol{\xi}_j \cdot \boldsymbol{\nu}), \quad (4-22)$$

$$\hat{f}_j = \frac{1}{(2L_\nu)^3} \int f(\boldsymbol{\nu}) \exp(-i\boldsymbol{\xi}_j \cdot \boldsymbol{\nu}) d\boldsymbol{\nu}, \quad (4-23)$$

where  $\boldsymbol{\xi}_j = \mathbf{j}\pi/L$  are the frequency components with  $\mathbf{j} = (j_1, j_2, j_3)$ .

The Boltzmann collision operator (4-20) is also truncated, with the infinite velocity space replaced by the finite one in  $\mathcal{B}_R$ , where the truncation radius  $R$  satisfies [80, 26]:

$$R \geq \sqrt{2}S. \quad (4-24)$$

Numerical analysis in Fig. 4-5 will show that, however,  $R$  cannot be larger than  $L$ . Expanding the truncated collision operator by Fourier series, we find that the  $\mathbf{j}$ -th spectrum of the truncated collision operator is related to spectrum  $\hat{f}$  as:

$$\hat{Q}_j = \sum_{\substack{l+m=j \\ l,m=-(N_1, N_2, N_3)/2}}^{(N_1, N_2, N_3)/2-1} \hat{f}_l \hat{f}_m [\beta(\mathbf{l}, \mathbf{m}) - \beta(\mathbf{m}, \mathbf{m})], \quad (4-25)$$

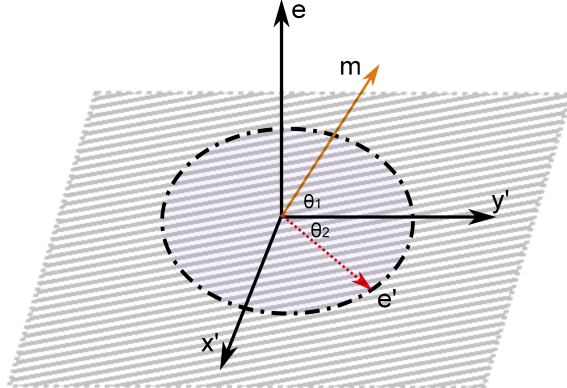


图 4-2 Demonstration of the integral with respect to  $\mathbf{e}'$  used in the calculation of kernel mode (4-26). When the vector  $\mathbf{e}$  is fixed, we can make the  $x'y'$  plane perpendicular to  $\mathbf{e}$  and  $\mathbf{m}$  fall in the  $ey'$  plane. The vector  $\mathbf{e}'$  degenerates to a two-dimensional vector characterized by the polar angle  $\theta_2$  varying from 0 to  $2\pi$ . The polar and azimuthal angles of  $\mathbf{e}'$  in the new coordinate system are  $\theta$  and  $\pi/2 - \theta_2$ , respectively, and the angle between the vector  $\mathbf{m}$  and  $y'$ -axis is  $\theta_1$ .

where  $\mathbf{l} = (l_1, l_2, l_3)$ ,  $\mathbf{m} = (m_1, m_2, m_3)$ , and the kernel mode  $\beta(\mathbf{l}, \mathbf{m})$  is simplified to

$$\begin{aligned}\beta(\mathbf{l}, \mathbf{m}) &= \frac{4}{Kn'} \iint \delta(\mathbf{y} \cdot \mathbf{z}) |\mathbf{y}|^{\alpha+\gamma-1} |\mathbf{z}|^{-\gamma} \exp(i\xi_{\mathbf{l}} \cdot \mathbf{y} + i\xi_{\mathbf{m}} \cdot \mathbf{z}) d\mathbf{y} d\mathbf{z} \\ &= \frac{1}{Kn'} \int \int \delta(\mathbf{e} \cdot \mathbf{e}') \left[ \int_{-R}^R |\rho|^{\alpha+\gamma} \exp(i\rho \xi_{\mathbf{l}} \cdot \mathbf{e}) d\rho \right] \\ &\quad \times \left[ \int_{-R}^R |\rho'|^{1-\gamma} \exp(i\rho' \xi_{\mathbf{m}} \cdot \mathbf{e}') d\rho' \right] d\mathbf{e}' d\mathbf{e} \\ &= \frac{1}{Kn'} \int_{\mathbb{S}^2} \phi_{\alpha+\gamma}(\xi_{\mathbf{l}} \cdot \mathbf{e}) \left[ \int_{\mathbb{S}^2} \delta(\mathbf{e} \cdot \mathbf{e}') \phi_{1-\gamma}(\xi_{\mathbf{m}} \cdot \mathbf{e}') d\mathbf{e}' \right] d\mathbf{e},\end{aligned}\quad (4-26)$$

with  $\mathbf{e}, \mathbf{e}'$  being the unit vectors in the sphere  $\mathbb{S}^2$ , and

$$\phi_{\delta}(s) = 2 \int_0^R \rho^{\delta} \cos(\rho s) d\rho. \quad (4-27)$$

Equation (4-26) can be simplified further. We construct a new Cartesian coordinate system, where its  $z'$  axis is parallel to  $\mathbf{e}$ , the  $y'$  axis is just the projection of vector  $\mathbf{m}$  into the plane  $e_{\perp}$  perpendicular to the  $z'$  axis, and the  $x'$  axis is in the plane  $e_{\perp}$  and perpendicular to the  $y'$  axis, see Fig. 4-2. Suppose the polar and azimuthal angles of  $\mathbf{e}'$  in the new coordinate system are  $\theta$  and  $\pi/2 - \theta_2$ , respectively, and the angle between the vector  $\mathbf{m}$  and  $y'$ -axis is  $\theta_1$ . Then, we have  $\delta(\mathbf{e} \cdot \mathbf{e}') = \delta(\cos \theta)$  so that  $\int_0^{\pi} g(\theta) \delta(\cos \theta) d\theta = g(\pi/2)$

for smooth function  $g(\theta)$ ,  $\xi_{\mathbf{m}} \cdot \mathbf{e}' = |\xi_{\mathbf{m}}| \cos \theta_1 \cos \theta_2$ , and the kernel mode becomes

$$\begin{aligned}
 \beta(\mathbf{l}, \mathbf{m}) &= \frac{1}{Kn'} \int_{S^2} d\mathbf{e} \phi_{\alpha+\gamma}(\xi_{\mathbf{l}} \cdot \mathbf{e}) \\
 &\quad \times \left[ \int_0^{2\pi} \int_0^\pi \delta(\cos \theta) \phi_{1-\gamma}(|\xi_{\mathbf{m}}| \cos \theta_1 \cos \theta_2) d\theta d\theta_2 \right] \\
 &= \frac{1}{Kn'} \int_{S^2} \phi_{\alpha+\gamma}(\xi_{\mathbf{l}} \cdot \mathbf{e}) \left[ \int_0^{2\pi} \phi_{1-\gamma}(|\xi_{\mathbf{m}}| \cos \theta_1 \cos \theta_2) d\theta_2 \right] d\mathbf{e} \\
 &= \frac{2}{Kn'} \int_{S^2} \phi_{\alpha+\gamma}(\xi_{\mathbf{l}} \cdot \mathbf{e}) \cdot \psi_\gamma(|\xi_{\mathbf{m}}| \cos \theta_1) d\mathbf{e}, \tag{4-28}
 \end{aligned}$$

where

$$\psi_\gamma(s) = \int_0^\pi \phi_{1-\gamma}(s \cos \theta_2) d\theta_2 = 2\pi \int_0^R \rho^{1-\gamma} J_0(\rho s) d\rho, \tag{4-29}$$

with  $J_0$  being the zeroth-order Bessel function.

Note that  $\xi_{\mathbf{l}}$  and  $\xi_{\mathbf{m}}$  in Eq. (4-28) appear in two functions. If they also appear in two different functions in the final form of  $\beta(\mathbf{l}, \mathbf{m})$ , Eq. (4-25) can be calculated effectively by the FFT-based convolution. The separation of  $\mathbf{l}$  and  $\mathbf{m}$  in Eq. (4-28) can be realized approximately using the numerical quadrature. Two different methods will be employed and compared:

- in the first method,  $\beta(\mathbf{l}, \mathbf{m})$  is calculated numerically in spherical coordinates by the trapezoidal rule. Suppose the polar and azimuthal angles of the unit vector  $\mathbf{e}$  are  $\theta$  and  $\varphi$ , respectively. We divide each region  $0 \leq \theta \leq \pi$  and  $0 \leq \varphi \leq \pi$  (for symmetry) into  $M$  sections:  $\theta_p = p\pi/M$  and  $\varphi_q = q\pi/M$  with  $p, q = 1, 2, \dots, M$ . Then the kernel mode (4-28) is approximated by

$$\beta(\mathbf{l}, \mathbf{m}) \simeq \frac{4\pi^2}{Kn' M^2} \sum_{p,q=1}^{M-1,M} \phi_{\alpha+\gamma}(\xi_{\mathbf{l}} \cdot \mathbf{e}_{\theta_p, \varphi_q}) \psi_\gamma(\xi_{\mathbf{l}}^\perp) \cdot \sin \theta_p, \tag{4-30}$$

where

$$\xi_{\mathbf{l}}^\perp = \sqrt{|\xi_{\mathbf{m}}|^2 - (\xi_{\mathbf{m}} \cdot \mathbf{e}_{\theta_p, \varphi_q})^2}. \tag{4-31}$$

- in the second method,  $\beta(\mathbf{l}, \mathbf{m})$  is approximated by a Gauss-Legendre quadrature

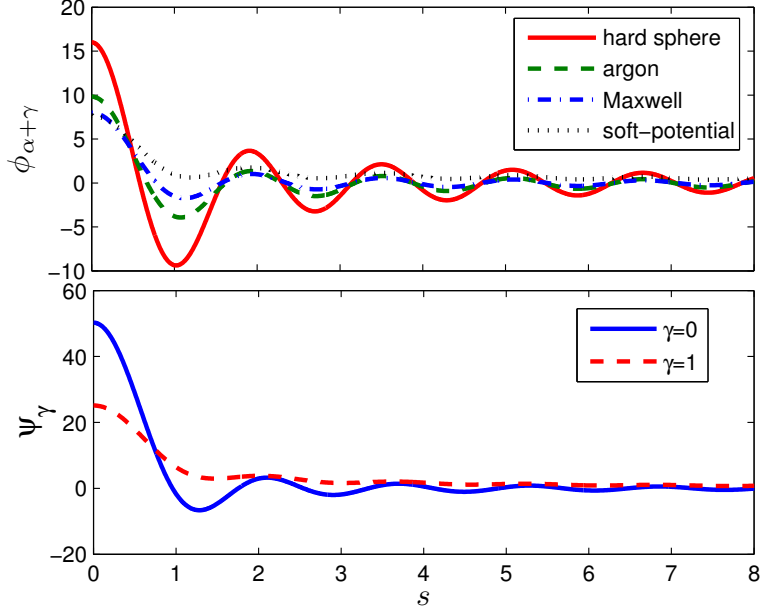


图 4-3 Profiles of  $\phi_{\alpha+\gamma}$  and  $\psi_\gamma$  according to Eqs. (4-27) and (4-29) when  $R = 4$  and  $\gamma = 0$ . Because of symmetry, the region  $s < 0$  is not plotted. For the soft potential, we use  $\alpha = -0.4$  and the shear viscosity is proportional to  $T^{1.2}$ .

of order  $M$  (see the Matlab code in Appendix ??):

$$\beta(\mathbf{l}, \mathbf{m}) \simeq \frac{4}{Kn'} \sum_{p,q=1}^M \omega_p \omega_q \phi_{\alpha+\gamma}(\xi_l \cdot \mathbf{e}_{\theta_p, \varphi_q}) \psi_\gamma(\xi_l^\perp) \cdot \sin \theta_p, \quad (4-32)$$

where  $\theta_p$  ( $\varphi_q$ ) and  $\omega_p$  ( $\omega_q$ ) are the  $p$  ( $q$ )-th point and weight in the Gauss-Legendre quadrature with  $\theta, \varphi \in [0, \pi]$ , and the unit vector is expressed as

$$\mathbf{e}_{\theta_p, \varphi_q} = (\sin \theta_p \cos \varphi_q, \sin \theta_p \sin \varphi_q, \cos \theta_p). \quad (4-33)$$

The analytical form of  $\phi_{\alpha+\gamma}(s)$  can be obtained when  $\alpha + \gamma$  is an integer. For instance, when  $\gamma = 0$ , for Maxwell molecules ( $\alpha = 0$ ) and HS ( $\alpha = 1$ ) molecules, we have

$$\begin{aligned} \phi_0(s) &= \frac{2 \sin(Rs)}{s}, \\ \phi_1(s) &= \frac{2R \sin(Rs)}{s} - \frac{4 \sin^2(Rs/2)}{s^2}, \end{aligned} \quad (4-34)$$

while for other cases  $\phi_{\alpha+\gamma}(s)$  and  $\psi_\gamma(s)$  can be accurately calculated by Gauss-Legendre quadrature numerically. Fig. 4-3 shows typical decaying-oscillating profiles of the two functions  $\phi_{\alpha+\gamma}$  and  $\psi_\gamma$ , where the quasi-period of oscillation is about  $2\pi/R$ .

Note that in the VHS model,  $-3 < \alpha \leq 1$ . From Eq. (4-27) it follows that  $\delta$  is restricted to the region  $(-1, +\infty)$ . Therefore,  $\alpha + \gamma > -1$  and  $1 - \gamma > -1$ . In the original collision kernel proposed by Mouhot and Pareschi [80],  $\gamma = 0$ , so that  $\alpha$  is restricted in

the region  $(-1, 1]$ . This means that the original collision kernel cannot deal with general forms of soft potentials. In our modified collision kernel (4-7), if we let  $\gamma \rightarrow 2$ ,  $\alpha$  can cover the whole region  $(-3, 1]$ , thus extending the applicability of FSM to all inverse power-law potentials except the Coulomb potential.

It should also be noted that for the Lennard-Jones potential, the storage of the kernel modes and computational cost of the collision operator is exactly the same as that for the single-term collision kernel (4-6) or (4-7). For the existence of  $\phi_{1+\gamma_1}$ ,  $\psi_{1-\gamma_1}$ ,  $\phi_{-1+\gamma_2}$ , and  $\psi_{1-\gamma_2}$ , one should choose  $-2 < \gamma_1 < 2$  and  $0 < \gamma_2 < 2$ . Therefore, we choose  $0 < \gamma_1 = \gamma_2 < 2$ . If  $\gamma_1 \neq \gamma_2$ , the storage and computational cost will be twice of that of the single-term collision kernel (4-7).

### 4.3.3 Detailed implementation

The detailed procedure to calculate the Boltzmann collision operator is now outlined. Let us assume Eq. (4-28) is approximated by the trapezoidal rule. First, the kernel modes is pre-computed and stored. The storage of  $\phi_{\alpha+\gamma}(\xi_l, \theta_p, \varphi_q)$  and  $\psi_\gamma(\xi_m, \theta_p, \varphi_q)$  requires  $2M(M-1)N_1N_2N_3$  units of compute memory. We also need  $N_1N_2N_3$  units of storage for

$$\phi_{loss} = \sum_{p,q=1}^{M-1,M} \phi_{\alpha+\gamma}(\xi_m, \theta_p, \varphi_q) \psi_\gamma(\xi_m, \theta_p, \varphi_q) \sin \theta_p, \quad (4-35)$$

which is used to calculate the collision frequency in Eq. (4-12). For space-homogeneous problems, such storage is relatively large when compared to the storage of VDF. However, when it comes to space-inhomogeneous problems, the storage will be relatively small because different spatial grids share the same kernel modes.

Second, we obtain the spectrum of VDF by applying the inverse FFT to  $f$ . Then, with Eq. (4-30), Eq. (4-25) becomes

$$\begin{aligned} \hat{Q}_j \approx & \frac{4\pi^2}{Kn'M^2} \underbrace{\sum_{p,q=1}^{M-1,M} \sum_{l+m=j} [\hat{f}_l \phi_{\alpha+\gamma}(\xi_l, \theta_p, \varphi_q)] \cdot [\hat{f}_m \psi_\gamma(\xi_m, \theta_p, \varphi_q)] \cdot \sin \theta_p}_{gain} \\ & - \underbrace{\frac{4\pi^2}{Kn'M^2} \sum_{l+m=j} \hat{f}_l \cdot [\hat{f}_m \phi_{loss}]}_{loss}. \end{aligned}$$

The loss term can be effectively calculated by FFT-based convolution, using the zero-padding technique [16]. For the gain term, one has to do FFT-based convolution for each pair of  $(p, q)$ , that is,  $M(M-1)$  times. The implementation is listed in Steps 2, 3, and

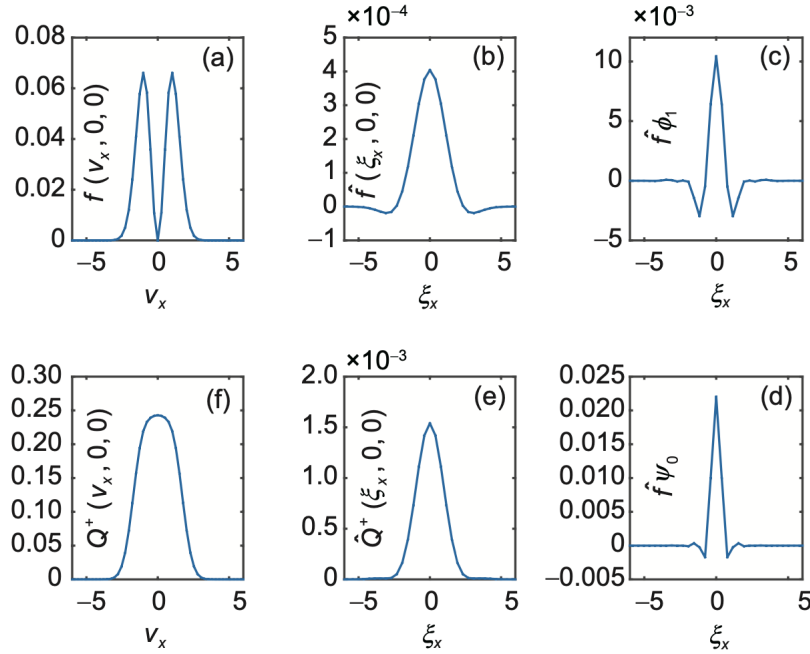


图 4-4 Numerical implementation of the FSM for the gain part of Boltzmann collision operator (4-11). Given the VDF in (a), its spectrum is obtained in (b) by inverse FFT. Then the spectrum is respectively multiplied with the kernel modes  $\phi$  and  $\psi$  (the results are in (c) and (d), respectively), and their convolution is shown in (e). The FFT of (e) gives the gain part of the Boltzmann collision operator for specific combination of  $p$  and  $q$  in (f). Summing  $Q^+$  for all combinations of  $p$  and  $q$  gives the gain part of the Boltzmann collision operator. Note that the whole process is done in three-dimensional velocity space and spectrum space, but for clarity only the one-dimensional results are shown.

4 in the algorithm 1 of Appendix ???. Finally, the collision operator  $Q$  is calculated by applying the FFT to  $\hat{Q}$  (Step 5). The whole process is visualized in Fig. 4-4.

Note that in algorithm 1 the zero-padding technique is employed to eliminate the aliasing error in FFT-based convolution. This process is accurate for arbitrary values of  $t_1$  and  $t_2$  (defined in Appendix ???) when the padding size in each direction is larger than one half of the velocity grid number. Considering the fact that the spectrum  $\hat{f}$  is non-zero only in the central region of frequency domain, we can expedite the calculation by ignoring zero-padding. This leads to the simpler and faster algorithm 2: numerical simulations show that both algorithms produce identical results, but the algorithm 2 is about 4 times faster than the algorithm 1.

Now we see that the computational cost of FSM is  $O(M^2 N^3 \log N)$ , where  $N$  is the same order as  $N_1, N_2$  and  $N_3$ . Note that  $\mathbf{l}$  and  $\mathbf{m}$  are not separable in classical spectral methods, and the computational cost of Eq. (4-25) is  $O(N^6)$  [28, 90]. A rough estimate of the speed-up can be given. In algorithm 2, one needs to do  $2M(M - 1) + 2$  times FFT (the array size is  $N_1 \times N_2 \times N_3$ ), while in classical spectral methods the computational

cost is the same with one direct convolution of one complex and one real array of size  $N_1 \times N_2 \times N_3$ . For comparison, we take  $M = 7$  and run our Matlab (version 2012a) programs on a PC with an Intel Xeon 3.3 GHz CPU. For  $N = 32$  (or 64), algorithm 2 is about 18 (or 62) times faster than the classical spectral methods. Further speed-up can be achieved by reducing the value of  $M$ , say, to 5.

#### 4.3.3.1 Conservation enforcement

One of the drawbacks of FSM, as with any spectral methods in the approximation of Boltzmann collision operator, is that it does not exactly conserve the momentum and energy. To ensure the conservation of momentum and energy, the method of Lagrangian multipliers can be employed [28]: after the collision operator  $Q$  is approximated, we construct  $Q^{new}$  by minimizing the function  $\sum_j (Q_j - Q_j^{new})^2$  under the constraints  $\sum_j Q_j^{new} = \sum_j \mathbf{v} Q_j^{new} = \sum_j v^2 Q_j^{new} = 0$ , yielding

$$Q^{new} = Q - (\lambda_n + \lambda_{\mathbf{v}} \cdot \mathbf{v} + \lambda_e v^2),$$

where the five Lagrangian multipliers satisfy

$$\begin{aligned} \sum_j Q &= \sum_j (\lambda_n + \lambda_{\mathbf{v}} \cdot \mathbf{v} + \lambda_e |\mathbf{v}|^2), \\ \sum_j \mathbf{v} Q &= \sum_j \mathbf{v} (\lambda_n + \lambda_{\mathbf{v}} \cdot \mathbf{v} + \lambda_e v^2), \\ \sum_j v^2 Q &= \sum_j v^2 (\lambda_n + \lambda_{\mathbf{v}} \cdot \mathbf{v} + \lambda_e v^2). \end{aligned}$$

Since the errors for the momentum and energy in FSM are spectrally small [80], the Lagrangian multipliers are very small. In practice, we normally do not use conservation enforcement if the steady-state solution of the Boltzmann equation can be quickly found.

#### 4.3.4 Non-uniform discretization of velocity space

In the simulation of rarefied gas flows with large Knudsen numbers, the “over concentration” phenomenon are frequently encountered [124], where the VDF concentrates or has sharp variations around  $v \sim 0$  due to the wall effect. To tackle this problem, the molecular velocity space should be discretized non-uniformly, with more points placed near  $v = 0$ . In microflows, we usually use the following non-uniform discretization:

$$v_i = \frac{L_v}{(N_v - 1)^l} (-N_v + 1, -N_v + 3, \dots, N_v - 1)^t, \quad (4-36)$$

where  $\iota$  is a positive odd number,  $L_v$  is the velocity bound, and  $N_v$  is the total number of discretized velocity in the  $i$ -th direction.

However, the frequency space must be discretized uniformly, otherwise the FFT-based convolution cannot be applied efficiently. This means that Steps 2 and 3 in the algorithm of Appendix ?? remain unchanged, but the Fourier transform in Steps 1 and 4 is calculated by direct summation. Fortunately, the computational cost can be reduced by considering the following two factors:

- the number of discretized frequency components  $N_\xi$  can be different from the corresponding velocity components  $N_v$ . In fact,  $N_\xi$  can be much smaller than  $N_v$  due to the spectral accuracy of FSM; hence the computational cost of the convolution is  $O(M^2 N_\xi \ln N_\xi)$ .
- in the rectangular Cartesian coordinates, the Fourier transform in Steps 1 and 4 can be done by direct summation in each direction sequentially, thus the cost will be at the order of  $N_v^3 N_\xi \ln N_v$ . This cost is certainly higher than the FFT on uniform grids, but is only comparable to the FFT-based convolution in Steps 2 and 3.

Therefore, compared to the uniform discretization with large number of velocity grids, the use of non-uniform velocity grids will not only reduce computational memory, but also computational time.

## 4.4 Accuracy in homogeneous relaxation

To assess the accuracy of FSM, the relax-to-equilibrium process of Maxwell molecules ( $\alpha, \gamma = 0$ ) is considered. This is a spatial-homogeneous problem, where the Boltzmann equation becomes

$$\frac{\partial f}{\partial t} = \frac{1}{Kn'} \iint \sin^{-1}\left(\frac{\theta}{2}\right) [f(\boldsymbol{v}')f(\boldsymbol{v}') - f(\boldsymbol{v}_*)f(\boldsymbol{v})] d\Omega d\boldsymbol{v}_*. \quad (4-37)$$

Without loss of generality, we choose  $Kn' = 32\pi/5$ . And for simplicity we consider the uniform discretization of molecular velocity space.

### 4.4.1 Bobylev-Krook-Wu solution

Equation (4-37) possesses the exact Bobylev-Krook-Wu (BKW) solution [54]:

$$f(\boldsymbol{v}, t) = \frac{1}{2(2\pi K)^{3/2}} \exp\left(-\frac{v^2}{2K}\right) \left(\frac{5K-3}{K} + \frac{1-K}{K^2} v^2\right), \quad (4-38)$$

表 4-1 Relative error  $\sum_j |Q_j^{nu} - Q_j^{an}| / \sum_j |Q_j^{an}|$  in the approximation of the Boltzmann collision operator. T (G) stands for the trapezoidal (Gauss-Legendre) quadrature used in the approximation of Eq. (4-28). Parameters are  $L = 8$  and  $R = 6$ .

N		$M = 5$	6	7	8	12	16
16	T	4.58E-1	4.73E-1	4.55E-1	4.52E-1	4.78E-1	4.83E-1
	G	2.10E-1	3.35E-1	2.48E-1	2.77E-1	2.74E-1	2.69E-1
24	T	7.94E-2	5.20E-2	4.73E-2	3.93E-2	2.92E-2	2.59E-2
	G	4.61E-2	2.09E-2	9.16E-3	2.10E-2	1.72E-2	1.37E-2
32	T	5.54E-2	3.51E-2	2.57E-2	1.93E-2	8.39E-3	4.75E-3
	G	4.26E-2	6.18E-3	6.49E-4	2.11E-4	1.86E-4	1.57E-4
48	T	4.26E-2	3.88E-2	2.77E-2	2.08E-2	8.99E-3	5.01E-3
	G	4.31E-2	6.17E-3	6.09E-4	4.56E-5	4.94E-6	3.85E-6
64	T	5.90E-2	3.87E-2	2.77E-2	2.08E-2	8.99E-3	5.02E-3
	G	4.30E-2	6.16E-3	6.10E-4	4.70E-5	3.87E-6	4.31E-6

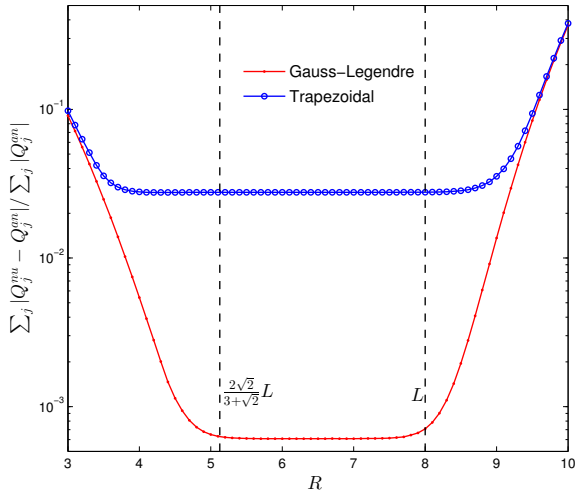


图 4-5 The relative error versus the truncation radius  $R$ . Parameters are  $L = 8$ ,  $N = 48$ , and  $M = 7$ . The Gauss-Legendre quadrature is used in the approximation of the kernel mode.

where  $K = 1 - 0.4 \exp(-t/6)$ . The evolution of the fourth- and sixth-order moments is given by

$$\begin{aligned} M_4 &= \int f v_1^4 d\mathbf{v} = 6K - 3K^2, \\ M_6 &= \int f v_1^6 d\mathbf{v} = 45K^2 - 30K^3. \end{aligned} \quad (4-39)$$

The integration of Eq. (4-37) with respect to  $t$  will introduce some numerical error. In order to assess how accurately the FSM can approximate the Boltzmann collision operator, we compare  $Q^{nu}$ , the numerical approximation of  $Q$ , to the analytical solution  $Q^{an}$ , which

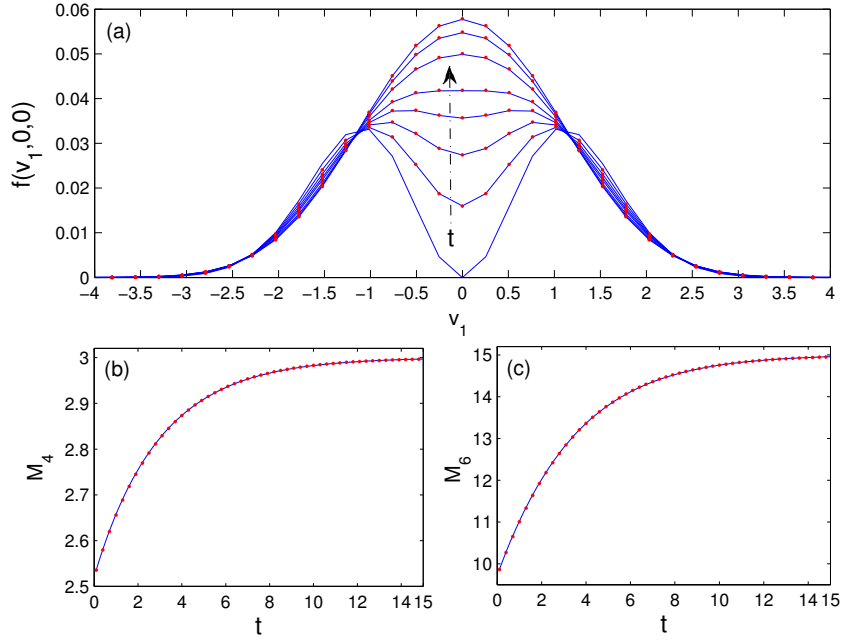


图 4-6 (a) Evolution of  $f(v_1, 0, 0)$  of space-homogeneous Maxwell molecules, from the initial condition (4-38). From bottom to top (near  $v_1 = 0$ ), the time corresponding to each line is 0, 0.5, 1, 1.5, 2, 3, 4, and 5. (b) and (c) Evolution of the fourth- and sixth-order moments, respectively. Solid lines: numerical result. Dots: analytical solution. Other parameters used in the numerical simulation are:  $L = 8, R = 6, N = 64$ , and  $M = 5$  with Eq. (4-30).

is calculated by

$$Q^{an}(\nu) = \frac{f(\Delta t, \nu) - f(0, \nu)}{\Delta t}, \quad (4-40)$$

with  $\Delta t=1.0E-5$  (which is far smaller than the characteristic relaxation time  $\text{Kn}'$ ). The following two factors affect the accuracy:

- $N$ , which decides the accuracy of the spectrum  $\hat{f}$  of VDF;
- $M$ , which determines how accurately we approximate Eq. (4-28).

The influence of  $M$  is analyzed as follows. For simplicity, let us ignore  $\xi_m$  and  $\varphi$  in Eq. (4-28). Notice that  $\phi_{\alpha+\gamma}$  is a decaying-oscillating function with the quasi-period  $2\pi/R$  (see Eq. (4-34) and Fig. 4-3). Then, for a fixed value of  $\xi_l$ , the integral kernel in Eq. (4-28) oscillates  $R|\xi_l|/\pi$  times as  $\theta$  varies from 0 to  $\pi$ . In the worst case ( $\xi_l \rightarrow N\pi/2L$ ), it oscillates  $O(N)$  times. This implies that  $M$  should be  $O(N)$ . In practical calculations, however,  $M$  can be far less than  $N$  because, if the VDF has a support  $S$ , its spectrum has a support  $1/S \sim 1/R$ . Within this support, the integral kernel in Eq. (4-28) oscillates only a few times, and hence a small value of  $M$  can lead to accurate result.

We vary the values of  $N$  and  $M$  to see their influence on the numerical accuracy; the results are tabulated in Table 4-1. When  $N = 16$ , the relative error is large because the resolution of VDF is not high enough so that a large error exists in the spectrum  $\hat{f}$ . As

$N$  increases to 24, the error is reduced by one order of magnitude. When the trapezoidal rule is used, the error mainly comes from the approximation of Eq. (4-28), which decays at  $O(M^{-2})$  when  $N$  is fixed. When  $M$  is fixed, the numerical accuracy does not improve when  $N \geq 32$ . If we increase the value of  $M$  by a factor of 2 when the value of  $N$  is increased by the same factor, we find that the spectral accuracy of FSM is roughly maintained. When Eq. (4-28) is approximated by the Gauss-Legendre quadrature, the spectral accuracy is clearly seen for  $N \leq 32$  and  $M \geq 6$ . When  $N > 32$ , if  $M$  is increased linearly with  $N$ , spectral accuracy is maintained. For example, if we choose the minimum error between  $6 \leq M \leq 12$  for each  $N$ , the order of accuracy is 8.1 when  $N$  increases from 16 to 24; 13.5 when  $N$  increases from 24 to 32; and 8.9 when  $N$  increases from 32 to 48. Thus, in general, the approximation of Eq. (4-28) by the Gauss-Legendre quadrature is better than that by the trapezoidal rule.

We now fix the values of  $N$  and  $M$  to check the influence of  $R$  on the accuracy, see Eq. (4-24). Fig. 4-5 indicates that  $R$  cannot be smaller than  $2\sqrt{2}L/(3 + \sqrt{2})$ , which is roughly  $\sqrt{2}$  times the support of VDF; otherwise, some collisions will be ignored in the truncated collision operator. Also,  $R$  cannot be larger than the size of velocity domain, otherwise the aliasing error may destroy accuracy.

Next, we demonstrate the accuracy of FSM in the homogeneous relaxation, where Eq. (4-37) is solved by the Euler forward method with a time step of 0.001. Figure 4-6 depicts the evolution of VDF, as well as the fourth- and sixth-order moments. Excellent agreement is found between the numerical and analytical solutions, even when Eq. (4-28) is approximated by the trapezoidal rule with  $M = 5$ .

#### 4.4.2 Discontinuous velocity distribution function

The initial VDF used in the preceding case is smooth, where the spectral accuracy of FSM can be proven analytically [80]. Now we consider the case where the initial VDF is not smooth, but has an abrupt jump at  $v_1 = 0$ :

$$f(\boldsymbol{v}, t = 0) = \frac{1}{3(2\pi)^{3/2}} \begin{cases} 4 \exp\left(-\frac{v^2}{2}\right), & v_1 \geq 0, \\ \exp\left(-\frac{v_1^2}{8} - \frac{v_2^2 + v_3^2}{2}\right), & v_1 < 0. \end{cases} \quad (4-41)$$

Although the analytical solution for the VDF cannot be obtained, it can be shown

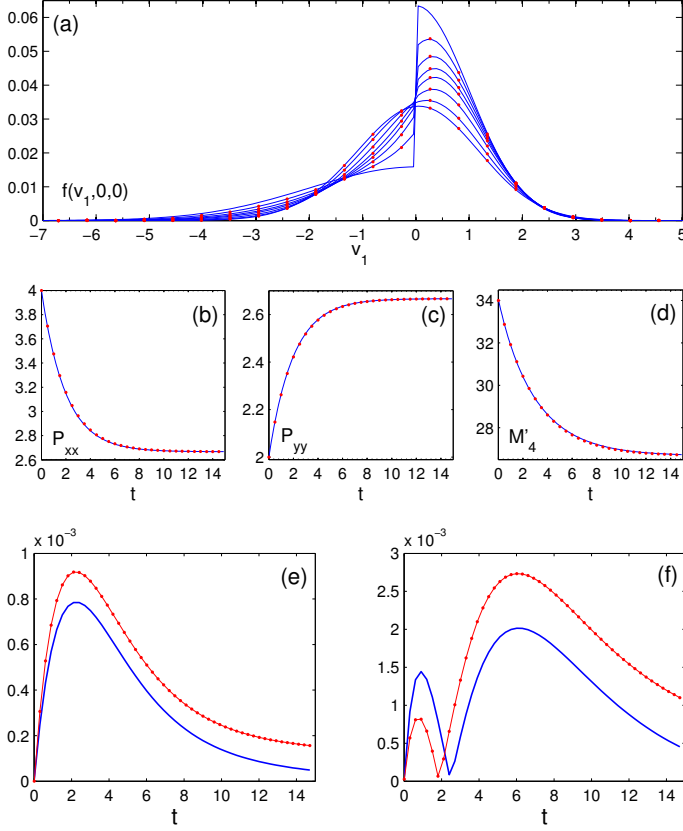


图 4-7 (a) Evolution of the VDF when the initial VDF at  $v_1 = +0$  is four times larger than at  $v_1 = -0$ . From top to bottom (at  $v_1 > 0$ ), the times corresponding to the lines are  $t = 0, 0.5, 1, 1.5, 2, 3, 5$ , and  $9$ , respectively. (b-d) Evolution of the second- and fourth-order moments. Relative error (e)  $|p_{xx}^{nu} - p_{xx}|/p_{xx}$  and (f)  $|M'_4^{nu} - M'_4|/M'_4$  when  $N = 42$ . Dots are the numerical results when  $N_1 = N_2 = N_3 = 42$ , solid lines in (a), (e), and (f) are the numerical results with  $N_1 = 256, N_2, N_3 = 42$ , while solid lines in (b-d) are analytical solutions. Other parameters are  $L_v = 11, R = 2\sqrt{2}L_v/(3 + \sqrt{2})$ , and  $M = 5$  with Eq. (4-30).

analytically that the evolution of the second- and fourth-order moments is given by

$$\begin{aligned} P_{xx} &= \frac{4}{3} \exp\left(-\frac{t}{2}\right) + \frac{8}{3}, \\ P_{yy} &= -\frac{2}{3} \exp\left(-\frac{t}{2}\right) + \frac{8}{3}, \\ M'_4 &= \int f v^4 d\mathbf{v} = \frac{22}{3} \exp\left(-\frac{t}{3}\right) + \frac{80}{3}. \end{aligned} \quad (4-42)$$

Figure 4-7 demonstrates that the FSM can accurately capture the evolution of second- and fourth-order moments, even when the initial VDF has a large jump at  $v_1 = 0$ . Also, no Gibbs oscillation has been observed in the central region of VDF where the abrupt jump exists; only in the tails do we find small Gibbs oscillations. This is because the convolution in the Boltzmann collision operator can smear out discontinuities.

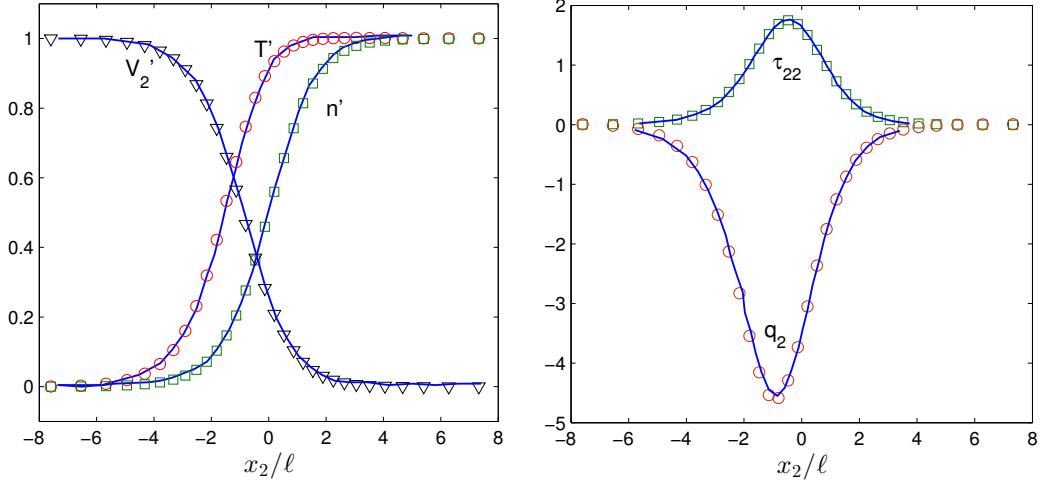


图 4-8 The structure of normal shock wave when  $\text{Ma} = 3$ , where the reduced macroscopic quantity  $\mathcal{M} = \rho, u, T$  is normalized as  $(\mathcal{M} - \mathcal{M}_u)/(\mathcal{M}_d - \mathcal{M}_u)$ , with the subscripts  $u$  and  $d$  represent upstream and downstream, respectively. Solid lines are the results from Ref. [85], while symbols are our FSM results.

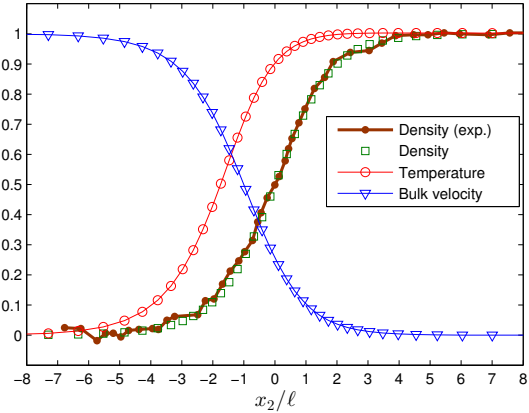


图 4-9 Reduced number density, temperature, and bulk velocity for the normal shock wave of  $\text{Ma} = 2.80$  in the argon gas, with the upstream temperature of  $298 \pm 3$  K. The experimental density is obtained from Ref. [52]. Numerical parameters are the same as those in Fig. 4-8.

## 4.5 Accuracy in inhomogeneous problems

The Boltzmann equation is solved by the CIS (??), where the spatial derivative  $\partial f / \partial x$  is approximated by the second-order upwind scheme.

### 4.5.1 Normal shock waves

The normal shock wave problem is ideal for testing the accuracy of FSM in capturing strong rarefaction effects, since this is a one-dimensional problem where the boundary effects are absent. The structure of the planar shock wave varies in the  $x_2$  direction. The flow is uniform at the upstream ( $x_2 = -\infty$ ) and downstream ( $x_2 = \infty$ ) ends. The upstream molecule number density, temperature, and Mach number are denoted by  $n_0$ ,

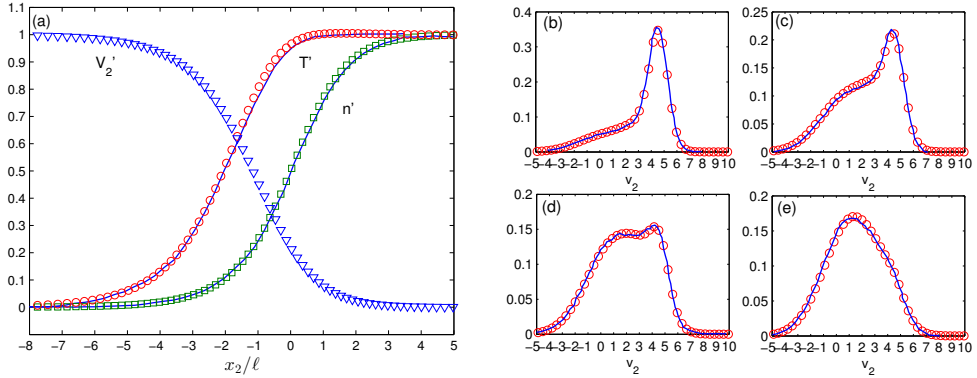


图 4-10 (a) Reduced molecular number density, temperature, and bulk velocity for the normal shock with  $\text{Ma} = 5$  in argon gas (Lennard-Jones potential). The marginal VDF  $\int \int f dv_1 dv_3 / n$  vs  $v_2$  is presented when the reduced density is (b) 0.151, (c) 0.350, (d) 0.511, and (e) 0.759. Solid lines are the results from Ref. [130], while symbols are our results from the FSM. The velocity domain  $[-18, 18]^3$  is divided into  $42 \times 84 \times 42$  grid points.

$T_0$ , and  $\text{Ma}$ , respectively, while those of the downstream end is determined through the Rankine-Hugoniot relations:

$$n_d = \frac{4\text{Ma}^2}{\text{Ma}^2 + 3}, \quad u_d = \sqrt{\frac{5}{96} \frac{\text{Ma}^2 + 3}{\text{Ma}}}, \quad T_d = \frac{(5\text{Ma}^2 - 1)(\text{Ma}^2 + 3)}{16\text{Ma}^2},$$

hence the normalized VDF at the upstream end is

$$f = \frac{1}{\pi^{3/2}} \exp \left[ -v_1^2 - \left( v_2 - \sqrt{\frac{5}{6}\text{Ma}} \right)^2 - v_3^2 \right], \quad (4-43)$$

and that at the downstream end is

$$f = \frac{n_d}{(\pi T_d)^{3/2}} \exp \left[ -\frac{v_1^2 + (v_2 - u_d)^2 + v_3^2}{T_d} \right]. \quad (4-44)$$

#### 4.5.1.1 Hard-sphere potential

We first consider the shock wave in a gas of HS molecules. Ohwada solved the Boltzmann equation by means of the numerical kernel method [85]. For comparison, we set  $L$  to be the mean free path in the upstream part

$$\lambda_0 = \frac{16}{5\pi} \sqrt{\frac{\pi}{2mk_B T_0}} \frac{\mu}{n_0}, \quad (4-45)$$

and  $\text{Kn} = 5\pi/16$ . Figure 4-8 shows the shock wave structure for a Mach number of 3. In FSM the velocity domain  $[-10, 10]^3$  is uniformly divided into  $42 \times 42 \times 42$  grid points, and  $M = 5$ . It can be seen that the two deterministic numerical methods for the Boltzmann equation give identical results.

#### 4.5.1.2 Lennard-Jones potential

We then consider argon with the Lennard-Jones potential. To compare with experimental data [52], we set the upstream temperature to be  $T_0 = 298$  K,  $L$  to be the mean free path in the upstream part, and hence  $\text{Kn} = 5\pi/16$  in Eq. (4-15). Good agreement between the numerical and experimental density profiles is seen in Fig. 4-9. The agreement is due to the fact that we have correctly incorporated the shear viscosity of argon into the collision kernel, shown in Eq. (4-8).

Finally, we solve the Boltzmann equation for argon with the Lennard-Jones potential (??) and compare our results with molecular dynamics simulation [130]. For comparison, we set the upstream temperature to be  $T_0 = 300$  K,  $L$  to be the mean free path in the upstream part and  $\text{Kn} = 5\pi/16$ . Fig. 4-10 shows the shock wave structure for Mach number of 5, as well as the marginal VDFs. The FSM produces nearly the same results as the molecular dynamics simulation, not only in macroscopic quantities, but also in mesoscopic VDFs. Note that in this case the downstream temperature is about 2600 K. The excellent agreement with molecular dynamics data illustrates that the collision kernel (4-15) for the Lennard-Jones potential works well in this temperature range.

#### 4.5.2 Force-driven Poiseuille flows

Consider a rarefied monatomic gas between two parallel infinite plates located at  $x_2 = L/2$  and  $x_2 = -L/2$ . The walls are stationary, and the temperature is kept at  $T_0$ . The gas is subject to a uniform external acceleration  $a_1$  in the  $x_1$  direction; the acceleration term  $\mathbf{a} \cdot \partial f / \partial \mathbf{v}$  is calculated according to the Fourier transform derivative theorem. Diffuse boundary condition is employed to account for the wall effects.

We solve the discretized Boltzmann equation by the CIS. At the  $(k + 1)$ -th iteration step, the VDF at the wall (entering the cavity) is determined according to the diffuse boundary condition, using the VDF at the same position at the previous iteration step:

$$\begin{aligned} f^{(k+1)} &= \frac{n}{\pi^{3/2}} \exp[-(\nu_1 + u_w)^2 - \nu_2^2 - \nu_3^2], \quad \text{for } \nu_2 \leq 0, \\ n &= 2\sqrt{\pi} \int_{\nu_2 < 0} \nu_2 f^{(k)}(x_2 = -0.5, \nu) d\nu, \end{aligned} \quad (4-46)$$

This numerical scheme is efficient when the Knudsen number is not small. However, the total mass is not conserved since the mass flux entering the computational domain at the  $(k + 1)$ -th step (which is equal to that leaving the computational domain at the  $k$ -th step) is not equal to that leaving the computational domain at the  $(k + 1)$ -th step. To

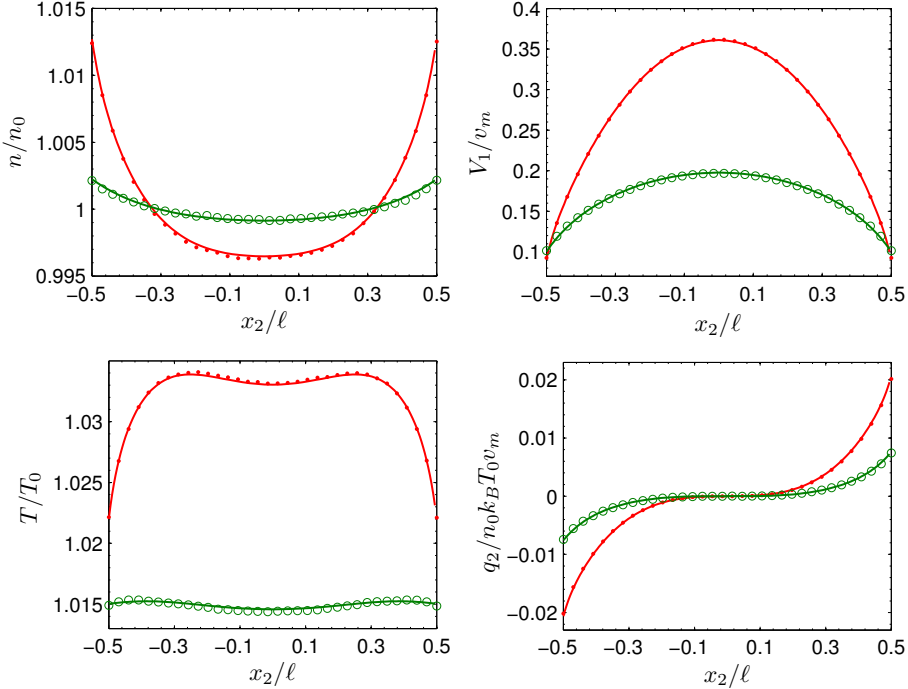


图 4-11 The density, velocity, temperature, and heat flux in the force-driven Poiseuille flow of HS molecules when  $\text{Kn} = 0.1$  (dots) and  $\text{Kn} = 0.5$  (open circles). Solid lines are FSM results, while symbols are DSMC results [77].

overcome this, at the end of each iteration, the VDF is re-scaled so that the total mass is conserved [78]. Physically, when the average molecular number density  $n_0$  and the intermolecular potential are known, the stationary state will be uniquely determined.

Consider HS molecules when  $\text{Kn} = 0.1$  and  $0.5$ . The normalized acceleration is  $0.11$  and the wall temperature is  $T_0 = 273$  K. The spatial region (halved due to the symmetry) is divided into 50 unequally spaced cells with more cells near the boundary. The maximum velocity is at  $L_v = 6$ , and there are 32 velocity mesh points in each direction. The numerical results are depicted in Fig. 4-11, where good agreements can be found. Note that in this case, the temperature profile has double peaks, which is in sharp contrast with the parabolic profiles predicted by the NSF equations [150].

#### 4.5.3 Thermal transpiration

Consider the thermal transpiration in a 2D closed rectangular channel with a length-to-width ratio of 5. The temperature at the right side is set to be twice that of the left side, while the temperature of the top and bottom walls varies linearly along the channel. Using the mean density, the temperature of the left wall, and the channel width, the Knudsen number is set to be  $\text{Kn} = 0.08, 0.2, 0.25, 0.6, 2$ , and  $10$ .

Figure 4-12 presents the streamlines and temperature distributions inside the channel

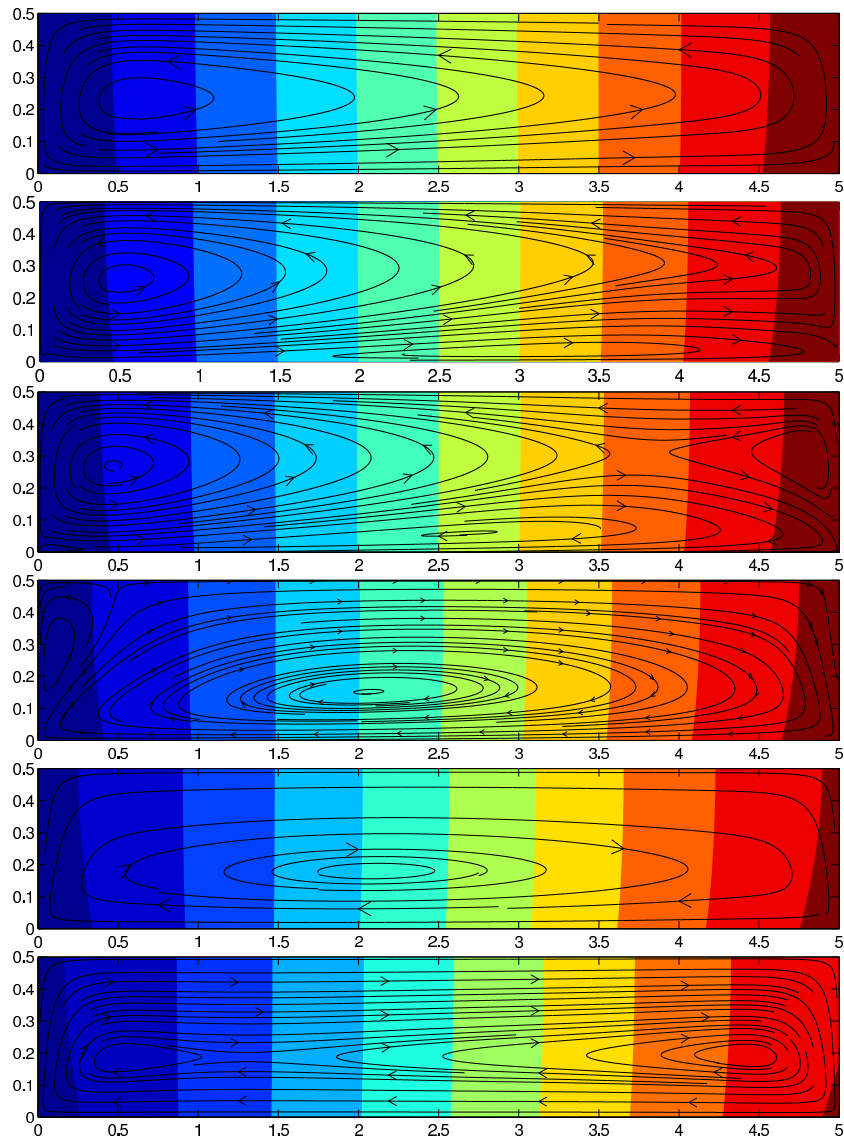


图 4-12 Temperature contours and velocity streamlines in the thermal transpiration of argon gas within a closed rectangular channel (only the down half domain is shown). In each figure, from left to right, the dimensionless temperature of each contour is  $1 + 0.1i$ , where  $i = 1, 2, \dots, 9$ . From the top to bottom,  $\text{Kn} = 0.08, 0.2, 0.25, 0.6, 2$ , and  $10$ , respectively.

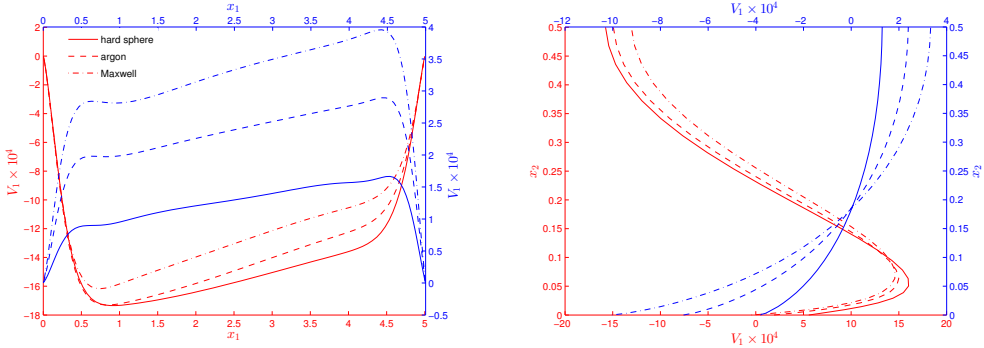


图 4-13 Velocity profiles for thermal transpiration within a closed rectangular channel: (a) along the central horizontal line and (b) along the central vertical line.  $\text{Kn} = 0.08$  and 10 are represented by the red and blue lines, respectively.

for the flow of argon gas. Due to symmetry, only half of the spatial domain is shown. At  $\text{Kn} = 0.08$ , the gas flows from the cold region to the hot region along the bottom wall, and returns in the central region. At  $\text{Kn} = 0.2$ , the flow still moves from hot to cold in the central region, however, near the lower wall the flow moves towards the hot region when  $x_1 < 2$  and towards the cold region for at  $x_1 > 2$ , i.e., a circulation emerges near the lower corner of the domain. At  $\text{Kn} = 0.25$ , the circulation near the lower wall grows, which divides the flow in the central region into two circulation zones. The lower circulation zone keeps expanding, and pushes the other two circulations in the central region towards the left and right boundaries, as  $\text{Kn}$  increases. At  $\text{Kn} = 0.6$ , the flow direction is reversed (as compared to that when  $\text{Kn} = 0.08$ ) and only one circulation zone remains near the left wall. The reversal of flow direction persists but the circulations near the left wall gradually disappear as the Knudsen number increases further, for instance, to  $\text{Kn} = 2$ . By  $\text{Kn} = 10$ , the gas near the bottom wall moves from hot to cold, and two clockwise circulations emerge near the left and right sides. Finally, when the flow enters the free molecular regime, the streamline pattern does not change, but the velocity magnitudes are proportional to  $1/\text{Kn}$ . The magnitudes of density, pressure, and temperature, however, remain unchanged irrespective of the Knudsen number [144].

Comparison of the velocity profiles for different molecular models at the start and the end of the transition flow regime are shown in Fig. 4-13; it can be seen that the molecular model (reflected in terms of the viscosity index) affects the velocity magnitudes significantly.

## 4.6 Linearization

The linearized BCO (??) cannot be solved by FSM, because in general the perturbation function  $\phi(-L_\nu) \neq \phi(L_\nu)$ . However, the product of the equilibrium distribution function and  $\phi$  vanishes at large molecular speed. Therefore, the Boltzmann equation is linearized by expressing the VDF as (the normalization in Section 4.2 is used):

$$f(t, \mathbf{x}, \mathbf{v}) = f_{eq}(\mathbf{v}) + \beta h(t, \mathbf{x}, \mathbf{v}) \quad (4-47)$$

with the equilibrium distribution function

$$f_{eq}(\mathbf{v}) = \pi^{-3/2} \exp(-\nu^2), \quad (4-48)$$

where  $\beta$  is a small constant related to the dimensionless strength of perturbation (e.g., in the linear Couette flow  $\beta$  is the wall velocity divided by the most probable speed), and  $\beta h$  is the VDF for small perturbation satisfying  $|\beta h/f_{eq}| \ll 1$ . The Boltzmann equation (2-8) is linearized to

$$\frac{\partial h}{\partial t} + \mathbf{v} \cdot \frac{\partial h}{\partial \mathbf{x}} - 2\mathbf{a} \cdot \mathbf{v} f_{eq} = \mathcal{L}(h) \equiv \mathcal{L}^+ - v_{eq}(\mathbf{v})h, \quad (4-49)$$

where

$$\mathcal{L}^+(h) = \iint B(\theta, \nu_r) [f_{eq}(\mathbf{v}')h(\mathbf{v}'_*) + f_{eq}(\mathbf{v}'_*)h(\mathbf{v}') - f_{eq}(\mathbf{v})h(\mathbf{v}_*)] d\Omega d\nu_* \quad (4-50)$$

can be viewed as a gain term of the linearized BCO, while  $v_{eq}(\mathbf{v})h$  is the loss term, with the equilibrium collision frequency being

$$v_{eq}(\mathbf{v}) = \iint B(\theta, \nu_r) f_{eq}(\mathbf{v}_*) d\Omega d\nu_*. \quad (4-51)$$

The macroscopic quantities deviated from their corresponding values in equilibrium state, such as the number density  $\varrho$ , bulk velocity  $\mathbf{u}$ , temperature  $T$ , stress tensor  $\sigma_{ij}$  and heat flux  $\mathbf{q}$  can be calculated as

$$[\varrho, \mathbf{u}, T, \sigma_{ij}, \mathbf{q}] = \int \left[ 1, \mathbf{v}, \frac{2}{3} \left( \nu^2 - \frac{3}{2} \right), 2\nu_{(i}\nu_{j)}, \mathbf{v} \left( \nu^2 - \frac{5}{2} \right) \right] h d\mathbf{v}, \quad (4-52)$$

which, on top of the normalization (4-9), are further normalized by the dimensionless constant  $\beta$ .

The equilibrium collision frequency can be calculated analytically, or approximated by the algorithm in Appendix ??, if  $\hat{f}$  is replaced by the spectrum of equilibrium distribution function  $\hat{f}_{eq}$ . This term only needs to be calculated once, since each spatial cell uses the same equilibrium collision frequency. Typical profiles are shown in Fig. ??.

The gain term is calculated similarly by the method introduced in the previous chap-

ter. Let

$$\phi_{loss} = \sum_{p,q=1}^M \omega_p \omega_q \sin \theta_p \phi_{\alpha+\gamma}(\xi_m, \theta_p, \varphi_q) \psi_\gamma(\xi_m, \theta_p, \varphi_q), \quad (4-53)$$

and  $\hat{h}$  the spectrum of  $h$ . If Eq. (4-28) is approximated by Gauss-Legendre quadrature, its  $j$ -th Fourier mode of the gain term  $\mathcal{L}^+$  is

$$\begin{aligned} \hat{\mathcal{L}}_j^+ &\approx \frac{4}{Kn'} \sum_{p,q=1}^M \sum_{l+m=j} \omega_p \omega_q \sin \theta_p [\hat{f}_{eq}(l) \phi_{\alpha+\gamma}(\xi_l, \theta_p, \varphi_q)] \cdot [\hat{h}_m \psi_\gamma(\xi_m, \theta_p, \varphi_q)] \\ &+ \frac{4}{Kn'} \sum_{p,q=1}^M \sum_{l+m=j} \omega_p \omega_q \sin \theta_p [\hat{h}_l \phi_{\alpha+\gamma}(\xi_l, \theta_p, \varphi_q)] \cdot [\hat{f}_{eq}(m) \psi_\gamma(\xi_m, \theta_p, \varphi_q)] \\ &- \frac{4}{Kn'} \sum_{l+m=j} \hat{f}_{eq}(l) \cdot [\hat{h}_m \phi_{loss}]. \end{aligned} \quad (4-54)$$

The gain term  $\mathcal{L}^+$  can be calculated by the second algorithm in Appendix ???. Since the Fourier transform of  $\hat{f}_{eq}(l) \phi_{\alpha+\gamma}(\xi_l, \theta_p, \varphi_q)$  and  $\hat{f}_{eq}(m) \psi_\gamma(\xi_m, \theta_p, \varphi_q)$  can be pre-computed and stored, the computational time of the linearized BCO is nearly the same as that of the full BCO. Therefore, it seems that there is no need to consider the Boltzmann equation in linearized form. However, the following three factors indicate that the linearization is necessary and beneficial:

- In LBE the small signal is magnified thus can be better resolved, while in the full Boltzmann equation this signal might be contaminated by numerical error.
- In oscillatory flows the time derivative can be removed if one is interested in the “steady-state” solution, where the flow oscillation has been fully established (see Chapter ??); the use of FSM for LBE facilitates the fast convergence to final solution, without running time-explicit numerical solvers.
- For inverse power-law potentials, if we choose  $\gamma = (1 - \alpha)/2$  in the collision kernel (4-7), the linearized gain term  $\mathcal{L}^+(h)$  becomes

$$\begin{aligned} &\frac{4}{Kn'} \iint d\mathbf{y} d\mathbf{z} \delta(\mathbf{y} \cdot \mathbf{z}) (|\mathbf{y}| |\mathbf{z}|)^{-\gamma} \\ &\times [f_{eq}(\mathbf{v} + \mathbf{z}) h(\mathbf{v} + \mathbf{y}) + h(\mathbf{v} + \mathbf{z}) f_{eq}(\mathbf{v} + \mathbf{y}) - h(\mathbf{v} + \mathbf{y} + \mathbf{z}) f_{eq}(\mathbf{v})] \end{aligned} \quad (4-55)$$

after the Carleman representation. Since the interchange of  $\mathbf{y}$  and  $\mathbf{z}$  does not change the

linearized gain term, Eq. (4-54) can be simplified to

$$\begin{aligned}\widehat{\mathcal{L}}_j^+ \approx & \frac{8}{\text{Kn}'} \sum_{p,q=1}^M \sum_{l+m=j} \omega_p \omega_q [\hat{f}_{eq}(\mathbf{l}) \phi_{\alpha+\gamma}(\xi_l, \theta_p, \varphi_q)] [\hat{h}_m \psi_\gamma(\xi_m, \theta_p, \varphi_q)] \sin \theta_p \\ & - \frac{4}{\text{Kn}'} \sum_{l+m=j} \hat{f}_{eq}(\mathbf{l}) [\hat{h}_m \phi_{loss}].\end{aligned}\quad (4-56)$$

Therefore, the computational cost will be reduced by half when compared to that of the full Boltzmann equation.

#### 4.6.1 Lennard-Jones potential

When the Lennard-Jones potential is considered, after the normalization in Section 4.2, the collision kernel  $B(\theta, v_r)$  in Eqs. (4-50) and (4-51) becomes [143]:

$$B(\theta, v_r) = (n_0 d_{LJ}^2 L) \sigma_D v_r, \quad (4-57)$$

where the differential cross-section, after the Carleman representation, is

$$\sigma_D = \sigma_D \left( 2 \arctan \frac{|y|}{|z|}, v_m \sqrt{y^2 + z^2} \right) \equiv \sigma'_D(|y|, |z|). \quad (4-58)$$

In general,  $y$  and  $z$  in  $\sigma'_D(|y|, |z|)$  cannot be separated as  $\sigma_1(|y|)\sigma_2(|z|)$ , and the kernel mode  $\beta(\mathbf{l}, \mathbf{m})$  can only be simplified to

$$\begin{aligned}\beta(\mathbf{l}, \mathbf{m}) = & (n_0 d_{LJ}^2 L) \iint d\mathbf{e}' d\mathbf{e} \delta(\mathbf{e} \cdot \mathbf{e}') \\ & \times \int_{-R}^R \int_{-R}^R |\rho \rho'| \sigma'_D(|\rho|, |\rho'|) \exp(i\rho \xi_l \cdot \mathbf{e} + i\rho' \xi_m \cdot \mathbf{e}') d\rho d\rho'.\end{aligned}\quad (4-59)$$

To enable the FFT-based convolution, the integration with respect to  $\rho$  is approximated by a numerical quadrature [47, 143], and the integration with respect to  $\rho'$  is calculated accurately, or vice versa. Suppose  $\rho_r$  and  $\omega_r$  with  $r = 1, 2, \dots, M_r$  are the abscissas and weights of a quadrature in the region  $[0, R]$ , Eq. (4-59) becomes

$$\beta(\mathbf{l}, \mathbf{m}) = (n_0 d_{LJ}^2 L) \sum_r \omega_r \iint \delta(\mathbf{e} \cdot \mathbf{e}') \phi(\rho_r, \xi_l \cdot \mathbf{e}) \psi(\rho_r, \xi_m \cdot \mathbf{e}') d\mathbf{e}' d\mathbf{e}, \quad (4-60)$$

where  $\psi(\rho_r, s) = 2 \int_0^R \rho' \sigma'_D(\rho_r, \rho') \cos(\rho' s) d\rho'$  and  $\phi(\rho_r, s) = 2\rho_r \cos(\rho_r s)$ . Then, following the straightforward algebraic calculation in Section 4.3.2, we have

$$\beta(\mathbf{l}, \mathbf{m}) = 4(n_0 d_{LJ}^2 L) \sum_{p,q,r=1}^{M_r, M_r} \omega_p \omega_q \omega_r \phi(\rho_r, \xi_l \cdot \mathbf{e}_{\theta_p, \varphi_q}) \psi'(\rho_r, \xi_l^\perp) \sin \theta_p, \quad (4-61)$$

where

$$\psi'(\rho_r, s) = 2\pi \int_0^R \rho' \sigma'_D(\rho_r, \rho') J_0(\rho' s) d\rho'. \quad (4-62)$$

Thus, the BCO for the Lennard-Jones potential can be calculated through the FFT-based convolution, with a computational cost of  $O(M^2 M_r N^3 \log N)$ . Normally  $M_r \sim N$ , so the computational cost for the Lennard-Jones potential is high than the modeled collision kernel (4-7) by about one order of magnitude. Detailed numerical method to calculate the differential cross-section and the corresponding kernel mode is given in Ref. [143].

#### 4.6.2 Accurate transport coefficients

Note that the shear viscosity (3-26) is derived based on the eigenvalues and eigenfunctions of the LBE for Maxwell molecules. For general intermolecular potentials, however, Eq. (3-26) is not accurate, and its high-order correction is cumbersome. Here we show how to obtain accurate transport coefficients of the Boltzmann equation via FSM.

According to the Chapman-Enskog expansion, the exact shear viscosity  $\mu$  and thermal conductivity  $\kappa$  of the Boltzmann equation are calculated by

$$\begin{aligned} \mu &= \frac{mv_m}{d_{LJ}^2} \int h_\mu(v) v_1 v_2 dv \equiv \frac{mv_m}{d_{LJ}^2} \mu', \\ \kappa &= \frac{k_B v_m}{d_{LJ}^2} \int h_\kappa(v) v_1 \left( v^2 - \frac{5}{2} \right) dv \equiv \frac{k_B v_m}{d_{LJ}^2} \kappa', \end{aligned} \quad (4-63)$$

where  $\mu'$  and  $\kappa'$  are the reduced viscosity and thermal conductivity, respectively. The two functions  $h_\mu(v)$  and  $h_\kappa(v)$  satisfy the following integral equations if we choose  $n_0 d_{LJ}^2 L = 1$  in the collision kernel:

$$\begin{aligned} \mathcal{L}(h_\mu) &= -2f_{eq}v_1v_2, \\ \mathcal{L}(h_\kappa) &= -f_{eq}v_1 \left( v^2 - \frac{5}{2} \right), \quad \text{and} \int h_\kappa v_1 dv = 0. \end{aligned} \quad (4-64)$$

To find  $h_\mu$ , we use the following iterative scheme:

$$h_\mu^{(k+1)} = \frac{\mathcal{L}^+(h_\mu^{(k)}) + 2f_{eq}v_1v_2}{v_{eq}}, \quad (4-65)$$

while to find  $h_\kappa$ , we use

$$\begin{aligned} \tilde{h}_\kappa^{(k+1)} &= \frac{\mathcal{L}^+(h_\kappa^{(k)}) + f_{eq}v_1 \left( v^2 - \frac{5}{2} \right)}{v_{eq}}, \\ h_\kappa^{(k+1)} &= \tilde{h}_\kappa^{(k+1)} - 2f_{eq}v_1 \int \tilde{h}_\kappa^{(k+1)} v_1 dv. \end{aligned} \quad (4-66)$$

表 4-2 Comparisons of reduced transport coefficients obtained from the FSM at temperature 300 K [143] with those from the variational method with first- and third-order Chapman-Cowling approximation [25].

Gas	$\mu'^{[1]}$	$\mu'^{[3]}$	FSM $\mu'$	$\kappa'^{[1]}$	$\kappa'^{[3]}$	FSM $\kappa'$
He	0.1773	0.1787	0.1789	0.6650	0.6732	0.6742
Ne	0.1477	0.1488	0.1486	0.5539	0.5602	0.5596
Ar	0.1129	0.1131	0.1132	0.4234	0.4248	0.4251
Kr	0.0969	0.0969	0.0967	0.3632	0.3635	0.3629
Xe	0.0892	0.0893	0.0894	0.3348	0.3349	0.3354

The Lennard-Jones potential for five noble gases, He, Ne, Ar, Kr, and Xe, are considered at  $T_0 = 300$  K, with the potential depths  $k_B T_0 / \epsilon = 29.35, 8.403, 2.419, 1.579$ , and 1.310. Numerical results in Table 4-2 confirms the accuracy of FSM in the approximation of BCO when the collision kernel is directly calculated from the Lennard-Jones potential.

#### 4.6.3 Poiseuille flow

The LBE is solved with the Lennard-Jones potential. It is noted that the spatial and temporal Knudsen numbers, as well as the rarefaction parameter, are defined in terms of the shear viscosity. To obtain accurate numerical results from the Boltzmann equation, accurate transport coefficients should be used. In this case, in the simulation of Lennard-Jones potential, the term  $n_0 d_{LJ}^2 L$  in the collision kernel (4-57) should be modified as

$$n_0 d_{LJ}^2 L \rightarrow 2\mu' \delta_{rp}, \quad (4-67)$$

while in the power-law potential with the modeled collision kernel (4-7), after obtaining the reduced shear viscosity  $\mu'$ , the term  $1/\text{Kn}'$  in Eqs. (4-11) and (4-12) should be modified as

$$\frac{1}{\text{Kn}'} \rightarrow \frac{2\mu' \delta_{rp}}{\text{Kn}'}. \quad (4-68)$$

Such a modification, although only introduces a relative difference less than 2.5%, becomes important when calculating the Knudsen layer function.

## 4.7 Concluding remarks

We briefly analyze why the FSM is suitable for the simulation of rarefied microflows. When the Knudsen number is large, the VDFs have large discontinuities, hence a significant number of velocity grids are needed. This poses an extremely difficult problem for other deterministic methods that handle binary collisions in velocity space. However, it is circumvented in FSM because collisions are treated in frequency space. Since the FSM approximates the collision operator with spectral accuracy [80], the number of frequency components does not need to be as large as the velocity grids. One reason for this is that discontinuities in VDF produce high frequency components in its spectrum (and this is usually smooth, or at least smoother than the VDF); in calculating the spectrum of the collision operator, the spectrum of VDF is multiplied by a weight function which is very small for high frequency components, see Fig. 4-3. Therefore, very high frequencies can be safely ignored: in the transition flow regime, we have shown that 32 frequency components in each direction is adequate.

## 第 5 章 单原子气体的简化动理论模型

### 5.1 模型方程

玻尔兹曼方程碰撞项的复杂性给数值求解带来极大挑战 [? ]，因此，学者建议使用简化的碰撞模型来代替。在简化玻尔兹曼方程的碰撞项时，一般认为需要满足以下几点：

- (1) 动理学模型必须保证质量、动量、能量守恒；
- (2) 理想气体的局部平衡态速度分布函数为麦克斯韦分布；
- (3) 从模型方程导出的粘性系数与热导率应与玻尔兹曼方程导出的结果保持一致；
- (4) 满足熵增定理，当且仅当孤立系统处于平衡态时熵增为零，并达到其最大值。

其中，前两项是基本要求，第三项要求在连续流区域通过 Chapman-Enskog 展开恢复出纳维-斯托克斯方程，而第四项仅为从物理角度出发的考量，并不能保证模型方程的精度：如果一个动理学模型方程与玻尔兹曼方程完全一致，那么熵增速率也应该相同，然而这通常是不可能做到的。实际上，大多数时候，仅在线性化情况下满足熵增定理的 Shakhov 模型的精度优于完全满足熵增定理的 ES-BGK 模型。

由于玻尔兹曼碰撞项在形式上可记为  $Q = Q^+ - f/\tau$ ，因此，动理学模型方程的碰撞项一般采取如下形式

$$Q = \frac{f_r - f}{\tau}, \quad (5-1)$$

其中， $f_r$  为参考速度分布函数， $\tau$  为特征碰撞弛豫时间，表征速度分布函数趋向参考分布函数的快慢。为简单计，通常假设与分子速度无关。

#### 5.1.1 BGK 模型

BGK 模型是最著名的气体动理学简化模型，由 Bhatnagar, Gross 和 Krook 提出 [7]，其参考速度分布函数是局部麦克斯韦分布：

$$f_r^{BGK} = F_{eq}. \quad (5-2)$$

易见此模型满足三大守恒律，且给出了在平衡态下的正确解  $f = F_{eq}$ 。在空间均匀系统中，由于  $\ln F_{eq}$  是碰撞不变量的线性组合，有  $\int (F_{eq} - f) \ln F_{eq} d\mathbf{v} = 0$ ，所

以可以证明 BGK 模型满足熵增原理:

$$\begin{aligned}\frac{\partial H}{\partial t} &= - \int \frac{F_{eq} - f}{\tau} \ln f d\boldsymbol{v} \\ &= - \int \frac{F_{eq} - f}{\tau} (\ln F_{eq} - \ln f) d\boldsymbol{v} \geq 0.\end{aligned}\quad (5-3)$$

空间均匀系统中应力偏量和热流的弛豫时间均为  $\tau$ , 因此根据公式 (2-48) 随后段落的描述, 可知剪切粘性为  $\mu = p\tau$ , 而普朗特数为 1. 然而, 通过玻尔兹曼方程推导得到的普朗特数正确值为  $2/3$ . 这说明 BGK 模型不可能同时得到正确的剪切粘性和热导率. 对于粘性主导的流动, 一般选取  $\tau$  以恢复剪切粘性; 对于热传导主导的流动, 则以恢复热导率为目标来选取  $\tau$ .

### 5.1.2 ES-BGK 模型

Holway [?] 提出了 ES-BGK 模型以修正 BGK 模型中错误的普朗特数, 其中参考速度分布函数是在给定质量、动量、能量和应力张量信息下, 通过最大化熵函数 (2-18) 而来:

$$f_r^{ES} = \frac{n}{\sqrt{\det[2\pi\lambda_{ij}]}} \exp\left(-\frac{1}{2}\lambda_{ij}^{-1}c_i c_j\right), \quad (5-4)$$

其中

$$\lambda_{ij} = (1-b)\frac{k_B T}{m}\delta_{ij} + b\frac{p_{ij}}{nm} = \frac{p\delta_{ij} + b\sigma_{ij}}{nm}. \quad (5-5)$$

若  $b = 0$ , 二阶张量  $\lambda_{ij}$  中仅有主对角元素非零, 模型恢复为 BGK 模型.

容易证明, 应力偏量的弛豫时间为  $\tau/(1-b)$ , 而热流的弛豫时间为  $\tau$ . 因此, 剪切粘性和普朗特数分别为

$$\begin{aligned}\mu &= \frac{1}{1-b}p\tau, \\ \text{Pr} &= \frac{1}{1-b}.\end{aligned}\quad (5-6)$$

为确保弛豫时间为正, 则有  $b < 1$ . 另外,  $f_r^{ES}$  有界的充要条件是  $b \geq -1/2$ . 因此, ES-BGK 模型的普朗特数范围为  $[2/3, +\infty)$ . 为了恢复单原子气体的普朗特数  $2/3$ , 取

$$b = -\frac{1}{2}. \quad (5-7)$$

可以看出, 当碰撞项为零时, ES-BGK 方程给出  $f = f_r^{ES}$ , 当且仅当  $\sigma_{ij} = 0$  时, 速度分布函数退化为麦克斯韦平衡态分布. 而这并不违背动理论建模的第二个要求, 因为当局部平衡态为  $f = f_r^{ES}$  时, 应力偏量的演化满足如下形式  $\partial\sigma_{ij}/\partial t = -p\sigma_{ij}/\mu$ , 即应力偏量将随时间推进逐渐衰减至零. 因此, ES-BGK 模型中趋于平衡

态的过程可以解释为：当速度分布函数朝着椭球分布 (5-4) 松弛，椭球分布也朝着麦克斯韦分布演化，最终实现  $f = F_{eq}$ .

Andries 等人 [?] 证明了 ES-BGK 模型满足熵增定理，使之成为唯一满足熵增定理且能正确恢复各输运系数的动理论学模型，因此，ES-BGK 模型受到广泛关注.

### 5.1.3 Shakhov 模型

不同于 ES-BGK 模型在参考速度分布函数中引入应力修正项，Shakhov 模型通过在参考速度分布函数中引入热流修正项来恢复正确的输运系数：

$$f_r^S = F_{eq} \left[ 1 + (1 - \text{Pr}) \frac{2m\mathbf{q} \cdot \mathbf{c}}{5n(k_B T)^2} \left( \frac{mc^2}{2k_B T} - \frac{5}{2} \right) \right]. \quad (5-8)$$

此模型同样满足三大守恒律。从偏应力和热流的弛豫时间可以看出，该模型的粘性为  $\mu = p\tau$ ，且能实现正确的普朗特数。此外，由于热流弛豫过程满足  $\partial\mathbf{q}/\partial t = -(2p/3\mu)\mathbf{q}$ ，在速度分布函数向  $f_r^S$  靠近的过程中，参考速度分布函数也将逐渐演化为麦克斯韦分布，从而使 Shakhov 模型在平衡态时满足  $f = F_{eq}$ .

线性化的 Shakhov 模型满足熵增定理。而对于非线性流动，熵增定理未被证明但也无从证伪；另外，速度分布函数可能出现非物理的负值。尽管如此，Shakhov 模型仍能在许多问题中给出准确结果，得到了广泛应用。

### 5.1.4 Gross-Jackson 模型及其非线性化

针对麦克斯韦分子，根据线化玻尔兹曼碰撞项的本征值与本征函数，Gross 和 Jackson 提出的以下形式的动理论学模型去逼近线性化玻尔兹曼碰撞项  $J(\phi)$ ：

$$\begin{aligned} L_{GJ} = & \lambda_{st}\phi + \sum_{nl} (\lambda_{nl} - \lambda_{st}) \frac{2l+1}{4\pi} \\ & \times \int P_l(\cos\theta') g_{nl}(\xi) g_{nl}(\xi_1) \phi(\xi_1) d\xi_1, \end{aligned} \quad (5-9)$$

式中， $\lambda_{st}$  是一个任意负数， $\lambda_{nl}$  是线性化玻尔兹曼项的本征值 (2-26)， $\theta'$  为  $\mathbf{v}$  和  $\mathbf{v}'$  的夹角。该模型的物理意义在于保证模型方程和线性化玻尔兹曼方程各阶矩的弛豫率相同。

Gross 和 Jackson 将  $L(h)$  的  $N$  阶近似表示为

$$\begin{aligned} L_{GJ}^{(N)} = & \lambda_{0N}\phi - \lambda_{0N} \sum_{2n+l \leq N} \left( 1 - \frac{\lambda_{nl}}{\lambda_{0N}} \right) g_{nl}(\xi) \\ & \times \frac{2l+1}{4\pi} \int P_l(\cos\phi') g_{nl}(\xi_1) \phi(\xi_1) d\xi_1, \end{aligned} \quad (5-10)$$

即保留了所有阶数小于或等于  $N$  的多项式，并且取  $\lambda_{st} = \lambda_{0N}$ ，因此该截断模型的最大弛豫率为  $\lambda_{0N}$ .

在线性化情况下，即把速度分布函数在全局平衡态下根据公式(2-22)展开，BGK、ES-BGK 和 Shakhov 模型有如下形式：

$$\begin{aligned}\frac{\partial \phi}{\partial t} + \boldsymbol{\xi} \cdot \frac{\partial \phi}{\partial \mathbf{x}} &= \frac{\ell}{v_m} L, \\ L_{BGK} &= \frac{p}{\mu} \left[ n + 2\mathbf{u} \cdot \boldsymbol{\xi} + T \left( \boldsymbol{\xi}^2 - \frac{3}{2} \right) - \phi \right], \\ L_{ES} &= \frac{2}{3} L_{BGK} - \frac{2p}{3\mu} \frac{\sigma_{ij}}{2} \xi_{\langle i} \xi_{j \rangle}, \\ L_S &= L_{BGK} + \frac{p}{\mu} \frac{4(1 - \text{Pr})}{5} \mathbf{q} \cdot \boldsymbol{\xi} \left( \boldsymbol{\xi}^2 - \frac{5}{2} \right),\end{aligned}\quad (5-11)$$

其中扰动宏观物理量的定义请参考公式(2-28)。它们都可以看作是 Gross-Jackson 模型的特例。当  $N = 2$  时，从公式 (5-10) 可以得到  $L_{GJ}^{(2)} = L_{BGK}$ ；令  $N = 3$ ，根据公式(2-26)有

$$\lambda_{03} = \frac{3}{2} \lambda_{02} = \frac{3p}{2\mu}, \quad (5-12)$$

从而公式 (5-10) 给出

$$\begin{aligned}L_{GJ}^{(3)} &= \frac{3}{2} L_{BGK} + \frac{p}{\mu} \left[ \frac{\sigma_{ij}}{2} \xi_{\langle i} \xi_{j \rangle} + \frac{2}{3} \mathbf{q} \cdot \mathbf{v} \left( \boldsymbol{\xi}^2 - \frac{5}{2} \right) \right] f_{eq} \\ &= -\frac{3}{2} L_{ES} + \frac{5}{2} L_S.\end{aligned}$$

虽然，这既不符合线性化 ES-BGK 模型，也不符合线性化 Shakhov 模型，但是可将其视为这两个模型的线性组合。另一方面，若给定约束  $2n+l \leq 3$ ，当  $\lambda_{st} = -2p/3\mu$  时，式 (5-9) 恰好展开为线性化 ES-BGK 模型；而当  $\lambda_{st} = -p/\mu$  时，式 (5-9) 展开为线性化 Shakhov 模型。

因此，通过 Gross-Jackson 模型和线性化 BGK、ES-BGK、Shakhov 模型的关系，可以反推出各种形式的非线性动理论模型。例如，陈松泽等人将 ES-BGK 模型与 Shakhov 模型线性组合为一个复合模型，通过改变两模型所占的比例和普朗特数，复合模型能够分别恢复到 BGK、ES-BGK 和 Shakhov 模型式 [? ]。类似地，吴雷在博士论文也提出一个带有自由参数  $b$  复合模型 [139]：

$$\begin{aligned}f_r &= F_{eq} \left[ 1 + \frac{\sigma_{ij}}{p} \frac{c_{\langle i} c_{j \rangle}}{2k_B T/m} \right. \\ &\quad \left. + [1 - \text{Pr}(1 - b)] \frac{2m\mathbf{q} \cdot \mathbf{c}}{5n(k_B T)^2} \left( \frac{mc^2}{2k_B T} - \frac{5}{2} \right) \right]. \\ \tau &= (1 - b) \frac{\mu}{p}.\end{aligned}\quad (5-13)$$

该模型实际上是在 Gross-Jackson 模型(5-9)中取  $2n+l \leq N = 3$  和  $\lambda_{st} = 1/\tau$ ，并通过

过将如下的线性化碰撞项变为非线性碰撞项得来：

$$\begin{aligned} n + 2\mathbf{u} \cdot \boldsymbol{\xi} + T \left( \xi^2 - \frac{3}{2} \right) - \phi &\rightarrow F_{eq} - f, \\ \frac{\sigma_{ij}}{2} \xi_{\langle i} \xi_{j \rangle} &\rightarrow \frac{\sigma_{ij}}{p} \frac{c_{\langle i} c_{j \rangle}}{2k_B T} F_{eq} \\ \mathbf{q} \cdot \boldsymbol{\xi} \left( \xi^2 - \frac{5}{2} \right) &\rightarrow \frac{m \mathbf{q} \cdot \mathbf{c}}{2n(k_B T)^2} \left( \frac{mc^2}{2k_B T} - \frac{5}{2} \right) F_{eq}. \end{aligned} \quad (5-14)$$

需要注意，含有应力偏量的项既可以被吸收到指数函数里使参考分布函数变成类似公式(5-4)的形式，也可以放在外面（此时对  $b$  的限制仅为  $b < 1$ ），对数值计算的结果并无多少影响 [139]。通过将 Gross-Jackson 模型中的其它高阶本征函数非线性化为相应的形式，可以构造更加准确的动理学模型。

## 第6章 合成迭代加速算法

The conventional iterative scheme used in previous chapters works well in finding the steady-state solution of the Boltzmann equation when the Knudsen number is not small. However, it becomes inefficient and inaccurate when the Knudsen number is small. The general synthetic iterative scheme is proposed to fix these problems, with the properties of fast convergence, asymptotic preserving and universality.

### 6.1 Problems of CIS

We take the following linearized Shakhov model to analyze the mathematical properties of CIS in the search of steady-state solutions:

$$\boldsymbol{v} \cdot \nabla h^{k+1} = \mathcal{L}_s^{+,k} - \delta_{rp} h^{k+1} + \text{source term}, \quad (6-1)$$

where the gain part of the linearized collision operator is

$$\mathcal{L}_s^+ = \delta_{rp} \left[ \varrho + 2\boldsymbol{u} \cdot \boldsymbol{v} + T \left( v^2 - \frac{3}{2} \right) + \frac{4(1-\text{Pr})}{5} \boldsymbol{q} \cdot \boldsymbol{v} \left( v^2 - \frac{5}{2} \right) \right] f_{eq}, \quad (6-2)$$

and the source term is due to, e.g., the presence of pressure and temperature gradients.

Figure 6-1 shows the iteration numbers needed to get the steady-state solution in the Poiseuille flow between two parallel plates. When the Knudsen number Kn is large, stationary solution can be found in about 10 iterations, which means that CIS is very efficient. However, when Kn is small, about one million iterations are needed, and yet the solution is contaminated by large numerical dissipation when the spatial cell size is not small enough.

#### 6.1.1 Slow convergence

We adopt the Fourier stability analysis to rigorously investigate the efficiency of CIS. We define the error functions between VDFs at two consecutive iterations as

$$Y^{k+1}(\boldsymbol{x}, \boldsymbol{v}) = h^{k+1}(\boldsymbol{x}, \boldsymbol{v}) - h^k(\boldsymbol{x}, \boldsymbol{v}), \quad (6-3)$$

and the corresponding error functions for macroscopic quantities  $M = [\varrho, \boldsymbol{u}, T, \boldsymbol{q}]$  as

$$\Phi^{k+1}(\boldsymbol{x}) = M^{k+1}(\boldsymbol{x}) - M^k(\boldsymbol{x}) = \int Y^{k+1}(\boldsymbol{x}, \boldsymbol{v}) \phi(\boldsymbol{v}) d\boldsymbol{v}, \quad (6-4)$$

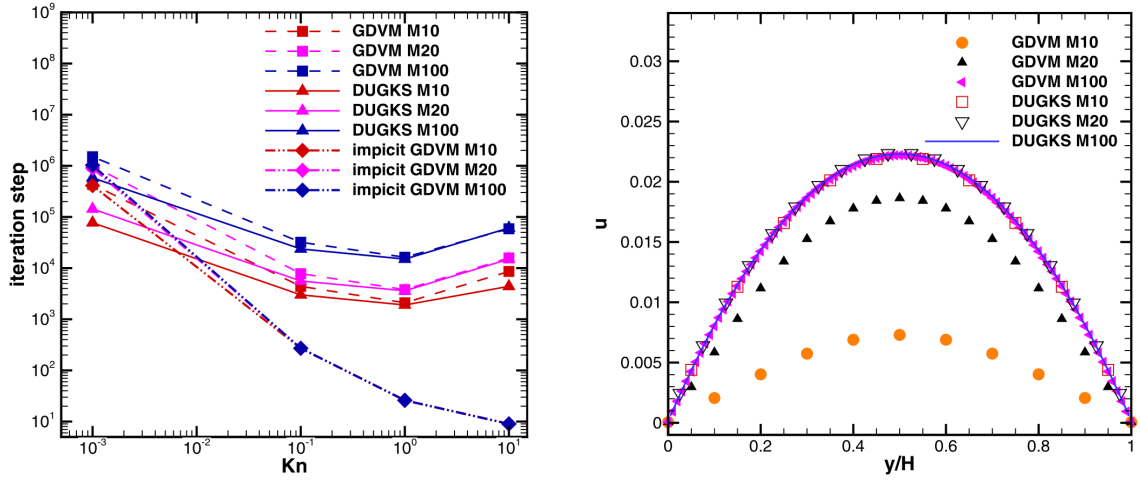


图 6-1 (Left) The iteration number needed to find the steady-state solution of force-driven Poiseuille flow, for both the CIS and discrete UGKS [40]. (Right) Velocity profiles obtained at different numbers of spatial cells (M) when  $\text{Kn} = 0.001$ , which demonstrates that the CIS is highly dissipative when the spatial resolution is not adequate [135].

where

$$\phi(\boldsymbol{v}) = \left[ 1, v_1, v_2, v_3, \frac{2}{3}v^2 - 1, v_1 \left( v^2 - \frac{5}{2} \right), v_2 \left( v^2 - \frac{5}{2} \right), v_3 \left( v^2 - \frac{5}{2} \right) \right]. \quad (6-5)$$

To determine how fast the error decays, we seek the eigenfunctions  $\bar{Y}(\boldsymbol{v})$  and  $\alpha = [\alpha_\varrho, \boldsymbol{\alpha}_u, \alpha_T, \boldsymbol{\alpha}_q]$  of the following forms:

$$\begin{aligned} Y^{k+1}(\boldsymbol{x}, \boldsymbol{v}) &= e^{k\bar{Y}(\boldsymbol{v})} \exp(i\boldsymbol{\theta} \cdot \boldsymbol{x}), \\ \Phi^{k+1}(\boldsymbol{x}) &= e^{k+1}\alpha \exp(i\boldsymbol{\theta} \cdot \boldsymbol{x}), \end{aligned} \quad (6-6)$$

where  $\boldsymbol{\theta} = (\theta_1, \theta_2, \theta_3)$  is the wavevector of perturbation. Note that the two exponents in the right-hand-side are different, due to the fact that in CIS we first need macroscopic quantities to start the iteration. The iteration is unstable when the error decay rate  $e$  is larger than unity, and slow (fast) convergence occurs when the error decay rate  $|e|$  approaches one (zero).

From Eqs. (6-4) and (6-6) we have

$$e\alpha = \int \bar{Y}(\boldsymbol{v})\phi(\boldsymbol{v})d\boldsymbol{v}, \quad (6-7)$$

and from Eqs. (6-1), (6-3), and (6-6), we have

$$\bar{Y}(\boldsymbol{v}) = \frac{\alpha_\varrho + 2\boldsymbol{\alpha}_u \cdot \boldsymbol{v} + \alpha_T \left( v^2 - \frac{3}{2} \right) + \frac{4(1-\text{Pr})}{5} \boldsymbol{\alpha}_q \cdot \boldsymbol{v} \left( v^2 - \frac{5}{2} \right)}{1 + i\delta_{rp}^{-1}\boldsymbol{\theta} \cdot \boldsymbol{v}} f_{\text{eq}}. \quad (6-8)$$

On multiplying Eq. (6-8) with  $\phi(\boldsymbol{v})$  and integrating the resultant equations with respect to  $\boldsymbol{v}$ , we obtain eight linear equations for eight unknown elements in  $\alpha$  with the help

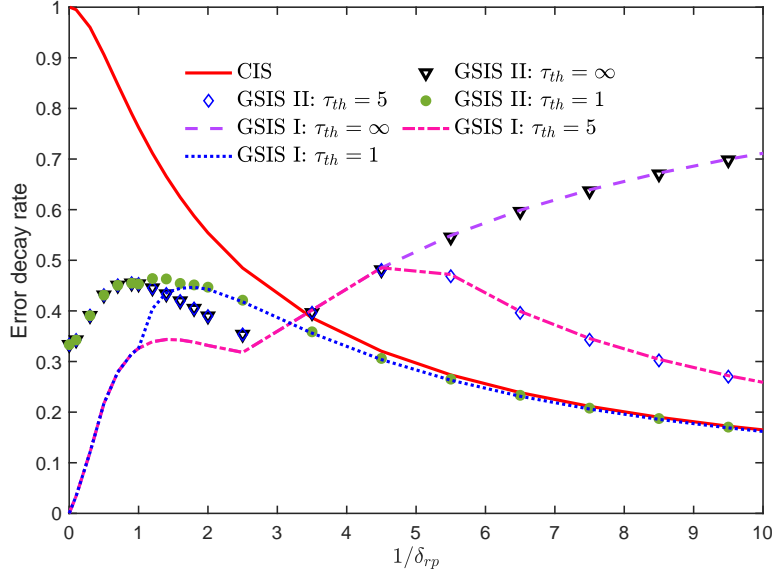


图 6-2 The error decay rate calculated from the linearized Shakhov model by the Fourier stability analysis [120]. In GSIS, different threshold rarefaction parameters  $\delta_{rp}^{th}$  are considered, see Eq. (6-33).

of Eq. (6-7):

$$C_8 \alpha^T = e \alpha^T, \quad (6-9)$$

where the superscript T is the transpose operator. The error decay rate is the maximum eigenvalue in magnitude of matrix  $C_8$ ; the result<sup>①</sup> is shown in Fig. 6-2. Specifically, when  $\text{Kn} \rightarrow 0$ , the error decay rate is calculated analytically [120]:

$$e_{CIS} = 1 - \frac{1}{2\delta_{rp}^2}. \quad (6-10)$$

The results show that CIS is efficient in the free-molecular regime, as  $e \rightarrow 0$  so that the error decays quickly. On the other hand, the CIS is extremely slow in the near-continuum flow regime, as  $e \rightarrow 1$  when  $\text{Kn} \rightarrow 0$ .

### 6.1.2 False convergence

In addition to the slow convergence when  $\text{Kn} \rightarrow 0$ , CIS suffers the problem of “false convergence”. This can be analyzed following the work of Adam and Larsen for radiation transfer equation [1]. We rewrite the iterative scheme (6-1) as

$$h^k = \mathcal{I} h^{k-1}, \quad \text{with } \mathcal{I} = \frac{\mathcal{L}_s^+}{\delta_{rp} + \boldsymbol{\nu} \cdot \nabla}. \quad (6-11)$$

The exact solution  $h$  (the corresponding macroscopic quantities are denoted by  $\Phi_M$ )

<sup>①</sup> If without specification, the perturbation wavevector is chosen as  $|\boldsymbol{\theta}| = 1$ ; Behaviors of the error decay rate are similar for other values of  $|\boldsymbol{\theta}|$ .

satisfies  $h = \mathcal{I}h$ . Therefore, at the  $k$ -th step, the difference from the exact solution is  $h - h^k = \mathcal{I}(h - h^{k-1}) = \mathcal{I}(h - h^k) + \mathcal{I}(h^k - h^{k-1})$ , so

$$h - h^k = \frac{\mathcal{I}}{1-\mathcal{I}}(h^k - h^{k-1}). \quad (6-12)$$

This yields an estimation:

$$|h - h^k| \leq \left| \frac{\mathcal{I}}{1-\mathcal{I}} \right| |h^k - h^{k-1}| \approx \frac{e}{1-e} |h^k - h^{k-1}|, \quad (6-13)$$

which implies that, if the iteration is terminated with the convergence criterion  $|\Phi_M^{k+1} - \Phi_M^k| < \epsilon$ , the relative difference from the true steady-state solution  $\Phi_M$  can be estimated as

$$|\Phi_M^{k+1} - \Phi_M| < \frac{e_{CIS}}{1-e_{CIS}} \epsilon. \quad (6-14)$$

With Eq. (6-10), it is found that the error in the final step of iteration is much larger than the preassigned value  $\epsilon$ :

$$|\Phi_M^{k+1} - \Phi_M| \rightarrow \frac{\epsilon}{Kn^2}, \quad \text{when } Kn \rightarrow 0. \quad (6-15)$$

Therefore, false convergence occurs if  $\epsilon$  is not set small enough.

## 6.2 General synthetic iterative scheme

To eliminate the deficiencies in CIS, the synthetic iterative scheme, which is initially designed for radiation transport problem [1], is extended to solve rarefied gas flows. Success examples include the Poiseuille flow, Couette flow, thermal transpiration, and flows driven by concentration gradient [131, 59, 123, 84, 82-83, 122, 147, 117], where the flow velocity is perpendicular to the computational domain.

In synthetic iterative scheme, macroscopic synthetic equation is exactly derived from the kinetic equation, which, in the limit of  $Kn \rightarrow 0$ , becomes the diffusion equation. When the Knudsen number is not negligible, however, the macroscopic equation has an additional source term, or high-order term, which describes the rarefaction effects. The gas kinetic equation and macroscopic synthetic equation are solved on the same spatial grids in the entire domain: at each iteration, the kinetic equation provides high-order terms to the macroscopic equation, which, when solved to the steady state, is used to correct the VDF and macroscopic quantities. Since the diffusion equation is efficient in exchange the flow information, faster convergence is achieved when  $Kn \rightarrow 0$ .

Synthetic equations should be carefully designed when the general rarefied gas flow

is concerned. For generality we consider the LBE. We multiply Eq. (4-49) by the five fundamental collision invariants and integrate the resultant equations with respect to the molecular velocity  $\boldsymbol{v}$ , yielding:

$$\begin{aligned}\frac{\partial \varrho}{\partial t} + \frac{\partial u_i}{\partial x_i} &= 0, \\ 2\frac{\partial u_i}{\partial t} + \frac{\partial \varrho}{\partial x_i} + \frac{\partial T}{\partial x_i} + \frac{\partial \sigma_{ij}}{\partial x_j} &= 0, \\ \frac{3}{2}\frac{\partial T}{\partial t} + \frac{\partial q_j}{\partial x_j} + \frac{\partial u_j}{\partial x_j} &= 0.\end{aligned}\quad (6-16)$$

To develop a general fast-converging scheme, it is beneficial to construct macroscopic diffusion-type equations that contain Newton's law for stress and Fourier's law for heat conduction explicitly to recover the macroscopic transport mechanism; we express the shear stress and heat flux as follows:

$$\sigma_{ij} = -2\delta_{rp}^{-1}\frac{\partial u_{<i}}{\partial x_{j>}} + \text{HoT}_{\sigma_{ij}}, \quad (6-17)$$

$$q_i = -\frac{5}{4\text{Pr}}\delta_{rp}^{-1}\frac{\partial T}{\partial x_i} + \text{HoT}_{q_i}, \quad (6-18)$$

where  $\text{HoT}_{\sigma_{ij}}$  and  $\text{HoT}_{q_i}$  are the high-order terms containing contributions of all the orders  $O(\text{Kn}^\alpha)$  with  $\alpha = 2, 3, \dots, \infty$ . These high-order terms cannot be obtained from Burnett, super-Burnett equations, nor from the Grad moment equations, but have to be determined from the kinetic equation that are valid in the whole range of rarefaction.

### 6.2.1 Scheme-I GSIS

To obtain Eq. (6-17), we multiply Eq. (4-49) by  $2v_{<i}v_{j>}$  and integrate the resultant equation with respect to  $\boldsymbol{v}$ :

$$\frac{\partial \sigma_{ij}}{\partial t} + 2 \int v_{<i}v_{j>} \boldsymbol{v} \cdot \frac{\partial h}{\partial \boldsymbol{x}} d\boldsymbol{v} = 2 \int \mathcal{L}v_iv_j d\boldsymbol{v}, \quad (6-19)$$

which is rewritten as

$$\begin{aligned}\frac{\partial \sigma_{ij}}{\partial t} + \underbrace{2 \int v_{<i}v_{j>} \boldsymbol{v} \cdot \frac{\partial h}{\partial \boldsymbol{x}} d\boldsymbol{v} - 2\frac{\partial u_{<i}}{\partial x_{j>}}}_{\text{HoT}_{\sigma_{ij}}} \\ + \underbrace{2\frac{\partial u_{<i}}{\partial x_{j>}}}_{\text{Newton's law}} &= -\delta_{rp}\sigma_{ij} + 2 \int (\mathcal{L} - \mathcal{L}_s)v_iv_j d\boldsymbol{v}.\end{aligned}\quad (6-20)$$

Note that the purpose of introducing  $\mathcal{L}_s$  is only to produce the term  $\delta_{rp}\sigma_{ij}$ , so that the Newton law appears in the synthetic equation naturally; this turns out to be crucial in

boosting convergence. Also note that, for the linearized BCO, comparing to  $\delta_{rp}\sigma_{ij}$ , the term  $2\int(\mathcal{L} - \mathcal{L}_s)v_i v_j d\boldsymbol{v}$  is negligible. For instances, this term is zero for Maxwell gas, while for the HS gas this term is only about 2% of  $\delta_{rp}\sigma_{ij}$ , see Eq. (3-29). It will be shown later that the high-order terms is evaluated at the  $k$ -th iteration step, while Newton's law for stress is calculated at the  $(k + 1)$ -th step.

Similarly, to obtain Eq. (6-18), we multiply Eq. (4-49) by  $v_i(v^2 - 5/2)$  and integrate the resultant equation with respect to  $\boldsymbol{v}$ :

$$\begin{aligned} & \frac{\partial q_i}{\partial t} + \underbrace{\int \left( v^2 - \frac{5}{2} \right) v_i \boldsymbol{v} \cdot \frac{\partial h}{\partial \boldsymbol{x}} d\boldsymbol{v} - \frac{3C_q}{2} \frac{\partial T}{\partial x_i}}_{\text{HoT}_{q_i}} \\ & + \underbrace{\frac{3C_q}{2} \frac{\partial T}{\partial x_i}}_{\text{Fourier's law}} = -\delta_{rp} \text{Pr} q_i + \int (\mathcal{L} - \mathcal{L}_s) v_i v^2 d\boldsymbol{v}. \end{aligned} \quad (6-21)$$

For the linearized BCO, the term  $\int (\mathcal{L} - \mathcal{L}_s) v_i v^2 d\boldsymbol{v}$  is negligible small when compared to  $\delta_{rp} q_i$ . If we choose  $C_q = 5/6$ , Fourier's heat conduction law appears naturally.

The GSIS is designed to find steady-state solutions of the LBE through the following steps (4-49):

- Step 1. When the VDF  $h^k$  and the corresponding macroscopic quantities are known, calculate  $2\int(\mathcal{L} - \mathcal{L}_s)v_i v_j d\boldsymbol{v}$  and  $\int(\mathcal{L} - \mathcal{L}_s)v_i v^2 d\boldsymbol{v}$ . Also calculate the VDF  $h^{k+1/2}$  at the intermediate iterative step as:

$$v_{eq}(\boldsymbol{v})h^{k+1/2} + \boldsymbol{v} \cdot \frac{\partial h^{k+1/2}}{\partial \boldsymbol{x}} = \mathcal{L}^+(h^k, f_{eq}). \quad (6-22)$$

- Step 2. From  $h^{k+1/2}$ , calculate the macroscopic quantities at the intermediate step, and the high-order terms.
- Step 3. Calculate the macroscopic quantities, in the bulk region, at the  $(k + 1)$ -th step by solving synthetic equations (6-16), (6-20) and (6-21) to the steady state, where the boundary conditions in the vicinity of walls are obtained from Step 2.
- Step 4. The VDF is corrected in the following manner so that its corresponding macroscopic quantities is the same as those obtained in Step 3:

$$\begin{aligned} h^{k+1} = & h^{k+1/2} + \left[ \lambda_\rho + 2\lambda_u \cdot \boldsymbol{v} + \lambda_T \left( v^2 - \frac{3}{2} \right) \right] f_{eq} \\ & + \left[ \lambda_{\sigma_{ij}} \left( v_i v_j - \frac{v^2}{3} \delta_{ij} \right) + \frac{4}{5} \lambda_q \cdot \boldsymbol{v} \left( v^2 - \frac{5}{2} \right) \right] f_{eq}, \end{aligned} \quad (6-23)$$

where  $\lambda_u = \boldsymbol{u}^{k+1} - \boldsymbol{u}^{k+1/2}$ ,  $\lambda_q = \boldsymbol{q}^{k+1} - \boldsymbol{q}^{k+1/2}$ ,  $\lambda_\rho = \rho^{k+1} - \rho^{k+1/2}$ ,  $\lambda_T = T^{k+1} - T^{k+1/2}$ , and  $\lambda_{\sigma_{ij}} = \sigma_{ij}^{k+1} - \sigma_{ij}^{k+1/2}$ .

- Step 5. The above steps are repeated until convergence.

### 6.2.2 Scheme-II GSIS

High-order terms in Eqs. (6-20) and (6-21) are constructed by considering the evolution equation of stress and heat flux, which involves the calculation of complicated collision operator when the Boltzmann equation is considered. This is not a problem for deterministic numerical methods, but will be not easy for DSMC. As we aim to develop a generalized scheme, not only for deterministic methods, but also for stochastic methods such as DSMC, we propose the following easy-to-use constitutive relations [152]:

$$\begin{aligned} \text{HoT}_{\sigma_{ij}} &= \sigma_{ij}^{k+1/2} + 2\delta_{rp}^{-1} \frac{\partial u_{<i}^{k+1/2}}{\partial x_{j>}}, \\ \text{HoT}_{q_i} &= q_i^{k+1/2} + \frac{5}{4\text{Pr}} \delta_{rp}^{-1} \frac{\partial T^{k+1/2}}{\partial x_i}. \end{aligned} \quad (6-24)$$

## 6.3 Properties of GSIS

Two important questions in the multiscale simulation of rarefied gas flows are: can we find the steady-state efficiently and can we get accurate results even at coarse spatial grid? This section is dedicated to proving both.

### 6.3.1 Super convergence

The linearized Shakhov model is used to analyze the error decay rate of GSIS. That of the Boltzmann equation can only be shown in numerical simulation, due to the complicated structure of the BCO.

The error functions in Eqs. (6-3), (6-4), and (6-6) are redefined as

$$\begin{aligned} Y^{k+1/2}(\mathbf{x}, \mathbf{v}) &= h^{k+1/2}(\mathbf{x}, \mathbf{v}) - h^k(\mathbf{x}, \mathbf{v}) = e^{k\bar{Y}(\mathbf{v})} \exp(i\boldsymbol{\theta} \cdot \mathbf{x}), \\ \Phi^{k+1}(\mathbf{x}) &= M^{k+1}(\mathbf{x}) - M^k(\mathbf{x}) = e^{k+1}\alpha \exp(i\boldsymbol{\theta} \cdot \mathbf{x}), \end{aligned} \quad (6-25)$$

where  $\bar{Y}(\mathbf{v})$  is still given by Eq. (6-8). Note that now  $\Phi$  are calculated from the synthetic equations, rather than from the VDF. That is, macroscopic quantities at the  $(k+1)$ -th iteration step are obtained by solving the following synthetic equations:

$$\frac{\partial u_i^{k+1}}{\partial x_i} = 0, \quad \frac{\partial \varrho^{k+1}}{\partial x_i} + \frac{\partial T^{k+1}}{\partial x_i} + \frac{\partial \sigma_{ij}^{k+1}}{\partial x_j} = 0, \quad \frac{\partial q_i^{k+1}}{\partial x_i} = 0. \quad (6-26)$$

With Eqs. (6-8), (6-20), (6-21), (6-26), and (6-25), we obtain the following eight

linear equations:

$$\begin{aligned} e(i\theta_1\alpha_{u_1} + i\theta_2\alpha_{u_2} + i\theta_3\alpha_{u_3}) &= 0, \\ e[i\theta_j(\alpha_\varrho + \alpha_T) + |\boldsymbol{\theta}|^2\delta_{rp}^{-1}\alpha_{u_j}] &= S_{j+1}, \\ e(i\theta_1\alpha_{q_1} + i\theta_2\alpha_{q_2} + i\theta_3\alpha_{q_3}) &= 0, \\ e\left(\frac{5i}{4Pr}\theta_j\delta_{rp}^{-1}\alpha_T + \alpha_{q_j}\right) &= S_{j+5}, \end{aligned} \quad (6-27)$$

where  $j = 1, 2, 3$ , and the source terms in the scheme I, due to the HoTs in Eqs. (6-20) and (6-21), are also linear functions of  $\alpha_M$ :

$$\begin{aligned} S_{j+1} &= \delta_{rp}^{-1} \int (|\boldsymbol{\theta}|^2 v_j - 2\theta_k v_{<j} v_{k>}) \bar{Y}(\boldsymbol{v}) d^3 \boldsymbol{v}, \\ S_{j+5} &= \frac{i}{\delta_{rp} Pr} \int \left[ \frac{5}{4Pr} \theta_j \left( \frac{2}{3} v^2 - 1 \right) - \theta v_j \left( v^2 - \frac{5}{2} \right) \right] \bar{Y}(\boldsymbol{v}) d^3 \boldsymbol{v}, \end{aligned} \quad (6-28)$$

where  $\theta = \theta_1 v_1 + \theta_2 v_2 + \theta_3 v_3$ ,  $k = 1, 2, 3$  is the dummy index, while that in the scheme II, with Eq. (6-24), are

$$\begin{aligned} S_{j+1} &= \int (\delta_{rp}^{-1} |\boldsymbol{\theta}|^2 v_j - 2i\theta_k v_{<j} v_{k>}) \bar{Y}(\boldsymbol{v}) d^3 \boldsymbol{v}, \\ S_{j+5} &= \int \left[ \frac{5i}{4Pr} \theta_j \delta_{rp}^{-1} \left( \frac{2}{3} v^2 - 1 \right) + v_j \left( v^2 - \frac{5}{2} \right) \right] \bar{Y}(\boldsymbol{v}) d^3 \boldsymbol{v}, \end{aligned} \quad (6-29)$$

For the scheme I, the error decay rate is obtained by solving Eqs. (6-27) and (6-28), which are rewritten in the matrix form as

$$L_8 e \alpha^\top = R_8 \alpha^\top, \quad (6-30)$$

where  $L_8$  and  $R_8$  are two  $8 \times 8$  matrices. By introducing  $G_1 = L_8^{-1}R_8$  and numerically computing its eigenvalues we obtain the error decay rate  $e$  in Fig. 6-2. When  $Kn \rightarrow 0$ , that is,  $e \propto Kn^2$ , so GSIS can boost convergence in near-continuum flows. As a matter of fact, compared to the false convergence of CIS described by Eq. (6-15), GSIS possesses the properties of super convergence, since according to the following equation

$$|\Phi_M^{k+1} - \Phi_M| \rightarrow \epsilon Kn^2, \quad \text{when } Kn \rightarrow 0, \quad (6-31)$$

the convergence criterion  $\epsilon$  can be set at a relative larger value.

When  $Kn \rightarrow \infty$ , however,  $e \rightarrow 1$ . To fix this problem, macroscopic quantities are updated as

$$M^{k+1}(\boldsymbol{x}) = \beta M_{\text{syn}}(\boldsymbol{x}) + (1 - \beta) M^{k+1/2}(\boldsymbol{x}), \quad (6-32)$$

where the parameter  $\beta$  is chosen as

$$\beta = \frac{\delta_{rp}}{\max(\delta_{rp}, \delta_{rp}^{\text{th}})}. \quad (6-33)$$

with  $\delta_{rp}^{\text{th}}$  being the threshold rarefaction parameter. That is,  $\beta = 1$  when the rarefaction parameter is larger than  $\delta_{rp}^{\text{th}}$ ; when  $\delta_{rp} < \delta_{rp}^{\text{th}}$ ,  $\beta$  gradually decreases to zero as the Knudsen number approaches infinity. The error decay rate is obtained by computing the eigenvalue of the matrix  $G = \beta L_8^{-1} R_8 + (1 - \beta) C_8$ .

Results in Fig. 6-2 show that the maximum error decay rate can be restrained to be less than 0.5 for all Knudsen number, by choosing approximate value of  $\beta$ . Thus, theoretically, GSIS can achieve fast convergence in the whole range of Knudsen number, because the error is reduced by three orders of magnitude in 10 iterations.

Likewise, for the scheme II, the error decay rate is obtained by solving Eqs. (6-27) and (6-29). It is seen from Fig. 6-2 that when  $\text{Kn} \rightarrow 0$ , the error decay rate of the scheme II is reduced from one in CIS, but does not go to zero<sup>①</sup>. Nevertheless, like the scheme I, by choosing appropriate value of  $\delta_{rp}^{\text{th}}$ , the error decay rate can also be controlled within 0.5 in the whole range of rarefaction parameter.

### 6.3.2 Asymptotic preserving

In GSIS the mesoscopic kinetic equation and macroscopic synthetic equations can be solved by different numerical methods with different order of accuracy. It is important to investigate the influence of spatial discretization of the gas kinetic solver on the accuracy of GSIS, based on the assumptions that (i) synthetic equations can be solved exactly and (ii) the spatial cell size  $\Delta x$  is adequate to capture the physical solution of NSF equations. This is equivalent to check whether the NSF equations can be exactly derived or not, through the Chapman-Enskog expansion [20], from the discretized gas kinetic equation

$$\boldsymbol{v} \cdot \frac{\partial h}{\partial \boldsymbol{x}} + O(\Delta x^n) \delta(h) = \mathcal{L}_s - \delta_{rp} h, \quad (6-34)$$

with the following scaling ( $\Delta x$  has been normalized by the characteristic flow length  $L$ ):

$$\Delta x \sim \text{Kn}^{1/\alpha}, \quad (6-35)$$

where  $n$  is the order of approximation for the spatial derivative,  $\delta(h)$  is the  $(n+1)$ -th order derivative of  $h$ , and  $\alpha$  is order of accuracy in the asymptotic preserving of NSF

<sup>①</sup> This is because the heat flux enters the collision term in the Shakhov model, and in the Scheme II the evolution equation (6-21) of heat flux is not considered in the macroscopic synthetic equation. If we use the linearized BGK model, we find that the error decay rate approaches zero when  $\text{Kn} \rightarrow 0$ .

equations.

### 6.3.2.1 Scheme I

By subsisting the expansion  $h = h_0 + \text{Kn}h_1 + \dots$  into Eq. (6-34) and collecting terms with the order of  $\text{Kn}^{-1}$ , we have  $h_0 = f_{eq}$ , when the following largest scaling is chosen

$$\Delta x \sim \text{Kn}^{1/\infty} = O(1). \quad (6-36)$$

Under this scaling, at the order  $\text{Kn}^0$ , we obtain:

$$h_1 = -\mathbf{v} \cdot \frac{\partial h_{eq}}{\partial \mathbf{x}} - \delta(h_{eq}). \quad (6-37)$$

Thus, according to Eqs. (6-20) and (6-21), the linear constitutive relations are recovered in synthetic equations with accuracy  $O(\text{Kn}^2)$ :

$$\begin{aligned} \sigma_{ij} &= -2\delta_{rp}^{-1} \frac{\partial u_{<i}}{\partial x_j} + O(\text{Kn}^2), \\ q_i &= -\frac{5}{4\text{Pr}} \delta_{rp}^{-1} \frac{\partial T}{\partial x_i} + O(\text{Kn}^2). \end{aligned} \quad (6-38)$$

Thus, GSIS asymptotically preserves the NSF equations, provided that the spatial resolution  $\Delta x = O(1)$  is able to capture the physical solution of NSF equations. In practice, however,  $\Delta x = O(1)$  cannot be used in regions where the physical solutions require a resolution of  $O(\text{Kn})$ , e.g., the Knudsen layer and shock structure. Fortunately, these kinetic layers only occupy a small fraction of the computational domain, which can be captured by implicit schemes with non-uniform spatial discretization.

### 6.3.2.2 Scheme II

In order to recover the NSF constitutive relations (6-38), the VDF to the first order of Knudsen number must be exactly recovered as

$$h_1 = -\mathbf{v} \cdot \frac{\partial h_{eq}}{\partial \mathbf{x}}. \quad (6-39)$$

And this requires the following largest scaling:

$$\Delta x \sim \text{Kn}^{1/2}. \quad (6-40)$$

## 6.4 Numerical tests

Several numerical simulations are carried out to demonstrate the major properties of GSIS, including the 1D coherent Rayleigh-Brillouin scattering problem where the influence of gas-surface interaction is absent, the planar Fourier flow, and 2D Couette flow

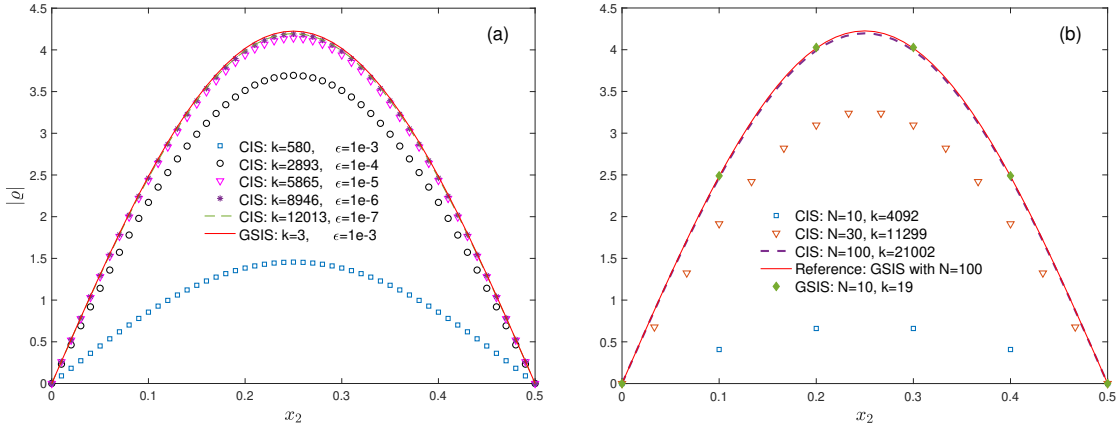


图 6-3 密度 profile 在相干瑞利-布里渊散射 [120]，当  $\delta_{rp} = 200$ 。 (a) CIS 的收敛历史。空间区域  $x_2 \in [0, 1]$  分为  $N = 100$  均匀单元。由于对称性，只绘制了密度 profile 的一半。 (b) 密度 profiles 和迭代次数，其中迭代终止于  $\epsilon < 10^{-10}$ 。

between two non-coaxial cylinders. More challenging numerical examples can be found in Refs. [119-120, 118, 115, 152].

#### 6.4.1 Coherent Rayleigh-Brillouin scattering

This problem is ideal to show the fast-converging and asymptotic-preserving properties of the GSIS, as well as the flexibility, importance, and advantage of GSIS that the kinetic and synthetic equations are solved by different methods with different order of accuracy.

The theory of coherent RBS is elaborated in Chapter ???. Here we directly write the evolution equation for the perturbed VDF as

$$2\pi i f_s h + v_2 \frac{\partial h}{\partial x_2} = \mathcal{L}_s^{+,k} - \delta_{rp} h + 2v_2 \cos(2\pi x_2), \quad (6-41)$$

where the normalized scattering frequency is chosen as  $f_s = \sqrt{5/6}$  and the last term presents the external acceleration generated by the optical lattice. The problem is spatially periodic, with the influence of gas-surface interaction. The presence of the first term in Eq. (6-41) is due to the temporal periodicity. Correspondingly, the time derivative  $\partial/\partial t$  in the synthetic equations should be replaced by  $2\pi i f_s$ .

We first consider the case where the kinetic and synthetic equations are solved by the second-order upwind finite difference and Fourier spectral methods, respectively. Figure 6-3(a) shows the convergence history of both CIS and GSIS, when the rarefaction parameter is  $\delta_{rp} = 200$ . It is clearly seen that, GSIS produces the converged solution

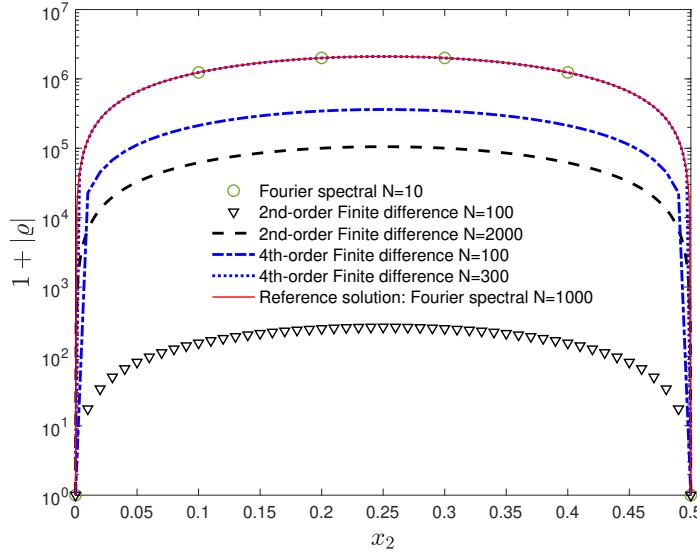


图 6-4 Comparisons of the density profile in coherent Rayleigh-Brillouin scattering [120], where the kinetic equation is solved by the second-order upwind finite difference, while macroscopic equations are solved by various schemes with different number of spatial points ( $N$ ). The Knudsen number is  $K = 10^{-8}$ . The density amplitude is shifted by one in order to show it in the log scale.

after only 3 iterations, and when the convergence criterion

$$\epsilon = \left| \frac{\int |\varrho^{(k+1)}| dx_2}{\int |\varrho^{(k)}| dx_2} - 1 \right| \quad (6-42)$$

is  $10^{-3}$ . This is due to the super-converging property given in Eq. (6-31). However, due to the false convergence proven in Eq. (6-15), CIS needs huge number of iterations and the convergence criterion has to be set very small, i.e.,  $\epsilon = 10^{-10}$  in this case.

Figure 6-3(b) shows that GSIS-I asymptotically preserves the NSF limit, when only 10 uniform spatial cells are used. This is in agreement with the theoretical prove (6-36). When the same number of spatial cells are used in CIS, the density amplitude is about 5 times smaller than the true solution, which indicates a strong numerical dissipation. Only when the number of cells is increased to 100 can the CIS capture the density profile at  $\delta_{rp} = 200$ . Taking into account both the spatial discretization and iteration number, GSIS is about 6,000 times faster than CIS.

We further consider an extreme case of  $\delta_{rp} = 10^8$ . In this case, normally the Euler equation is used to describe the gas dynamics, and many kinetic schemes are proposed to asymptotically preserve the Euler limit. However, it should be emphasized that, Euler equation cannot be used here, otherwise the amplitude of perturbation will go to infinity due to the omission of viscosity. The extremely large value of  $\delta_{rp}$  poses a grand challenge to the numerical method for kinetic equations, as any small value of numer-

ical dissipation could easily contaminate the final solution, which leads to a significant smaller amplitude of density perturbation. Even at such a small Knudsen number, if the macroscopic equation is solved exactly (by the Fourier spectral method) and  $\Delta x \sim O(1)$  is able to capture the spatial variation, GSIS has infinite order of accuracy, see the circles in Fig. 6-4. However, when the second-order finite difference scheme is used to solve the synthetic equations, we need more than 2000 spatial points to capture the density perturbation; this is understandable since the numerical dissipation (or numerical viscosity)  $(\Delta x)^2 = 2.5 \times 10^{-7}$  is larger than the physical viscosity (here it is reflected by the inverse rarefaction parameter). When the synthetic equations are solved by the fourth-order finite difference, we see that  $N = 100$  leads to wrong solutions, while  $N = 300$  yields accurate solution. This is because the numerical dissipation is about  $(\Delta x)^4 = 10^{-8}$  and  $1.2 \times 10^{-10}$ , respectively, so that the former is too dissipative while the latter is accurate.

The last numerical example in Fig. 6-4 illustrates the flexibility, importance, and advantage of GSIS that the kinetic and synthetic equations are solved by different methods with different order of accuracy. Since many sophisticated high-order methods have been developed for NSF equations, they can be directly incorporated in the GSIS framework to boost convergence and reduce the use of spatial cells and hence the computational memory.

#### 6.4.2 Planar Fourier flow

We consider the heat conduction in gas between two plates located at  $x_2 = 0$  and  $1$ , see Section 7.3, the see the influence of solid walls in the fast-converging properties of GSIS.

From the synthetic equations (6-16), (6-20) and (6-21), as well as the symmetry condition, we know  $\mathbf{u} = 0, \sigma_{ij} = 0$  when  $i \neq j$ , and  $q_1, q_3 = 0$ ; the heat flux  $q_2$  is a constant, and the perturbed temperature is governed by the following ordinary differential equation:

$$\begin{aligned} \frac{\partial T}{\partial x_2} = & -\frac{4\delta_{rp}}{9C_q}q_2 + \underbrace{\frac{2}{3C_q} \int v_2 v^2 (\mathcal{L} - \mathcal{L}_s) d\nu}_{H_1^k(x_2)} \\ & - \underbrace{\frac{2}{3C_q} \frac{\partial}{\partial x_2} \int (v_2^2 - C_q) \left(v^2 - \frac{3}{2}\right) h d\nu}_{H_2^{k+1/2}(x_2)}, \end{aligned} \quad (6-43)$$

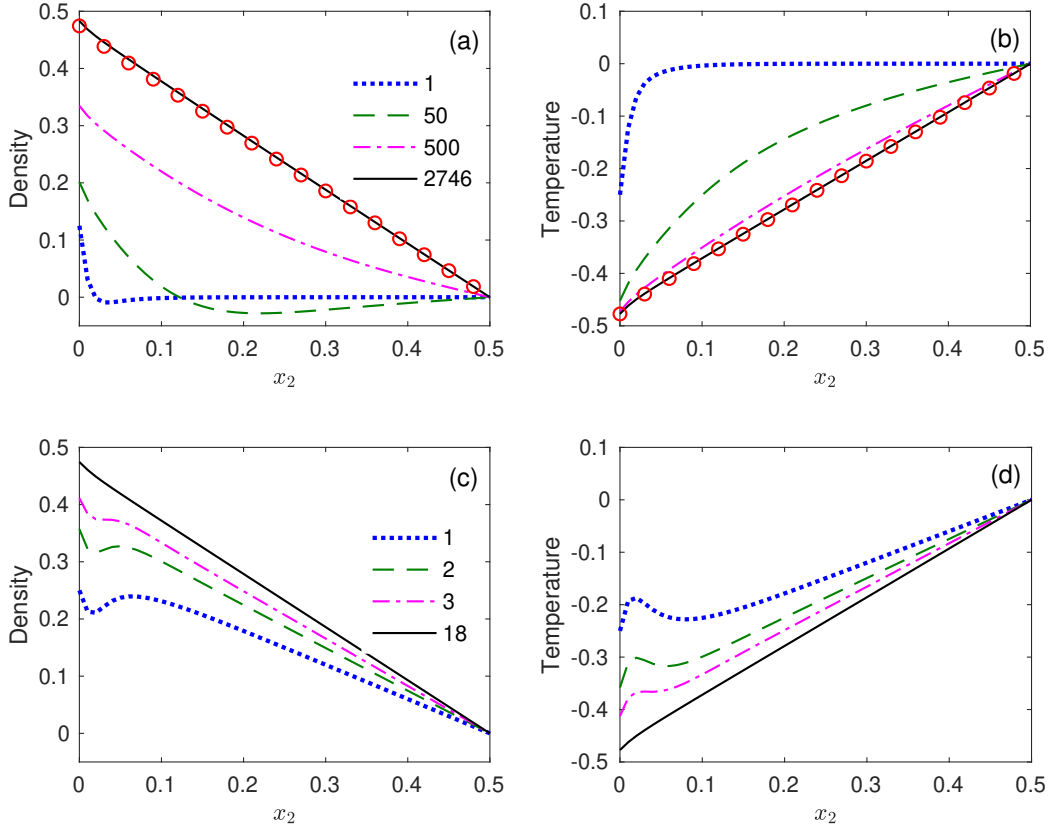


图 6-5 Convergence history in planar Fourier flow at  $\delta_{rp} = 50$  [119]. (Top) CIS, (Bottom) GSIS. Circles: converged solution from GSIS. The linearized Shakhov model is used with the initial condition  $h(x_2, \boldsymbol{v}) = 0$ . Iteration steps are shown in the legends.

whose solution at the  $(k + 1)$ -th iteration step is given by

$$T^{k+1}(x_2) = -\frac{4\delta_{rp}q_2}{9C_q} \left( x_2 - \frac{1}{2} \right) + \int_{1/2}^{x_2} H_1^k(x_2) dx_2 - H_2^{k+1/2}(x_2), \quad (6-44)$$

where the constant heat flux  $q_2$  is

$$q_2 = \frac{9C_q}{2\delta_{rp}} \left[ T^{k+1/2}(0) + H_2^{k+1/2}(0) - H_1^k(0) \right]. \quad (6-45)$$

The density can be easily obtained by  $\varrho + T + \sigma_{22} = 0$ , where from Eq. (6-20) the stress  $\sigma_{22}$  is calculated as

$$\sigma_{22} = -\frac{\frac{\partial}{\partial x_2} \int 2v_{<2} v_{2>} v_2 h d\boldsymbol{v}}{\delta_{rp}} + \frac{2}{\delta_{rp}} \int (\mathcal{L} - \mathcal{L}_s) v_2^2 d\boldsymbol{v}. \quad (6-46)$$

The efficiency of GSIS and CIS is compared in Fig. 6-5. Starting from the initial condition  $h(x_2, \boldsymbol{v}) = 0$ , the perturbation from the solid surface quickly changes the density and temperature nearby in the CIS. However, the perturbation can hardly penetrates into the bulk region. Such a slow convergence is completely changed in GSIS. As can be seen

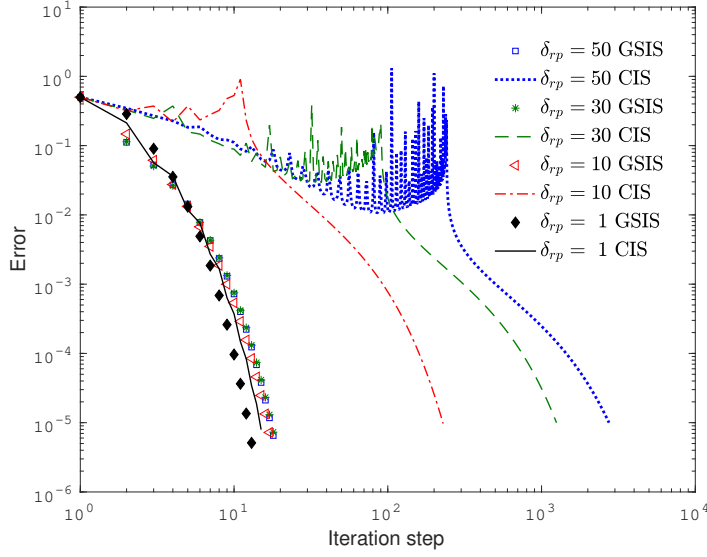


图 6-6 The decay of error  $\epsilon$  as a function of the iteration step, for the Fourier flow between two parallel plates. The spatial region is discretized by 51 equidistant points.

from Fig. 6-5(d), after the first iteration, although the gas temperature near the wall is the same as that in CIS, the bulk temperature in GSIS is adjusted to be nearly linear, by the synthetic equation whose dominant parts are

$$\frac{\partial T}{\partial x_2} = -\frac{4Pr\delta_{rp}}{5}q_2, \quad \text{and} \quad \varrho = -T. \quad (6-47)$$

Then, due to the correction of VDF as per Eq. (6-23), at the second iterative step, the boundary condition (7-8) in GSIS is more close to the final steady-state than that in CIS. Hence after the second iteration, the GSIS results are closer to the final solution both at the boundary and in the bulk, i.e., fast convergence is achieved.

Figure 6-6 shows the history of error decay of both CIS and GSIS, from the continuum to transition flow regimes. In CIS, the number of iteration steps increases drastically with  $\delta_{rp}$ , while in GSIS converged solutions are found within 20 iterations for  $\delta_{rp} = 1, 10, 30$ , and 50. Theoretically, according to Eq. (6-31), the number of iterations should be very small when  $\delta_{rp}$  is large. This discrepancy is in fact caused by the present of solid wall, where the local Knudsen number inside the Knudsen layer is about 1, therefore, the effective error decay rate of GSIS, as shown in Fig. 6-2, is about 0.5. This means that, for wall-bounded rarefied gas flows, the error is reduced by 3 orders of magnitude after 10 iterations in GSIS, no matter what the Knudsen number is. This explanation is in strong agreement with the results in Fig. 6-6. Therefore, in terms of fast-converging, GSIS-I and GSIS-II have similar performance.

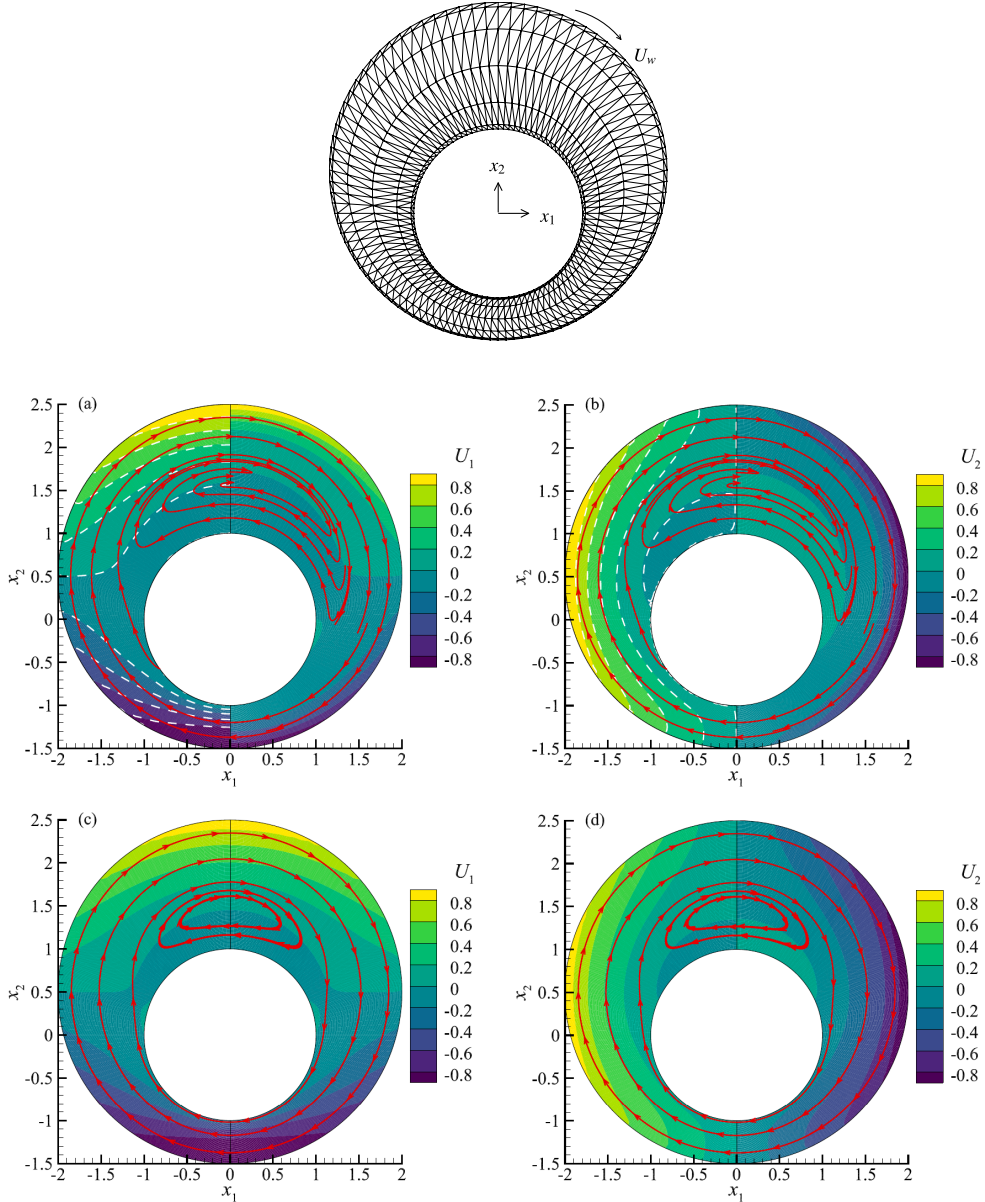


图 6-7 Contours and streamlines in the Couette flow between two eccentric cylinders [119]. (a, b)  $\delta_{rp} = 1000$ . (c, d)  $\delta_{rp} = 10$ . GSIS (CIS) results are plotted in the left (right) half domain. Dashed lines in (a) and (b): velocity contours from the Navier-Stokes equations with non-slip velocity boundary.

### 6.4.3 Couette flow between eccentric cylinders

Consider a Couette flow between two non-coaxial cylinders in Fig. 6-7. The inner cylinder is stationary, while the outer cylinder rotates clockwise at a constant speed of  $u_w$ . The Shakhov model is linearized when  $\beta$  in Eq. (4-47) takes the value of  $u_w/v_m$ . The high-order discontinuous (DG) methods are employed to solve the linearized Shakhov model and synthetic equations, on structured triangular mesh [119].

Figure 6-7 shows the velocity contours and streamlines. When  $\delta_{rp} = 1000$ , the

表 6-1 Number of iteration steps and CPU time to reach convergence for the Couette flow between two eccentric cylinders [119]. Iteration terminates when the relative error in flow velocity between two consecutive iteration steps is less than  $10^{-5}$ . Simulations are run on 12 processors using OpenMP, on double precision Intel Xeon-E5-2680 processors.

$\delta_{rp}$	Number of triangles	Discrete velocities	Iteration steps		CPU time (s)	
			CIS	GSIS	CIS	GSIS
1000	2400	$8 \times 8 \times 12$	49454	26	33861.2	26.3
10	1600	$32 \times 32 \times 24$	296	26	2849.8	580.3

flow is in the continuum regime, and the GSIS results overlap with the ones from the NSF equations even when the maximum cell size is about 260 times of MFP, which proves the asymptotically preserving property of GSIS. However, the CIS fails to predict the velocity profile due to its numerical dissipation on such a coarse mesh. When  $\delta_{rp} = 10$ , CIS produces close solutions to GSIS, because the mesh resolution is adequate.

Table 6-1 shows the iteration numbers and CPU time. While GSIS obtains the converged solution within dozens of iterations, CIS needs 49454 and 296 iteration steps when  $\delta_{rp} = 1000$  and 10, respectively; as a result, GSIS is about 1300 and 5 times faster.

## 6.5 Concluding remarks and Outlooks

Various numerical results have demonstrated that GSIS is able to find the converged solution within dozens of iterations at any Knudsen number, even when the spatial cell size is much larger than the MFP in the bulk flow region. Moreover, the fast converging property of GSIS enables the numerical error decay fast and the convergence criterion can be set at a much higher value than the CIS.

In addition to the fast-converging and asymptotic-persevering properties that have been proved rigorously, GSIS has the following advantages:

(1) **Compatibility with CFD techniques.** The gas kinetic equation and synthetic equations can be solved by sophisticated methods in computational fluid dynamics, and the kinetic and macroscopic solvers can have different orders of accuracy. For highly rarefied gas flows, the spatial cell size is usually smaller than the MFP and both methods yield high accuracy. For continuum/or near continuum flows, as long as the macroscopic solver for synthetic equations (which are essentially the NSF equations) is able to capture the continuum flow behaviors, the accuracy of GSIS is guaranteed, that is, the numerical cell size can be much larger than the MFP, but should be smaller than the variation scale

(such as the sound wavelength) of the flow.

(2) **Universality.** GSIS can be easily extended to nonlinear flows, time-dependent systems, and rarefied flow of polyatomic gas [152, 118]. Extension to DSMC (to remove the limitation on cell size and boost convergence) is also possible, since the GSIS relies on no specific collision operator so that it can be extended naturally to multi-species flows and even flows involving chemical reactions.

With these development implemented, it is hoped that the multiscale simulation of rarefied gas flows is solved completely in the near future. Also, the essential idea is ready to be applied to other kinetic equations such as the Enskog equation for dense gases with applications to gas extraction in unconventional reservoirs and non-equilibrium evaporation and condensation at the nanoscale [148, 142], as well as the Callaway model on nonequilibrium phonon transport with dual relaxation times [63].

## 第 7 章 Couette 流动

作为最基本的稀薄气体流动之一，对 Couette 流动的研究有助于我们加深对稀薄气体动力学的了解。在本章中，我们先使用合成迭代加速算法计算全流域的 Couette 流动，分析速度剖面、切向热流、剪切应力随克努森数的影响。然后着重研究近连续流下的速度滑移边界条件和克努森层形状。

### 7.1 Planar Couette flow

The geometry is the same as that of the Fourier flow, except that the plate at  $x_2 = -0.5$  moves with a speed  $u_w$  in the  $x_3$  direction, while the plate at the plate at  $x_2 = 0.5$  moves in the opposite direction with the same speed. When the wall speed is far less than the most probable speed  $v_m$ , the Boltzmann equation is linearized to Eq. (4-49) by choosing  $\beta = u_w/v_m$ . The diffuse BC for the perturbation VDF reflected from the wall is

$$h(\boldsymbol{v}, x_2 = -0.5) = 2v_3 f_{eq}, \quad (7-1)$$

while at the channel center  $h(v_1, v_2, v_3, x_2 = 0) = h(v_1, -v_2, -v_3, x_2 = 0)$ .

Figure 7-6 shows the velocity when  $\delta_{rp} = 0.1$ . The intermolecular potential has a strong influence on the velocity profile, but little influence on the wall shear stress.

### 7.2 Viscous slip

The LBE is solved for the Couette flow between two parallel plates. When the steady-state solution is obtained, the velocity profile in the bulk region is linearly fitted by  $u_{NS} = k_1(x_2 - 1/2)$  in the dimensionless form, where  $k_0$  is the coefficient from the least square fitting. Then the KLF is calculated according to the following equation:

$$u_s\left(\frac{x_2}{Kn}\right) = \frac{u_{NS}(x_2) - u_1(x_2)}{k_1 Kn}, \quad (7-2)$$

and the VSC is calculated as

$$\sigma_P = -\frac{2 - k_1}{2 \bar{P}}, \quad (7-3)$$

where  $\bar{P}$  is the wall shear stress.

表 7-1 The VSC for HS, VHS with  $\omega = 0.81$ , and Maxwell molecules under Cercignani-Lampis BC with different TMAC  $\alpha_t$  and EAC  $\alpha_n$ .

$\alpha_t$	$\omega$	$\alpha_n = 0.25$	0.5	0.75	1
0.25	0.5	6.365427	6.343336	6.324267	6.307321
	0.81	6.400178	6.372316	6.347638	6.325202
	1	6.426786	6.394845	6.366237	6.339971
0.5	0.5	2.799516	2.785158	2.772602	2.761338
	0.81	2.829277	2.811279	2.795092	2.780207
	1	2.851688	2.831142	2.812430	2.795028
0.75	0.5	1.598122	1.591127	1.584932	1.579323
	0.81	1.622629	1.613906	1.605945	1.598540
	1	1.641138	1.631215	1.622031	1.613380
1.0	0.5	0.988451	0.988451	0.988451	0.988451
	0.81	1.007717	1.007717	1.007717	1.007717
	1	1.022560	1.022560	1.022560	1.022560
1.25	0.5	0.615670	0.622315	0.628343	0.633906
	0.81	0.629985	0.638188	0.645891	0.653221
	1	0.641382	0.650657	0.659514	0.668067
1.5	0.5	0.361248	0.374217	0.386121	0.397213
	0.81	0.371198	0.387115	0.402275	0.416866
	1	0.379386	0.397328	0.414721	0.431729
1.75	0.5	0.174178	0.193187	0.210840	0.227456
	0.81	0.180631	0.203809	0.226193	0.247988
	1.0	0.185886	0.211919	0.237535	0.262897
2	0.5	0.028851	0.053665	0.076984	0.099153
	0.81	0.032881	0.062901	0.092298	0.121255
	1.0	0.035527	0.069105	0.102637	0.136246

### 7.2.1 Viscous slip coefficient

The LBE is solved with the Cercignani-Lampis BC for HS, VHS with  $\omega = 0.81$ , and Maxwell molecules; results are summarized in Table 7-1. When the EAC  $\alpha_n$  and the intermolecular potential ( $\omega$ ) are fixed, VSC increases rapidly when the TMAC  $\alpha_t$  decreases. The additional free parameter  $\alpha_n$  in the Cercignani-Lampis BC introduces

new interesting results. When  $\alpha_t < 1$ , for a fixed  $\alpha_t$  and intermolecular potential, the VSC decreases slightly as  $\alpha_n$  increases, where the maximum drop in the VSC is less than 2%. When  $\alpha_t = 1$ , the Cercignani-Lampis BC is reduced to the fully diffuse one in this problem, and the VSC does not vary with  $\alpha_n$ . When  $\alpha_t > 1$ , the variation of VSC on  $\alpha_n$  reverses when compared to that of  $\alpha_t < 1$ ; and it is strongly influenced by  $\alpha_n$ , especially when  $\alpha_t$  is large. For instance, for HS molecules at  $\alpha_t = 2$ , the VSC is increased by more than three times when  $\alpha_n$  changes from 0.25 to 1.

For fixed  $\alpha_n$  and  $\alpha_t$ , VSC is insensitive to the intermolecular potentials when  $\alpha_t \lesssim 1.75$ . However, when  $\alpha_t$  is close to two (the “backward” scattering), the influence of intermolecular potential becomes considerable. For example, when  $\alpha_t = 2$  and  $\alpha_n = 1$ , Maxwell molecules have a VSC that is about 37% higher than that for HS molecules.

The VSC can be fitted by a general function as the one used by Lilley & Sader [61] for both diffuse-specular and Cercignani-Lampis BCs:

$$\sigma_P(\alpha) = \frac{a}{\alpha} - b\alpha - c, \quad (7-4)$$

where the fitting coefficients  $a$ ,  $b$ , and  $c$  are shown in Table 7-2 for typical inverse power-law intermolecular potentials.

### 7.2.2 Knudsen layer function

The structure of the Knudsen layer provides a critical information to formulate the effective viscosity. Lockerby *et al.* first proposed a curve-fitted approximation to the Knudsen layer function (KLF) as [66]

$$u_s(x) \approx \frac{7}{20(1+x)^2}, \quad (7-5)$$

where  $x$  is the distance to the solid surface normalized by the MFP  $\lambda$ . It is found that the Navier-Stokes equations with the effective viscosity can predict the velocity profiles in Poiseuille and Couette flows, up to  $\text{Kn} = 0.4$ . Later, by fitting the data from LBE solution of HS gas and the DSMC for Couette flow [87], Lilley & Sader obtained a power-law KLF [60-61]:

$$u_s(x) = u_s(0) - Cx^n, \quad (7-6)$$

where  $C$  is a constant and the exponent  $n \approx 0.82$ . Despite the fact that the fitting is carried out in the region  $0.1 \lesssim x \lesssim 1$ , they predicted the power-law divergence of the velocity gradient in the vicinity of solid surface, that is,  $du_s/dx \rightarrow \infty$  as  $x \rightarrow 0$ .

The singular behavior of velocity gradient at the planar surface is rigorously proved

表 7-2 Fitting coefficients in Eq. (7-4) for HS, VHS with  $\omega = 0.81$ , and Maxwell molecules under the diffuse-specular and Cercignani-Lampis BCs.

BC	$\alpha_n$	$\omega$	$a$	$b \cdot 10$	$c$
Diffuse-specular	n/a	0.5	1.773	1.1660	0.6687
	n/a	0.81	1.773	1.4270	0.6238
	n/a	1	1.773	1.6370	0.5885
Cercignani-Lampis	0.25	0.5	1.774	0.7266	0.7127
		0.81	1.775	0.8889	0.6781
		1	1.776	1.0130	0.6516
Cercignani-Lampis	0.5	0.5	1.773	0.4772	0.7367
		0.81	1.774	0.5867	0.7069
		1	1.774	0.5742	0.6837
Cercignani-Lampis	0.75	0.5	1.772	0.2434	0.7597
		0.81	1.773	0.2915	0.7358
		1	1.773	0.3373	0.7164
Cercignani-Lampis	1.0	0.5	1.772	0.0218	0.7818
		0.81	1.766	0.0543	0.7370
		1	1.772	0.0000	0.7499

by Takata & Funagane, when analyzing the thermal transpiration based on the LBE of HS molecules [125]. Instead of the power-law divergence, they found logarithmic divergence of velocity gradient; that is, the spatial singularity is not stronger than  $\ln x$  in the vicinity of solid surface. This conclusion is confirmed by Jiang & Luo who, through the asymptotic analysis of BGK model [8], found that the velocity profile of Couette flow near the solid surface can be described by the following power series [60-61]:

$$u_s(x) = \sum_{n=0}^N \sum_{m=0}^M c_{n,m} x^n (x \ln x)^m, \quad x \rightarrow 0. \quad (7-7)$$

### 7.2.2.1 Influence of intermolecular potential

Figure 7-1 illustrates the KLFs obtained from the LBE with the diffuse BC, for the inverse power-law potential, the Lennard-Jones potential (??) of helium and xenon, and the shielded Coulomb potential (??). For the inverse power-law potential, the KLF increases with the viscosity index in the whole Knudsen layer. For the Lennard-Jones potential, the

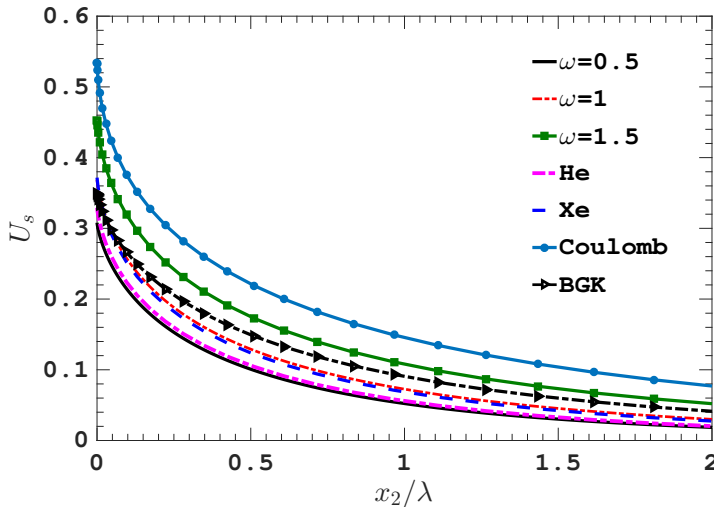


图 7-1 KLFs from the LBE solutions for the inverse power-law potentials, the Lennard-Jones potentials of Helium and Xenon when the gas temperature is 300K, and the shielded Coulomb potential of charged molecules when  $\epsilon = k_B T_w$ . The result from BGK equation is also included for comparison. The diffuse BC is used.

KLF of xenon molecules is larger than that of helium, but the results of both helium and xenon lie between those of HS and Maxwell molecules. This is comprehensible because the effective viscosity indexes of helium and xenon at a temperature of 300K are 0.66 and 0.85 [9], respectively. The KLF predicted by the BGK is even larger than that from the Maxwell molecules, but is smaller than that of  $\omega = 1.5$  where the gas molecules interact with soft potentials. The shielded Coulomb potential has the largest KLF, since its effective viscosity is close to 2.5 [20].

Thus, contrary to the VSC whose value is insensitive to the intermolecular potential, the KLF is strongly affected by the intermolecular potential. That is, when the effective viscosity index increases, (i) the value of the KLF increases, and (ii) the KLF decays more slowly, or equivalently, the Knudsen layer becomes wider. For example, at the solid surface, the relative difference between KLFs of Maxwell and HS molecules is approximate 20%, and that between the shielded Coulomb and HS potentials reaches 60%. Relative differences at distances one to two MFP away from the solid surface are even larger, say, when  $x_2/\lambda = 2$  the value of the KLF of the shielded Coulomb potential is about 4 times of that of HS potential. On the other hand, when  $u_s$  is decreased to 0.01 of its value at the solid surface, the corresponding distances to the solid surface for the HS and Maxwell molecules are about  $2.7\lambda$  and  $3.5\lambda$ , respectively.

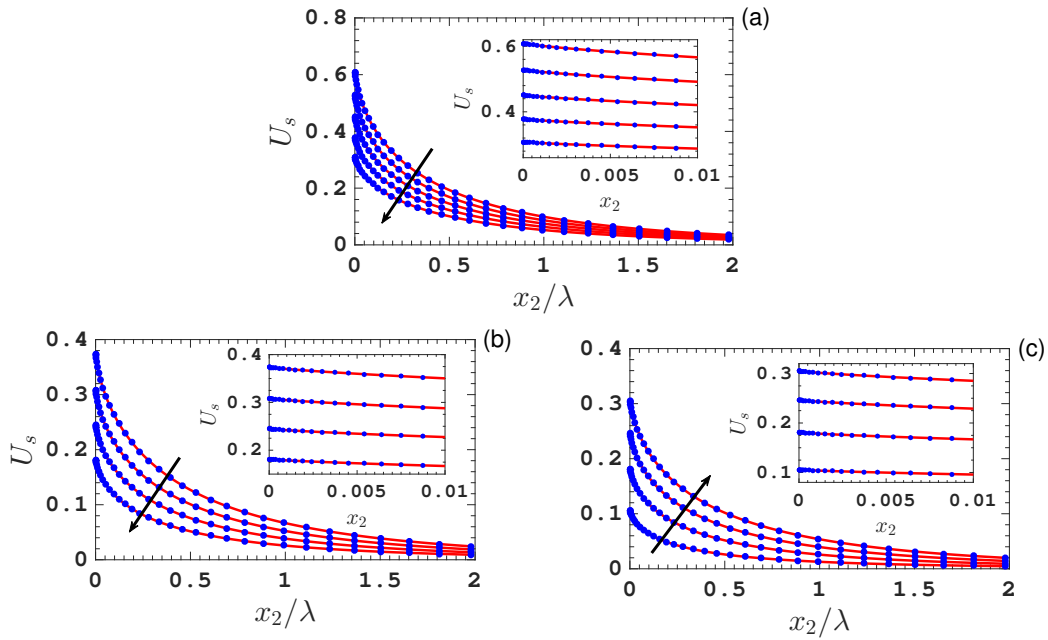


图 7-2 The KLF for HS molecules. (a) The diffuse-specular BC. Along the arrow,  $\alpha_M = 0.2, 0.4, 0.6, 0.8, 1$ . (b) The Cercignani-Lampis BC with  $\alpha_n = 0.25$ . Along the arrow,  $\alpha_t = 0.5, 1, 1.5$  and 2. (c) The Cercignani-Lampis BC with  $\alpha_t = 2$ . Along the arrow,  $\alpha_n = 0.25, 0.5, 0.75$  and 1. Dots: LBE solutions. Solid lines: fitted curves using Eq. (7-7) with  $M, N = 2$ . Insets: zoomed regions in the vicinity of the solid surface.

### 7.2.2.2 Influence of boundary condition

For the sake of clarity, we only focus on HS molecules. The diffuse-specular BC is shown in Fig. 7-2(a), where the KLF increases as  $\alpha_M$  decreases. Typical KLFs under Cercignani-Lampis BC are plotted in Figs. 7-2(b) and (c). When  $\alpha_n$  is fixed, for example, for  $\alpha_n = 0.25$ , the KLF decreases as  $\alpha_t$  increases. The relative reduction in  $u_s(x_2 = 0)$  is about 40% when  $\alpha_t$  rises from 0.25 to 1. However, the variation of the KLF with respect to  $\alpha_t$  becomes weaken as  $\alpha_n$  increases, such that at  $\alpha_n = 1$  the reduction in  $u_s(x_2 = 0)$  with  $\alpha_t$  falls below 3%. When  $\alpha_t (\neq 1)$  is fixed, the influence of  $\alpha_n$  on the KLF becomes larger when  $\alpha_n$  increases. And the greater the TMAC  $\alpha_t$  exceeds 1, the more pronounced the change in the KLF with  $\alpha_n$ . As an example, when  $\alpha_t = 2$ , the KLF is increased by three times, as the  $\alpha_n$  varies from 0.25 to 1, see Fig. 7-2(c).

### 7.2.2.3 Similarity in Knudsen layer function

We study the KLF normalized by its value on the solid surface  $x_2 = 0$ , when the HS molecules are used. Results of other types of molecules are similar. For Cercignani-Lampis BC, as can be seen from Fig. 7-3, when  $\alpha_n = 1$ , the maximum relative discrepancy for all  $\alpha_t$  is less than 10%. When  $\alpha_n$  decreases, however, the deviation of the

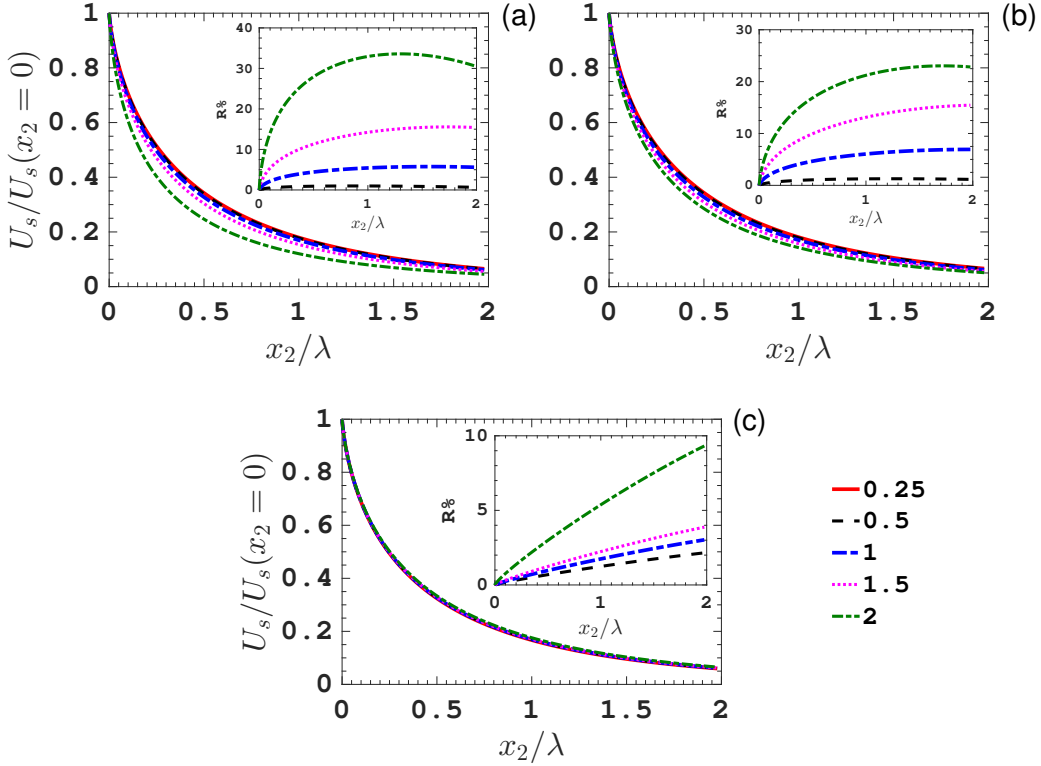


图 7-3 The rescaled KLF  $u_s/U_s(x_2 = 0)$  of HS molecules when (a)  $\alpha_n = 0.25$ , (b)  $\alpha_n = 0.5$ , and (c)  $\alpha_n = 1$ , when the Cercignani-Lampis BC with  $\alpha_t = 0.25, 0.5, 1.0, 1.5$ , and  $2.0$  are used. Inset: the relative difference ( $R\%$ ) of  $u_s/U_s(x_2 = 0)$  at various TMAC, when compared to that of  $\alpha_t = 0.25$ .

rescaled KLF between different  $\alpha_t$  increases. For instance, when  $\alpha_n = 0.25$ , the maximum relative difference for  $\alpha_t = 2$  is about 30%, as compared with  $\alpha_t = 0.25$ , see the inset in figure 7-3. Nevertheless, it should be noted that, for all  $\alpha_n$  with  $\alpha_t \leq 1$ , the relative difference of the rescaled KLF is less than 7%.

Approximately, the KLFs is defined to have similarity if the relative difference of the rescaled KLF for different TMAC is less than 10%. Therefore, the KLF has the similarity when the diffuse-specular BC and the Cercignani-Lampis BC with  $\alpha_n = 1$  are considered, in the full range of the effective TMAC; for Cercignani-Lampis BC with other values of  $\alpha_n$ , the similarity is preserved when  $\alpha_t \leq 1$ .

### 7.2.3 Comparison with experiments

Reynolds et al. measured the VSC and KLF for air passing along the surface of a highly polished aluminum plate [95], and found that the KLF is different from the results predicted by the BGK model. Loyalka pointed out that such discrepancy is due to the

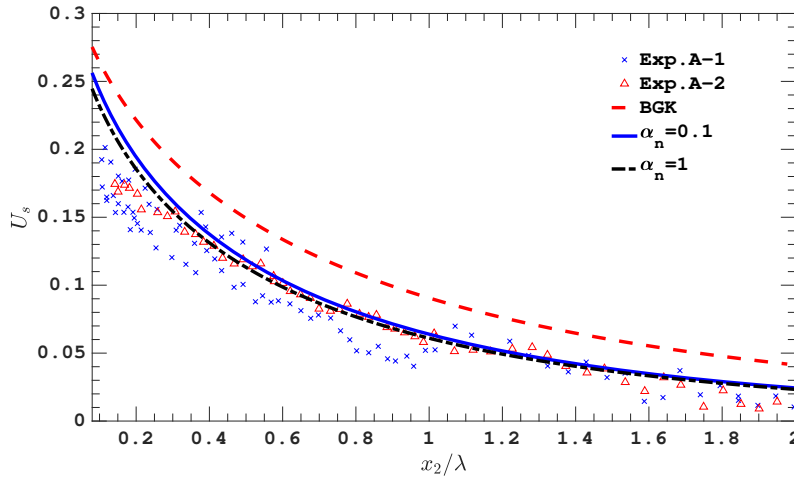


图 7-4 Comparisons of the KLFs between the experiments and the LBE solution with  $\alpha_t = 0.88$ , when the air molecules of  $\omega = 0.75$  and various  $\alpha_n$  are applied. Exp. A-1 and Exp. A-2 were measured by Reynolds et al. [95]. The diffuse-specular BC with  $\alpha_M = 0.88$  is used in the BGK model.

deficiency of BGK model, where the collision frequency does not depend on the molecular velocity; by using a kinetic model with a variable collision frequency, a reasonable agreement of the velocity profile with the experimental data was observed [67]. Given the apparent deficiency of kinetic models, results from the LBE of HS molecules were also compared with the experimental data [87]. However, all the previous works were based on the HS gas with an viscosity index of  $\omega = 0.5$ , while air has an effective viscosity index of 0.75 at room temperature. Moreover, the TMAC used in numerical simulations was unity, which results in a VSC of about one, while the measured TMAC has an average value of  $\sigma_P = 1.1$  (which has been adjusted by multiplying a factor of  $\sqrt{\pi}/2$ ).

We explain the experimental data using the LBE solutions for the inverse power-law potential with  $\omega = 0.75$ . Although air is a mixture of oxygen and nitrogen, we treat it as a single-species monatomic gas, since (i) the molecular masses of oxygen and nitrogen are close to each other and (ii) for isothermal flow the VSC is insensitive to the internal structure of gas molecules [146, 68].

Figure 7-4 shows the KLF obtained from the LBE with  $\alpha_t = 0.95$ , and  $\alpha_n = 0.1$  and 1 under the Cercignani-Lampis BC, as well as the experimental data. The result from the BGK equation is also included for comparison. We use the value of TMAC  $\alpha = 0.95$ , as our numerical calculation in the previous section suggests that the predicted VSC from the LBE agrees well with the experimental value of 1.1 [95]. It is found that the KLF changes slightly under different  $\alpha_n$ , and the results of  $\alpha_n = 1$  seems better than the others in the agreement with the experimental data, while the solution of the BGK equation has a

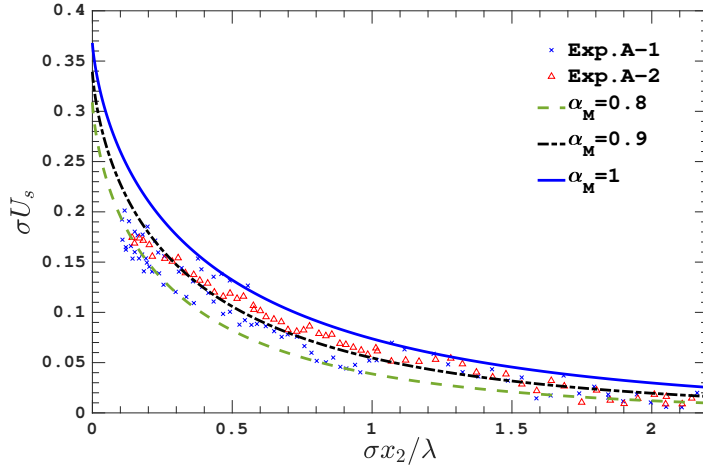


图 7-5 Comparisons of the KLF between the experiments and the LBE solution with  $\alpha_M = 0.8, 0.9$  and  $1$ , when the air molecules with  $\omega = 0.75$  are used. LBE results are scaled by a factor  $\sigma = \sigma_{P,Exp}/\sigma_P(\alpha_M)$ , where  $\sigma_{P,Exp} = 1.1$  is the average VSC from the experiments [95].

visible deviation from the experimental results. Note that when using the diffuse-specular BC, similar results can also be obtained for  $\alpha_M = 0.95$ .

We note that the KLF from the experiments are scattered, which is inconsistent with the theoretical analysis that the normalized velocity near the solid surface should be independent of the MFP and shear gradient. Reynolds et al. [95] argued that the most possible reason was the inaccurate determination of the MFP. Therefore, intuitively, in order to interpret the experimental results, one should take this factor into account. To this end, we first assume the actual TMAC for the interaction of air with the polished aluminum plate is  $\alpha_M$  in the diffuse-specular BC. Then we calculate the VSC  $\sigma_P(\alpha_M)$  from the LBE. If  $\sigma_{P,Exp} < \sigma_P(\alpha_M)$ , the MFP in the experiment has been overestimated due to the inaccurate measuring of the gas pressure. Therefore, the value of the KLF from the experiment [95] should be multiplied by  $1/\sigma = \sigma_P(\alpha_M)/\sigma_{P,Exp}$ , while the width of the KLF should be stretched by a factor of  $1/\sigma$ . In the numerical simulation, various values of  $\alpha_M$  are attempted, until good agreement between the results of experiment and numerical simulation are achieved.

To show all the results in one figure, however, the KLF  $u_s(x_2)$  obtained from the numerical simulation of the LBE has been rescaled to  $\sigma u_s(\sigma x_2)$ . Comparisons between the numerical and experimental results are depicted in Fig. 7-5. It is seen that, when the TMAC varies from 0.8 to 1, the results of LBE can cover almost all the experimental data. In other words, the TMAC of the aluminum plate used in the air experiments is most likely  $0.9 \pm 0.1$ . If the TMAC is 0.9, we have  $\sigma = 0.9$ , this means that the MFP in the experiment is overestimated by 10%, which seems reasonable due to the accuracy of

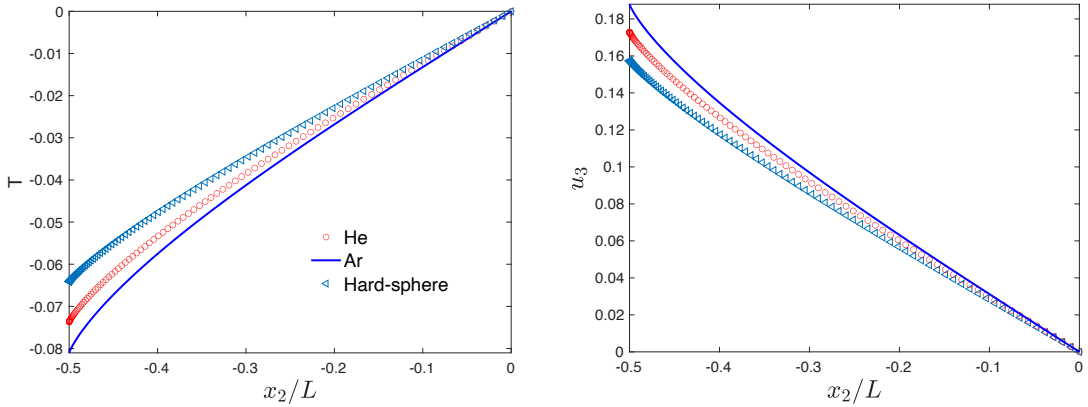


图 7-6 Normalized density (velocity) in the planar Fourier (Couette) flow [143], obtained from the LBE with the collision kernel directly calculated from the Lennard-Jones potential. Results from the HS gas are shown for comparison. The rarefaction parameter is  $\delta_{rp} = 0.1$ .

the micro-manometers at that time.

### 7.3 Planar Fourier flows

Consider the Fourier heat conduction between two plates located at  $x_2 = -0.5$  and  $x_2 = 0.5$ , where the temperature is  $T_0 - \Delta T/2$  and  $T_0 + \Delta T/2$ , respectively. The temperature difference  $\Delta T$  is negligible compared to  $T_0$ , so that the Boltzmann equation (4-10) is linearized to Eq. (4-49) by choosing as  $\beta = \Delta T/T_0$ . Assuming diffuse BC, the VDF reflected from the wall reads

$$h = \left[ 1 - \frac{v^2}{2} - 2\sqrt{\pi} \int_{v_2 < 0} v_2 h(v, x_2 = -0.5) dv \right] f_{eq}, \quad (7-8)$$

while at  $x_2 = 0$ , the symmetry leads to  $h(v_1, v_2, v_3) = -h(v_1, -v_2, v_3)$ .

Figure 7-6 shows the density when  $\delta_{rp} = 0.1$  and  $T_0 = 300$  K; the temperature has similar behavior (not shown). The influence of intermolecular potential is clearly seen, e.g., the density of Xe at the wall is 40% larger than that of the HS gas. As  $\delta_{rp}$  increases, the difference decreases, which eventually disappears in near-continuum flow. Interestingly, differences in heat flux between various gases is small over the whole range of rarefaction parameter.

### 7.4 Thermal transpiration

Thermal transpiration, where the gas moves towards a hotter region even in the absence of a pressure gradient, is one of the fundamental problems in RGD [96, 74]. The

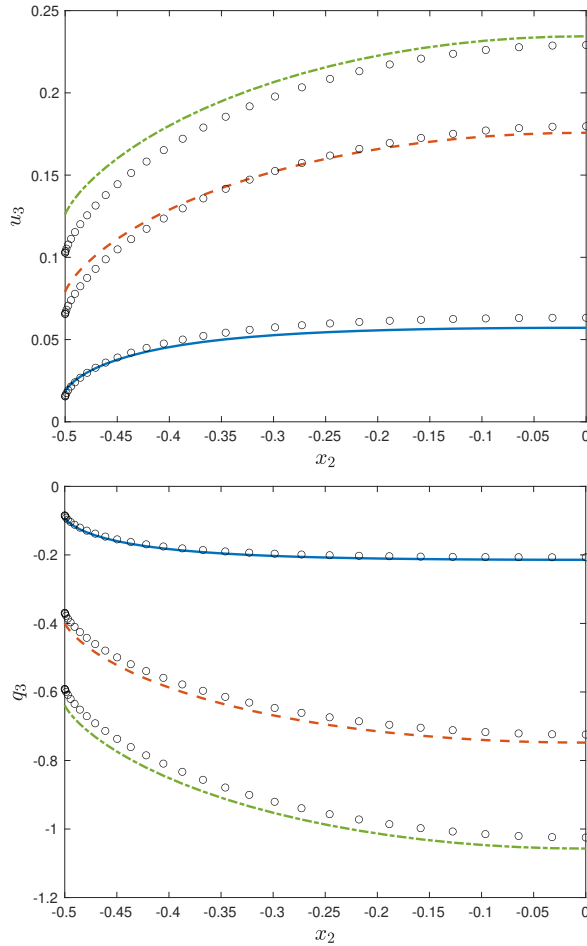


图 7-7 Profiles of velocity and heat flux in the thermal transpiration between two parallel plates. Solid, dashed, dash-dotted lines are the results of HS gas, when  $\text{Kn} = 0.1, 0.5$ , and  $1$ , respectively, while circles are the corresponding results of Maxwell gas.

gas pressure is maintained constant, while the wall temperature varies linearly in the  $x_3$  direction as

$$T = T_0 \left( 1 + \beta_T \frac{x_3}{L} \right), \quad \beta_T = \frac{L}{T_0} \frac{dT}{dx_3}, \quad (7-9)$$

where the dimensionless temperature gradient  $\beta_T$  is very small. The Boltzmann equation can be linearized around the equilibrium state, when  $h$  in Eq. (4-47) is replaced by  $h + x_3 f_{eq} (\nu^2 - \frac{5}{2})$ , resulting

$$\nu_1 \frac{\partial h}{\partial x_1} + \nu_2 \frac{\partial h}{\partial x_2} = \mathcal{L}^+(h) - \nu_{eq} h - \nu_3 \left( \nu^2 - \frac{5}{2} \right) f_{eq}. \quad (7-10)$$

The MFR and HFR are expressed as

$$\begin{aligned} \dot{M} &= \frac{2p_0 S}{\nu_m} \beta_T G_T, \quad G_T = \frac{1}{A} \iiint \nu_3 h dx_1 dx_2 d\nu, \\ \dot{E} &= -p_0 \nu_m S \beta_T Q_T, \quad Q_T = -\frac{1}{A} \iiint \left( \nu^2 - \frac{5}{2} \right) \nu_3 h dx_1 dx_2 d\nu. \end{aligned} \quad (7-11)$$

Typical profiles of the velocity and heat flux are shown in Fig. 7-7, whose magnitudes increase with the Knudsen number. Again, it is observed that although the Knudsen number is the same, different intermolecular potential (viscosity index) has different macroscopic profiles.

For the rectangular cross-section, the mass flow rate is  $G_T = \mathcal{M}/2$  and the heat flow rate in the free-molecular flow regime [70] is  $G_T = 9\mathcal{M}/4$ , where  $\mathcal{M}$  is given by Eq. (7-19).

## 7.5 Poiseuille flow

Consider an infinite long channel of a cross-section area  $S$  located in the  $x_1x_2$  plane. The gas inside is subject to a uniform pressure gradient in the  $x_3$  direction:

$$p = p_0 \left(1 + \beta_p \frac{x_3}{L}\right), \quad \beta_p = \frac{L}{p_0} \frac{dp}{dx_3}, \quad (7-12)$$

and the dimensionless pressure gradient  $\beta_p$  is very small. Both the wall and gas temperature are kept at  $T_0$ . The mass flow rate (MFR) and heat flow rate (HFR), are defined as

$$\dot{M} = n_0 m \iint u_3(x_1, x_2) dx_1 dx_2, \quad \dot{E} = \iint q_3(x_1, x_2) dx_1 dx_2. \quad (7-13)$$

The Boltzmann equation can be linearized around the equilibrium state, when  $h$  in Eq. (4-47) is replaced by  $h + x_3 f_{eq}$ , resulting

$$v_1 \frac{\partial h}{\partial x_1} + v_2 \frac{\partial h}{\partial x_2} = \mathcal{L}^+(h) - v_{eq} h - v_3 f_{eq}. \quad (7-14)$$

Note that here the macroscopic variables and VDF have been normalized, so that the MFT and HFR are expressed as

$$\dot{M} = -\frac{2p_0 S}{v_m} \beta_p G_P, \quad \dot{E} = p_0 v_m S \beta_p Q_p, \quad (7-15)$$

with the normalized MFT and HFR

$$G_P = -\frac{1}{A} \iint u_3 dx_1 dx_2 \equiv -\frac{1}{A} \iiint v_3 h dx_1 dx_2 d\mathbf{v},$$

$$Q_p = \frac{1}{A} \iint q_3 dx_1 dx_2 \equiv \frac{1}{A} \iiint \left(v^2 - \frac{5}{2}\right) v_3 h dx_1 dx_2 d\mathbf{v}, \quad (7-16)$$

where  $A = S/L^2$ .

### 7.5.0.1 Poiseuille flow between parallel plates

Consider the Poiseuille flow between two plates located at  $x_2 = \pm 1/2$ . The spatial region is divided into  $N_s = 50$  non-uniform cells, as

$$x = (10 - 15s + 6s^2)s^3, \quad (7-17)$$

with  $s = (0, 1, \dots, N_s)/N_s$ . Such a non-uniform discretization has refined grids in the vicinity of solid walls, hence helps to capture the Knudsen layer structure. Because of symmetry, we only consider the half spatial region  $-1/2 \leq x_2 \leq 0$  with the specular-reflection BC being imposed at  $x_2 = 0$ . The diffuse BC is adopted at the wall:

$$h(x_2 = -1/2, v_2 > 0) = 0. \quad (7-18)$$

The maximum molecular velocity is  $L_v = 6$ . Because of the symmetry and smoothness of the VDF in  $v_1 (> 0)$  and  $v_3 (> 0)$  directions,  $12 \times 12$  uniform grids are used. In the discretization of  $v_2$ ,  $N_v = 64$  nonuniform velocity grids (4-36) with  $\iota = 3$  are used to resolve the over-concentration of VDF at large Knudsen numbers. The number of frequency components in the  $\xi_1$  and  $\xi_3$  directions are 24. Although we use  $N_v$  nonuniform velocity grids in  $v_2$  direction, the corresponding frequency domain is divided into 32 equidistant points. In the approximation of the kernel mode (4-28), the Gauss-Legendre quadrature with  $M = 10$  is used. The Matlab code is given in Appendix ??, where besides the CIS, the general synthetic iterative scheme [147, 119] detailed in Chapter 6 is implemented to find the steady-state solution efficiently and accurately.

Typical profiles of the velocity and heat flux are shown in Fig. 7-8. When  $\text{Kn} = 0.1$ , the velocity is large. The velocity profile becomes flatter when the Knudsen number increases, due to the increased friction between gas molecules. When the Knudsen number is larger than 1, however, the velocity slip at the solid wall increases, which compensates the friction. As a result, a minimum MFR around  $\text{Kn} \sim 1$  appears, which is known as the Knudsen minimum. The HFR always increases with the Knudsen number.

At large Knudsen number, the MFR and HFR are sensitive to the intermolecular potential (reflected through the viscosity index  $\omega$ ), even when the Knudsen number is fixed. That is, the smaller the viscosity index, the larger the mass and heat flow rates.

Because of the “over-concentration” in VDF [124], numerical simulation of highly rarefied gas flows is a difficult task; for a long time the accurate numerical results have been limited to HS molecules when  $\text{Kn} \lesssim 20$  [86, 21]. With FSM, the LBE can be solved accurately and efficiently up to  $\text{Kn} \sim 10^6$ . Typical VDF profiles demonstrating the over-

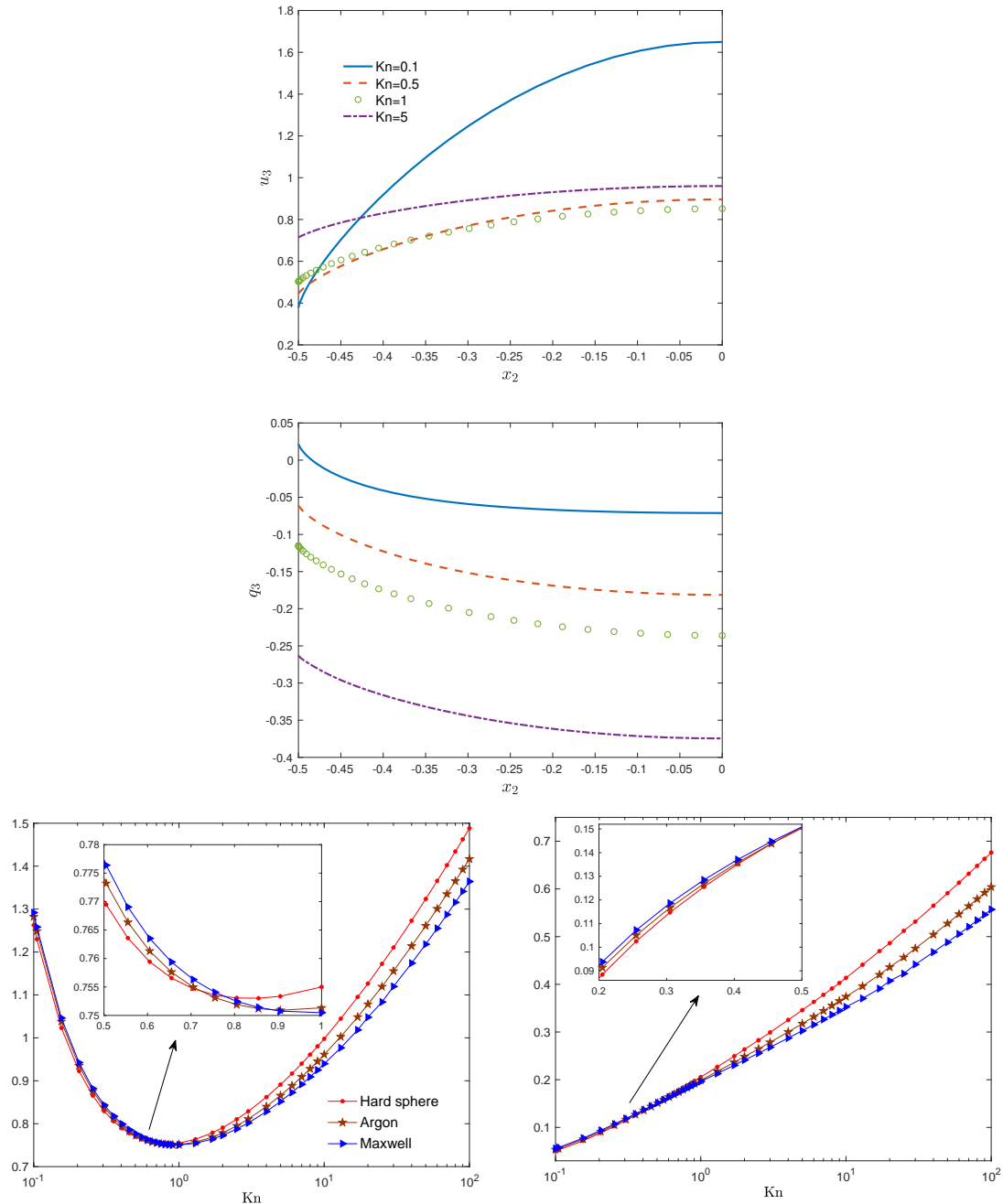


图 7-8 Poiseuille gas flow between parallel plates. (Top row) Velocity and heat flux in the HS gas. (Bottom row) Comparisons in MFR (left) and HFR (right) for different inverse power-law potentials [144]. The viscosity index for argon is  $\omega = 0.81$ .

concentration phenomena are shown in Fig. 7-9. When  $\text{Kn} = 1$ , the marginal VDF is roughly proportional to  $\exp(-v_2^2)$ . However, in the free-molecular regime, the marginal VDF has a long tail, and its width shrinks drastically as  $1/\text{Kn}$ , while its amplitude scales as  $\text{Kn}$ . If the velocity discretization is not refined around  $v_2 \sim 0$ , the calculated flow rates will be wrong.

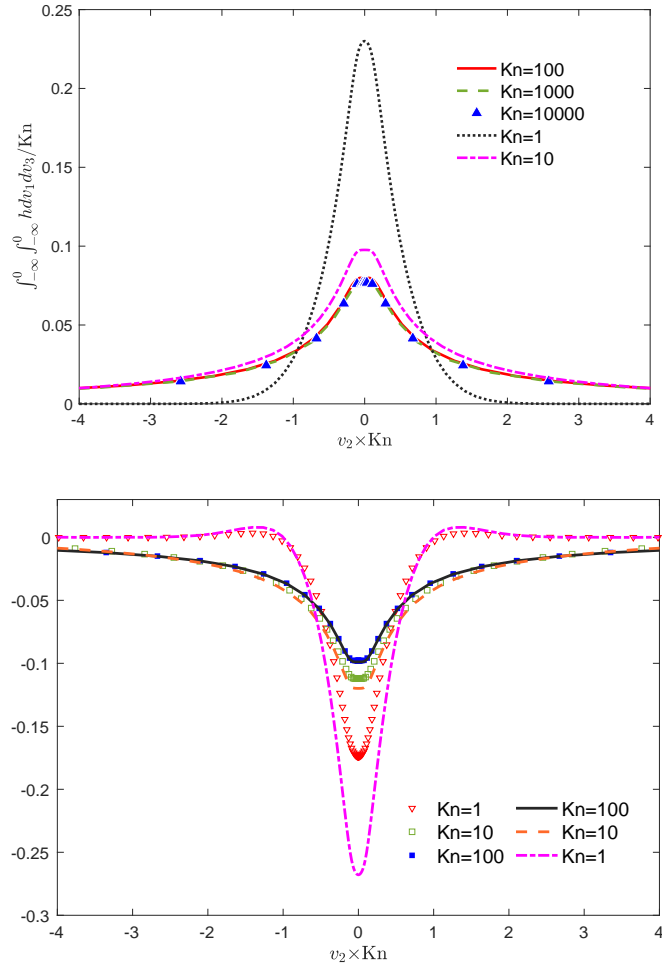


图 7-9 (Top) The marginal VDF in the Poiseuille flow at the channel center. When  $Kn \geq 100$ , the velocity distribution perpendicular to the plate shrinks as  $1/Kn$ , which is known as the “over-concentration” [124]. (Bottom) The Onsager-Casimir relation at the mesoscopic level. Symbols: the marginal VDFs  $\int_{-\infty}^0 \int_{-\infty}^0 h dv_1 dv_3 / Kn$ , where  $h$  is obtained in the thermal transpiration. Lines: the marginal VDFs  $\int_{-\infty}^0 \left(v^2 - \frac{5}{2}\right) h dv_1 dv_3 / Kn$ , where  $h$  is obtained in the Poiseuille flow.

### 7.5.0.2 Poiseuille flow through a long duct

Consider the Poiseuille flow in a long duct with the aspect ratio  $A = S/L^2$ , under the diffuse BC. Unlike the Poiseuille flow between parallel plates where the flow rates increase logarithmically at large  $Kn$ , here they saturate at  $G_P = \mathcal{M}$  and  $Q_P = \mathcal{M}/2$  when  $Kn \rightarrow \infty$  [70], where

$$\begin{aligned} \mathcal{M} = \frac{1}{4\sqrt{\pi}} & \left[ \frac{2(A^3 + 1)}{3A} - \frac{2(A^2 + 1)^{3/2}}{3A} \right. \\ & \left. + \ln \frac{(A^2 + 1)^{1/2} + A}{(A^2 + 1)^{1/2} - A} + A \ln \frac{(A^2 + 1)^{1/2} + 1}{(A^2 + 1)^{1/2} - 1} \right]. \end{aligned} \quad (7-19)$$

Nice agreement in the mass and heat flow rates of HS gas between the FSM and numerical kernel method are observed in Table 7-3. To show the numerical efficiency we

表 7-3 MFR and HFR in the Poiseuille flow of HS gas through a rectangular channel [139]. Note that  $\text{Kn} = 5\pi k'/16$ .

$A = 1$				$A = 2$				
FSM		Doi [21]		FSM		Doi [21]		
$k'$	$G_P$	$Q_P$	$G_P$	$Q_P$	$G_P$	$Q_P$	$G_P$	$Q_P$
0.1	0.6116	0.0445	0.613	0.045	0.9009	0.0476	0.905	0.048
0.3	0.4260	0.0889	0.426	0.089	0.5950	0.1013	0.595	0.101
0.5	0.3960	0.1103	0.396	0.110	0.5433	0.1301	0.544	0.130
0.8	0.3833	0.1280	0.383	0.128	0.5203	0.1554	0.520	0.156
1	0.3811	0.1356	0.381	0.136	0.5141	0.1664	0.515	0.167
3	0.3835	0.1656	0.383	0.166	0.5148	0.2131	0.516	0.214
5	0.3886	0.1760	0.388	0.176	0.5228	0.2300	0.523	0.230
8	0.3938	0.1837	0.394	0.184	0.5314	0.2428	0.532	0.243
10	0.3963	0.1869	0.396	0.187	0.5354	0.2481	0.536	0.248
20	0.4033	0.1948	-	-	0.5479	0.2613	-	-
50	0.4102	0.2016	-	-	0.5596	0.2734	-	-
$10^2$	0.4136	0.2048	-	-	0.5657	0.2791	-	-
$10^3$	0.4183	0.2089	-	-	0.5742	0.2865	-	-
$10^4$	0.4191	0.2095	-	-	0.5758	0.2878	-	-
$\infty^{\circledR}$	0.4194	0.2097	0.4194	0.2097	0.5762	0.2881	0.5762	0.2881

consider the HS gas inside a square channels; with a  $25 \times 25$  spatial cells,  $32 \times 32 \times 24$  frequency components, and  $M = 6$ , the flow rates at  $\text{Kn}_{vhs} = 1$  and 10 are obtained in about 1 minute, when our Fortran code runs on a single core of an Intel Q9650 (3.0 GHz Core 2 Quad processor), while the low-noise DSMC takes respectively 66 and 12 minutes [21, 92].

### 7.5.1 Onsager-Casimir relation

The Onsager-Casimir relation states that the MFR in the thermal transpiration is equal to the HFR in the Poiseuille flow. In the numerical simulation we find that this relation is held with the absolute error smaller than  $10^{-4}$ .

Takata and Funagane [124] made the important observation that at large  $\text{Kn}$ ,  $u_3[h_T]$

and  $q_3[h_P]$  are even identical at the level of spatial profile:

$$u_3[h_T] = q_3[h_P] + O\left(\frac{(\ln \text{Kn})^2}{\text{Kn}}\right). \quad (7-20)$$

Our numerical results in Fig. 7-9 further show that the agreement is even at the mesoscopic level:

$$h_T \approx \left(v^2 - \frac{5}{2}\right) h_P. \quad (7-21)$$

## 7.6 Influence of intermolecular potential

Note that except for the HS gas, the collision kernels in the previous chapter are modeled to recover the shear viscosity, rather than calculated directly from the intermolecular potential. Here we extend the FSM to solve the LBE with the collision kernel directly calculated from the Lennard-Jones potential (??), rather than using the modeled kernel (4-8).

The numerical results in Table 7-4 shows that different parameters in the Lennard-Jones potential (??) lead to different flow rate, especially when the rarefaction parameter is small.

## 7.7 Cercignani-Lampis boundary condition

We present the LBE solutions for the Poiseuille flow between two plates and through a circular cross section [145]. Although this classical problem has been investigated extensively, accurate numerical results based on the LBE and the Cercignani-Lampis BC is scarce.

### 7.7.1 Poiseuille flow through parallel plates

Table 7-5 shows the flow rates for HS molecules. When the rarefaction parameter  $\delta_{rp}$  and the EAC  $\alpha_n$  are fixed, the MFR increases rapidly when the TMAC  $\alpha_t$  decreases. However, the influence of  $\alpha_n$  on MFR is limited.

The variation of HFR with respect to  $\alpha_n$  and  $\alpha_t$  is complicated. First, when  $\alpha_n$  and  $\delta_{rp}$  are fixed, the HFR increases slightly with  $\alpha_t$  when  $\delta_{rp}$  is large, while it increases with decreasing  $\alpha_t$  when  $\delta_{rp}$  is small. Second, when  $\alpha_t = 1$  and  $\delta_{rp}$  is fixed, the HFR does not change with  $\alpha_n$ : in fact, in this case the Cercignani-Lampis BC is reduced to the diffuse BC [102]. Third, when  $\alpha_t (\neq 1)$  and  $\delta_{rp}$  are fixed, the HFR increases slightly with  $\alpha_n$  when  $\delta_{rp}$  is large, but it increases with decreasing  $\alpha_n$  when  $\delta_{rp}$  small.

表 7-4 Mass flow rate  $G_P$  and heat flow rate  $Q_P$  in the Poiseuille flow between parallel infinite plates, when the Lennard-Jones potential is considered [143].

$\delta_{rp}$	He		Ne		Ar		Kr		Xe	
	$G_P$	$Q_P$								
0.01	2.713	1.152	2.607	1.070	2.535	1.057	2.538	1.065	2.547	1.072
0.02	2.432	1.021	2.362	0.961	2.292	0.930	2.286	0.933	2.290	0.938
0.025	2.348	0.981	2.289	0.929	2.219	0.893	2.211	0.894	2.214	0.898
0.04	2.180	0.900	2.141	0.862	2.076	0.819	2.063	0.815	2.064	0.818
0.05	2.105	0.863	2.074	0.831	2.011	0.785	1.998	0.780	1.998	0.782
0.10	1.892	0.749	1.879	0.732	1.829	0.688	1.815	0.679	1.813	0.679
0.20	1.713	0.637	1.708	0.629	1.677	0.596	1.666	0.586	1.663	0.584
0.25	1.665	0.601	1.661	0.595	1.636	0.566	1.626	0.557	1.624	0.555
0.40	1.581	0.526	1.579	0.523	1.564	0.504	1.558	0.497	1.556	0.495
0.50	1.550	0.491	1.549	0.489	1.539	0.474	1.534	0.468	1.532	0.466
1.00	1.505	0.385	1.505	0.384	1.505	0.380	1.505	0.378	1.505	0.377
1.60	1.532	0.315	1.533	0.315	1.537	0.315	1.540	0.316	1.541	0.315
2.00	1.568	0.282	1.568	0.283	1.575	0.285	1.579	0.286	1.580	0.286
2.50	1.622	0.251	1.623	0.251	1.630	0.254	1.636	0.256	1.637	0.257
4.00	1.817	0.188	1.818	0.189	1.828	0.193	1.835	0.196	1.838	0.197
5.00	1.960	0.161	1.961	0.162	1.972	0.166	1.980	0.169	1.983	0.170
10.0	2.732	0.093	2.732	0.093	2.743	0.097	2.752	0.099	2.756	0.100

The influence of intermolecular potential is visualized in Fig. 7-10, where we choose xenon and helium, as the results of other noble gases are similar. Large difference is found at small rarefaction parameter. For example, when  $\delta_{rp} = 0.01$ , the relative differences in the MFR and HFR between HS gas and xenon are about 12% and 23%, respectively, when the Cercignani-Lampis BC with  $\alpha_n = 1$  and  $\alpha_t = 0.75$  is used.

Figure 7-10(c) shows the exponent of thermalmolecular pressure difference (TPD), which is an important parameter determining the performance of a Knudsen pump. In the range of  $\delta_{rp}$  considered, the HS gas has the largest TPD, while xenon has the smallest. This difference increases when  $\delta_{rp}$  decreases. In the Cercignani-Lampis BC, when  $\delta_{rp}$  is fixed, the TPD exponent decreases with  $\alpha_t$ . In the diffuse BC, when the TMAC  $\alpha_M$  decreases, the TPD exponent decreases at large values of  $\delta_{rp}$ , but at free-molecular flow

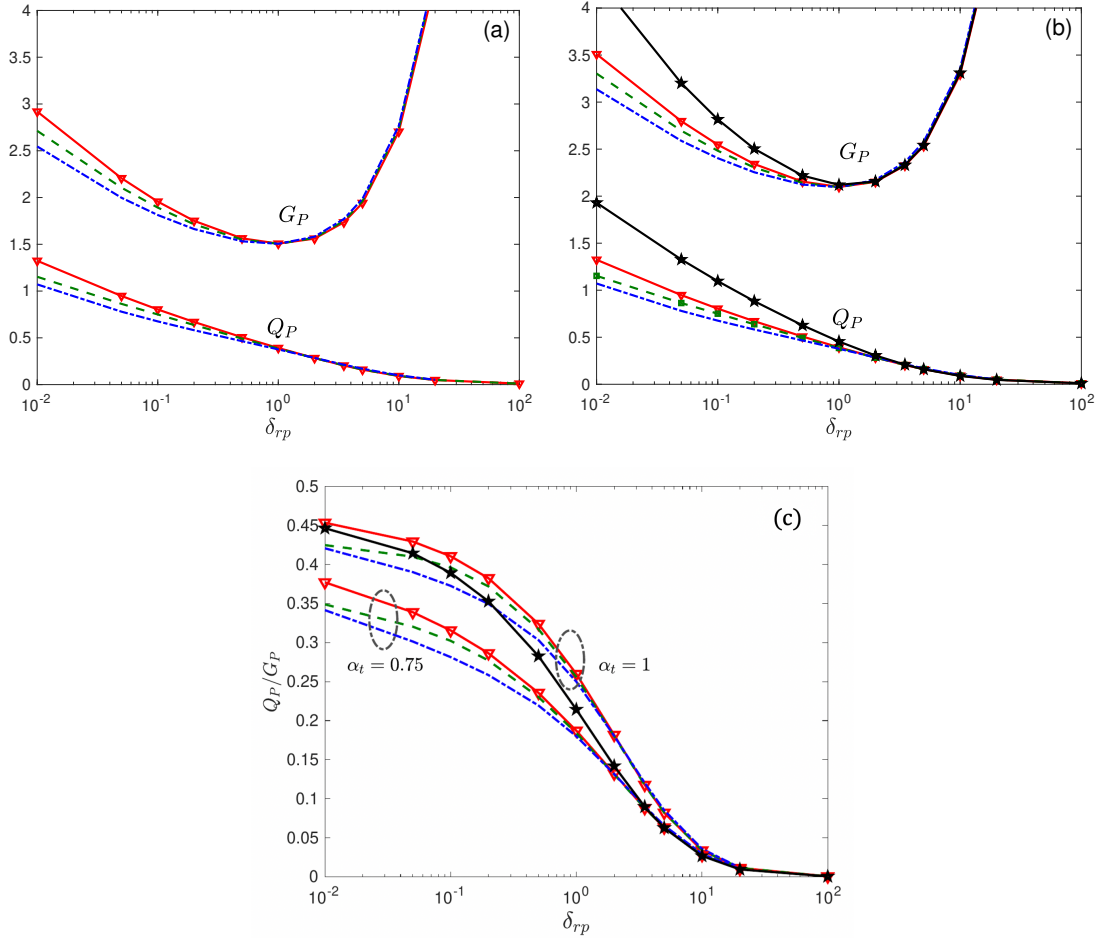


图 7-10 Flow rates in the Poiseuille flow between two parallel plates [145]. Triangles: HS gas. Dashed lines: He. Dash-dotted lines: Xe. When the Lennard-Jones potential is used, the wall temperature is  $T_w = 300$  K. In the Cercignani-Lampis BC,  $\alpha_n = 1$ , (a)  $\alpha_t = 1$  and (b)  $\alpha_t = 0.75$ . In the Maxwell BC,  $\alpha_M = 0.75$  is used (Pentagrams). (c) The exponent of thermal pressure difference, i.e., the ratio of MFR  $G_T/G_P$ , or  $Q_P/G_P$  as per the Onsager-Casimir relation. regime,  $\alpha_M$  does not have any influence on the TPD exponent.

### 7.7.2 Poiseuille flow through long tube

For flows through circular cross sections, the polar coordinates can be applied to reduce the computational cost. Introducing the polar coordinates in the spatial space

$$x_1 = r \cos \theta, \quad x_2 = r \sin \theta \quad (7-22)$$

and the cylindrical coordinates in the molecular velocity space

$$v_1 = v_r \cos \theta, \quad v_2 = v_r \sin \theta, \quad (7-23)$$

and defining the VDF as  $h = h(r, \theta, v_r, v_3)$ , the LBE can be written as:

$$v_1 \frac{\partial h}{\partial r} - \frac{v_2}{r} \frac{\partial h}{\partial \theta} = \mathcal{L}^+(h) - v_{eq}h - v_3 f_{eq}. \quad (7-24)$$

In the numerical simulation,  $r$  is discretized by 150 nonuniform points, with most points located near the pipe surface  $r = 1$ . Due to symmetry, the truncated velocity  $v_r \in (0, 4)$  is discretized by 64 nonuniform points, with most points located near  $v_r = 0$  to capture the discontinuities in the VDF, while  $\theta \in [0, \pi]$  and  $v_3 \in (0, 6)$  are discretized by 40 and 12 uniform points, respectively.

The FSM is implemented in the following way [147]: first, the spectrum of the VDF is calculated by Fourier transform from the cylindrical molecular velocity space to the Cartesian frequency space, where the frequency are uniformly discretized. This is more expansive than the use of non-uniform velocity grids in Cartesian coordinates (see Section ??). Second, the FSM is applied to find the spectrum of the linearized BCO in the Cartesian coordinate. Finally, the inverse Fourier transform is used to find the collision operator in the cylindrical space.

The MFR and HFR of the HS molecules through a long tube are shown in Table 7-6. The influence of BC exists, but is not as large as that between parallel plates. This is because, in the free-molecular flow regime, the flow rates in tube flow are constant, while that between parallel plates increase logarithmically with the Knudsen number.

表 7-5 Dimensionless flow rates in the Poiseuille flow of HS molecules between two parallel plates [145]. The Cercignani-Lampis BC is used, but the data in the last two columns are from the Maxwell BC.

$\delta_{rp}$	$\alpha_t$	$G_P$	$Q_P$	$G_P$	$Q_P$	$G_P$	$Q_P$	$G_P$	$Q_P$	$G_P$	$Q_P$
		$\alpha_n=0.25$		$\alpha_n=0.5$		$\alpha_n=0.75$		$\alpha_n=1$		$\alpha_M = \alpha_t$	
0.01	0.5	5.115	1.699	4.871	1.499	4.752	1.390	4.684	1.322	6.844	2.991
	1	2.911	1.320	2.911	1.320	2.911	1.320	2.911	1.320	2.911	1.320
	1.5	2.084	1.122	2.196	1.205	2.265	1.265	2.320	1.319		
0.1	0.5	3.996	1.098	3.854	0.953	3.774	0.866	3.724	0.807	4.389	1.570
	1	1.951	0.801	1.951	0.801	1.951	0.801	1.951	0.801	1.951	0.801
	1.5	1.200	0.634	1.270	0.699	1.319	0.749	1.360	0.796		
0.2	0.5	3.710	0.906	3.616	0.798	3.558	0.726	3.519	0.675	3.907	1.211
	1	1.747	0.667	1.747	0.667	1.747	0.667	1.747	0.667	1.747	0.667
	1.5	1.037	0.525	1.086	0.577	1.123	0.620	1.156	0.661		
1	0.5	3.308	0.458	3.297	0.435	3.288	0.415	3.280	0.398	3.327	0.529
	1	1.507	0.389	1.507	0.389	1.507	0.389	1.507	0.389	1.507	0.389
	1.5	0.894	0.336	0.901	0.351	0.908	0.366	0.915	0.381		
2	0.5	3.340	0.300	3.339	0.296	3.338	0.292	3.337	0.288	3.347	0.328
	1	1.564	0.281	1.564	0.281	1.564	0.281	1.564	0.281	1.564	0.281
	1.5	0.970	0.265	0.971	0.268	0.971	0.272	0.972	0.275		
10	0.5	4.522	.0834	4.514	.0861	4.508	.0887	4.503	.0912	4.535	.0843
	1	2.729	.0900	2.729	.0900	2.729	.0900	2.729	.0900	2.729	.0900
	1.5	2.120	.0962	2.127	.0938	2.133	.0913	2.138	.0889		
20	0.5	6.162	.0437	6.151	.0454	6.142	.0470	6.133	.0485	6.177	.0437
	1	4.360	.0480	4.360	.0480	4.360	.0480	4.360	.0480	4.360	.0480
	1.5	3.743	.0519	3.752	.0505	3.761	.0490	3.769	.0474		
100	0.5	19.47	.0091	19.45	.0094	19.44	.0098	19.43	.0102	19.49	.0090
	1	17.66	.0101	17.66	.0101	17.66	.0101	17.66	.0101	17.66	.0101
	1.5	17.03	.0110	17.05	.0107	17.06	.0103	17.07	.0100		

表 7-6 Dimensionless flow rates in the Poiseuille flow of HS molecules through a circular tube, using the Cercignani-Lampis BC. The characteristic length  $L$  is the radius of circular cross section [145].

$\delta_{rp}$	$\alpha_t$	$G_P$	$Q_P$	$G_P$	$Q_P$	$G_P$	$Q_P$	$G_P$	$Q_P$
		$\alpha_n=0.25$		$\alpha_n=0.5$		$\alpha_n=0.75$		$\alpha_n=1$	
0.01	0.5	3.363	0.989	3.321	0.881	3.295	0.809	3.277	0.759
	1	1.472	0.725	1.472	0.725	1.472	0.725	1.472	0.725
	1.5	0.809	0.584	0.825	0.620	0.840	0.657	0.855	0.697
0.1	0.5	3.251	0.837	3.227	0.763	3.210	0.709	3.198	0.669
	1	1.397	0.634	1.397	0.634	1.397	0.634	1.397	0.634
	1.5	0.753	0.516	0.763	0.545	0.773	0.574	0.784	0.607
0.5	0.5	3.181	0.574	3.176	0.553	3.172	0.536	3.169	0.520
	1	1.381	0.492	1.381	0.492	1.381	0.492	1.381	0.492
	1.5	0.767	0.432	0.770	0.443	0.772	0.455	0.775	0.468
1	0.5	3.233	0.432	3.232	0.429	3.231	0.426	3.230	0.423
	1	1.448	0.403	1.448	0.403	1.448	0.403	1.448	0.403
	1.5	0.845	0.379	0.847	0.380	0.847	0.383	0.848	0.385
2	0.5	3.423	0.295	3.420	0.300	3.418	0.305	3.417	0.309
	1	1.639	0.298	1.639	0.298	1.639	0.298	1.639	0.298
	1.5	1.038	0.301	1.040	0.297	1.042	0.293	1.043	0.288
5	0.5	4.113	0.152	4.105	0.157	4.098	0.162	4.093	0.167
	1	2.319	0.164	2.319	0.164	2.319	0.164	2.319	0.164
	1.5	1.708	0.175	1.715	0.170	1.721	0.165	1.726	0.161
10	0.5	5.333	.0835	5.322	.0868	5.313	.0899	5.305	.0929
	1	3.531	.0917	3.531	.0917	3.531	.0917	3.531	.0917
	1.5	2.913	.0992	2.923	.0963	2.932	.0934	2.939	.0904
20	0.5	7.815	.0437	7.802	.0456	7.791	.0472	7.782	.0489
	1	6.007	.0484	6.007	.0484	6.007	.0484	6.007	.0484
	1.5	5.385	.0527	5.396	.0511	5.406	.0495	5.416	.0479
50	0.5	15.30	.0179	15.28	.0187	15.27	.0194	15.26	.0201
	1	13.49	.0200	13.49	.0200	13.49	.0200	13.49	.0200
	1.5	12.86	.0218	12.87	.0212	12.89	.0205	12.89	.0198
100	0.5	27.78	.0090	27.77	.0094	27.75	.0098	27.74	.0101
	1	25.97	.0101	25.97	<sup>118</sup> .0101	25.97	.0101	25.97	.0101
	1.5	25.34	.0110	25.35	.0107	25.37	.0103	25.38	.0100

## 第8章 分子气体的简化动理论模型

### 8.1 分子气体的特性

玻尔兹曼方程是仅针对单原子气体提出的。为模拟具有两个或多个原子的分子结构的气体的动力学行为，则需要在气体动理论层面重新建模。对于分子气体，两体碰撞保持动量守恒，但是能量却可以在各形式自由度和能级之间进行交换。因此，相比于仅具有剪切粘性的单原子气体，分子气体还存在体积粘性。另外，除了由分子平动引起的平动热导率外，还有由分子转动和振动引起的内部热导率。复杂的物理过程和更多的输运参数都对分子气体动理论建模带来挑战。

分子的内能可以表示为转动能量、振动能量、以及电离能之和，分子气体内部自由度导致了更加复杂的碰撞项。王承书和乌伦贝克从量子力学角度出发建立了 WCU 方程，定义  $f_i(t, \mathbf{x}, \mathbf{v})$  为第  $i$  个能量为  $e_i$  的能级的速度分布函数。并对每个能级的分布函数都写出一个玻尔兹曼方程，迁移项保持不变，而碰撞项  $Q_i$  是玻尔兹曼碰撞项的唯象扩展

$$Q_i = \sum_{jkl} \iint P_{ij}^{kl} B(\theta, v_r) d\Omega d\mathbf{v}_* \\ \times \left[ \omega_{ij}^{kl} f_l(\mathbf{v}'_*) f_k(\mathbf{v}') - f_j(\mathbf{v}_*) f_i(\mathbf{v}) \right]. \quad (8-1)$$

其中， $g_i$  表示第  $i$  能级的简并度，而  $\omega_{ij}^{kl} = g_k g_l / g_i g_j$ 。此碰撞积分表征两个“粒子”之间的碰撞，第一个粒子在碰撞前处于  $i$  能级，平动速度为  $\mathbf{v}$ ，在碰撞后跃迁到  $k$  能级，平动速度变为  $\mathbf{v}'$ ；第二个粒子在碰撞前处于  $j$  能级，平动速度为  $\mathbf{v}_*$ ，在碰撞后跃迁到  $l$  能级，平动速度变为  $\mathbf{v}'_*$ 。两粒子分别从  $(i, j)$  能级跃迁至  $(k, l)$  能级的概率为  $P_{ij}^{kl}$ ，由于二体碰撞的总能量守恒，上述跃迁只在以下条件发生

$$|\mathbf{v}'_r|^2 = |\mathbf{v}_r|^2 + \frac{4}{m}(e_i + e_j - e_k - e_l) > 0. \quad (8-2)$$

碰撞后的分子速度为

$$\begin{aligned} \mathbf{v}' &= \frac{\mathbf{v} + \mathbf{v}_*}{2} + \frac{v'_r}{2}\Omega, \\ \mathbf{v}'_* &= \frac{\mathbf{v} + \mathbf{v}_*}{2} - \frac{v'_r}{2}\Omega. \end{aligned} \quad (8-3)$$

碰撞核和跃迁概率的具体表达式是非常复杂的。这里以氮气为例，考虑在只存在转动自由度的情况下，对 WCU 方程的计算复杂性进行说明。在 Lennard-Jones 作

用势下，转动能可表达为

$$e_i = 2.9i(i+1) \text{ K},$$

而转动能级的简并度为

$$g_i = 2i+1, \quad i = 0, 1, \dots, \infty.$$

对照分子动力学模拟数据 [6, 126]，将跃迁概率拟合为

$$\begin{aligned} P_{ij}^{kl} = P_0 \omega_{ij}^{kl} & \left[ \frac{2e_{tot}}{5e_{tr0}} \exp(-\Delta_1 - \Delta_2 - \Delta_3 - \Delta_4) \right. \\ & \left. + \frac{5e_{tr0}}{2e_{tot}} \exp(-\Delta_3 - \Delta_4) \right], \end{aligned}$$

其中， $P_0$  为一常数，

$$\begin{aligned} \Delta_1 &= \frac{|e_i + e_j - e_k - e_l|}{e_{tr0}}, \\ \Delta_2 &= 2 \frac{|e_i + e_l - e_k - e_j|}{e_{tot}}, \\ \Delta_3 &= 4 \frac{|e_i - e_k|}{e_{tr0} + e_i}, \quad \Delta_4 = 2 \frac{|e_j - e_l|}{e_{tr0} + e_j}, \\ e_{tr0} &= \frac{m}{4} v_r^2, \quad e_{tot} = \frac{m}{4} v_r^2 + e_i + e_j. \end{aligned}$$

显然，如果总能级数为  $N$ ，公式 (8-1) 的计算量为单原子玻尔兹曼碰撞项 (2-9) 的  $N^4$  倍，时间成本巨大。

根据碰撞过程中平动能是否守恒，WCU 方程中的碰撞项可以分为弹性碰撞与非弹性碰撞。若处在  $i$  能级和  $j$  能级的两个分子发生碰撞，碰撞后仍然能分别处在  $i$  能级和  $j$  能级，则为弹性碰撞，否则为非弹性碰撞：

$$\begin{aligned} Q_i = & \sum_j \iint P_{ij}^{ij} B [f_j(\mathbf{v}'_*) f_i(\mathbf{v}') - f_j(\mathbf{v}_*) f_i(\mathbf{v})] d\Omega d\mathbf{v}_* \\ & + \sum_{jkl} (1 - \delta_{jk} \delta_{il}) \\ & \times \iint P_{ij}^{kl} B [f_k(\mathbf{v}'_*) f_l(\mathbf{v}') - f_j(\mathbf{v}_*) f_i(\mathbf{v})] d\Omega d\mathbf{v}_*. \end{aligned}$$

对于弹性碰撞和非弹性碰撞，可以分别引入两个等效的弛豫时间 [79]

$$\begin{aligned} \frac{1}{\tau_{el}} &= \sum_j \iint P_{ij}^{ij} B f_j(\mathbf{v}_*) d\Omega d\mathbf{v}_*, \\ \frac{1}{\tau_{in}} &= \sum_{jkl} (1 - \delta_{jk} \delta_{il}) \iint P_{ij}^{kl} B f_j(\mathbf{v}_*) d\Omega d\mathbf{v}_*, \end{aligned}$$

而将 WCU 碰撞项形式地改写为

$$\begin{aligned} Q_i &= \sum_j \iint P_{ij}^{ij} B f_j(\boldsymbol{v}'_*) f_i(\boldsymbol{v}') d\Omega d\boldsymbol{v}_* \\ &\quad + \sum_{jkl} (1 - \delta_{jk} \delta_{il}) \iint P_{ij}^{kl} B f_k(\boldsymbol{v}'_*) f_l(\boldsymbol{v}') d\Omega d\boldsymbol{v}_* \\ &\quad - \frac{f_i(\boldsymbol{v})}{\tau_{el}} - \frac{f_i(\boldsymbol{v})}{\tau_{in}}. \end{aligned}$$

这两个等效的碰撞时间，表征着能量在各种自由度或能级间的弛豫速度，因而与下面将讨论的分子气体输运系数，体积粘性和平动、转动热导率等，有着直接的关联。

### 8.1.1 体积粘性

体积粘性表征了气体无剪切膨胀或压缩时所受的阻力，对于稀疏气体，这种阻力来自于气体分子平动能与内能的交换过程：在膨胀或者压缩过程中，压力做功会立刻改变平动能，但在一定的延迟后才会通过非弹性碰撞而改变内能。为方便起见，在下述推导中，假设只存在一个转动能级。

引入非弹性碰撞所对应的平动能与转动能交换的弛豫时间  $\tau_r$ ，在空间均匀系统中，转动温度  $T_r$  的弛豫过程由 Jeans-Landau 方程描述：

$$\frac{\partial T_r}{\partial t} = \frac{T_t - T_r}{\tau_r}, \quad (8-4)$$

式中， $T_t$  和  $T_r$  分别为平动和转动温度，而平衡态温度  $T$  可表达为

$$T = \frac{3T_t + d_r T_r}{3 + d_r}. \quad (8-5)$$

忽略剪切粘性和热传导的影响，通过膨胀压缩过程中能量守恒可得到

$$\begin{aligned} \frac{3nk_B}{2} \frac{DT_t}{Dt} &= -p_t \nabla \cdot \mathbf{u} - \frac{d_r}{2} nk_B \frac{T_t - T_r}{\tau_r}, \\ \frac{d_r}{2} nk_B \frac{DT_r}{Dt} &= \frac{d_r}{2} nk_B \frac{T_t - T_r}{\tau_r}, \end{aligned} \quad (8-6)$$

式中， $D/Dt$  为物质导数，推导得到

$$\frac{D}{Dt}(T_t - T_r) = -\frac{2}{3} T_t \nabla \cdot \mathbf{u} - \frac{3 + d_r}{3} \frac{T_t - T_r}{\tau_r}. \quad (8-7)$$

将  $T_t - T_r$  基于小量  $\tau_r$  展开为  $T_t - T_r = T_1 \tau_r + O(\tau_r^2)$ ，可知上式左侧的时间导数项较右侧为更高阶小量，于是得到

$$T_t - T_r \approx -\frac{2\tau_r}{3 + d_r} T_t \nabla \cdot \mathbf{u} \approx -\frac{2\tau_r}{3 + d_r} T \nabla \cdot \mathbf{u}, \quad (8-8)$$

这说明，内能弛豫的影响将压力从原始压力  $p_0 = nk_B T$  改变为平动压力  $p_t =$

$nk_B T_t$ , 结合公式(8-5)可得:

$$p_t = nk_B T_t = p_0 \left[ 1 - \frac{2d_r}{(3+d_r)^2} \tau_r \nabla \cdot \mathbf{u} \right]. \quad (8-9)$$

式中速度散度前的系数即为体积粘性  $\mu_b$ . 在此, 可以引入无量纲转动碰撞数  $Z$

$$Z = \frac{3}{d_r + 3} \frac{\tau_r}{\tau}, \quad (8-10)$$

其中由分子平动引起的平均碰撞时间为  $\tau = \mu/n_0 k_B T_t$ . 于是体积粘性与剪切粘性的比值有如下关系

$$\frac{\mu_b}{\mu} = \frac{2d_r Z}{3(d_r + 3)}. \quad (8-11)$$

从公式(8-10)和(8-11)可知, 体积粘性正比于能量交换时间. 对于单原子气体, 若不考虑电离, 不存在内部能量的交换, 因此体积粘性为零. 而对于一些分子气体, 例如二氧化碳, 体积粘性可以是剪切粘性的上千倍 [? ]. 但是, 需要强调的是, 公式(8-8)成立的条件是  $\tau_r$  很小, 即能量弛豫的时间远远小于系统的特征时间. 如果系统特征频率  $\omega$  过高, 则等效的体积粘性一般跟系统频率有如下近似关系 [14, 75-76, 48]:

$$\mu_b = 2n_0 k_B T_t \frac{d_r \tau_r / (1 + \omega^2 \tau_r^2)}{[3 + d_r / (1 + \omega^2 \tau_r^2)]^2}. \quad (8-12)$$

也就是说, 在  $\omega \tau_r \rightarrow \infty$  极限下, 体积粘性趋向零而不是无穷大, 这是因为能量交换时间过长以至于系统无法感知, 此时可以认为内部自由度是冻结的. 因此, 与公式(2-48)中提到的剪切粘性和热导率的弛豫速率是本质而剪切粘性和热导率是表象一样, 这里 Jeans-Landau 方程里的能量交换也是本质, 而体积粘性只是连续流下的一个表象.

### 8.1.2 热导率

分子气体的热流由两部分组成, 一部分由分子的平动引起的动能传递, 一部分由分子的扩散引起的内能的传递. 由于气体分子迁移过程中存在动能和内能交换, 这一非弹性碰撞改变了能量在不同自由度下的分布, 从而间接改变了动能传递与内能随扩散传递的结果. 因而, 平动热流和转动热流的弛豫过程是相互耦合的. 于是, 在空间均匀系统中, 类似于公式(2-48), 平动热流  $\mathbf{q}_t$  和转动热流  $\mathbf{q}_r$  的弛豫过程一般可以写成如下形式:

$$\begin{aligned} \frac{\partial \mathbf{q}_t}{\partial t} &= -\frac{p}{\mu} (A_{tt} \mathbf{q}_t + A_{tr} \mathbf{q}_r), \\ \frac{\partial \mathbf{q}_r}{\partial t} &= -\frac{p}{\mu} (A_{rt} \mathbf{q}_t + A_{rr} \mathbf{q}_r), \end{aligned} \quad (8-13)$$

而通过 Chapman-Enskog 展开得到的连续流下的平动热导率  $\kappa_{tr}$  和转动热导率  $\kappa_{rot}$  可表示为

$$\begin{aligned} A_{tt}\kappa_{tr} + A_{tr}\kappa_{rot} &= \frac{5}{2} \frac{k_B\mu}{m}, \\ A_{rt}\kappa_{tr} + A_{rr}\kappa_{rot} &= \frac{d_r}{2} \frac{k_B\mu}{m}. \end{aligned} \quad (8-14)$$

将方程(8-14)代入方程(??), 就可以通过热弛豫系数求解如下方程得到对应的 Eucken 系数:

$$\begin{bmatrix} f_{tr} \\ f_{rot} \end{bmatrix} = \begin{bmatrix} 3A_{tt} & d_r A_{tr} \\ 3A_{rt} & d_r A_{rr} \end{bmatrix}^{-1} \begin{bmatrix} 5 \\ d_r \end{bmatrix}. \quad (8-15)$$

基于 WCU 方程(8-1), Manson 和 Manchick 通过修正的 Chapman-Enskog 展开推导出四个无量纲热弛豫系数的具体形式:

$$\begin{aligned} A_{tt} &= \frac{2}{3} + \frac{5}{6Z} \frac{d_r}{3+d_r}, \\ A_{rr} &= \frac{\mu}{\rho D'} + \frac{3}{2(3+d_r)Z}, \\ A_{tr} &= -\frac{5}{2(3+d_r)Z}, \\ A_{rt} &= -\frac{d_r}{2(3+d_r)Z}, \end{aligned} \quad (8-16)$$

其中  $D'$  是有效扩散系数, 如果极性分子发生强共振碰撞, 该系数可能与自扩散系数  $D$  有明显差异, 例如氯化氢的有效扩散系数满足  $\rho D'/\mu = 0.89$ , 而  $\rho D/\mu = 1.33$ . 根据公式(8-15), 忽略  $1/Z$  的高阶项, 可将平动 Eucken 因子和转动 Eucken 因子写为 [?]

$$\begin{aligned} f_{tr} &= \frac{5}{2} \left[ 1 - \frac{5d_r}{4(d_r+3)Z} \left( 1 - \frac{2\rho D'}{5\mu} \right) \right], \\ f_{rot} &= \frac{\rho D'}{\mu} \left[ 1 + \frac{15}{4(d_r+3)Z} \left( 1 - \frac{2\rho D'}{5\mu} \right) \right]. \end{aligned} \quad (8-17)$$

注意到,  $f_{tr}$  随着转动碰撞数  $Z$  的减小而减小, 即内能交换越频繁, 平动热导率降低. 这是因为在分子气体的碰撞过程中, 部分平动能转化为内能, 当  $D'$  增加,  $Z$  减小时, 能量转化效率增强. 这在物理上是合理的.

Mason 与 Monchick 的解析解依然存在的一个问题, 即无法保证通过公式(8-16)推导而来的无量纲热弛豫系数  $A$  与实际气体参数保持一致. 其原因在于, 在粘性和扩散系数确定的条件下, 转动碰撞数  $Z$  作为公式中唯一用来调节 Eucken 因子的参数, 只能使得总热导率可能达到与实验数据相近的数值, 但无法分别独立调整平动与内能 Eucken 因子. 与此同时, 由于  $Z$  也是决定分子气体体积粘性的

唯一调节参数，参考公式(8-11)，则总热导率与体积粘性的准确性通常无法同时被满足。

### 8.1.3 DSMC 中的热弛豫速率

对于单原子气体，在粒子数和空间网格足够多的情况下，DSMC 已被证明收敛于玻尔兹曼方程的解 [133]。实际上，由于 DSMC 中二体碰撞后粒子速度的更新方式与玻尔兹曼方程一致，公式(3-27)在可接受的误差范围内恒成立，即 DSMC 可确保平动 Eucken 因子  $f_{tr}$  非常接近 2.5。但对于分子气体，DSMC 不一定能够准确恢复热导率。在 DSMC 的碰撞模型中，可变软球模型的提出是为了获得准确的剪切粘性与自扩散系数；唯象的 Larsen-Borgnakke 模型 [12] 可以通过恢复能量交换速率 [13, 42, 30] 从而准确获取体积黏性。然而迄今为止，尚无研究证明 DSMC 能够在分子气体模拟中正确恢复热导率。

我们通过提取 DSMC 中的热弛豫速率  $A$  来分析其恢复热导率的能力。具体而言，在 Larsen-Borgnakke 模型中选取不同的转动碰撞数，对非极性气体氮气与极性气体氯化氢进行研究。参照 Brid 书中的公式 (4.50) 和 (5.67)，DSMC 中非弹性碰撞概率  $\Lambda$  与本文中定义的转动碰撞数  $Z$  通过 Jeans-Landau 方程 (8-4) 联系在一起 [9]：

$$Z = \frac{1}{\Lambda} \frac{\alpha(5 - 2\omega)(7 - 2\omega)}{5(\alpha + 1)(\alpha + 2)}, \quad (8-18)$$

式中， $\omega$  为粘性温度幂指数，见公式(4-4)； $\alpha$  是可变软球模型中与斯密特数相关的参数：

$$Sc = \frac{\mu}{\rho D} = \frac{5(2 + \alpha)}{3(7 - 2\omega)\alpha}. \quad (8-19)$$

我们使用开源软件 SPARTA 在空间均匀系统中提取 DSMC 方法中的热弛豫系数矩阵  $A$ 。将一百万个 DSMC 模拟粒子均匀地分布在边长为 10 纳米的立方体内，所有的边界设置为周期性边界条件。气体数密度为  $n_0 = 2.69 \times 10^{25} \text{ m}^{-3}$ ，温度为  $T_0 = 300 \text{ K}$ 。如图 8-1(a) 所示，在模拟初始时刻，沿  $x$  轴正方向运动的粒子的速度分布函数为 200 K 温度下的麦克斯韦分布，沿  $x$  轴负方向运动的粒子速度分布函数为 400 K 温度下的麦克斯韦分布。类似地，沿  $x$  轴正方向运动的粒子的转动能满足 200 K 温度下的麦克斯韦分布，而沿反方向运动的粒子转动能满足 400 K 温度下的麦克斯韦分布，见图 8-1(b)。这样的设置是为了建立初始平动和转动热流分布。随后记录平动和转动热流随时间的演化，直至它们在系统中按照熵增原理达到热平衡后消失。图 8-1(c) 展示的是通过 100 次系综平均得到的平滑计算结果。

图 8-1(d) 给出氮气的热流变化率的演化过程，可以看出平动热流的时间导数随时间先增加后减小，这可以解释为平动热流与转动热流之间存在强耦合效应，即

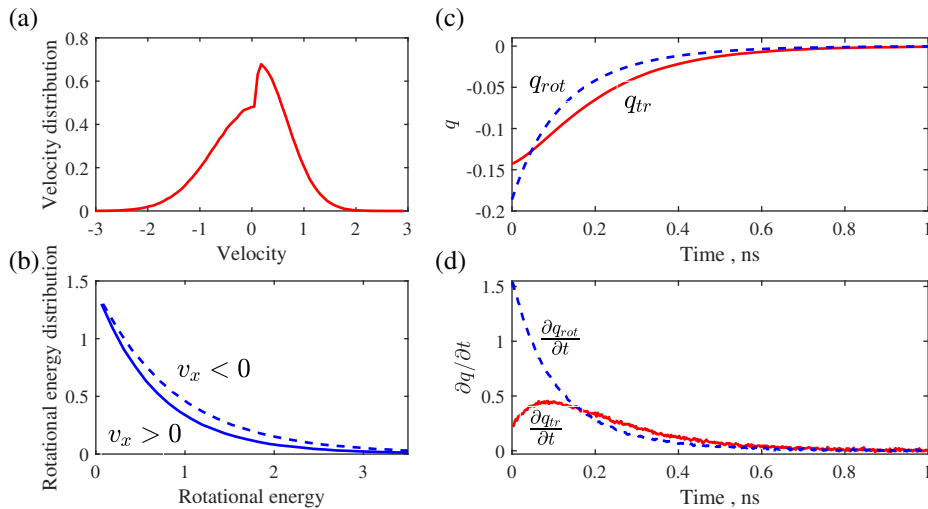


图 8-1 (a) 初始状态用于激发平动热流的速度分布函数; 横坐标由最概然速率  $v_m$  归一化. (b) 初始状态用于转动热流的转动能分布函数; 横坐标由  $k_B T_0$  归一化. (c, d) 氮气平动热流和转动热流的弛豫过程. 模拟参数为: 公式(8-18)中的非弹性碰撞概率取  $\Lambda = 0.25$ , 施密特数取  $Sc = 1/1.33$ , 转动自由度取  $d_r = 2$ , 温度粘性指数取  $\omega = 0.74$ . 图中数据来源于文献 [? ].

在平动热流衰减的同时得到了转动热流的补偿, 且根据公式 (8-13) 可知,  $A_{tr}$  必定小于零.

图 8-2 显示通过最小二乘法求解线性回归问题 (8-13) 得到的热流弛豫速率  $A$ . 可以看出在相同的转动碰撞数  $Z$  和斯密特数下, 氮气与氯化氢气体的热弛豫速率几乎相同. 另外, 当  $Z \rightarrow \infty$  时, 有  $A_{tt} = 2/3, A_{rr} = Sc, A_{tr} = A_{rt} = 0$ , 可以得到与公式 (??) 一致的结果. 图中虚线为 Mason 和 Manchick 的结果 (8-16), 由于忽略了  $1/Z$  的高阶项, 其结果在  $1/Z$  较大时与 DSMC 的结果出现明显偏差.

图 8-3 给出根据公式(8-14)和(8-15)计算得到的 Eucken 因子, 并与常温下的实验结果对比. 对于氮气, 当施密特数取  $1/1.33$  时, 通过选择特定的碰撞数  $1/\Lambda \approx 3.5$ , DSMC 可以恢复实验测量得到的总热导率, 但由于缺少相应实验数据, 我们无法分辨其是否能正确恢复平动与转动热导率分量. 若此温度下氮气的体积粘性要求  $1/\Lambda \approx 3.5$ , 则 DSMC 给出的总热导率必然存在误差. 对于极性气体氯化氢, 实验中常温下测得的总 Eucken 因子约为 1.7, 但是从图 8-3(a) 中, 如果取施密特数为  $1/1.33$ , 从 DSMC 中导出的总 Eucken 因子最小只能达到 1.8; 因此无论如何选择碰撞数, DSMC 都不能恢复总热导率.

从公式 (8-17) 可得, 当气体种类确定时, 转动碰撞数决定了体积粘性, 因此我们可以通过调整 DSMC 中的扩散系数以恢复总热导率, 见图 8-3(b). 然而, 即便在体积粘性与总热导率均与实验值相同的情况下, 方程 (8-17) 的近似解与使用 Larsen-Borgnakke 模型的 DSMC 方法得到的平动热导率  $f_{tr}$  并不一致, 且两者的准确性都尚不确定. 对于氯化氢气体, 极性分子的共振相互作用 [?] 导致  $\rho D'/\mu$  从

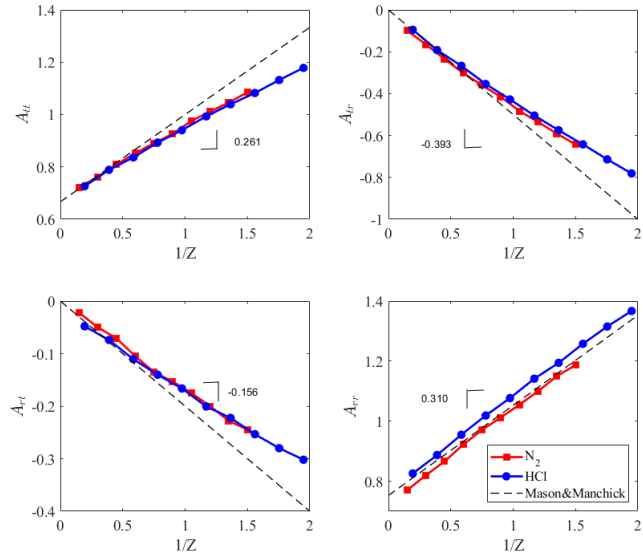


图 8-2 根据理论公式(8-16)从 DSMC 模拟中提取的热弛豫速率. 施密特数为  $\text{Sc} = 1/1.33$ , 转动自由度为  $d_r = 2$ ; 对氮气和氯化氢, 温度粘性指数  $\omega$  分别取 0.74 和 1. 图中数据来源于文献 [? ].

The extracted rates  $\mathbf{A}$  in the relaxation of heat fluxes from the DSMC simulation, as per Eq. (8-16). The Schmidt number is  $\text{Sc} = 1/1.33$ , and the rotational degree of freedom is  $d_r = 2$ ; the viscosity index for Nitrogen and hydrogen chloride is  $\omega = 0.74$  and 1, respectively. The figures are modified from figure 1 in reference [? ].

1.33 降低至 0.89, 为了恢复实验测量的总热导率, 从图 8-3(b) 可知, DSMC 的非弹性碰撞概率约等于 1, 达到了平动能与内能交换的极限, 因此并不是一个满足物理要求的值. 若选择合理的非弹性碰撞概率, 则将要求 DSMC 中的有效扩散系数远小于自扩散系数. 这将带来另一个问题: 对于多组分气体, 扩散系数与热导率同等重要, 而 Larsen-Borgnakke 模型难以同时正确恢复这两个输运系数, 亟需改进.

## 8.2 分子气体的动理论模型及精度

WCU 方程的每一个内能能级都对应一个速度分布函数, 因而计算代价巨大. 对于强激波问题, 氮气的能级数可达到 70, 给数值求解带来了极大的困难 [126]. 因此对 WCU 方程进行简化是非常必要的, 而简化的基本原则与单原子气体相同, 即需要满足必要的守恒律和平衡态分布, 还需要尽量使各物理量的输运系数与 WCU 方程保持一致, 例如, 扩散系数、剪切粘性、体积粘性、热导率及其在各自由度下的分量等. 更接近本质的说法是, 各输运系数对应的物理量的弛豫速率与实际气体保持一致. 学者们提出了许多描述分子气体稀薄效应的动理论模型方程, 如 Rykov 模型和 ES-BGK 模型等. 如同在单原子气体中 Gross-Jackson 模型可以视为所有模型的源头, 在分子气体中可以认为 Hanson-Morse 模型 [43] 是所有动理论模型的源头.

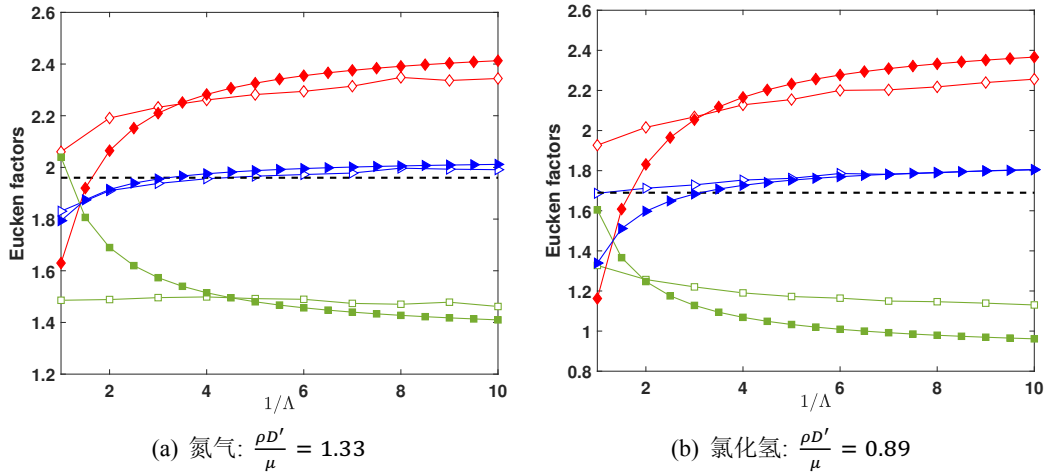


图 8-3 室温下 Eucken 因子的解析解(8-17)与 DSMC 数值解的对比. DSMC 中使用可变软球模型, 自扩散系数  $D$  取值为  $D'$ . 菱形、正方形、三角形分别表示平动、内能和总 Eucken 因子, 实心点为解析解, 空心点为 DSMC 结果, 虚线表示 300 K 温度下实验测量的总 Eucken 因子. 图中数据来源于文献 [141]

The thermal conductivity obtained from the analytical solution (8-17) and the DSMC at room temperature, as a function of the inelastic collision probability  $\Lambda$ . The variable-soft-sphere model is used and the self-diffusion coefficient  $D$  in DSMC takes the value of  $D'$ . Open diamonds, squares and triangles represent the translational, internal and total Eucken factors from Eq. (8-17), respectively, while the filled symbols are the corresponding results from DSMC. Dashed lines show the total Eucken factor obtained from experiments at a temperature of 300 K. The figures are from reference [141].

在小克努森数情况下, 从简化模型方程和 WCU 方程推导出的纳维-斯托克斯方程必须是一致的. 事实上, 这种一致性的根本要求是, 模型方程中所对应的各个分子气体输运系数 (例如: 剪切粘性、体积粘性、热导率及其在各自由度下的分量等) 需与原方程保持一致. 基于以上要求,

### 8.2.1 Hanson-Morse 线性化模型

此模型在线性化情况下逼近 WCU 方程 (8-1) 的碰撞项. 这种构造方法类似于单原子气体的 Gross-Jackson 模型 [37], 即通过对玻尔兹曼碰撞项进行正交多项式展开, 并保证各多项式对应的宏观量的弛豫速率与 WCU 方程一致而获得. 对于分子气体, 关于分子速度的多项式仍由麦克斯韦分子的本征函数(2-26)给出; 关于内部能量的多项式的前两项取为 1 和  $\epsilon = e_i - \bar{e}$ , 其中  $\bar{e}$  为平均内部能量 [137].

分子气体的平衡态速度分布函数可表示为  $f_i = o_i F_{eq}$ , 其中

$$o_i = \frac{g_i \exp(-e_i/k_B T)}{\sum_j g_j \exp(-e_j/k_B T)} \quad (8-20)$$

表征了内能为  $e_i$  的分子比例. 在线性化问题中, 通常考虑宏观速度为零的全局平

衡态，并将速度分布函数写为如下形式：

$$f_i(t, \mathbf{x}, \boldsymbol{\xi}) = o_i f_{eq}(\boldsymbol{\xi}) [1 + \phi_i(t, \mathbf{x}, \boldsymbol{\xi})], \quad (8-21)$$

其中每个内部能级对应的扰动分布函数  $\phi_i$  满足  $|\phi_i| \ll 1$ . 注意到与上文的单原子线性化模型保持一致，这里的速度和空间坐标分别通过最概然速率  $v_m$  和特征尺寸  $\ell$  进行无量纲化；时间通过  $\ell/v_m$  归一化，加速度通过  $v_m^2/\ell$  无量纲化，内能  $e_i$  通过  $k_B T_0$  无量纲化. 归一化后的扰动物理量可以通过对扰动分布函数求矩得到：

$$\begin{aligned} n_i &= \int f_{eq} \phi_i d\boldsymbol{\xi}, \quad \bar{e} = \sum_i o_i e_i, \\ [\mathbf{u}, \sigma_{\alpha\beta}] &= \sum_i o_i \int f_{eq} \phi_i [\boldsymbol{\xi}, \xi_{\langle\alpha} \xi_{\rangle\beta}] d\boldsymbol{\xi}, \\ T_t &= \sum_i o_i \int f_{eq} \phi_i \left( \frac{2}{3} \xi^2 - 1 \right) d\boldsymbol{\xi}, \\ \mathbf{q}_t &= \sum_i o_i \int f_{eq} \phi_i \left( \xi^2 - \frac{5}{2} \right) \boldsymbol{\xi} d\boldsymbol{\xi}, \\ [T_r, \mathbf{q}_r] &= \sum_i o_i \int f_{eq} \phi_i \epsilon_i \left[ \frac{2}{d_r}, \boldsymbol{\xi} \right] d\boldsymbol{\xi}, \end{aligned} \quad (8-22)$$

同时，总扰动密度为  $n = \sum_i n_i o_i$ .

若加速度为小量，WCU 方程的线性化形式为

$$\frac{\partial \phi_i}{\partial t} + \boldsymbol{\xi} \cdot \frac{\partial \phi_i}{\partial \mathbf{x}} - 2\mathbf{a} \cdot \boldsymbol{\xi} = \frac{\ell}{v_m} J_i, \quad (8-23)$$

其中  $J_i$  的形式与公式(2-23)类似，不再赘述. 根据 Hanson-Morse 模型 [43]，该线性化碰撞项可近似为 [43]

$$\begin{aligned} J_i &= -J_{030}(n_i + 2\boldsymbol{\xi} \cdot \mathbf{u} - \phi_i) + 2\sigma_{\alpha\beta}(J_{020} - J_{030})\xi_{\langle\alpha} \xi_{\rangle\beta} \\ &\quad + T_t \left[ (-J_{030} + J_{100}) \left( \xi^2 - \frac{3}{2} \right) - \frac{3}{d_r} J_{100} \epsilon \right] \\ &\quad + 2\boldsymbol{\xi} \cdot \mathbf{q}_t \left[ (J_{110} - J_{030}) \frac{2}{5} \left( \xi^2 - \frac{5}{2} \right) - J_{011}^{110} \sqrt{\frac{4}{5d_r}} \epsilon \right] \\ &\quad + T_r \left[ -J_{100} \left( \xi^2 - \frac{3}{2} \right) + \left( \frac{3}{d_r} J_{100} - J_{030} \right) \epsilon \right] \\ &\quad + 2\boldsymbol{\xi} \cdot \mathbf{q}_r \left[ -J_{011}^{110} \sqrt{\frac{4}{5d_r}} \left( \xi^2 - \frac{5}{2} \right) + 2(J_{011} - J_{030}) \frac{\epsilon}{d_r} \right]. \end{aligned}$$

Hanson-Morse 模型假设各内部能级的弛豫时间相同，则与公式(8-16)对应的弛豫率

为

$$\begin{aligned}
 \tau &= \frac{\mu}{p_t}, \\
 J_{020} &= -\tau^{-1}, \quad J_{030} = -\frac{3}{2}\tau^{-1}, \\
 J_{100} &= -\frac{1}{Z\tau} \frac{d_r}{3+d_r}, \quad J_{110} = -\frac{2}{3\tau} - \frac{5}{6Z\tau} \frac{d_r}{3+d_r}, \\
 J_{011}^{110} &= -\sqrt{\frac{5}{4d_r}} \frac{1}{Z\tau} \frac{d_r}{3+d_r}, \\
 J_{011} &= -\frac{\mu}{\rho D'} - \frac{3}{2(3+d_r)Z}. \tag{8-24}
 \end{aligned}$$

在自发瑞利-布里渊散射中,如果模型中包含应力偏量  $\sigma_{\alpha\beta}$ ,则该模型称为 Tenti-S7 模型 [11, 127], 其缺点在于不能得到实验散射光谱. Tenti-S6 模型通过移除应力偏量  $\sigma_{\alpha\beta}$ , 即令模型中的  $\sigma_{\alpha\beta} = 0$ , 获得与实验一致的散射光谱. 实际上,如果不考虑内部能级, Tenti-S7 和 Tenti-S6 模型分别退化为单原子 ES-BGK 模型和 Shakhov 模型,而在大多数情况下 Shakhov 模型的精度高于 ES-BGK 模型.

当在 Hanson-Morse 模型中移除应力偏量,为了复现应力偏量、能量弛豫、热流的弛豫过程,式 (8-24) 中的  $J_{030}$  应该改成  $-1/\tau$ . 同时,将系数  $J_{011}$  修改为以下形式 [11, 89]:

$$J_{011} = -\frac{2d_r}{3(3+d_r)\tau} \frac{\frac{1}{5}(3+d_r) + \frac{6+d_r}{4Z} + \frac{9}{16Z^2}f_u}{\frac{2}{15}f_u(3+d_r) + \frac{d_r}{6Z}f_u - 1}, \tag{8-25}$$

从而保证正确恢复热导率. so that the thermal conductivity is exactly recovered.

Let's consider the Hanson-Morse model involving not the pressure tensor.

### 8.2.2 Hanson-Morse 模型的约化及非线性化

并定义  $\phi = \sum_i o_i \phi_i$ , 为了减小计算量, 引入如下两个约化速度分布函数

$$\begin{aligned}
 g &= \sum_i o_i f_{eq} \phi_i, \\
 r &= \sum_i o_i f_{eq} \phi_i (e_i - \bar{e}), \tag{8-26}
 \end{aligned}$$

消去内能自由度, 则 Hanson-Morse 模型可以简化为

$$\begin{aligned}
 \frac{\partial g}{\partial t} + \boldsymbol{\xi} \cdot \frac{\partial g}{\partial \mathbf{x}} - 2\mathbf{a} \cdot \boldsymbol{\xi} &= \frac{\ell}{v_m} J_g, \\
 \frac{\partial r}{\partial t} + \boldsymbol{\xi} \cdot \frac{\partial r}{\partial \mathbf{x}} - 2\mathbf{a} \cdot \boldsymbol{\xi} &= \frac{\ell}{v_m} J_r, \tag{8-27}
 \end{aligned}$$

其中

$$\begin{aligned}
 J_g = & -J_{030} \left[ n + 2\boldsymbol{\xi} \cdot \mathbf{u} + \boldsymbol{\xi} \cdot \mathbf{q}_t \frac{4}{15} \left( \xi^2 - \frac{5}{2} \right) - g \right] \\
 & - J_{030} T_t \left( \xi^2 - \frac{3}{2} \right) + 2\sigma_{\alpha\beta} (J_{020} - J_{030}) \xi_{(\alpha} \xi_{\beta)} \\
 & - (T_r - T_t) J_{100} \left( \xi^2 - \frac{3}{2} \right) \\
 & - \boldsymbol{\xi} \cdot \left[ \mathbf{q}_t \frac{2d_r}{3Z\tau(3+d_r)} + 2\mathbf{q}_r J_{011}^{110} \sqrt{\frac{4}{5d_r}} \right] \left( \xi^2 - \frac{5}{2} \right), \tag{8-28}
 \end{aligned}$$

and

$$\begin{aligned}
 J_r = & -J_{030} \left( \frac{d_r}{2} T_r + 2\boldsymbol{\xi} \cdot \mathbf{q}_r - r \right) \\
 & - \frac{3}{2} J_{100} (T_t - T_r) \\
 & - 2\boldsymbol{\xi} \cdot \mathbf{q}_t J_{011}^{110} \sqrt{\frac{d_r}{5}} + 2\boldsymbol{\xi} \cdot \mathbf{q}_r J_{011}. \tag{8-29}
 \end{aligned}$$

很明显，带下括号的项为能量与热流的弛豫项，因此，Hanson-Morse 模型也可以改写为公式(8-32)的通用形式。

至此，注意到单原子气体中 Gross-Jackson 模型与 BGK、ES-BGK、Shakhov 等模型的关系，我们可以通过类似于公式(5-14)中展示的非线性化程序构造出分子气体的动理论模型。即首先写出扰动量  $g$  和  $r$  对应的速度分布函数：

$$\begin{aligned}
 G(t, \mathbf{x}, \mathbf{v}) &= \sum_i o_i f_i, \\
 R(t, \mathbf{x}, \mathbf{v}) &= \sum_i o_i f_i e_i, \tag{8-30}
 \end{aligned}$$

并定义宏观量如下

$$\begin{aligned}
 [n, \mathbf{u}, T_t] &= \int \left[ 1, \frac{\mathbf{v}}{n}, \frac{mc^2}{3nk_B} \right] G d\mathbf{v}, \\
 [p_{ij}, \mathbf{q}_t] &= \int \left[ mc_i c_j, \frac{mc^2 \mathbf{c}}{2} \right] G d\mathbf{v}, \\
 [T_r, \mathbf{q}_r] &= \int \left[ \frac{2}{d_r nk_B}, \mathbf{c} \right] R d\mathbf{v}. \tag{8-31}
 \end{aligned}$$

总热流定义为  $\mathbf{q} = \mathbf{q}_t + \mathbf{q}_r$ ，平动压力、转动压力和总压力分别定义为  $p_t = nkT_t$ ,  $p_r = nkT_r$  and  $p = nkT$ 。注意此处  $G$  可以线性化为  $G = f_{eq}(1+g)$ ，而  $R$  应该线性化为  $R = (d_r k_B T / 2) f_{eq}(1+g+r)$ 。其次，把速度分布函数的演化过程形

式地写为

$$\begin{aligned}\frac{\partial G}{\partial t} + \boldsymbol{v} \cdot \frac{\partial G}{\partial \boldsymbol{x}} + \boldsymbol{a} \cdot \frac{\partial G}{\partial \boldsymbol{v}} &= \underbrace{\frac{G_t - G}{\tau}}_{\text{弹性}} + \underbrace{\frac{G_r - G_t}{Z\tau}}_{\text{非弹性}}, \\ \frac{\partial R}{\partial t} + \boldsymbol{v} \cdot \frac{\partial R}{\partial \boldsymbol{x}} + \boldsymbol{a} \cdot \frac{\partial R}{\partial \boldsymbol{v}} &= \underbrace{\frac{R_t - R}{\tau}}_{\text{弹性}} + \underbrace{\frac{R_r - R_t}{Z\tau}}_{\text{非弹性}}.\end{aligned}\quad (8-32)$$

最后, 根据公式(8-28)和(8-29)中的碰撞项, 类比公式(5-14), 写出四个参考分布函数  $G_t$ ,  $G_r$ ,  $R_t$  和  $R_r$  的形式.

例如, 考虑 Hanson-Morse 模型中不出现应力偏量. 公式(8-28)中的第一行和第二行即为线性化 Shakhov 模型的碰撞项, 可以非线性化为

$$\begin{aligned}\frac{p_t}{\mu} \left\{ F_{eq}(T_t) \left[ 1 + \frac{2m\boldsymbol{q}_t \cdot \boldsymbol{c}}{15k_B T_t p_t} \left( \frac{mc^2}{2k_B T_t} - \frac{5}{2} \right) \right] - G \right\} \\ = \frac{p_t}{\mu} (G_t - G).\end{aligned}\quad (8-33)$$

结合非线性模型(8-32)中的非弹性碰撞项  $(G_r - G_t)/Z\tau$ , 可以选取

$$\begin{aligned}G_r &= F_{eq}(T) \left[ 1 + \frac{2m\boldsymbol{q}' \cdot \boldsymbol{c}}{15k_B T p} \left( \frac{mc^2}{2k_B T} - \frac{5}{2} \right) \right], \\ \boldsymbol{q}' &= \left[ 1 - \frac{5d_r}{2(3+d_r)} \right] \boldsymbol{q}_t + \frac{15}{2(3+d_r)} \boldsymbol{q}_r,\end{aligned}\quad (8-34)$$

以在线性化情况下退化为公式(8-28)中的后两项, 其中能量交换由  $F_{eq}(T)$  和  $F_{eq}(T_t)$  的差距而来, 热流松弛由  $\boldsymbol{q}'$  决定.

### 8.2.3 非线性模型

然而, 历史并没有选择这条非线性化路线, 而是由许多学者各自提出了非线性动理论模型 [? ? ? 32? ? ?, 128? ]. 下面我们将先介绍主要的 Rykov 模型和 ES-BGK 模型, 并揭示与 Hanson-Morse 模型的内在联系. 最后我们介绍吴模型.

#### 8.2.3.1 Rykov 模型

原始的 Rykov 模型 [?] 仅适用于无振动模态的双原子气体, 但是构造思想可以直接拓展至多原子分子气体建模 [? ]. 在该模型中, 四个参考速度分布函数定义

为:

$$\begin{aligned} G_t &= F_{eq}(T_t) \left[ 1 + \frac{2m\mathbf{q}_t \cdot \mathbf{c}}{15k_B T_t p_t} \left( \frac{mc^2}{2k_B T_t} - \frac{5}{2} \right) \right], \\ G_r &= F_{eq}(T) \left[ 1 + \omega_0 \frac{2m\mathbf{q}_t \cdot \mathbf{c}}{15k_B T p} \left( \frac{mc^2}{2k_B T} - \frac{5}{2} \right) \right], \\ R_t &= \frac{d_r k_B T_r}{2} G_t + F_{eq}(T_t)(1 - Sc) \frac{m\mathbf{q}_r \cdot \mathbf{c}}{p_t}, \\ R_r &= \frac{d_r k_B T}{2} G_r + F_{eq}(T) \omega_1 (1 - Sc) \frac{m\mathbf{q}_r \cdot \mathbf{c}}{p}. \end{aligned} \quad (8-35)$$

选取弹性碰撞弛豫时间  $\tau = \mu/p_t$  以及适当的转动碰撞数  $Z$ , 可保证恢复正确的剪切粘性和体积粘性. 四个热流弛豫系数为

$$\begin{aligned} A_{tt} &= \frac{2}{3} \left( 1 + \frac{1 - \omega_0}{2Z} \right), \\ A_{rr} &= Sc + \frac{(1 - Sc)(1 - \omega_1)}{Z}, \\ A_{tr} &= A_{rt} = 0. \end{aligned} \quad (8-36)$$

因此通过公式 (8-15) 可以得到 Eucken 因子的表达式如下:

$$\begin{aligned} f_{tr} &= \frac{5}{2} \left( 1 + \frac{1 - \omega_0}{2Z} \right)^{-1}, \\ f_{rot} &= \left( Sc + \frac{(1 - Sc)(1 - \omega_1)}{Z} \right)^{-1}. \end{aligned} \quad (8-37)$$

这说明, 在 Rykov 模型中, 可通过调整自由参数  $\omega_0$  和  $\omega_1$  修改 Eucken 系数.

当  $Z \rightarrow \infty$ , 该模型退化为单原子气体的 Shakhov 模型. 如果将其线性化, 可以得到类似于 8.2.2 中的约化 Hanson-Morse 模型. 不同之处在于空间均匀系统中, Rykov 模型中平动和转动热流的弛豫不会相互干扰, 这是因为公式(8-14)中  $A_{tr} = A_{rt} = 0$ .

### 8.2.3.2 ES-BGK 模型

Holway 通过最大熵原理提出了 ES-BGK 模型, 该模型保留了标准 BGK 模型的数学简便性, 并且能够恢复正确的普朗特数, 同时满足熵增定理 [? ? ]. 速度分布函数的演化方程为:

$$\begin{aligned} \frac{\partial G}{\partial t} + \mathbf{v} \cdot \frac{\partial G}{\partial x} + \mathbf{a} \cdot \frac{\partial G}{\partial \mathbf{v}} &= \frac{1}{\tau} (f_r^{ES} - G), \\ \frac{\partial R}{\partial t} + \mathbf{v} \cdot \frac{\partial R}{\partial x} + \mathbf{a} \cdot \frac{\partial R}{\partial \mathbf{v}} &= \frac{1}{\tau} \left( \frac{d_r}{2} k_B T_{rel} f_r^{ES} - R \right), \end{aligned} \quad (8-38)$$

其中，弛豫温度  $T_{rel}$  定义为转动温度与总温度的加权平均值

$$T_{rel} = \left(1 - \frac{1}{Z}\right) T_r + \frac{T}{Z}, \quad (8-39)$$

参考分布函数  $f_r^{ES}$  由公式(5-4)给出，但是此处

$$\lambda_{ij} = \left(1 - \frac{1}{Z}\right) \left[ (1-b) \frac{k_B T_t}{m} \delta_{ij} + b \frac{p_{ij}}{nm} \right] + \frac{k_B T}{Zm} \delta_{ij}. \quad (8-40)$$

当  $Z \rightarrow \infty$ ，转动和平动能量交换消失，因此模型方程退化为单原子气体的 ES-BGK 方程。

with  $I$  being the unit tensor and  $\nu$  the other adjustable parameter in the range of  $-1/2 \leq \nu \leq 1$ . In (8-40),  $B^{-1}$  and  $\det(B)$  are the inverse and determinant of  $B$ , respectively. 取弹性碰撞弛豫时间  $\tau = \mu/p_t \text{Pr}$  及适当的转动碰撞数  $Z$ ，则分子气体的剪切和体积粘性自动满足要求。其中普朗特数可以通过调整  $b$  的取值得到：

$$\text{Pr} = \frac{1}{1 - b + b/Z}. \quad (8-41)$$

为使参考分布函数有界且在物理上有意义，要求  $-1/2 \leq b \leq 1$  和  $Z \geq 1$ . 因此，普朗特数范围为  $2/3 \leq \text{Pr} \leq +\infty$ . 对于大部分双原子分子来说，普朗特数大约为  $5/7$ ，因此可以保证要求。

与 Rykov 模型一样，ES-BGK 模型的平动热流和转动热流的弛豫过程互不干涉；从它们的弛豫率可知，Eucken 因子可以表达为

$$\begin{aligned} f_{tr} &= \frac{5}{3 \text{Pr}}, \\ f_{rot} &= \frac{1}{\text{Pr}} = \frac{3 + d_r}{5 + d_r} f_{eu}. \end{aligned} \quad (8-42)$$

注意到，对于多原子 ES-BGK 模型，平动 Eucken 因子与转动 Eucken 因子的比值始终为  $5/3$ ，并且 Eucken 因子完全由普朗特数决定。

### 8.2.3.3 吴模型

上述气体动理论模型的弛豫时间  $\tau$  都与分子速度无关，与玻尔兹曼方程的弛豫时间不相符。因此，在正激波问题中，Rykov 模型计算得到的结果可能会出现波前温升的误差，且随着马赫数的增加，这一偏离显著增长。由此，为了提高模型方程准确性，吴雷等人首先将 Rykov 模型中的弹性碰撞项  $(G_t - G)/\tau$  替换为单原子玻尔兹曼方程的碰撞项  $Q(G)$ ，以使弹性碰撞弛豫时间是分子速度的函数 [? ]；其后，又考虑引入更为准确的热流弛豫过程 [? ]，从而在相同参数条件下，得到更为符合 DSMC 的模拟结果。

吴模型的演化方程为:

$$\begin{aligned}\frac{\partial G}{\partial t} + \boldsymbol{v} \cdot \frac{\partial G}{\partial x} + \boldsymbol{a} \cdot \frac{\partial G}{\partial \boldsymbol{v}} &= Q(G) + \frac{G_r - G_t}{Z\tau}, \\ \frac{\partial R}{\partial t} + \boldsymbol{v} \cdot \frac{\partial R}{\partial x} + \boldsymbol{a} \cdot \frac{\partial R}{\partial \boldsymbol{v}} &= \frac{R'_t - R}{\tau} + \frac{R_r - R_t}{Z\tau}.\end{aligned}\quad (8-43)$$

式中,  $R'_t = (d_r/2)k_B T_r(\tau Q + G)$ , 驰豫时间为  $\tau = \mu/p_t$ , 对应的参考速度分布函数为:

$$\begin{aligned}G_t &= F_{eq}(T_t) \left[ 1 + \frac{2m\boldsymbol{q}_t \cdot \boldsymbol{c}}{15k_B T_t p_t} \left( \frac{mc^2}{2k_B T_t} - \frac{5}{2} \right) \right], \\ G_r &= F_{eq}(T) \left[ 1 + \frac{2m\boldsymbol{q}' \cdot \boldsymbol{c}}{15k_B T p} \left( \frac{mc^2}{2k_B T} - \frac{5}{2} \right) \right], \\ R_t &= \frac{d_r k_B T_r}{2} G_t, \\ R_r &= \frac{d_r k_B T}{2} G_r + F_{eq}(T) \frac{m\boldsymbol{q}'' \cdot \boldsymbol{c}}{p}.\end{aligned}\quad (8-44)$$

为了恢复热流弛豫过程 (8-13), 选取  $\boldsymbol{q}'$  和  $\boldsymbol{q}''$  如下:

$$\begin{aligned}\boldsymbol{q}' &= \left[ -3Z(A_{tt} - \frac{2}{3}) + 1 \right] \boldsymbol{q}_t - 3ZA_{tr}\boldsymbol{q}_r, \\ \boldsymbol{q}'' &= -Z [A_{rt}q_t + (A_{rr} - 1)\boldsymbol{q}_r].\end{aligned}\quad (8-45)$$

当  $Z \rightarrow \infty$ , 吴模型完全退化为单原子玻尔兹曼方程. 另一方面, 如果将玻尔兹曼碰撞项换回 Shakhov 碰撞模型, 在线性化的情况下, 吴模型则完全与 8.2.2 中的约化 Hanson-Morse 模型一致.

Eucken 因子同样可以通过公式 (8-15) 计算, 此模型提供了两个调整 Eucken 因子的自由度, 因此能够保证恢复全部输运系数.

#### 8.2.4 模型方程精度比较

以下, 以正激波结构, 库特流、热蠕动、以及二维热驱动问题为例, 比较不同模型描述稀薄气体流动的精度. 模拟中, 分子气体为氮气, 转动自由度  $d_r = 2$ , 模型中的相关参数选为  $Z = 2.6671, \omega = 0.74$ , 施密特数  $Sc = 1/1.33$ . 吴模型中的热弛豫系数矩阵  $\boldsymbol{A}$  来自 8.1.3 中的 DSMC 模拟, 从而保证吴模型的 Eucken 因子为  $f_{eu} = 1.993, f_{tr} = 2.365$ , 和  $f_{rot} = 1.436$ , 与 DSMC 保持一致; 此外, 我们进一步假设这些参数不随温度变化. Rykov 模型可以通过公式 (8-37) 调整  $\omega_0$  和  $\omega_1$  恢复正确的 Eucken 系数. 从公式 (8-42) 可知, ES-BGK 模型只有一个自由度来恢复总 Eucken 系数, 即 ES-BGK 模型没有分辨平动 Eucken 系数和转动 Eucken 系数的机制. 幸运的是, 对于氮气, ES-BGK 模型给出的平动和转动热导率与 DSMC 非常接近, 见表 8-1 中关于 Eucken 参数的汇总. 再次强调, ES-BGK 和 Rykov 模型中平

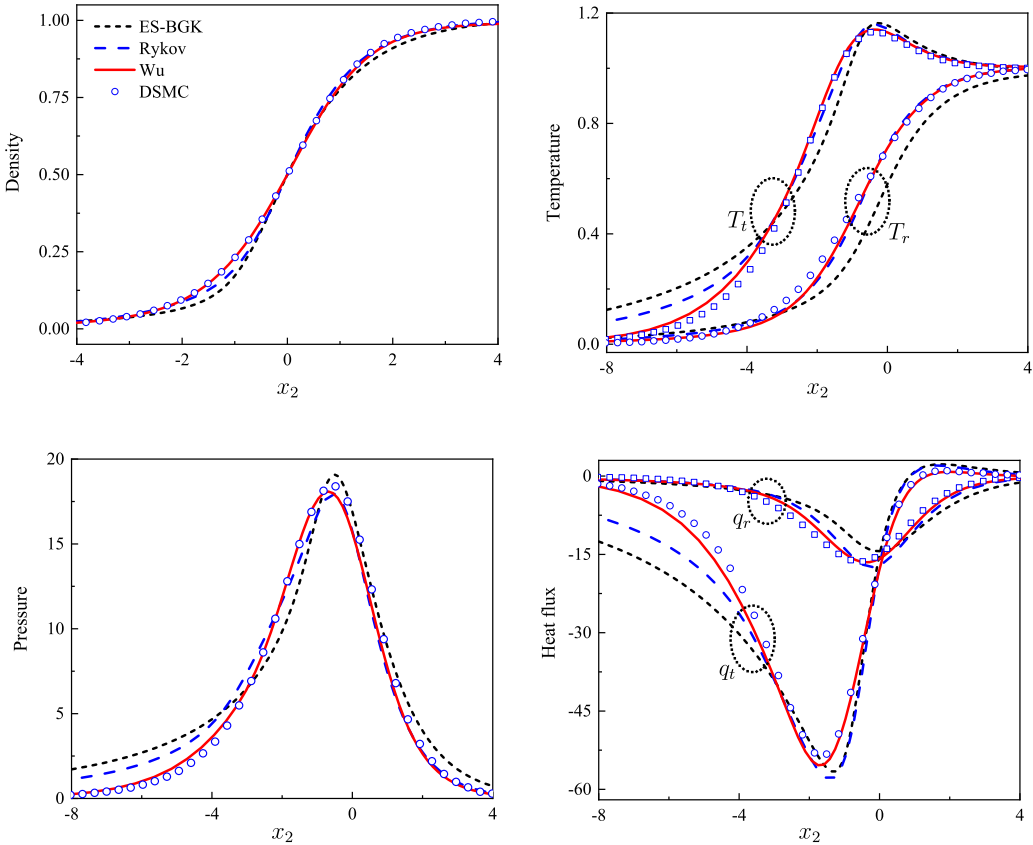


图 8-4 不同动理论模型预测的马赫数为 7 的氮气正激波的密度、温度，应力偏量  $\sigma_{22}$  和热流的对比。

Comparisons in the density, temperature, stress, and heat flux between different kinetic models for a normal shock in Nitrogen gas with Mach number 7.

动和转动热流的弛豫过程是相互独立的。

引入参考密度  $n_0$ 、参考温度  $T_0$ 、最概然速率  $v_m = \sqrt{2k_B T_0/m}$ 、参考压力  $n_0 k_B T_0$ 、参考热流  $n_0 k_B T_0 v_m$ 。宏观量通过参考值进行无量纲化，且无量纲克努森数定义为：

$$\text{Kn} = \frac{\mu(T_0)}{n_0 \ell} \sqrt{\frac{\pi}{2m k_B T_0}}, \quad (8-46)$$

用于表征流动的稀薄程度，其中  $\ell$  为流动特征长度。

在以下各研究问题中，气体在固体表面的反射均用完全漫反射作为边界条件，即气体反射速度分布为满足固体表面宏观量的麦克斯韦分布。在数值解法上，使用离散速度法求解动理论模型，快速谱方法求解玻尔兹曼碰撞项 [? ]，开源软件 SPARTA 进行 DSMC 模拟。

表 8-1 不同动理论模型和 DSMC 模拟中所使用的 Eucken 因子与热弛豫速率. 氮气的 Eucken 因子为  $f_{eu} = 1.993$ .

Eucken factors and heat flux relaxation rates used in different gas kinetic models and DSMC. The total Eucken factor of the Nitrogen at room temperature is  $f_{eu} = 1.993$ .

	ES-BGK	Rykov	Wu	DSMC
$f_{tr}$	2.373	2.365	2.365	2.365
$f_{rot}$	1.424	1.436	1.436	1.436
$A_{tt}$	0.702	0.705	0.786	0.786
$A_{tr}$	0	0	-0.201	-0.201
$A_{rt}$	0	0	-0.059	-0.059
$A_{rr}$	0.702	0.696	0.842	0.842

### 8.2.4.1 正激波

图 8-4 给出马赫数为 7 的一维氮气正激波的结构. 空间坐标用激波上游的分子平均自由程  $L = 16\mu/5n\sqrt{2\pi mk_B T}$  对其进行无量纲化, 密度与温度通过  $(Q - Q_u)/(Q_d - Q_u)$  归一化, 其中  $Q = n, T_t, T_r$ , 下标  $u$  和  $d$  分别代表上游和下游的物理量. 所有动理论模型的密度分布均与 DSMC 计算结果大体上相符, 只有 ES-BGK 模型给出的密度在波前稍低一些. Shakhov 模型和 ES-BGK 模型的平动温度在波前存在“过早温升”现象, 其中 ES-BGK 的平动与转动温度分布偏离最大, 这是因为这两个模型方程的碰撞时间与分子速度无关. 而吴模型和 DSMC 中的碰撞时间都是分子速度的单调递增函数, 因而得到最为接近的结果. 图 8-4(c,d) 给出了压力与热流分布的计算结果, 可见吴模型与 DSMC 符合得非常好, 而其它模型均存在显著误差, 尤其是对比热流的分布.

### 8.2.4.2 库特流动

平板库特流动的上下两板温度相同, 处在  $x_2 = L/2$  的上板速度是  $v_w = v_m$ , 处在  $x_2 = -L/2$  的下板速度相反. 图 8-5 给出各模型和 DSMC 的对比结果. 当  $\text{Kn} = 0.1$ , 所有动理论模型都给出了良好的密度分布. ES-BGK 模型高估了平动温度和平动热流, 却低估了转动热流. Rykov 模型给出良好的温度和转动热流, 却高估了平动热流. 吴模型跟 DSMC 的对比结果非常好. 当  $\text{Kn} = 1$ , 吴模型同样能给出与 DSMC 较为一致的结果. Rykov 模型方程的密度分布与 DSMC 的结果稍有差

别，在两板中心区域略低。ES-BGK 模型的转动温度也略低于其他模型。

### 8.2.4.3 麦克斯韦妖驱动的微流动

考察处在两平行静止的无限长平板间的分子气体，每个气体分子受到与其速度相关的外力的作用：

$$a_y = a_0 \left( \frac{v^2}{v_m^2} - \frac{3}{2} \right), \quad (8-47)$$

在此例中，取  $2a_0 L/v_m^2 = 0.0718$ ，以保证系统仅略微偏离平衡态。可以看出，当分子速率大于  $\sqrt{3/2}v_m$  时，其加速度为正，反之则为负。因此该加速度可以看出是一种特殊形式的麦克斯韦妖，见图 8-6。

图 8-6 给出克努森数分别为 0.1 和 1 的模拟结果对比。吴模型与 DSMC 非常符合，速度剖面与热流分布的最大误差仅为 2%。值得注意的是，ES-BGK 模型和 Rykov 模型的转动热流值远大于吴模型和 DSMC 的结果。其原因在于，这两个模型方程中的平动热流弛豫与转动热流弛豫相解耦，即  $A_{tr} = A_{rt} = 0$ ，即便热导率相近，但热弛豫系数的差别仍可导致显著的宏观量的差异。这正说明了采用正确的热弛豫速率的重要性。

### 8.2.4.4 封闭方腔中的热蠕动

最后，考察二维封闭方腔内的热蠕动问题。方腔宽度与高度比值为 5，固定左板和右板的温度分别为 200 K 和 400 K，而上下两板的温度在此间线性分布。由于此问题以  $x_2 = 0.5$  为轴具有对称性，实际计算区域为方腔的下半部分。取参考温度为 300 K，参考长度为方腔高度，模拟克努森数为  $Kn = 0.6$  的气体流动。

图 8-7 中给出各个动理论模型方程与 DSMC 结果的比较。吴模型的热流云图与速度剖面均与 DSMC 结果相符，而 ES-BGK 模型热流与速度剖面的解与 DSMC 的解有非常大的偏离，并且 ES-BGK 模型计算得到的中心涡更偏向右侧的高温区，且结构范围更小。另外，Rykov 模型在预测热流方面存在一定误差。

本节考察常用的气体动理论模型方程，Rykov 模型、ES-BGK 模型和吴模型，保证所有模型的剪切粘性、体积粘性和总热导率均与 DSMC 相同。在吴模型中，通过调整热弛豫系数分量可以自下而上恢复所有的热导率分量。Rykov 模型可以同时恢复正确的热导率分量，但是无法恢复所有的热弛豫系数，ES-BGK 模型仅有一个参数自由度，用于调整总热导率，其热导率分量的比例不可调整。数值结果表明：

(1) BGK 类模型方程，能很好地模拟低速稀薄流动问题，而对于热导率起主导作用的传热问题，需选择能够分别恢复热导率分量的模型方程。

(2) 在热蠕动中，速度与热流结果取决于平动热导率，并且热弛豫速率分

量对转动热流有影响。若 BGK 类型的模型方程不能独立调整热弛豫速率分量，则不适合用来研究热蠕动流动问题。

(3) 对于非平衡效应较强的正激波问题，即便 BGK 类模型方程能够同时恢复正确的热导率分量与部分热流弛豫速率，若碰撞频率不依赖与分子速度，在高马赫数下波前会有很明显的温度早起现象。

### 8.3 热弛豫速率不确定度量化

为了准确地预测稀薄分子气体的非平衡行为，气体动理论的建模过程应实现正确的剪切粘性、体积粘性以及平动、转动热导率。分子气体的热导率比剪切粘性和体积粘性更加复杂，实验通常只能确定总热导率，但是难以分辨平动与转动分量。虽然在连续流极限下，气体动力学行为取决于气体粘性与总热导率，但是在稀薄流区，分子气体的平动与内能热导率可能对非平衡效应有各自不同的影响。

上文的算例表明，热弛豫速率在稀薄气体流动中也起着重要作用。尽管在 DSMC 和其他分子气体动理论模型中 [79? , 98, 31]，已有大量关于温度弛豫效应（与体积粘性相关）的研究工作，却从未有过关于热弛豫速率矩阵  $A$  对稀薄气体非平衡效应的影响的相关研究。通过实验可以直接测量总热导率，并且在某些情况下，还可以提取平动热导率 [72, 41, 91, 141]。然而，根据公式 (8-13)，弛豫系数矩阵  $A$  中至少有两个元素不能确定，即不同的系数矩阵  $A$  可以对应一致的热导率及其分量。因此有必要量化在输运系数都一致的前提下，由系数  $A$  的变化所带来的宏观量的不确定性。

在 DSMC 中，因碰撞模型的原因，固定体积粘性后，热弛豫系数也随之确定。在吴模型中，可以通过独立修改  $A_{ij}$  以量化热弛豫系数的影响。上文已验证吴模型的准确性，这里我们使用吴模型来量化这种不确定性。首先，在约束  $f_{tr}$  和  $f_{rot}$  不变的前提下修改  $A_{ij}$ ，以研究热弛豫速率的影响。其次，在保持总热导率不变前提下，通过改变  $f_{tr}$  和  $f_{rot}$  来量化热导率分量的影响。

#### 8.3.1 正激波

给定  $f_{tr}$  和  $f_{rot}$ ，即体系中所有的热导率分量都被确定，若此时其余的输运系数也保持不变，则称此系统为宏观意义上的确定系统。然而，不同的  $A_{ij}$  的选择将可能导致结果的不确定性。

考察一维正激波问题， $A_{tr}$ 、 $A_{rt}$  的取值范围分别为  $[-5/(6Z), 0]$  和  $[-1/(3Z), 0]$ ，而  $A_{tt}$  和  $A_{rr}$  的值根据公式 (8-13) 调整，以保持  $f_{tr}$  和  $f_{rot}$  不变。在 DSMC 中非对角线元素为  $A_{tr} = -0.201$ ,  $A_{rt} = -0.059$ ，本例中，给定  $Z = 2.6671$ ,

$A_{rt}$  和  $A_{tr}$  的最小值分别为  $-0.3124$  和  $-0.1250$ , 数值大小约为 DSMC 对应参数的一到两倍. 我们发现, 热弛豫系数  $A$  的变化导致转动温度和转动热流稍有变化, 而对密度、速度和应力偏量几乎没有影响.

接着, 我们保持总热导率不变, 且选择  $A_{tr} = -5/(6Z), A_{rt} = -1/(3Z)$ , 研究热导率分量的改变对流动的影响. 图 8-8 展示了马赫数为 4 时, 不同平动 Eucken 因子下 W 模型的数值结果. 在实际中, 较小数值的平动 Eucken 因子  $f_{tr}$  是可能存在的, 特别是在极性气体中, 真实的平动 Eucken 因子可能远小于 2.5. 例如, 水的平动 Eucken 因子为  $f_{tr} = 1.78$ , 甲醇分子 [?] 的平动 Eucken 因子为  $f_{tr} = 0.41$ . 从对比中可以看出, 所有的宏观量都随  $f_{tr}$  改变而有明显的变化. 首先, 较大的  $f_{tr}$  使得平动温度更快上升到其最大值, 并在波后更快趋于下游温度, 对于应力偏量和总热流也有相同的趋势. 其次,  $f_{tr}$  变化所导致的转动温度变化则集中于激波结构的中心处, 较小的  $f_{tr}$  导致更高的转动温度. 最后, 较大的  $f_{tr}$  使得密度升高更快.

由此, 在正激波问题中, 由热弛豫系数  $A$  的变化引起的不确定性较小, 而热导率分量的变化则会带来显著的不确定性. 例如,  $f_{tr} = 1.5$  的转动热流大约是  $f_{tr} = 2.5$  的两倍, 几乎与平动热流相当.

而对于由不同热弛豫系数引起的不确定性, 图中 ?? 矩阵  $A$  给总热流带来的不确定性仅为 7.4%.

### 8.3.2 麦克斯韦妖驱动的微流动

使用正激波算例中的同一系列矩阵  $A$ , 并使  $f_{tr}$  和  $f_{rot}$  均保持不变, 来考察麦克斯韦妖驱动的微流动中, 热弛豫系数对流动速度和热流的影响. 图 8-9 第一行图片数据为  $\text{Kn} = 0.2$  的结果. 可以看出, 不同于正激波问题, 此问题中不同热弛豫系数  $A$  对应的流动速度与热流有相当明显的差别. 流动速度和平动热流的最大相对不确定性分别为 16.7% 和 17.6%. 同时可以看出, 流动的中间区域出现了较大的不确定性, 而壁面附近的速度滑移与热流几乎不变.

为进一步研究平动 Eucken 因子的影响, 考察 Eucken 因子  $f_{tr} = 1.5, 2.0, 2.5$  的算例, 其余参数为  $\text{Kn} = 0.2, f_u = 1.993, A_{tr} = -5/6Z, A_{rt} = -1/3Z$ . 如图 8-9 第二行图片数据所示, 速度曲线与平动热流随着平动 Eucken 因子的变化而剧烈变化.  $f_{tr} = 2.5$  时的流动速度和热流比  $f_{tr} = 1.5$  时增加了大约 68%. 在第一行图中, 在确定的  $f_{tr}$  下, 壁面速度滑移与热流不受平动 Eucken 因子的影响. 而在第二行图中, 速度与热流依赖于平动 Eucken 因子, 例如, 壁面附近的速度与热流均与  $f_{tr}$  呈正相关. 这说明, 在此问题中, 平动 Eucken 因子  $f_{tr}$  起主导作用.

平动 Eucken 因子在此问题中的重要性可得到如下解释: 从方程 (8-13) 可以看出, 热弛豫系数  $A_{tr}$  和  $A_{rt}$  与平动能与转动能之间的能量交换有关. 当  $A_{tr}$  与  $A_{rt}$

为零时，平动热流与转动热流的弛豫过程互相解耦。例如，更多的计算结果显示，在  $A_{rt} = 0$  的情况下，转动热流恒为零。这是因为麦克斯韦妖驱动的热蠕动流动中，外力项仅能直接影响平动能，而转动能和热流则需通过能量交换才能发生改变，具体取决于  $A_{tr}$ ,  $A_{rt}$  和  $Z$ 。由于矩阵的非对角元素相对于其他元素为小量，这导致  $q_{rot} \approx 0$ ，而平动效应 ( $q_{tr}$  或者  $f_{tr}$ ) 占主导。

## 8.4 确定热流弛豫速率的方法

上文的研究结果揭示了热流弛豫速率不确定性对稀薄气体流动的影响，因此有必要通过获取并使用正确的相应系数，来减少或消除模型的不确定性。我们认为可以尝试以下两种方法。

### 8.4.1 分子动力学模拟

从物理上来说，只要知道了分子间的相互作用势，根据牛顿第二运动定律，就可以通过分子动力学方法模拟气体的行为。由此，输运系数能够通过 Green-Kubo 公式获得 [34, 55]：

$$\mu = \frac{1}{V} \frac{1}{k_B T} \int_0^\infty \langle J_{xy}^p(0) J_{xy}^p(\tau) \rangle d\tau, \quad (8-48)$$

$$\frac{4}{3}\mu + \mu_b = \frac{1}{V} \frac{1}{k_B T} \int_0^\infty \langle J_{xx}^p(0) J_{xx}^p(\tau) \rangle d\tau, \quad (8-49)$$

$$\kappa = \frac{1}{V} \frac{1}{k_B T^2} \int_0^\infty \langle J_x^q(0) J_x^q(\tau) \rangle d\tau, \quad (8-50)$$

其中， $V$  和  $T$  分别是模拟系综的体积和温度， $\tau$  为时间，尖括号表示系综平均； $J^p = m\mathbf{c}_i \mathbf{c}_i - pV\mathbf{I}$ ,  $J^q = E_i \mathbf{c}_i$ ,  $\mathbf{I}$  是单位矩阵。对于单原子气体， $E_i = mc_i c_i / 2$  得到平动热导率。对于分子气体，取  $E_i = \epsilon_i$  为第  $i$  个分子的内部能量，则公式(8-50) 给出内部热导率。

然而，对于如何获得热流弛豫矩阵系数尚不清楚。一个可行的方法是仿照8.1.3中介绍的 DSMC 方法，即在分子动力学中设置带有初始热流的状态，模拟低密度气体的演化过程，然后通过拟合公式(8-13)获得弛豫系数。目前尚未有相关工作的报道，但是原理上是可行的。

### 8.4.2 瑞利-布里渊散射

瑞利-布里渊散射指的是光在气体中传播时，被气体分子的自发密度涨落散射。由于散射光谱包含气体信息，因此可以用来无损测量声速、流速、温度和体积粘性 [88, 132, 39]。例如，欧洲航天局于 2018 年发射的 ADM-Aeolus 卫星，测量从地球表面到 30 公里高度的全球风速，用于提高天气预报精度。

如图 8-11 所示，波矢为  $\mathbf{k}_i$  的入射光被散射，散射角为  $\theta$ ，则散射波数为  $k = |\mathbf{k}_i - \mathbf{k}_s| = 2|\mathbf{k}_i| \sin(\theta/2)$ 。散射光强度与光谱密度函数  $S(f_s)$  相关，即密度扰动相关函数  $G(\mathbf{r}, t)$  的时空傅里叶变换。假设散射波沿  $x_2$  方向传播，相关函数和谱密度函数的解 [121, 94] 为

$$G(x_2, t) = \int_{-\infty}^{\infty} n(l + x_2, t) n(l, 0) dl, \quad (8-51)$$

因此，频谱为

$$\begin{aligned} S(f_s) &= \int_{-\infty}^{\infty} \int_{-\infty}^{\infty} G(x_2, t) e^{i(kx_2 - 2\pi f_s t)} dx_2 dt, \\ &= \end{aligned} \quad (8-52)$$

式中， $i$  为虚数单位， $n(x_2, t)$  为密度扰动， $f_s$  为散射频率。

对于短波长和高散射频率，应该使用气体动理论来描述密度扰动的演化过程。以单原子气体为例说明瑞利-布里渊散射的计算。密度扰动量与公式(2-22)中分布函数扰动量  $\phi$  有关，初始密度脉动可定义为 [121, 146]： $\phi(t = 0, x_2, \xi) \propto \delta(x_2)$ 。取特征长度为散射波长  $\ell = 2\pi/k$ ，通过时间上的拉普拉斯变换与空间上的傅里叶变换求解线性化玻尔兹曼方程(2-23)，可得

$$2\pi i(f_s - \nu_2)\hat{\phi} = \frac{\ell}{v_m} J(\hat{\phi}) + 1, \quad (8-53)$$

其中方程右端的 1 来自于初始密度扰动对应的拉普拉斯变换， $\hat{\phi}(\mathbf{v})$  分别对应  $\phi$  的时空坐标下的拉普拉斯和傅里叶变换 [? ]。散射频谱可通过以下公式计算

$$S(f_s) = \text{Re} \left( \int \hat{\phi} f_{eq}(\xi) d\xi \right), \quad (8-54)$$

其中  $\text{Re}$  表示复数的实部。

### 8.4.3 氮气分子的体积粘性与 Eucken 因子

### 8.4.4 Bulk viscosity and Eucken factor of N<sub>2</sub>

此例中，我们根据荷兰自由大学的实验数据 [39] 来提取氮气的体积粘性和平动 Eucken 因子。其中，激光波长为 366.8 纳米，散射角为 90°，因此等效波长为  $\ell = 259.4$  纳米。实验条件下氮气的转动自由度与振动自由度分别为  $d_r = 2$  和 0。剪切粘性和热导率根据 Sutherland 公式计算。通过调整吴模型中非弹性碰撞数和平动热导率，使得实验数据和数值模拟得到的频谱偏差最小。表 8-2罗列了不同温度下气体物性参数和提取的碰撞数与热导率分量。

从上面的结果我们可以看出，误差函数存在全局最小值，并且为凸函数，因此，为了准确有效的确定转动碰撞数  $Z$  和平动 Eucken 因子  $f_{tr}$ ，我们使用了以下方法。

From the above results we find that the error function  $E(Z, f_{tr})$  has one global minimum and is convex. Therefore, to accurately and efficiently determine  $Z$  and  $f_{tr}$ , we adopt the following procedure.

(1) 首先给定平动 Eucken 因子  $f_{tr}$ ，改变  $Z$  的值，并基于吴模型计算 RBS 频谱。然后将获得的光谱与响应函数卷积得到  $S_{WU}(f_s)$  频谱，误差定义为：

$$E(Z) = \sum_{\ell=1}^N \frac{\{S_{exp}[f_s(\ell)] - S_{WU}[f_s(\ell)]\}^2}{N}, \quad (8-55)$$

式中， $N$  是在实验中测量的离散频率数。将  $E$  拟合为  $Z$  的四次多项式，并找到该函数的最小值，进而可以找到最小误差将  $E_m(f_{tr})$ 。此过程中，通常会计算 6 个不同的  $Z$  值。

(2) 对于不同的  $f_{tr}$ ，重复步骤 1。与步骤 1 相同，通常会计算 6 个不同的  $f_{tr}$  值。

(3) 将  $E_m(f_{tr})$  拟合为  $f_{tr}$  的四次多项式函数，进而确定函数最小值对应的  $f_{tr}$ 。

(4) 使用步骤 3 得到的  $f_{tr}$ ，再次执行步骤 1，以确定转动碰撞数  $Z$ ，最后可通过公式 (8-11)确定体积粘性。

实验结果与解析解的误差在 1% 内，

实验数据与吴模型最佳预测的比较如图 8-12所示。实验 [56] 测得氮气在标准温度和压力下的转动弛豫时间为  $\tau_r = 7.4 \times 10^{-10}$  s，在 296.7 K 下，测得的氮气体积粘性为  $\mu_b = 1.22 \times 10^{-5}$  kg · m<sup>-1</sup> · s<sup>-1</sup>。根据公式 (8-11)计算得到氮气的体积黏

表 8-2 自发瑞利-布里渊散射实验中, 氮气相关参数汇总以及根据吴模型从实验数据中提取的体积粘性与平动/转动 Eucken 因子. 剪切粘性与总热导率均使用国际单位制.

Experimental conditions in the spontaneous Rayleigh-Brillouin scattering, and the extracted bulk viscosity, translational/rotational Eucken factors from the Wu model. The SI units are adopted for the shear viscosity and thermal conductivity.

实验	$T$ (K)	$10^5 \mu_s$	$100\kappa$	$P$ (bar)	$\omega$	$\mu_b/\mu_s$	$f_{tr}$	$f_{rot}$
(a)	254.7	1.57	2.28	2.563	0.80	0.48	2.16	1.65
(b)	275.2	1.67	2.44	2.784	0.78	0.61	2.25	1.53
(c)	296.7	1.77	2.60	3.000	0.76	0.69	2.31	1.47
(d)	336.6	1.95	2.88	3.400	0.74	0.94	2.43	1.33

实验	$f_{tr}$	$f_{rot}$	$f'_{tr}$	$f'_{int}$	$f''_{tr}$	$f''_{int}$
(a)	2.16	1.65	2.17	1.58	2.12	1.61
(b)	2.25	1.53	2.24	1.52	2.14	1.59
(c)	2.31	1.47	2.27	1.50	2.16	1.58
(d)	2.43	1.33	2.33	1.45	2.18	1.56

性为

$$\mu_b = 2p\tau_r \frac{d_r}{(3 + d_r)^2} = 1.18 \times 10^{-5} \text{ kg} \cdot \text{m}^{-1} \cdot \text{s}^{-1}.$$

这一结果与实验值吻合较好. 另外, 提取的平动 Eucken 因子也在合理的范围.

Mason 推导了 WCU 方程的 Eucken 因子解析解, 而通过 RBS 试验同样可以得到平动 Eucken 因子与转动 Eucken 因子. 本节将对这两组结果进行比较. 在 Mason 的文章 [?] 中, 对于表 8-2 中的温度, 给定氮气的  $\rho D'/\mu = 1.32$ . 将实验提取的转动碰撞数  $Z$  代入 Eucken 因子解析解中, 并与表 8-2 的实验数据进行比较. 对比结果表明:  $f_{tr}$  与  $f'_{tr}$ , 以及  $f_{rot}$  与  $f'_{int}$  较为一致, 最大相对偏差不大于 10%. 进一步地, 考察了平动 Eucken 因子与转动 Eucken 因子解析解与测量值的区别. 对于单原子气体, 玻尔兹曼方程的输运系数解析解与实验值吻合较好, 相对误差小于 2%, 对于分子气体, 输运系数的解析解与实验数据差别较大, 这可能是因为在解析解的推导过程中引入了近似值.

从建模的角度出发, 经典模型方程把分子气体运动中的弹性碰撞与非弹性碰撞看做是简单的弛豫过程.

## 8.5 总结与展望

本文回顾了国内外学者在稀薄效应动理论建模中所取得的进展，包含单原子气体与分子气体。由于高温真实气体效应，当分子内自由度增加时，分子间复杂的相互作用通常伴随着更加新颖、复杂的物理现象，这对稀薄分子气体动理论建模提出了很高的要求。我们指出应力偏量、能量交换、热流的弛豫过程是运输现象的本质，而剪切粘性、体积粘性、平动/内部热导率等运输系数则是表象，即，随着克努森数的变化，这些运输系数对应的本构关系会失效，而相应的弛豫过程和速率不会改变。为了准确预测稀薄分子气体的非平衡行为，气体动理论的建模过程应尽可能准确地捕捉应力偏量、能量交换、热流的弛豫过程和速率。

本文还介绍了 DSMC 中提取热弛豫速率的方法，并讨论了 DSMC 方法恢复热导率的能力。虽然经典的 Larsen-Borgnakke 模型可以通过调整非弹性碰撞概率改变体积粘性，但是很难同时调整热导率及其分量。而这些分量的比例以及本质的热流弛豫时间对稀薄气体流动的影响巨大。因此，非常有必要对 DSMC 碰撞模型进行修改和优化。

非常有意思的是，基于王承书等人的工作，分子气体的线性化理论和方法已经非常成熟。而非线性模型虽然五花八门，但都与线性化模型存在着本质联系，即所有的非线性模型都可以通过对线性化 Gross-Jackson 模型和 Hanson-Morse 模型的非线性化而来。本文首次给出一个非线性化方案。

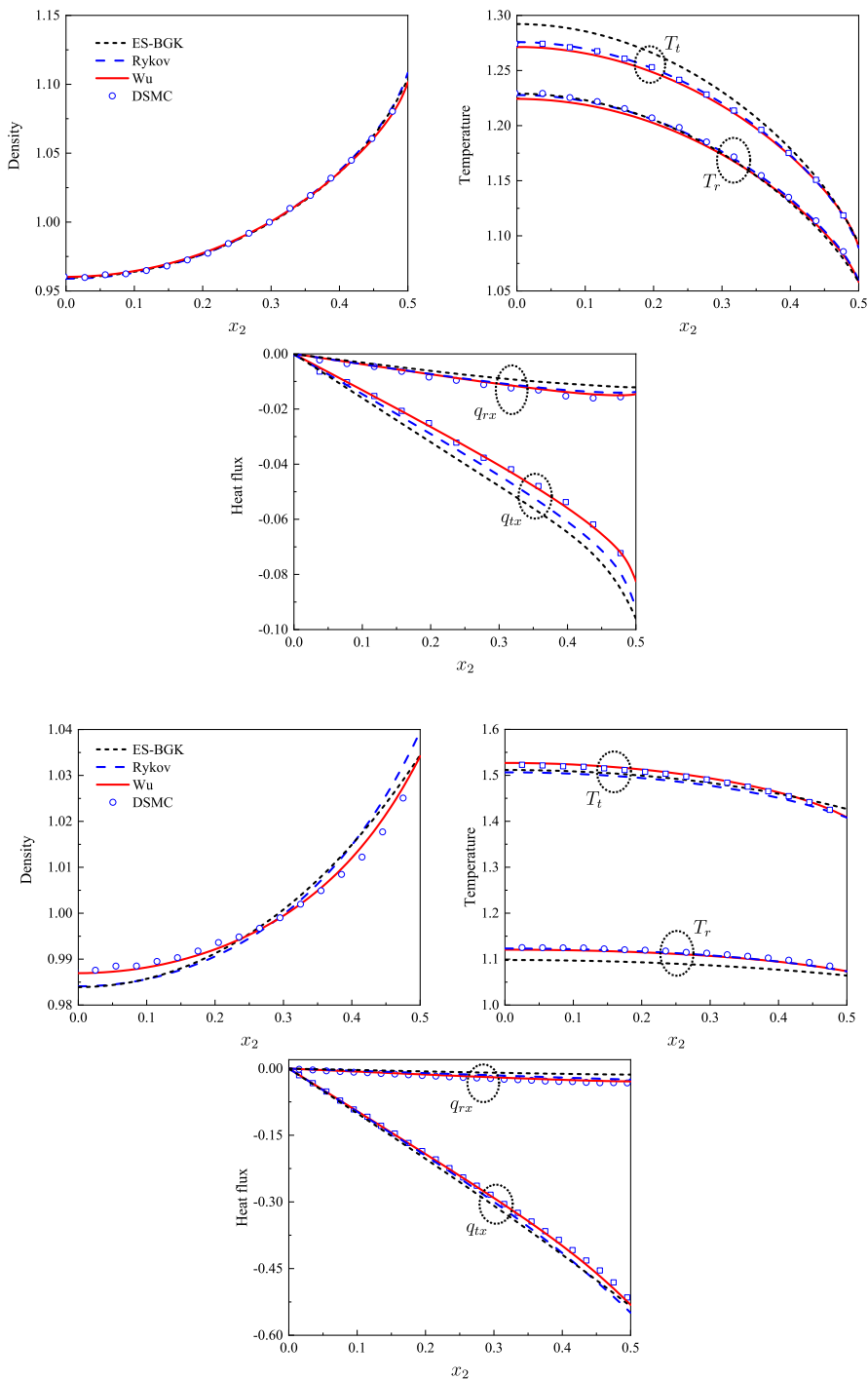


图 8-5 平板库特流动中的密度、温度和垂直于流动方向的热流分布. 第一行和第二行的克努森数分别为  $\text{Kn} = 0.1$  和 1. 基于对称性, 另一半区域  $-0.5 \leq x_1 \leq 0$  没有显示.

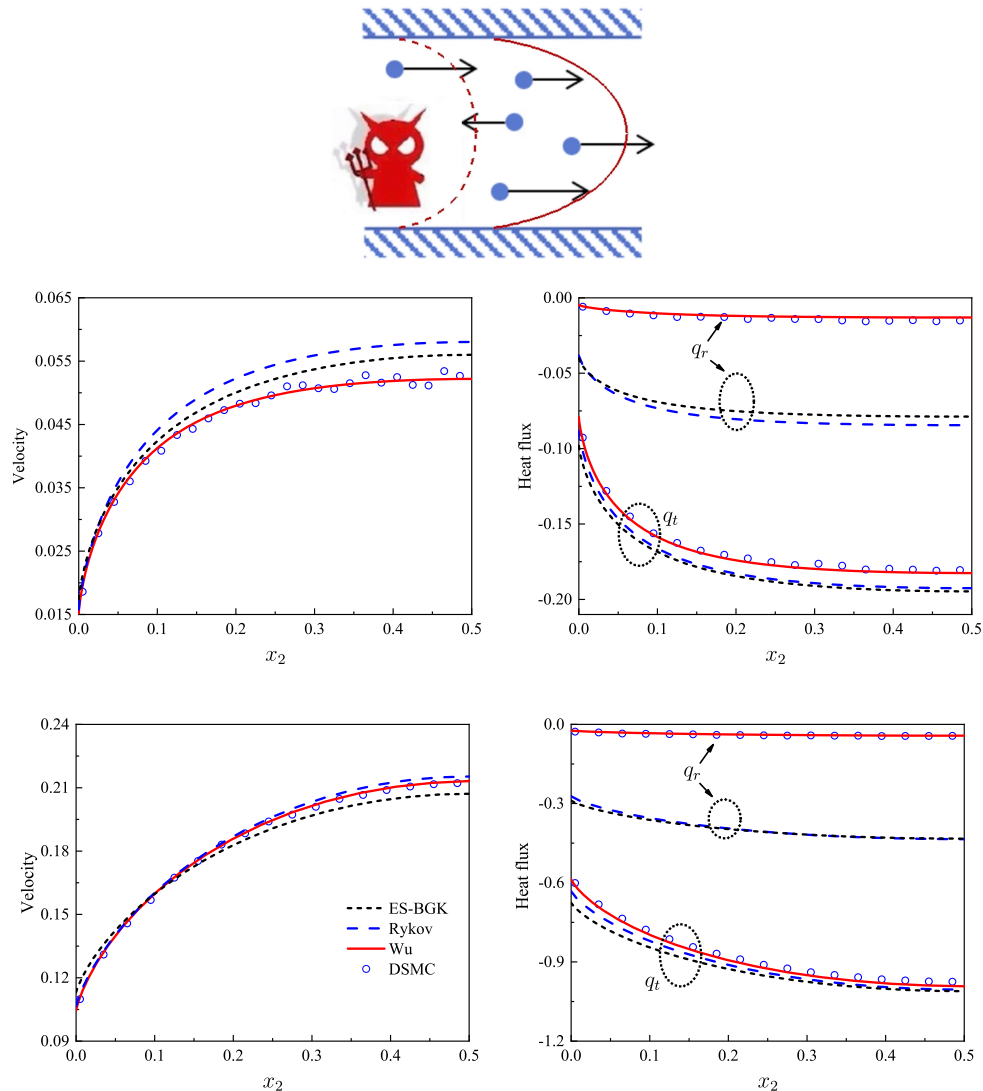


图 8-6 麦克斯韦妖驱动下的稀薄气体热蠕动, 其中速度和热流均沿  $x_1$  方向. 第二行和第三行图对应的克努森数分别为  $\text{Kn} = 0.1$  和 1. 基于对称性,  $0.5 \leq x_2 \leq 1$  的区域没有显示.  
Profiles of the vertical velocity and heat flux in the thermal creep flow driven by the Maxwell demon, where the Knudsen number in the second and third rows is  $\text{Kn} = 0.1$  and 1, respectively. Due to symmetry, the other half region  $0.5 \leq x_2 \leq 1$  is not shown.

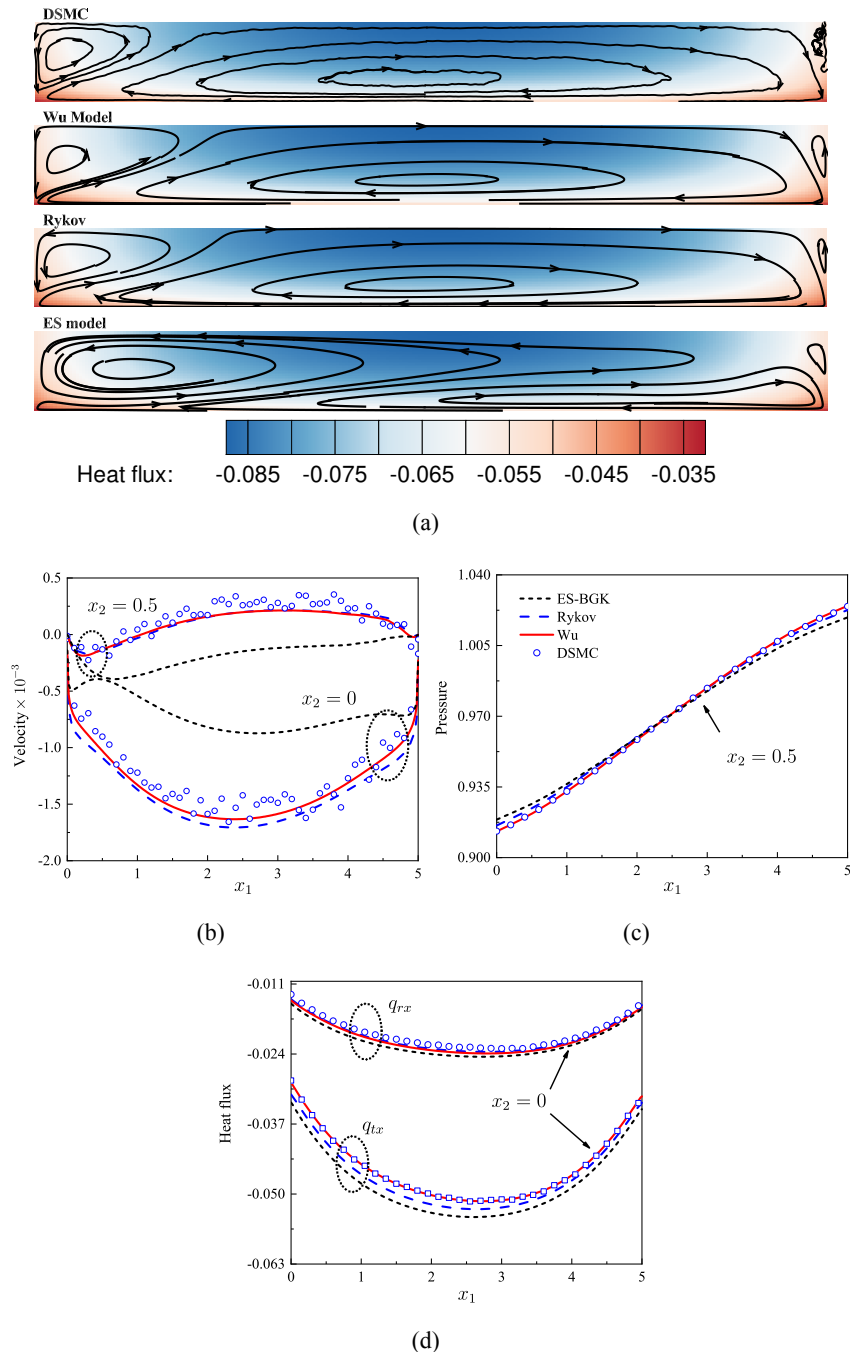


图 8-7 克努森数为 0.6 的稀薄气体在二维方腔内的热蠕动. (a) 流场与  $x_1$  方向的平动热流云图. (b)  $x_2 = 0, 0.5$  处的速度剖面. (c)  $x_2 = 0.5$  处的正压力. (d)  $x_2 = 0$  处的平动和转动热流.

Rarefied gas flow driven by temperature gradient in the solid walls. (a) The streamlines and the contour of translational heat flux in the  $x_1$  direction. (b) Velocity profiles at  $x_2 = 0$  and 0.5. (c) The normal pressure at  $x_2 = 0.5$ . (d) The translational and rotational heat fluxes along the bottom wall.

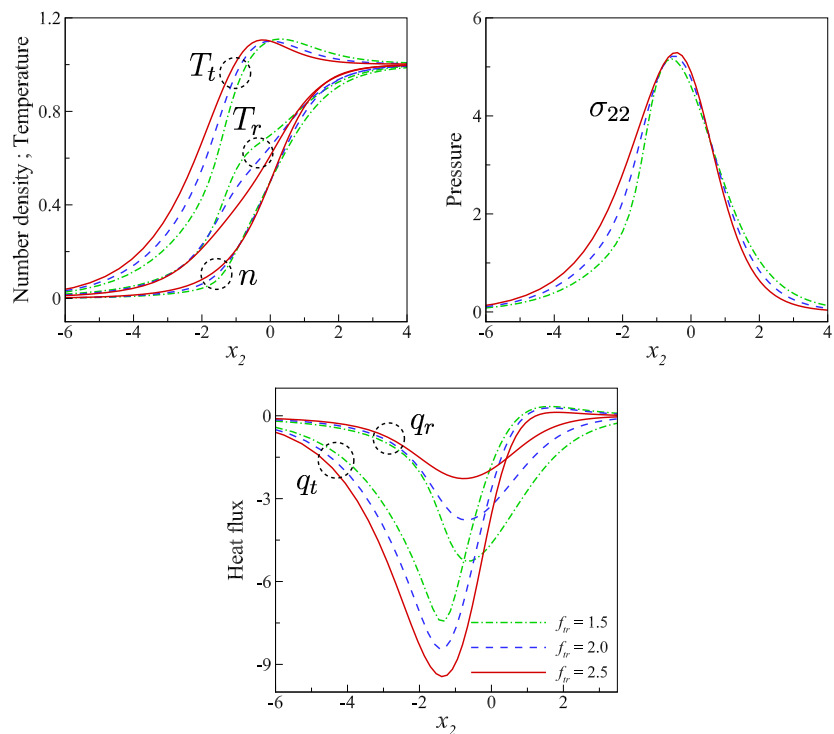


图 8-8 总 Eucken 因子不变时, 不同平动 Eucken 因子对马赫数为 4 的正激波结构的影响.  
图中数据来源于文献 [? ]

Influence of the translational Eucken factor on the structure of normal shock wave with Mach number 4. The figures are from reference [? ].

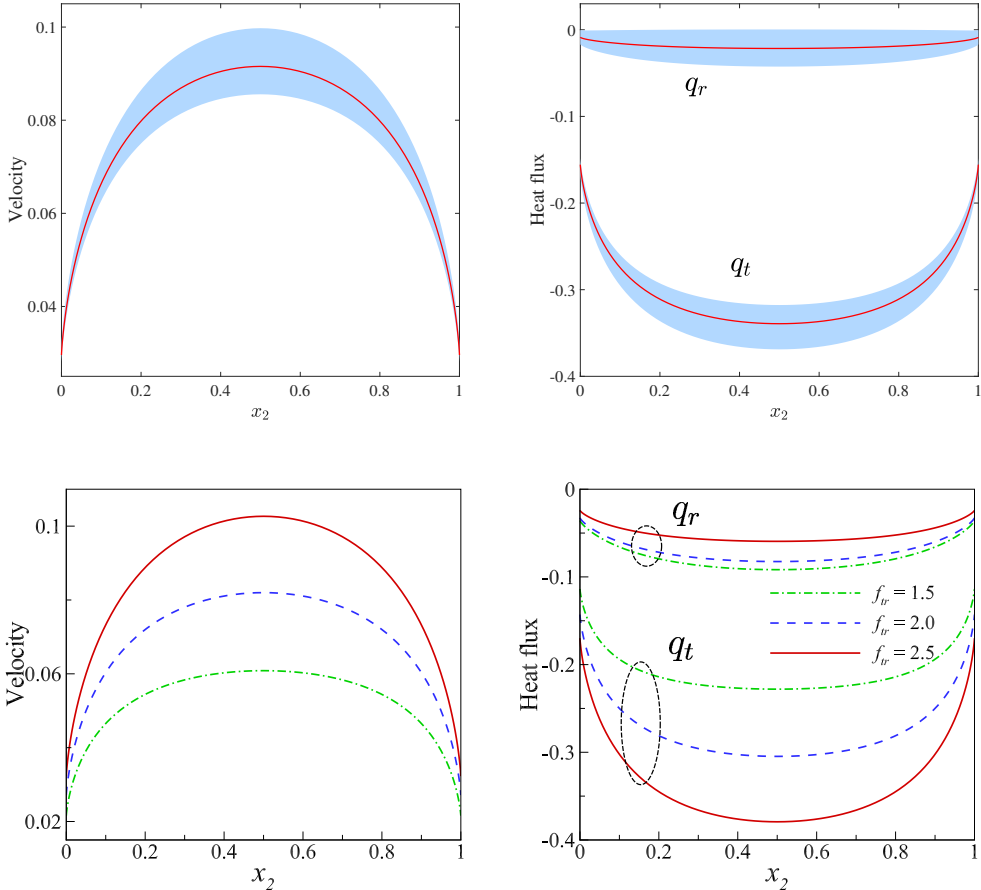


图 8-9 (第一行) 热流弛豫速率对麦克斯韦妖驱动的热蠕动速度和热流分布的影响. 吴模型中改变热弛豫速率的结果对比. 红色实线对应于 DSMC, 蓝色阴影部分来自吴模型计算结果, 对应的取值范围为  $A_{rt} \in [-0.3124, 0.0]$ 、 $A_{tr} \in [-0.1250, 0.0]$ . 其余参数为  $\text{Kn} = 0.2$ ,  $f_{tr} = 2.365$  以及  $f_{rot} = 1.435$ . (第二行) 总 Eucken 因子  $f_u$  保持不变, 改变平动 Eucken 因子的结果对比.  $\text{Kn} = 0.2$ . 图中数据来源于文献 [? ].

(First row) Influence of the thermal relaxation rates in the creep flow driven by the Maxwell demon. Red solid lines are the results with  $A$  extracted from DSMC, blue shade region shows the results from the kinetic model (8-43), with  $A_{rt} \in [-0.3124, 0.0]$  and  $A_{tr} \in [-0.1250, 0.0]$ . Other parameters are  $\text{Kn} = 0.2$ ,  $f_{tr} = 2.365$  and  $f_{rot} = 1.435$ . (Second row) Influence of the translational Eucken factor, while  $f_u$  is fixed. The Knudsen number is  $\text{Kn} = 0.2$ . The figures are from reference [? ].

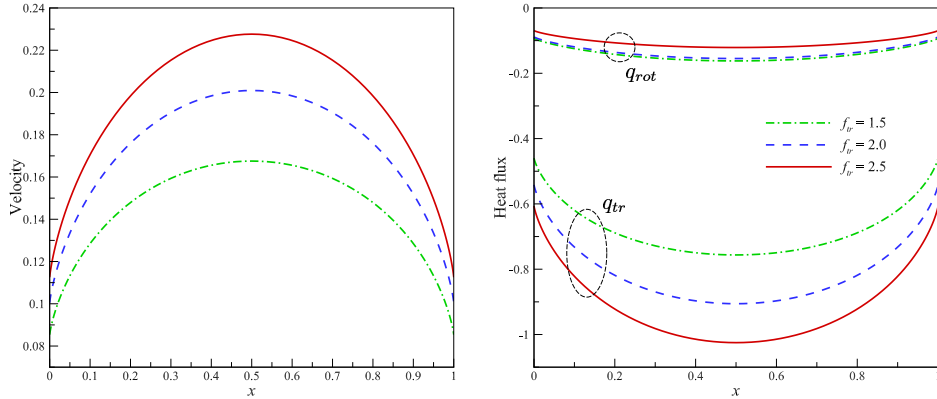


图 8-10 在麦克斯韦妖驱动的热蠕动中, 不同平动 Eucken 因子的结果对比. 总 Eucken 因子  $f_u$  保持不变,  $\text{Kn} = 1$ .

Influence of the translational Eucken factor in the creep flow driven by the Maxwell demon. All cases have the same  $f_u$  and  $\text{Kn} = 1$ , while  $f_{tr}$  for green dash-dot, blue dashed, and red solid lines are 1.5, 2.0, and 2.5, respectively.

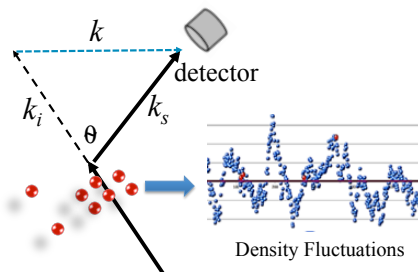


图 8-11 自发瑞利-布里渊散射示意图 [141], 在气体中传播的光被气体分子自发的密度涨落散射.

Schematic of the spontaneous Rayleigh-Brillouin scattering[141], where the light is scattered by the spontaneous density fluctuations in the gas.

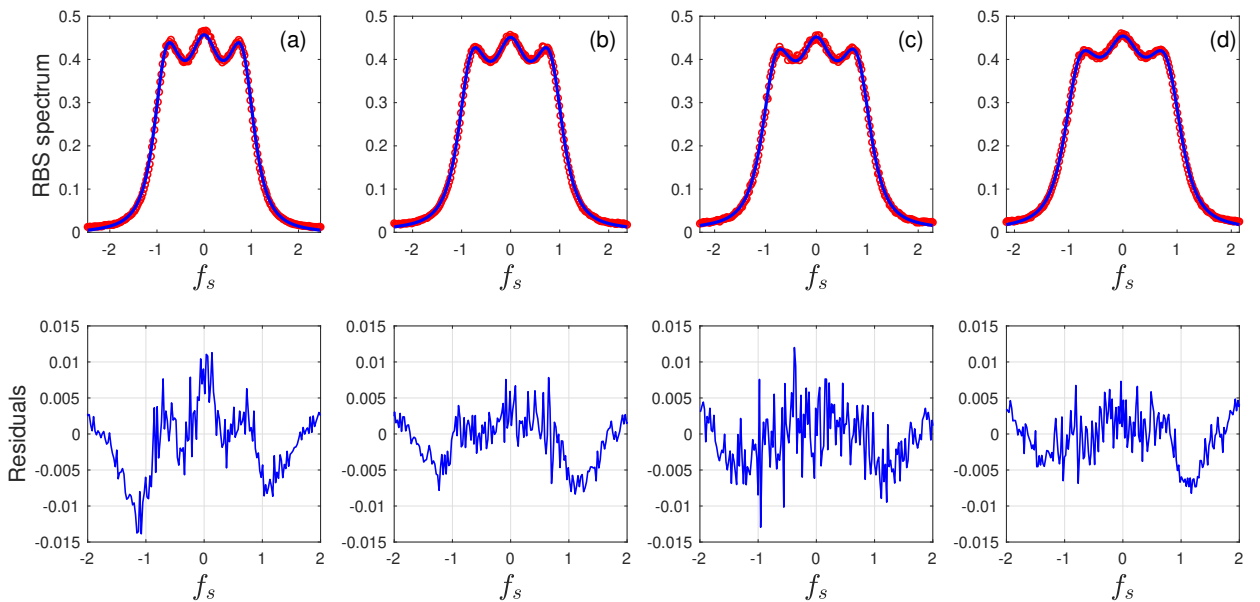


图 8-12 基于实验频谱(圆圈)和吴模型预测结果(线条), 提取氮气的体积粘性与平动 Eucken 因子 [141]. 第一行的实线为计算光谱, 通过计算给定  $f_{tr}$  和 Z 范围内的最小误差. 第二行给出了实验光谱与理论光谱之间的误差. 实验与计算中所用到的参数汇总在表 8-2 中. 频率  $f_s$  由  $v_m/\ell$  归一化.

Extraction of the bulk viscosity and translational Eucken factor of Nitrogen from the experimental spectra (circles) [141]. Lines in the first row show the spectra obtained from the Wu model, while those in the second row show the corresponding residuals between the experimental and theoretical spectra. Experimental conditions and extracted parameters are summarized in Table 8-2. The frequency  $f_s$  is normalized by  $v_m/\ell$ .

## 第 9 章 Slip and Jump Coefficients

When the Knudsen number is small, rarefaction effects only dominate in the Knudsen layer, hence techniques in the computational fluid dynamics can be used to describe RGD with the velocity-slip and temperature-jump boundary conditions [107, 65, 57]. This chapter is dedicated to the calculation of slip and jump coefficients, as well as the Knudsen layer function, based on the gas kinetic theory.

### 9.1 State of the problem

A sketch of the slip velocity and Knudsen layer around the planar plate is shown in Fig. 9-1. Based on the gas kinetic theory, Maxwell proposed an expression for the slip velocity  $u$  at solid surface [74]:

$$u|_{x_2=0} = \sigma_P \frac{v_m \mu}{p} \frac{\partial u}{\partial x_2} \Big|_{x_2=0} + \sigma_T \frac{\mu}{\rho T} \frac{\partial T}{\partial x_3} \Big|_{x_2=0}, \quad (9-1)$$

where  $x_3$  and  $x_2$  are respectively the Cartesian coordinates in the parallel and normal directions to the solid surface;  $\sigma_P$  and  $\sigma_T$  are respectively the viscous slip coefficient (VSC) and thermal slip coefficient (TSC), which can be determined from the LBE [87, 110, 117] or from experiments [4, 91, 97, 149]. With the diffuse-specular BC, Maxwell derived

$$\sigma_P = \frac{2 - \alpha_M}{\alpha_M}, \quad \sigma_T = \frac{3}{4}. \quad (9-2)$$

Likewise, the temperature jump at the solid wall is defined as (the schematic is the same as that in Kramer's problem when the velocity is replaced by the temperature)

$$T = T_w + \zeta_T \frac{\mu}{p} \sqrt{\frac{2k_B T_w}{m}} \frac{\partial T}{\partial \mathbf{n}}, \quad \text{at wall}, \quad (9-3)$$

where  $T$  and  $T_w$  are the gas temperature and the wall temperature, respectively;  $\zeta_T$  is the constant temperature jump coefficient, and  $\mathbf{n}$  is the unit inward normal vector at the wall. A rough estimation of the coefficient  $\zeta_T$  for the diffuse-specular boundary condition is written as [51, 62]

$$\zeta_T = \frac{\gamma \sqrt{\pi}}{(\gamma + 1) \text{Pr}} \left( \frac{2 - \alpha_M}{\alpha_M} + 0.17 \right), \quad (9-4)$$

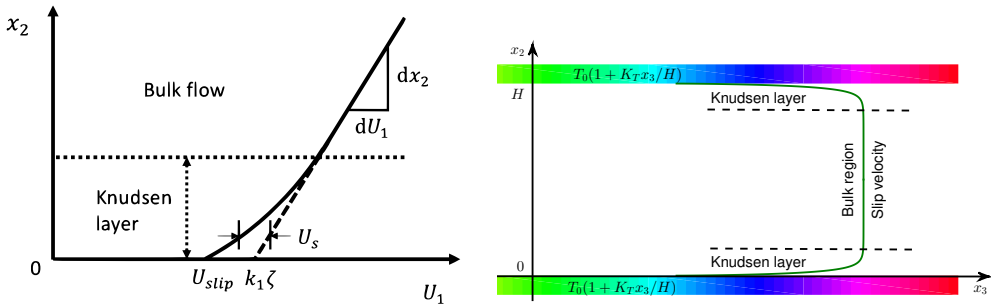


图 9-1 (左) 斯密特问题中 Knudsen 层的示意图。速度缺陷 (Knudsen 层函数)  $u_s$  描述了从 bulk 流区域 (实线) 到 Knudsen 层 (虚线) 的速度偏差。右侧展示了两平行板间的热传吸，气体从冷区 (蓝色) 向热区 (红色) 移动，尽管存在均匀气压。在 Knudsen 层内，真实速度与 bulk 区域的滑移速度存在显著偏差。

where  $\gamma$  is the specific heat ratio of gas.

Many problems remain, e.g., (i) why the TSC is not a function of TMAC and (ii) how does the intermolecular potential and internal structure of molecular gases affect the slip and jump coefficients, are not addressed. This chapter is dedicated to answering these questions.

## 9.2 Thermal slip

The GSIS is applied to find the steady-state solution of thermal transpiration [136, 118]. When the steady-state solution is obtained, the KLF, which is the defect velocity  $u_d$  inside the Knudsen layer, is calculated according to the following equation:

$$u_d\left(\frac{x_2}{Kn}\right) = \frac{1}{Kn} \left[ u_3\left(\frac{1}{2}\right) - u_3(x_2) \right]. \quad (9-5)$$

Meanwhile, the TSC is calculated as

$$\sigma_T = 2\delta_{rp}u_3\left(\frac{1}{2}\right). \quad (9-6)$$

### 9.2.1 Thermal slip coefficient

Very little data of TSC has been obtained from the LBE [134, 109], particularly the TSCs for different intermolecular potentials. Here, we close this gap by solving the LBE via SIS, for different intermolecular potentials and gas-surface interactions.

Figure 9-2 shows the TSC in the diffuse-specular BC. When  $\alpha_M$  is fixed, in most cases the TSC increases with the viscosity index, except that this trend is reversed when  $\alpha_M$  approaches zero. When the intermolecular potential is fixed, we find that the data

表 9-1 TSCs for HS, Maxwellian and VHS ( $\omega = 1.5$ ) molecules under the Cercignani-Lampis BC with different values of TMAC and EAC.

$\alpha_t$	$\omega$	$\alpha_n = 0.25$	$\alpha_n = 0.5$	$\alpha_n = 0.75$	$\alpha_n = 1$
0.25	0.5	0.878961	0.939289	0.997097	1.052749
	1.0	0.957507	1.031589	1.103622	1.173821
	1.5	1.073727	1.166016	1.256071	1.343934
	0.5	0.915032	0.953837	0.99152	1.028174
	1.0	1.038391	1.085497	1.132079	1.178087
	1.5	1.207714	1.265554	1.323069	1.380077
0.75	0.5	0.963946	0.982787	1.001310	1.019504
	1.0	1.111326	1.134018	1.156801	1.179587
	1.5	1.309165	1.336765	1.364675	1.392753
	0.5	1.018280	1.018280	1.018280	1.018280
	1.0	1.179794	1.179794	1.179794	1.179794
	1.5	1.394533	1.394533	1.394533	1.394533
1.25	0.5	1.070999	1.053104	1.035091	1.017060
	1.0	1.245767	1.224484	1.202513	1.180003
	1.5	1.476314	1.450674	1.423957	1.396309
	0.5	1.114835	1.079992	1.044506	1.008646
	1.0	1.310156	1.269058	1.226052	1.181462
	1.5	1.564814	1.515439	1.463286	1.408579
1.75	0.5	1.142984	1.092304	1.040058	0.986740
	1.0	1.372910	1.313785	1.251073	1.185256
	1.5	1.667706	1.596793	1.520959	1.440373
	0.5	1.150836	1.085729	1.017732	0.947616
	1.0	1.433179	1.358215	1.277626	1.191998
	1.5	1.788740	1.698623	1.601268	1.496587

obtained from the LBE can be approximately fitted by linear functions of  $\alpha_M$ , with the relative discrepancy between fitting results and numerical data being less than 1.5%; and the slope of fitting increases with the viscosity index.

Table 9-1 and Fig. 9-3 summarize the TSC computed from the LBE for HS, Maxwellian, and VHS ( $\omega = 1.5$ ) molecules with the Cercignani-Lampis BC . When

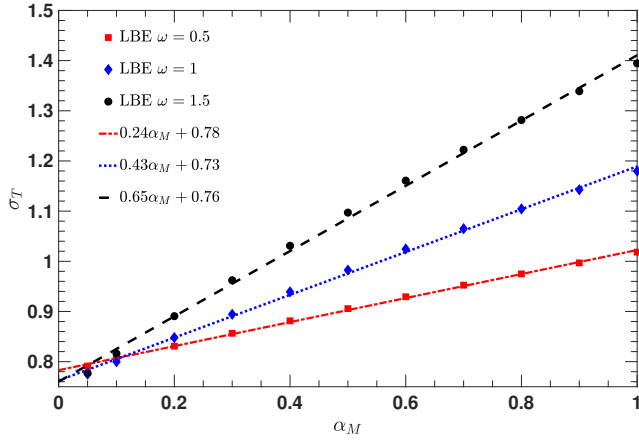


图 9-2 符号: TSCs obtained from the LBE for HS, Maxwellian, and variable hard sphere (VHS,  $\omega = 1.5$ ) molecules, when the diffuse-specular BC is used. 线: linear fittings of TSCs with respect to the TMAC.

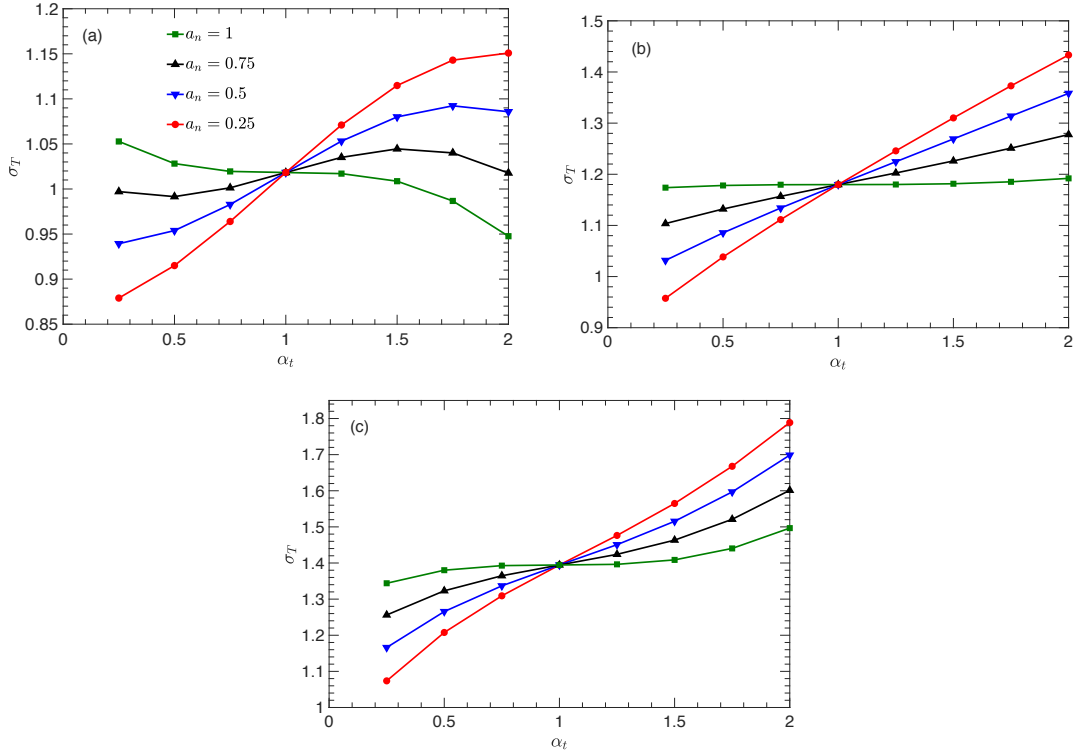


图 9-3 TSCs obtained from LBE for (a) HS, (b) Maxwellian, and (c) VHS ( $\omega = 1.5$ ) molecules, when the CLL BC is used.

$\alpha_t$  and  $\alpha_n$  are fixed, the TSC increases with the viscosity index. For example, when the HS and VHS with  $\omega = 1.5$  are considered, the maximum relative difference reaches 58% when  $\alpha_t = 2$  and  $\alpha_n = 1$ . When the viscosity index is fixed, however, the variation of TSC with respect to the effective TMAC  $\alpha_t$  and EAC  $\alpha_n$  is complicated. We first consider the case when the value of  $\alpha_t$  and the intermolecular potential are fixed. From Table 9-1 we see that, when  $\alpha_t < 1$ , the TSC increases with  $\alpha_n$ , where the maximum increment

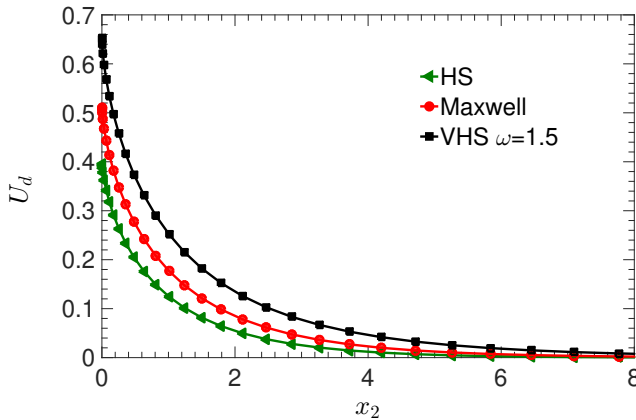


图 9-4 KLFs obtained from the LBE for HS, Maxwellian, and VHS ( $\omega = 1.5$ ) molecules, when the diffuse BC is applied.

is less than 20% when  $\alpha_n$  varies from 0.25 to 1. Furthermore, this kind of variation reduces when  $\alpha_t$  approaches 1; when  $\alpha_t = 1$ , the Cercignani-Lampis BC is reduced to the fully diffuse one in this problem, and the TSC does not vary with  $\alpha_n$ ; when  $\alpha_t > 1$ , the variation of TSC on  $\alpha_n$  reverses when compared to that of  $\alpha_t < 1$ . We then fix the value of  $\alpha_n$  and the intermolecular potential to see how  $\alpha_t$  affects the TSC. Unlike the diffuse-specular BC where the TSC is nearly a linear function of TMAC, here the change of TSC with respect to  $\alpha_t$  is nonlinear. Also, it is observed that the smaller the value of  $\alpha_n$ , the strong the variation in TSC with  $\alpha_t$ . For instance, when  $\omega = 0.5$  and  $\alpha_n = 0.75$ , the TSC first decreases to a minimum value at  $\alpha_t \approx 0.5$ , then increases to a maximum value at  $\alpha_t \approx 1.5$ . This is not observed in the work [103], where the Shakhov model [100] is employed and the TSC always increases with  $\alpha_t$  when  $\alpha_n$  is fixed.

### 9.2.2 Knudsen layer function

The influence of intermolecular potential on the KLF has been rarely studied, even for monatomic gases, due to the complexity of the Boltzmann collision operator and the lack of efficient numerical methods to simulate the near-continuum flow. Fortunately, these computational difficulties can be tackled by the FSM and GSIS developed in previous chapters.

Figure 9-4 shows the KLF obtained from the LBE for HS, Maxwellian, and VHS ( $\omega = 1.5$ ) molecules, when the diffuse BC is applied. Obviously, the KLF is strongly affected by the intermolecular potential, i.e. its value increases with the viscosity index  $\omega$ . For example, the value of the KLF at solid surface for VHS molecules with  $\omega = 1.5$  is larger than that of the HS molecules by approximately 60%.

Figure 9-5(a) further depicts the KLF when the specular-diffuse BC is used, from

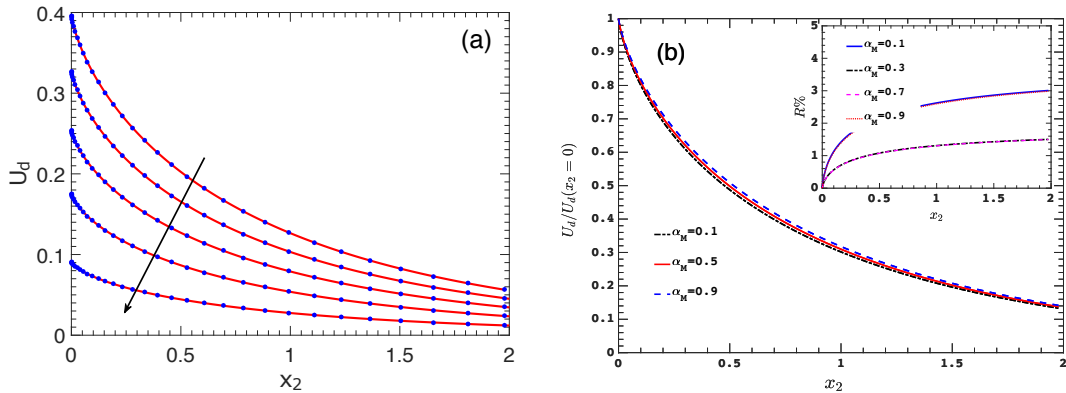


图 9-5 (a) KLFs for HS molecules with the diffuse-specular BC. Along the arrow, the TMAC is  $\alpha_M = 1.0, 0.8, 0.6, 0.4$ , and  $0.2$ , respectively. Solid lines: LBE results; dots: fitting results by Eq. (7-7). (b) The rescaled KLF  $u_d(x_2)/u_d(0)$ , when the HS molecules and diffuse-specular BC are used. For clarity, results at other values of  $\alpha_M$  are not shown. Inset: the relative difference of the rescaled KLF for various  $\alpha_M$  when compared to that of  $\alpha_M = 0.5$ .

the case of  $\alpha_M = 0.2$  where the specular reflection is strong. It is noticed that the KLF decreases with the TMAC; this is in sharp contrast to the KLF in Kramer's problem where its value increases when the TMAC decreases [117]. However, both the thermal transpiration and Couette flow possess the singularity of velocity gradient at the planar surface. That is,  $du_d/dx_2$  varies as  $x_2 \ln x_2$  in the vicinity of the wall, and such a gradient divergence is general in RGD [125]. This conclusion holds also in the Couette flow described by the BGK kinetic model [49], where the asymptotic analysis demonstrates that the KLF near the boundary can be described by Eq. (7-7). Interestingly, through numerical simulation and fitting, we find that the KLF in thermal transpiration can also be perfectly fitted by the same function, where the fitting coefficients are listed in Ref. [136].

Under the diffuse-specular BC, the similarity in KLF is found, that is, when the KLFs are rescaled by their values on the solid surface, they almost overlap with each other [Fig. 9-5(b)]. This happens not only for HS molecules, but also for other intermolecular potentials.

The KLFs are also obtained from the LBE with the Cercignani-Lampis BC. When  $\alpha_t$  and  $\alpha_n$  are fixed, the KLF increases with the viscosity index. However, unlike the diffuse-specular BC, the KLF only exhibits weak similarities when either  $\alpha_t$  or  $\alpha_n$  is fixed.

### 9.2.3 Molecular gases

So far no work has been devoted to finding the TSC and KLF of molecular gases based on the Boltzmann equation, although they can be roughly extracted from the nu-

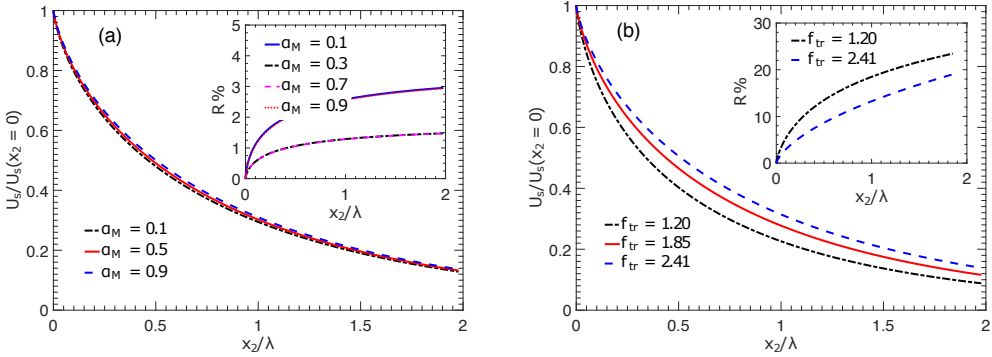


图 9-6 The rescaled KLF  $u_d(x_2)/u_d(0)$  obtained from the Wu model for the HS molecules, subject to the diffuse-specular BC. (a) The diffuse-specular BC at different  $\alpha_M$  is applied with  $f_{tr} = 2.37$ . Inset: the relative difference of the rescaled KLF for various  $\alpha_M$  when compared to that of  $\alpha_M = 0.5$ . (b) The fully diffuse BC is applied with different  $f_{tr}$ . Inset: the relative difference of the rescaled KLF for various  $f_{tr}$  when compared to that of  $f_{tr} = 1.85$ .

merical data given by Loyalka *et al.* [69] and Lo & Loyalka [64], where the thermal transpiration of molecular gases along planar channels and circular tubes were calculated based on the Hanson & Morse kinetic model [43]. However, this model is proposed only for Maxwellian molecules, so the influence of intermolecular potential cannot be captured.

Based on the numerical solution of the Wu model [146], we find TSC in the diffuse-specular BC can be fitted by

$$\sigma_T = f_{tr} (C_1 \alpha_M + 0.31), \quad (9-7)$$

where the fitting coefficients are  $C_1 = 0.095, 0.125$ , and  $0.165$ , for  $\omega = 0.5, 0.75$ , and  $1$ , respectively. For the Cercignani-Lampis BC, when  $\alpha_t$  does not deviate too much from 1, say, when  $|\alpha_t - 1| < 0.3$ , the TSC  $\sigma_T(\alpha_n, \alpha_t)$  can be expressed as

$$\sigma_T(\alpha_n, \alpha_t) = \frac{2}{5} f_{tr} \sigma_T^m(\alpha_n, \alpha_t), \quad (9-8)$$

where  $\sigma_T^m(\alpha_n, \alpha_t)$  is the TSC for monatomic gas, see typical values in Table 9-1. The relative error between the Wu model and Eq. (9-8) increases when  $\alpha_t$  further deviates away from one and  $f_{tr}$  deviates away from 2.5, e.g. to 7% when  $\alpha_t = 0.2$  and  $f_{tr} = 0.5$ .

Like the monatomic gas, the KLF of molecular gases holds similarity at different TMAC when the diffuse-specular BC is applied; this is demonstrated in Fig. 9-6(a), where the rescaled KLFs as well as their relative difference are presented. It is clearly seen that the rescaled KLFs for  $\alpha_M = 0.1, 0.5$  and  $0.9$  almost overlap with each other, and their maximum derivation from that of  $\alpha_M = 0.5$  is within 3%. Interestingly, although the TSC is proportional to the translational Eucken factor  $f_{tr}$ , the rescaled KLF does not preserve the similarity with respect to  $f_{tr}$ . As presented in Fig. 9-6(b), the rescaled KLF

profiles for  $f_{tr} = 1.2, 1.85$  and  $2.41$  have large discrepancies.

#### 9.2.4 Comparison with experiments

Experimental data on thermal transpiration of air and carbon dioxide in a circular tube are examined by the LBE calculations. From the discussions in previous sections we know that these data depend on the values of  $f_{tr}$ ,  $\omega$ , and TMAC. The same problem has been investigated by Loyalka *et al.* [69] based on the Hanson & Morse model [43] that is derived from the Wang-Chang & Uhlenbeck equation [137] for Maxwellian molecules, but with the diffuse BC only. The methodology we will adopt has two major advantages. First, in the Wu model [146] for molecular gases, the viscosity index can be properly chosen to reflect the intermolecular potential for each gas, which is not accessible in previous molecular gas models. Second,  $f_{tr}$  is extracted from the experiments of Rayleigh-Brillouin scattering, where the gas-surface interaction is absent so that it is obtained accurately [141]. Therefore, in the comparison between our LBE and experiential results, the gas-surface BC in thermal transpiration can be extracted with good accuracy.

In the experiment of thermal transpiration usually the TPD exponent  $\gamma$  is measured. When the temperature ratio of two gas reservoirs connected by a long circular tube is small, the TPD exponent can be calculated as

$$\gamma = -\frac{Q_T}{Q_P}, \quad (9-9)$$

where  $Q_T$  and  $Q_P$  are the mass flow rates along the tube in thermal transpiration and Poiseuille flows, respectively.

In the slip regime, with the aid of first-order slip BC, the dimensionless mass flow rate of the Poiseuille flow  $Q_P$  in a circular tube is [104]

$$Q_P = \frac{\delta_{rp}}{8} + \frac{\sigma_P}{2}, \quad (9-10)$$

where the VSC is set to  $\sigma_P = 1, 1.2$  and  $1.46$  for the cases of  $\alpha_M = 1, 0.9$  and  $0.8$ , respectively, as the intermolecular potential has negligible effect on these values [117]. Note that Eq. (9-10) is accurate when  $\delta_{rp} > 10$ .

When  $\delta_{rp}$  is large such that the two Knudsen layers do not overlap, from Eqs. (7-2) and (7-3) we find that the normalized mass flow rate  $Q$  can be calculated exactly as

$$Q = \frac{\sigma_T}{2\delta_{rp}} - \frac{\pi}{4\delta_{rp}^2} Q_d, \quad (9-11)$$

where

$$Q_d = \int_0^\infty u_d(x_2) dx_2, \quad (9-12)$$

is the mass flow rate correction due to defect velocity, whose values for typical values of viscosity index are listed in Ref. [136] when the Cercignani-Lampis BC is used. It is seen from Eq. (9-11) that the KLF provides a correction of the mass flow rate up to the second-order of Knudsen number.

The analytical solution of TPD exponent in the slip regime can be written as

$$\gamma = \frac{4\sigma_T \delta_{rp} - 2\pi Q_d}{\delta_{rp}^2 (\delta_{rp} + 4\sigma_P)}. \quad (9-13)$$

In our LBE simulations, the viscosity index  $\omega$  for each gas is set according to the gaseous property [9]. With the values of  $Q_d$ ,  $\sigma_T$ , and  $\sigma_P$  at a specific  $\alpha_M$  obtained from previous sections, the analytical solution (9-13) for the TPD exponent can be determined, which will be used to extract the TMAC by comparing with the experimental data when  $\delta_{rp} > 3.5$ .

Then we solve the Wu model towards smaller values of  $\delta_{rp} < 3.5$  to see whether our results still agree with experimental data or not.

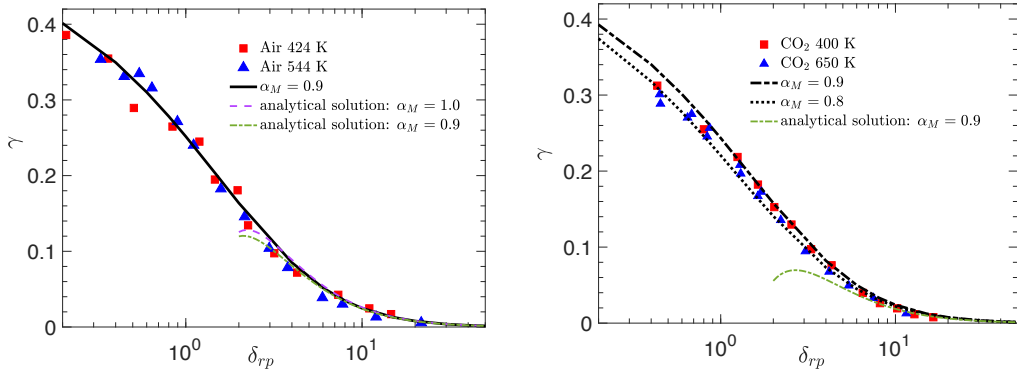


图 9-7 TPD exponent versus the rarefaction parameter  $\delta_{rp}$ , for air (left) and carbon dioxide (right) flows along a circular tube. Symbols: experimental data extracted from reference [5]. Black lines: numerical solutions of the Wu model [146]. The analytical solution is given by Eq. (9-13).

#### 9.2.4.1 Air

We first compare the calculated TPD exponent of thermal transpiration for air with the experimental data by Arney and Bailey [5] in Fig. 9-7. Since air is mainly the mixture of nitrogen and oxygen, an effective viscosity index of  $\omega = 0.75$  is chosen to reproduce the proper intermolecular potential of the air molecules [9, 117]. The number of rotational

degrees is 2. The translational Eucken factor is  $f_{tr} = 2.4$  as extracted from the Rayleigh-Brillouin experiments of nitrogen [141]. We first use the analytical expression (9-13) to obtain the TMAC by comparing with the experimental data at  $\delta_{rp} > 10$ . From the results in previous sections, the TSC can be extracted from the linear function

$$\sigma_T = 0.294\alpha_M + 0.752, \quad (9-14)$$

and the mass flow rate correction  $Q_d$  for air can be calculated from

$$Q_d = 4.182 [1 - \exp(-0.228\alpha_M)]. \quad (9-15)$$

We find that when  $\alpha_M$  varies from 0.8 to 1, the results in Eq. (9-13) can cover almost all the experimental data at temperature  $T = 424\text{K}$  and  $544\text{K}$ . Then we solve the Wu model over a wide range of rarefaction parameter and find that the TMAC in the air experiments is more likely 0.9, rather than  $\alpha_M = 1$  used in the reference [69].

#### 9.2.4.2 Carbon dioxide

The comparisons of TPD exponent for  $\text{CO}_2$  between the measurements and solutions of the Wu model are shown in Fig. 9-7, where the effective viscosity index is set to 0.93, while the translational Eucken factor is  $f_{tr} = 2.24$  as extracted from the Rayleigh-Brillouin experiments of carbon dioxide [141]. The rotational degrees is still equal to 2, since the three atoms in a  $\text{CO}_2$  molecule line up. We estimate the values of TSC and the mass flow correction  $Q_d$  as

$$\begin{aligned} \sigma_T &= 0.271\alpha_M + 0.576, \\ Q_d &= 4.726 [1 - \exp(-0.207\alpha_M)]. \end{aligned} \quad (9-16)$$

We can also see that, when  $\delta_{rp} > 1$  the experimental data at  $T = 400\text{K}$  can be well reproduced by the Wu model when  $\alpha_M = 0.9$ , while the data at a higher temperature of  $T = 650$  are more close to solutions of the Wu model when  $\alpha_M = 0.8$ . Note that the value of  $\gamma$  at  $\delta_{rp} \approx 0.45$  is even below the profile of  $\alpha_M = 0.8$ , which may be attributed to the inaccurate experimental measurement at low gas pressures. Nevertheless, all experimental data almost fall between the profiles of  $\alpha_M = 0.8$  and 0.9, which suggest that the TMAC in the  $\text{CO}_2$  experiment is more likely  $\alpha_M = 0.85 \pm 0.05$ .

### 9.3 Temperature jump

The temperature jump coefficient is calculated from the linear fitting of the temperature profile, named  $\tau_{NS}$ , in the bulk region ( $x_1 \in [0.3, 0.7]$ ), according to its definition (9-3) as

$$\zeta_T = -\frac{A+1}{2kA}, \quad (9-17)$$

where  $A$  is the slope coefficient in the linear fitting

$$\tau_{NS}(x_1) = A \left( x_1 - \frac{1}{2} \right) \Delta\tau, \quad (9-18)$$

with  $\Delta\tau = \Delta T/T_0$  the perturbation of wall temperature. The Knudsen lay function, i.e., defective temperature  $\Theta$ , is obtained by comparing the kinetic solution and the linear fitting within Knudsen layer

$$\Theta(x_1) = \frac{1}{Ak\Delta\tau} (\tau_{NS} - \tau). \quad (9-19)$$

We separately consider the translational and rotational temperatures, as the KLFs are different. However, the jump coefficients are the same.

In this section, we use the values of  $Z$  and  $\mathbf{A}$  extracted from the direct simulation Monte Carlo (DSMC) method [141, 58]:  $Z = 2.667$ ,  $A_{tt} = 0.786$ ,  $A_{tr} = -0.201$ ,  $A_{rt} = -0.059$ , and  $A_{rr} = 0.842$ , thus  $f_{tr} = 2.365$  and  $f_{rot} = 1.435$ .

#### 9.3.0.1 Influence of intermolecular potential

The translational and rotational Knudsen layer functions are plotted in Fig. 9-8. With the given  $Z$  and  $\mathbf{A}$ , the rotational Knudsen layer functions are larger than the translational ones. When the viscosity index  $\omega$  increases from 0.5 to 1, the jump coefficients slightly increase with magnitudes no larger than 3%. The Knudsen layer functions also become larger, and maximum increments, occurring in the vicinity of wall, are about 0.115 and 0.048 for the translational and rotational ones, respectively.

Therefore, like monatomic gases, the temperature jump in molecular gases are not sensitive to the elastic collision rate. In the following sections, we will use the Wu model, where the elastic collision is described by the Shakhov model. Since the translational and rotational jump coefficients have little difference, we will not particularly distinguish the translational or rotational one when demonstrate the results.

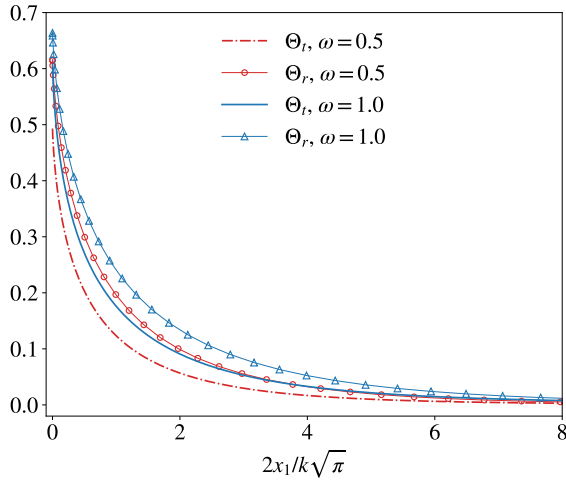


图 9-8 The obtained Knudsen layer functions for the translational and the rotational temperatures when the modeling of elastic collision in the kinetic model (??) is replaced by the Boltzmann collision operator for a more realistic collision rate. The inverse law potential is consider with the viscosity index  $\omega = 0.5$  and  $\omega = 1.0$ .

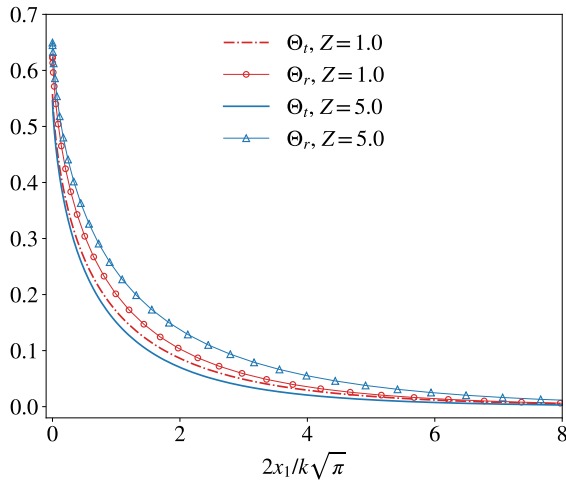


图 9-9 The Knudsen layer functions for the translational and the rotational temperatures with  $Z = 1.0$  and  $Z = 5.0$ .

### 9.3.0.2 Influence of rotational collision number

Now we investigate the influence of the temperature relaxation (??) by changing  $Z$  and keeping  $A_{ij}$ . The temperature jump coefficients  $\zeta_T$  obtained with  $Z$  equal to 1.0, 2.667 and 5.0 are listed in Table ???. It is shown that  $\zeta_T$  slightly increase as  $Z$  becomes larger. The obtained translational and rotational Knudsen layer functions are plotted in Fig. 9-9; when  $Z = 1.0$ , i.e., the occurring of inelastic collisions that exchange translational and rotational energies is frequent,  $\theta_t$  and  $\theta_r$  are close, while as  $Z$  increases to 5.0, i.e., the probability for inelastic collisions becomes smaller, the discrepancy between  $\theta_t$  and  $\theta_r$  enlarges. However, the variation is not significant.

### 9.3.0.3 Influence of thermal relaxation

Now we study the influence of thermal relaxations (??) by changing the relaxation rates and keeping  $Z = 2.667$ . The thermal conductivity and its components will alert with  $A_{ij}$ , therefore in order to make duly comparisons, the total Eucken factor  $f_u = 1.993$  is kept as the experimental value for nitrogen at  $T_0 = 300$  K.

We first fix the cross terms  $A_{tr}$  and  $A_{rt}$  and alter  $f_{tr}$  and  $f_{rot}$  that are the percentages of translational and rotational contributions to the thermal conductivity. The diagonal terms  $A_{tt}$  and  $A_{rr}$  will correspondingly vary. Figure 9-10(a) displays the temperature jump coefficient against the translational Eucken factor, where the three lines relate to the three groups of cross terms:  $A_{tr} = A_{rt} = 0.0$  without cross exchange;  $A_{tr} = -0.201$  and  $A_{rt} = -0.059$  the ones extracted from the DSMC;  $A_{tr} = -1.005$  and  $A_{rt} = -0.295$  that are 5 times larger, in magnitude, than those from the DSMC. It is found that the temperature jump coefficient first falls and then slightly rises as the translational Eucken factor increases (or the rotational Eucken factor decreases), and the minimum value that is about 1.715 appears when  $f_{tr}$  is around  $2.2 \sim 2.25$ . The most significant variation of  $\zeta_T$  when  $f_{tr}$  changes from 1.5 to 2.5 occurs when the cross exchange in thermal relaxation is intensified ( $A_{tr} = -1.005$  and  $A_{rt} = -0.295$ ), where the minimum jump coefficient is about 86% of the maximum one ( $\zeta_T = 1.9922$  at  $f_{tr} = 1.5$ ). The Knudsen layer functions are plotted in Fig. 9-10(b). We can find that, when  $f_{tr} = 1.5$  and  $f_{rot} = 2.733$ , the translational Knudsen layer function  $\theta_t$  is larger than the rotational one  $\theta_r$ , which means that  $\theta_t$  deviates more from the Navier-Stokes solution; while when  $f_{tr}$  increases to 2.5 and  $f_{rot}$  reduces, the situation reverses and now  $\theta_r$  is larger. When the two Knudsen layer functions meet in the middle at  $f_{tr} = 2.25$ , the minimum temperature jump coefficient emerges.

Then we fix  $f_{tr}$  and  $f_{rot}$ , and check how the cross terms  $A_{tr}$  and  $A_{rt}$  affect the jump coefficient. Figure 9-11(a) illustrates the obtained  $\zeta_T$  when  $A_{tr}$  varies and  $A_{rt}$  is fixed as -0.059, where the two lines correspond to the results at  $f_{tr} = 1.5$  and 2.5, respectively. It is found that when  $f_{tr} = 1.5$ , the translational part in the thermal conduction is relatively small, the jump coefficient increases as the magnitude of  $A_{tr}$  becomes larger, that is the contribution to the relaxation of translational heat flux from the rotational one intensifies; while the jump coefficient decreases when  $f_{tr} = 2.5$ , the translational part is relatively large. Figure 9-11(b) shows the obtained  $\zeta_T$  when  $A_{tr} = -0.201$  and  $A_{rt}$  varies. Now, as the magnitude of  $A_{rt}$  becomes larger, that is the contribution to the relaxation of rotational

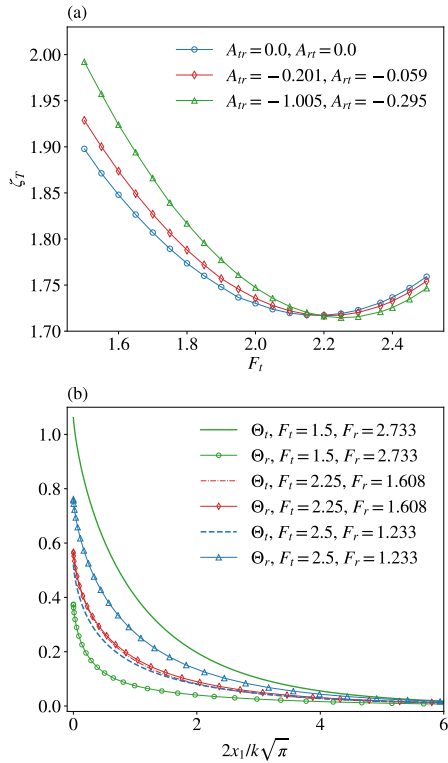


图 9-10 (a) Temperature jump coefficient displaying the influence of the translational Eucken factor when  $Z = 2.667$ ,  $f_u = 1.993$ , and the diagonal terms  $A_{tt}$  and  $A_{rr}$  altering. (b) Knudsen layer functions displaying the influence of the Eucken factors when  $Z = 2.667$ ,  $f_u = 1.993$ ,  $A_{tr} = -1.005$  and  $A_{rt} = -0.295$ .

heat flux from the translational one intensifies, the jump coefficient decreases at  $f_{tr} = 1.5$ ; while the jump coefficient increases at  $f_{tr} = 2.5$ .

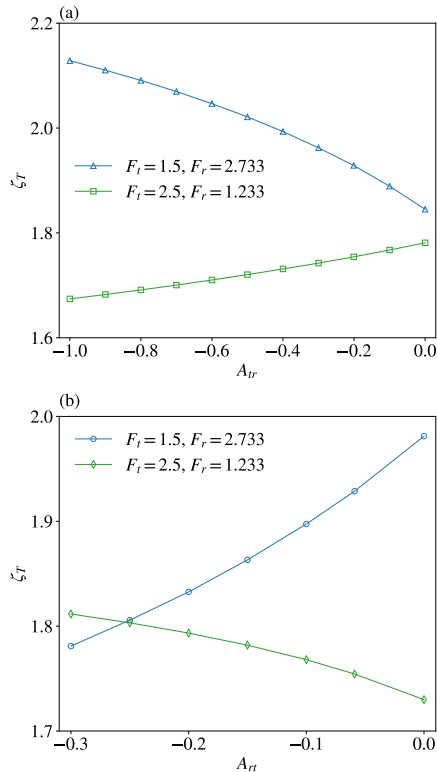


图 9-11 Temperature jump coefficient displaying the influence of the cross relaxation rates  $A_{tr}$  and  $A_{rt}$  when  $Z = 2.667$ ,  $f_u = 1.993$ , while  $f_{tr}$  and  $f_{rot}$  are fixed: (a)  $A_{tr}$  varies and  $A_{rt} = -0.059$ ; (b)  $A_{tr} = -0.201$  and  $A_{rt}$  varies.

## 参考文献

- [1] M. L. Adams and E. W. Larsen. Fast iterative methods for discrete-ordinates particle transport calculations. *Progr. Nucl. Energy*, 40:3–159, 2002.
- [2] A. Alsmeyer. Density profiles in argon and nitrogen shock waves measured by the absorption of an electron beam. *J. Fluid Mech.*, 74:497–513, 1976.
- [3] V. E. Ambruş and V. Sofonea. High-order thermal lattice Boltzmann models derived by means of Gauss quadrature in the spherical coordinate system. *Phys. Rev. E*, 86:016708, 2012.
- [4] B. K. Annis. Thermal creep in gases. *The Journal of Chemical Physics*, 57(7):2898–2905, 1972.
- [5] G. D. Arney and A. B. Bailey. An investigation of the equilibrium pressure along unequally heated tubes. Technical report, Arnold Engineering Development Center Arnold Air Force Station TENN, 1962.
- [6] A. A. Beylich. An interlaced system for Nitrogen gas. In *Proceedings of CECAM Workshop*, 2000.
- [7] P. L. Bhatnagar, E. P. Gross, and M. Krook. A model for collision processes in gases. I. Small amplitude processes in charged and neutral one-component systems. *Phys. Rev.*, 94:511–525, 1954.
- [8] P. L. Bhatnagar, E. P. Gross, and M. Krook. A model for collision processes in gases. I. Small amplitude processes in charged and neutral one-component systems. *Phys. Rev.*, 94:511, 1954.
- [9] G. A. Bird. *Molecular Gas Dynamics and the Direct Simulation of Gas Flows*. Oxford Science Publications, Oxford University Press Inc, New York, 1994.
- [10] A. V. Bobylev. Instabilities in the Chapman-Enskog expansion and hyperbolic Burnett equations. *J. Stat. Phys.*, 124:371–399, 2006.
- [11] C. D. Boley, R. C. Desai, and G. Tenti. Kinetic models and Brillouin scattering in a molecular gas. *Can. J. Phys.*, 50:2158–2172, 1972.
- [12] C. Borgnakke and P. Larsen. Statistical collision model for Monte Carlo simulation of polyatomic gas mixture. *J. Comput. Phys.*, 18(4):405–420, 1975.
- [13] I. D. Boyd. Rotational-translational energy transfer in rarefied nonequilibrium flows. *Phys. Fluids A*, 2:447, 1990.
- [14] D. Bruno, A. Frezzotti, and G. P. Ghiraldi. Oxygen transport properties estimation by classical trajectory–direct simulation Monte Carlo. *Phys. Fluids*, 27:057101, 2015.
- [15] Z. N. Cai and R. Li. Numerical regularized moment method of arbitrary order for Boltzmann-BGK equation. *SIAM J. Scientific Computing*, 32:2875–2907, 2010.
- [16] C. Canuto, M. Y. Hussaini, and A. Quarteroni. *Spectral Method in Fluid Dynamics*. Springer-verlag, 1998.

- 
- [17] C. Cercignani. *The Boltzmann Equation and its Applications*. Springer-Verlag, New York, 1988.
  - [18] C. Cercignani. *Mathematical Methods in Kinetic Theory*. Plenum Publishing Inc., 223 Spring Street, New York, N.Y. 10013, 1990.
  - [19] S. Chapman. On the law of distribution of molecular velocities, and the theory of viscosity and thermal conduction, in a non-uniform simple monatomic gas. *Phil. Trans. R. Soc. A*, 216:538–548, 1916.
  - [20] S. Chapman and T.G. Cowling. *The Mathematical Theory of Non-uniform Gases*. Cambridge University Press, 1970.
  - [21] T. Doi. Numerical analysis of the Poiseuille flow and thermal transpiration of a rarefied gas through a pipe with a rectangular cross section based on the linearized Boltzmann equation for a hard sphere molecular gas. *J. Vac. Sci. Technol. A*, 28:603–612, 2010.
  - [22] D. Enskog. *Kinetische Theorie der Vorgänge in mässig verdünnten Gasen*. Uppsala University, Sweden, 1917.
  - [23] T. Ewart, P. Perrier, I. A. Graur, and J. G. Méolans. Mass flow rate measurements in a microchannel, from hydrodynamic to near free molecular regimes. *J. Fluid Mech.*, 584:337–356, 2007.
  - [24] J. Fan. A generalized soft-sphere model for Monte Carlo simulation. *Phys. Fluids*, 14(12):4399–4405, 2002.
  - [25] J. H. Ferziger and H. G. Kaper. *Mathematical Theory of Transport Processes in Gases*. North-Holland Publishing Company, Amsterdam, 1972.
  - [26] F. Filbet, C. Mouhot, and L. Pareschi. Solving the Boltzmann equation in NlogN. *SIAM J. Scientific Computing*, 28(3):1029–1053, 2006.
  - [27] M. Gad-el-Hak. The fluid mechanics of microdevices - the Freeman Scholar lecture. *J. Fluids Eng.*, 121(1):5–33, 1999.
  - [28] I. M. Gamba and S. H. Tharkabhushanam. Spectral-Lagrangian methods for collisional models of non-equilibrium statistical states. *J. Comput. Phys.*, 228(6):2012–2036, 2009.
  - [29] L. S. Garcia-Colin, R. M. Velasco, and F. J. Uribe. Beyond the Navier-Stokes equations: Burnett hydrodynamics. *Phys. Rep.*, 465:149–189, 2008.
  - [30] N. E. Gimelshein, S. F. Gimelshein, and D. A. Lavin. Vibrational relaxation rates in the direct simulation Monte Carlo method. *Phys. Fluids*, 14:4452, 2002.
  - [31] M. H. Gorji and P. Jenny. A Fokker-Planck based kinetic model for diatomic rarefied gas flows. *Phys. Fluids*, 25:062002, 2013.
  - [32] M. H. Gorji, M. Torrilhon, and P. Jenny. Fokker-Planck model for computational studies of monatomic rarefied gas flows. *J. Fluid Mech.*, 680:574–601, 2011.
  - [33] H. Grad. On the kinetic theory of rarefied gases. *Comm. Pure Appl. Math.*, 2:331–407, 1949.
  - [34] M. S. Green. Markoff random processes and the statistical mechanics of time-dependent phenomena. ii. irreversible processes in fluids. *The Journal of Chemical Physics*, 22:398–413, 1954.

- 
- [35] P. T. Gressman and R. M. Strain. Global classical solutions of the Boltzmann equation with long-range interactions. *Proc. Natl. Acad. Sci. U.S.A.*, 107(13):5744–5749, 2010.
  - [36] T. J. Greytak and G. B. Benedek. Spectrum of light scattered from thermal fluctuations in gases. *Phys. Rev. Lett.*, 17:179–182, 1966.
  - [37] E. P. Gross and E. A. Jackson. Kinetic models and the linearized Boltzmann equation. *Phys. Fluids*, 2(4):432–441, 1959.
  - [38] X. J. Gu and D. R. Emerson. A high-order moment approach for capturing non-equilibrium phenomena in the transition regime. *J. Fluid Mech.*, 636:177–216, 2009.
  - [39] Z. Gu and W. Ubachs. Temperature-dependent bulk viscosity of nitrogen gas determined from spontaneous Rayleigh-Brillouin scattering. *Opt. Lett.*, 38(7):1110, 2013.
  - [40] Z. L. Guo, K. Xu, and R. J. Wang. Discrete unified gas kinetic scheme for all Knudsen number flows: Low-speed isothermal case. *Physical Review E*, 88:033305, 2013.
  - [41] A. D. Gupta and T. S. Storwick. Analysis of the heat conductivity data for polar and nonpolar gases using thermal transpiration measurements. *J. Chem. Phys.*, 52(2):742–749, 1970.
  - [42] B. L. Haas, D. B. Hash, G. A. Bird, F. E. Lumpkin III, and H. A. Hassan. Rates of thermal relaxation in direct simulation Monte Carlo methods. *Phys. Fluids*, 6:2191, 1994.
  - [43] F. B. Hanson and T. F. Morse. Kinetic models for a gas with internal structure. *Phys. Fluids*, 10:345, 1967.
  - [44] H. A. Hassan and D. B. Hash. A generalized hard-sphere model for Monte-Carlo simulation. *Phys. Fluids A: Fluid Dynamics*, 5(3):738–744, 1993.
  - [45] D. Hilbert. Mathematical problems. *Bull. Am. Math. Soc.*, 8:437–479, 1902.
  - [46] D. Hilbert. Begründung der kinetische gastheorie. *Math. Ann.*, 72:562–577, 1912.
  - [47] J. W. Hu and L. X. Ying. A fast spectral algorithm for the quantum Boltzmann collision operator. *Commun. Math. Sci.*, 10(3):989–999, 2012.
  - [48] F. Jaeger, O. K. Matar, and E. A. Muller. Bulk viscosity of molecular fluids. *J. Chem. Phys.*, 148:174504, 2018.
  - [49] S. Jiang and L. S. Luo. Analysis and accurate numerical solutions of the integral equation derived from the linearized BGKW equation for the steady Couette flow. *J. Comput. Phys.*, 316:416–434, 2016.
  - [50] G. Karniadakis, A. Beskok, and N. R. Aluru. *Microflows and Manoflows: Fundamentals and Simulations*. Springer, New York, 2005.
  - [51] E. Kennard. *Kinetic Theory of Gases*. McGraw-Hill Book Company, Inc., New York and London, 1938.
  - [52] P. Kowalczyk, A. Palczewski, G. Russo, and Z. Walenta. Numerical solutions of the Boltzmann equation: comparison of different algorithms. *Eur. J. Mech.B/Fluids*, 27(1):62–74, 2008.
  - [53] G. M. Kremer. *An Introduction to the Boltzmann Equation and Transport Processes in Gases*. Springer, 2009.
  - [54] M. Krook and T. T. Wu. Exact solutions of the Boltzmann equation. *Phys. Fluids*, 20:1589, 1977.

- 
- [55] R. Kubo. Statistical-mechanical theory of irreversible processes. i. general theory and simple applications to magnetic and conduction problems. *Journal of the Physical Society of Japan.*, 12:570–586, 1957.
  - [56] L. Lambert. *Vibrational and Rotational Relaxation in Gases*. Clarendon, 1977.
  - [57] V. Leontidis, J. Chen, L. Baldas, and S. Colin. Numerical design of a Knudsen pump with curved channels operating in the slip flow regime. *Heat and Mass Transfer*, 50:1065–1080, 2014.
  - [58] Q. Li, J. N. Zeng, W. Su, and L. Wu. Uncertainty quantification in rarefied dynamics of molecular gas: rate effect of thermal relaxation. *J. Fluid Mech.*, 917:338, 2021.
  - [59] J. Lihnaropoulos, S. Naris, and D. Valougeorgis. Formulation and stability analysis of rapidly convergent iteration schemes for the 2D linearized BGK equation. *Transport Theory and Statistical Physics*, 36(4-6):513–528, 2007.
  - [60] C. R. Lilley and J. E. Sader. Velocity gradient singularity and structure of the velocity profile in the Knudsen layer according to the Boltzmann equation. *Phys. Rev. E*, 76:026315, 2007.
  - [61] C. R. Lilley and J. E. Sader. Velocity profile in the Knudsen layer according to the Boltzmann equation. *Proc. Royal Soc. A*, 464:2015–2035, 2008.
  - [62] J. T. Lin and D. R. Willis. Kinetic theory analysis of temperature jump in a polyatomic gas. *The Physics of Fluids*, 15(1):31–38, 1972.
  - [63] J. Liu and L. Wu. A fast-converging scheme for the Phonon Boltzmann equation with dual relaxation times. *arXiv*, page 2107.06688, 2021.
  - [64] S. S. Lo and S. K. Loyalka. Flow of a rarefied polyatomic gas between parallel plates. *J. Vac. Sci. Technol. A: Vacuum, Surfaces, and Films*, 7:2766–2773, 1989.
  - [65] D. A. Lockerby, J. M. Reese, D. R. Emerson, and R. W. Barber. Velocity boundary condition at solid walls in rarefied gas calculations. *Physical Review E*, 70:017303, 2004.
  - [66] D. A. Lockerby, J. M. Reese, and M. A. Gallis. Capturing the Knudsen layer in continuum-fluid models of nonequilibrium gas flows. *AIAA Journal*, 43:1391–1393, 2005.
  - [67] S. K. Loyalka. Velocity profile in the Knudsen layer for the Kramer’s problem. *Phys. Fluids*, 18:1666–1669, 1975.
  - [68] S. K. Loyalka and T. S. Storwick. Kinetic theory of thermal transpiration and mechanocaloric effect. iii. flow of a polyatomic gas between parallel plates. *J. Chem. Phys.*, 71:339–350, 1979.
  - [69] S. K. Loyalka, T. S. Storwick, and S. S. Lo. Thermal transpiration and mechanocaloric effect. IV. Flow of a polyatomic gas in a cylindrical tube. *J. Chem. Phys.*, 76(8):4157–4170, 1982.
  - [70] S. K. Loyalka, T. S. Storwick, and H. S. Park. Poiseuille flow and thermal creep flow in long, rectangular channels in the molecular and transition flow regimes. *J. Vac. Sci. Technol.*, 13:1188, 1976.
  - [71] W. Marques Jr and G. M. Kremer. Spectral distribution of scattered light in polyatomic gases. *Physica A*, 197:352–363, 1993.
  - [72] E. A. Mason. Molecular relaxation times from thermal transpiration measurements. *J. Chem. Phys.*, 39:522–526, 1963.

- 
- [73] H. Matsumoto. Variable sphere molecular model for inverse power law and Lennard-Jones potentials in Monte Carlo simulations. *Phys. Fluids*, 14(12):4256–4265, 2002.
  - [74] J. C. Maxwell. VII. On stresses in rarified gases arising from inequalities of temperature. *Proc. Royal Soc. Lond.*, 170:231–256, 1879.
  - [75] W. E. Meador, G. A. Miner, and L. W. Townsend. Bulk viscosity as a relaxation parameter: Fact or fiction? *Phys. Fluids*, 8:258, 1996.
  - [76] A. S. Meijer, A. S. de Wijn, M. F. E. Peters, N. J. Dam, and W. van de Water. Coherent Rayleigh-Brillouin scattering measurements of bulk viscosity of polar and nonpolar gases, and kinetic theory. *J. Chem. Phys.*, 133:164315, 2010.
  - [77] J. P. Meng, L. Wu an J. M. Reese, and Y. H. Zhang. Assessment of the ellipsoidal-statistical Bhatnagar–Gross–Krook model for force-driven Poiseuille flows. *J. Comput. Phys.*, 251:383–395, 2013.
  - [78] L. Mieussens and H. Struchtrup. Numerical comparison of Bhatnagar-Gross-Krook models with proper Prandtl number. *Phys. Fluids*, 16(8):2297–2813, 2004.
  - [79] T. F. Morse. Kinetic model for gases with internal degrees of freedom. *Phys. Fluids*, 7:159–169, 1964.
  - [80] C. Mouhot and L. Pareschi. Fast algorithms for computing the Boltzmann collision operator. *Math. Comput.*, 75(256):1833–1852, 2006.
  - [81] S. Naris and D. Valougeorgis. The driven cavity flow over the whole range of the Knudsen number. *Phys. Fluids*, 17:097106, 2005.
  - [82] S. Naris, D. Valougeorgis, D. Kalempa, and F. Sharipov. Gaseous mixture flow between two parallel plates in the whole range of the gas rarefaction. *Physica A: Statistical Mechanics and its Applications*, 336:294–318, 2004.
  - [83] S. Naris, D. Valougeorgis, D. Kalempa, and F. Sharipov. Flow of gaseous mixtures through rectangular microchannels driven by pressure, temperature, and concentration gradients. *Phys. Fluids*, 17:100607, 2005.
  - [84] S. Naris, D. Valougeorgis, F. Sharipov, and D. Kalempa. Discrete velocity modelling of gaseous mixture flows in MEMS. *Superlattices and Microstructures*, 35:629–643, 2004.
  - [85] T. Ohwada. Structure of normal shock-waves: Direct numerical analysis of the Boltzmann equation for hard-sphere molecules. *Phys. Fluids A-Fluid Dynamics*, 5(1):217–234, 1993.
  - [86] T. Ohwada, Y. Sone, and K Aoki. Numerical analysis of the Poiseuille and thermal transpiration flows between two parallel plates on the basis of the Boltzmann equation for hard sphere molecules. *Phys. Fluids*, 1:2042, 1989.
  - [87] T. Ohwada, Y. Sone, and K. Aoki. Numerical analysis of the shear and thermal creep flows of a rarefied gas over a plane wall on the basis of the linearized Boltzmann equation for hard-sphere molecules. *Phys. Fluids A*, 1:1588–1599, 1989.
  - [88] X. Pan, M. N. Shneider, and R. B. Miles. Coherent Rayleigh-Brillouin Scattering. *Phys. Rev. Lett.*, 89(18):183001, 2002.
  - [89] X. Pan, M. N. Shneider, and R. B. Miles. Coherent Rayleigh-Brillouin scattering in molecular gases. *Phys. Rev. A*, 69:033814, 2004.

- [90] L. Pareschi and G. Russo. Numerical solution of the Boltzmann equation I: Spectrally accurate approximation of the collision operator. *SIAM J. Numerical Analysis*, 37(4):1217–1245, 2000.
- [91] B. T. Porodnov, A. N. Kulev, and F. T. Tuchvetov. Thermal transpiration in a circular capillary with a small temperature difference. *J. Fluid Mech.*, 88:609–622, 1978.
- [92] G. A. Radtke, N. G. Hadjiconstantinou, and W. Wagner. Low-noise Monte Carlo simulation of the variable hard sphere gas. *Phys. Fluids*, 23(3):030606, 2011.
- [93] A. Rana, M. Torrilhon, and H. Struchtrup. A robust numerical method for the R13 equations of rarefied gas dynamics: Application to lid driven cavity. *J. Comput. Phys.*, 236:169–186, 2013.
- [94] L. E. Reichl. *A Modern Course in Statistical Physics*. John Wiley & Sons, 2016.
- [95] M. A. Reynolds, J. J. Smolderen, and J. F. Wendt. Velocity profile measurements in the Knudsen layer for the Kramers problem. Technical report, In Proceedings of the Ninth International Symposium of Rarefied Gas Dynamics, M. Becker and M. Fiebig, eds., Dfvlr-Press, 1974.
- [96] O. Reynolds. On certain dimensional properties of matter in the gaseous state. *Philos. Trans. R. Soc. Part 1*, 170:727–845, 1879.
- [97] M. Rojas-Cárdenas, I. Graur, P. Perrier, and J. G. Méolans. A new method to measure the thermal slip coefficient. *Int. J. Heat Mass Transfer*, 88:766–774, 2015.
- [98] V. Rykov. A model kinetic equation for a gas with rotational degrees of freedom. *Fluid Dyn.*, 10:959–966, 1975.
- [99] R. Schotter. Rarefied gas acoustics in the noble gases. *Phys. Fluids*, 17:1163, 1974.
- [100] E. M. Shakhov. Generalization of the Krook kinetic relaxation equation. *Fluid Dyn.*, 3(5):95–96, 1968.
- [101] X. W. Shan, X. F. Yuan, and H. D. Chen. Kinetic theory representation of hydrodynamics: a way beyond the Navier–Stokes equation. *J. Fluid Mech.*, 550:413–441, 2006.
- [102] F. Sharipov. Application of the Cercignani–Lampis scattering kernel to calculations of rarefied gas flows. I. Plane flow between two parallel plates. *Eur. J. Mech. B/Fluids*, 21:113–123, 2002.
- [103] F. Sharipov. Application of the Cercignani–Lampis scattering kernel to calculations of rarefied gas flows. II. Slip and jump coefficients. *Eur. J. Mech. B-Fluids*, 22:133–143, 2003.
- [104] F. Sharipov. *Rarefied Gas Dynamics: Fundamentals for Research and Practice*. John Wiley & Sons, 2015.
- [105] F. Sharipov. Influence of quantum intermolecular interaction on internal flows of rarefied gases. *Vacuum*, 156:146–153, 2018.
- [106] F. Sharipov and D. Kalempa. Oscillatory Couette flow at arbitrary oscillation frequency over the whole range of the Knudsen number. *Microfluidics and Nanofluidics*, 4:363–374, 2008.
- [107] F. Sharipov and V. Sleznev. Data on internal rarefied gas flows. *J. Phys. Chem. Ref. Data*, 27:657–706, 1998.
- [108] M. Sh. Shavaliyev. Super-Burnett corrections to the stress tensor and the heat flux in a gas of Maxwellian molecules. *J. Appl. Maths. Mechs.*, 57:573–576, 1993.
- [109] C. E. Siewert. The linearized Boltzmann equation: concise and accurate solutions to basic flow problems. *Z. Angew. Math. Phys.*, 54:273–303, 2003.

- 
- [110] C. E. Siewert. Viscous-slip, thermal-slip, and temperature-jump coefficients as defined by the linearized Boltzmann equation and the Cercignani–Lampis boundary condition. *Phys. Fluids*, 15(6):1696–1701, 2003.
  - [111] Y. Sone. *Kinetic Theory and Fluid Dynamics*. Birkhauser Boston, 2002.
  - [112] H. Struchtrup. *Macroscopic Transport Equations for Rarefied Gas Flows: Approximation Methods in Kinetic Theory*. Heidelberg, Germany: Springer, 2005.
  - [113] H. Struchtrup. Resonance in rarefied gases. *Cont. Mech. Theromodyn.*, 34:361–376, 2011.
  - [114] H. Struchtrup and M. Torrilhon. Regularization of Grad’s 13 moment equations: Derivation and linear analysis. *Phys. Fluids*, 15:2668–2690, 2003.
  - [115] W. Su, M. T. Ho, Y. H. Zhang, and L. Wu. GSIS: an efficient and accurate numerical method to obtain the apparent gas permeability of porous media. *Comput. Fluids*, 206:104576, 2020.
  - [116] W. Su, S. Lindsay, H. H. Liu, and L. Wu. Comparative study of the discrete velocity and lattice Boltzmann methods for rarefied gas flows through irregular channels. *Phys. Rev. E*, 96:023309, 2017.
  - [117] W. Su, P. Wang, H. H. Liu, and L. Wu. Accurate and efficient computation of the Boltzmann equation for Couette flow: Influence of intermolecular potentials on Knudsen layer function and viscous slip coefficient. *J. Comput. Phys.*, 378:573–590, 2019.
  - [118] W. Su, Y. H. Zhang, and L. Wu. Multiscale simulation of molecular gas flows by the general synthetic iterative scheme. *Comput. Methods Appl. Mech. Engrg.*, 373:113548, 2021.
  - [119] W. Su, L. H. Zhu, P. Wang, Y. H. Zhang, and L. Wu. Can we find steady-state solutions to multiscale rarefied gas flows within dozens of iterations? *J. Comput. Phys.*, 407:109245, 2020.
  - [120] W. Su, L. H. Zhu, and L. Wu. Fast convergence and asymptotic preserving of the general synthetic iterative scheme. *SIAM J. Sci. Comput.*, 42:B1517–B1540, 2020.
  - [121] A. Sugawara, S. Yip, and L. Sirovich. Spectrum of density fluctuations in gases. *Phys. Fluids*, 11:925–932, 1968.
  - [122] L. Szalmás. An accelerated discrete velocity method for flows of rarefied ternary gas mixtures in long rectangular channels. *Comput. & Fluids*, 128:91–97, 2016.
  - [123] L. Szalmás and D. Valougeorgis. A fast iterative model for discrete velocity calculations on triangular grids. *J. Comput. Phys.*, 229:4315–4326, 2010.
  - [124] S. Takata and H. Funagane. Poiseuille and thermal transpiration flows of a highly rarefied gas: over-concentration in the velocity distribution function. *J. Fluid Mech.*, 669:242–259, 2011.
  - [125] S. Takata and H. Funagane. Singular behaviour of a rarefied gas on a planar boundary. *J. Fluid Mech.*, 717:30–47, 2013.
  - [126] F. G. Tcheremissine and R. K. Agarwal. Computation of hypersonic shock waves in diatomic gases using the generalized Boltzmann equation. *AIP Conf. Proc.*, 1084:427–433, 2008.
  - [127] G. Tenti, C. Boley, and R. Desai. On the kinetic model description of Rayleigh-Brillouin scattering from molecular gases. *Can. J. Phys.*, 52:285, 1974.
  - [128] V. A. Titarev and A. A. Frolova. Application of model kinetic equations to calculations of super- and hypersonic molecular gas flows. *Fluid Dyn.*, 53:536–551, 2018.

- [129] H. S. Tsien. Superaerodynamics, mechanics of rarefied gases. *J. Aero. Sci.*, 13:653–664, 1946.
- [130] P. Valentini and T. E. Schwartzenruber. Large-scale molecular dynamics simulations of normal shock waves in dilute argon. *Phys. Fluids*, 21(6), 2009.
- [131] D. Valougeorgis and S. Naris. Acceleration schemes of the discrete velocity method: Gaseous flows in rectangular microchannels. *SIAM J. Sci. Comput.*, 25:534–552, 2003.
- [132] M. O. Vieitez, E. J. van Duijn, W. Ubachs, B. Witschas, A. Meijer, A. S. de Wijn, N. J. Dam, and W. van de Water. Coherent and spontaneous Rayleigh-Brillouin scattering in atomic and molecular gases and gas mixtures. *Phys. Rev. A*, 82:043836, 2010.
- [133] W. Wagner. A convergence proof for Bird’s direct simulation Monte Carlo method for the Boltzmann equation. *J. Stat. Phys.*, 66:1011–1044, 1992.
- [134] M. Wakabayashi, T. Ohwada, and F. Golse. Numerical analysis of the shear and thermal creep flows of a rarefied gas over the plane wall of a Maxwell-type boundary on the basis of the linearized Boltzmann equation for hard-sphere molecules. *Eur. J. Mech. B-Fluids*, 15:175–201, 1996.
- [135] P. Wang, M. T. Ho, L. Wu, Z. L. Guo, and Y. H. Zhang. A comparative study of discrete velocity methods for low-speed rarefied gas flows. *Comput. Fluids*, 161:33 – 46, 2018.
- [136] P. Wang, W. Su, and L. Wu. Thermal transpiration in molecular gas. *Phys. Fluids*, 32:082005, 2020.
- [137] C. S. Wang-Chang and G. E. Uhlenbeck. *Transport Phenomena in Polyatomic Gases*. University of Michigan Engineering Research Rept. No. CM-681, 1951.
- [138] W. Weiss. Continuous shock structure in extended thermodynamics. *Phys. Rev. E*, 52:5760, 1995.
- [139] L. Wu. *Deterministic Numerical Simulation of the Boltzmann and Kinetic Model Equations for Classical and Quantum Dilute Gases*. PhD thesis, University of Strathclyde, Glasgow, 9 2013.
- [140] L. Wu and X. J. Gu. On the accuracy of macroscopic equations for linearized rarefied gas flows. *Advances in Aerodynamics*, 2:2, 2020.
- [141] L. Wu, Q. Li, H. Liu, and W. Ubachs. Extraction of the translational Eucken factor from light scattering by molecular gas. *J. Fluid Mech.*, 901:A23, 2020.
- [142] L. Wu, H. H. Liu, J. M. Reese, and Y. H. Zhang. Non-equilibrium dynamics of dense gas under tight confinement. *J. Fluid Mech.*, 794:252–266, 2016.
- [143] L. Wu, H. H. Liu, Y. H. Zhang, and J. M. Reese. Influence of intermolecular potentials on rarefied gas flows: Fast spectral solutions of the Boltzmann equation. *Phys. Fluids*, 27:082002, 2015.
- [144] L. Wu, J. M. Reese, and Y. H. Zhang. Solving the Boltzmann equation by the fast spectral method: application to microflows. *J. Fluid Mech.*, 746:53–84, 2014.
- [145] L. Wu and H. Struchtrup. Assessment and development of the gas kinetic boundary condition for the Boltzmann equation. *J. Fluid Mech.*, 823:511–537, 2017.
- [146] L. Wu, C. White, T. J. Scanlon, J. M. Reese, and Y. H. Zhang. A kinetic model of the Boltzmann equation for non-vibrating polyatomic gases. *J. Fluid Mech.*, 763:24–50, 2015.

- [147] L. Wu, J. Zhang, H. H. Liu, Y. H. Zhang, and J. M. Reese. A fast iterative scheme for the linearized Boltzmann equation. *J. Comput. Phys.*, 338:431–451, 2017.
- [148] L. Wu, Y. Zhang, and J. M. Reese. Fast spectral solution of the generalized Enskog equation for dense gases. *J. Comput. Phys.*, 303:66–79, 2015.
- [149] H. Yamaguchi, P. Perrier, M. T. Ho, J. G. Méolans, T. Niimi, and I. A. Graur. Mass flow rate measurement of thermal creep flow from transitional to slip flow regime. *J. Fluid Mech.*, 795:690–707, 2016.
- [150] Y. Zheng, A. L. Garcia, and B. J. Alder. Comparison of kinetic theory and hydrodynamics for Poiseuille flow. *J. Stat. Phys.*, 109:495–505, 2002.
- [151] X. Zhong, R. W. MacCormack, and D. R. Chapman. Stabilization of the Burnett equation and applications to hypersonic flows. *AIAA Journal*, 31:1036, 1993.
- [152] L. H. Zhu, X. C. Pi, W. Su, Z. H. Li, Y. H. Zhang, and L. Wu. General synthetic iterative scheme for nonlinear gas kinetic simulation of multi-scale rarefied gas flows. *J. Comput. Phys.*, 430:110091, 2021.